APPLIED COMPUTATIONAL ELECTROMAGNETICS SOCIETY JOURNAL

November 2023
Vol. 38 No. 11
ISSN 1054-4887

The ACES Journal is abstracted in INSPEC, in Engineering Index, DTIC, Science Citation Index Expanded, the Research Alert, and to Current Contents/Engineering, Computing & Technology.

The illustrations on the front cover have been obtained from the ARC research group at the Department of Electrical Engineering, Colorado School of Mines

Published, sold and distributed by: River Publishers, Alsbjergvej 10, 9260 Gistrup, Denmark

NOVEMBER 2023 REVIEWERS

Dillip Kumar Bisoyi
Halim Boutayeb
Yiming Chen
Weng Cho Chew
Arkaprovo Das
Zaheer Ahmed Dayo
Dileepan Dhanasekaran
Fangfang Fan
Alfredo Gomes Neto
Zi He
Pankaj Jha
Nikolaos V. Kantartzis
Enrique Melgoza
Rajesh Natarajan
Mahdi Oliaei
Antonio Orlandi
Andrew Peterson
Shi Pu
Alain Reineix
Kannadhasan S.
Manthan Shah
M. Mohammadi Shirkolaei
Yi Song
Grzegorz Tytko
Marsellas Waller
Li Wu
Xiaoyan Zhang
Wei-Hua Zong

THE APPLIED COMPUTATIONAL ELECTROMAGNETICS SOCIETY JOURNAL

Vol. 38 No. 11 November 2023

TABLE OF CONTENTS

Analysis of Moving Bodies with a Direct Finite Difference Time Domain Method

Mohammad Marvasti and Halim Boutayeb

Department of Electrical Engineering
University of Quebec in Outaouais, Gatineau, Canada, J8X 3X7
halim.boutayeb@uqo.ca

***Abstract* –** This paper proposes an original and thorough analysis of the behavior of electromagnetic waves in the presence of moving bodies by using the finite difference time domain (FDTD) method. Movements are implemented by changing positions of the objects at each time step, through the classical FDTD time loop. This technique is suitable for non-relativistic speeds, thus for most encountered problems in antennas and propagation domain. The numerical aspects that need to be considered are studied. Then, different bodies in motion are examined: plane wave source with matching resistors, observation point, inclined partially reflecting surface (PRS), line source, and metallic cylinder illuminated by a plane wave. The results are compared with those of special relativity which are considered as the references. Some aspects of special relativity are present in the direct FDTD approach, such as the independence of the velocity of electromagnetic wave propagation with the speed of the source and Lorentz local time (with a different physical interpretation). It is shown that the amplitude of the electric field for a moving plane wave source does not increase with the speed of motion, if the impedance of the source is small. Moreover, for a moving scattering metallic wire, one can observe a phenomenon similar to shock waves.

***Index Terms* –** Doppler effect, electromagnetic theory, FDTD method, numerical analysis.

I. INTRODUCTION

The main laws of electromagnetism are contained in Maxwell's equations. The finite difference time domain (FDTD) method is a rigorous and powerful tool for modeling electromagnetic devices. FDTD solves Maxwell's equations directly without any physical approximation, and the maximum problem size is limited only by the extent of the computing power available. The FDTD method is based on the discretization of Maxwell's equations in time and space domains. Invented in 1966 [1], it is applied for the first time in 1975 to study the effect of electromagnetic radiation on human eyes [2]. A microstrip patch antenna is analyzed in time domain in 1989, by using FDTD [3]. In 1990, the FDTD technique is used for the first time for microwave circuits [4]. In 1991, an algorithm is proposed to obtain the electromagnetic radiation in far field from near field results, in FDTD code [5]. Today, the FDTD method is used in a wide range of applications from DC to optics.

The problem of the interaction of electromagnetic waves with moving bodies has been an important subject of interest for a long time, due to its wide application in many domains such as radio sciences, optics, and astrophysics. Numerous investigations have been carried out in this area, which is interesting from a practical and theoretical point of view.

In the microwave domain, the study of electromagnetic problems with moving media is useful in many applications such as radar systems for the detection of vital signs [6, 7] or time-varying waveguides [8]. Time varying waveguides have been proposed for designing new RF devices such as magnet-less circulators or harmonic-free mixers [9-13].

In [14], the authors present a method based on the concept of propagators for analyzing the reflection and transmission of obliquely incident electromagnetic waves by a moving slab. The proposed propagators map the total field at any point inside the slab to the fields on the left-hand side boundary of the slab. In [15], Voigt-Lorentz transformations are used to obtain formulas for the intensity of the reflected and transmitted waves when electromagnetic radiation is incident on a moving dielectric slab. In [16], the reflection and transmission of a plane wave, with its electric vector polarized in the plane of incidence by a moving dielectric slab, are investigated theoretically. Two cases of movement are considered: the dielectric slab moves parallel to the interface, or the dielectric slab, moves perpendicular to the interface. In [17], the problem of the propagation of modes along a moving dielectric interface is considered, using a moving dielectric slab or a moving dielectric circular cylinder. In [18], the reflection of electromagnetic waves from

Submitted On: June 23, 2023
Accepted On: December 6, 2023

https://doi.org/10.13052/2023.ACES.J.381101

a moving dielectric half-space is investigated for parallel and perpendicular motions of a dielectric medium. The paper [19] deals with the scattering of electromagnetic waves from a moving dielectric cylinder illuminated by a plane wave, by using the three-dimensional finite element method (FEM).

The FDTD method has been used by several authors for analyzing electromagnetic problems with moving bodies [20-29]. In [22-29], the authors propose a technique based on the integration Voigt-Lorentz transformations in FDTD. The main challenges of such an approach are to implement a relative time in a full-wave simulator and to consider complex problems with, for example, multiple bodies moving at different speeds.

In this paper, continuing our previous work [30], we assess the effectiveness of a direct FDTD approach where the implementation of movements is done by changing the positions of bodies at each cycle of the FDTD time loop. With this "brute-force" approach, time is implicitly absolute, and Voigt-Lorentz transformations are not implemented. This technique is suitable for non-relativistic electromagnetic problems with moving bodies, thus for most encountered electromagnetic problems.

The numerical aspects that need to be considered in the proposed approach are studied in detail. Then, different problems are investigated: moving plane wave source with matching resistors, moving observation point, moving inclined partially reflecting surface (PRS), moving line source, and moving metallic cylinder illuminated by a plane wave. The results, in terms of Doppler frequency shift and changes in amplitude of the electric field, are compared with those of special relativity, which are considered as the references. Some aspects of special relativity are present in the direct FDTD approach, such as the independence of the velocity of electromagnetic wave propagation with the speed of the source and Lorentz local time (with a different physical interpretation). Some of the obtained results agree with special relativity. Other ones are different, but the differences are negligible for non-relativistic speeds. The results obtained with our analysis give new physical insights into the propagation of waves with moving bodies. In particular, it is shown that the amplitude of the electric field for a moving plane wave source does not increase with the speed of motion, if the impedance of the source is small. Moreover, for a moving scattering metallic wire, one can observe a phenomenon similar to shock waves. In the literature, electromagnetic shock waves were analyzed in different contexts, such as gyromagnetic media and non-linear transmission lines [31-33].

The remainder of the paper is organized as follows. Section II presents numerical aspects that need to be taken into account. Section III shows the study of the frequency shift and amplitude variation of the electric field in time and frequency domains for a moving plane wave source. A moving observation point is considered in Section IV. Section V deals with the illumination by a plane wave of a moving partially reflecting surface (PRS) with different angles of inclination of the PRS. Problems with moving line source and moving metallic wire are considered in Section VI. Concluding remarks are given in Section VII.

II. ANALYSIS OF THE NUMERICAL ASPECTS

A. Type of excitation

For better analysis and detection of the frequency variation due to the Doppler effect, we consider as the exciting source a windowed sine signal $E_i(t) = \Pi(\frac{f_0}{N}t)\sin(2\pi f_0 t)$, presenting a modulated sinusoid $E_i(f) = \frac{N}{f_0}\mathrm{Sinc}(\frac{f-f_0}{Nf_0})$ spectrum, where f_0 is the frequency of excitation and N is the number of periods of sine function considered for simulation. This excitation provides a sharp frequency spectrum and makes frequency identification accurate and simple.

B. Dispersion and stability

For simplicity, in the paper, we consider the same space mesh in all axes, $\delta_x = \delta_y = \delta_z$. Due to numerical dispersion, the phase velocity of the wave changes with the angle in the computational volume [34]. This effect decreases by reducing the size of the space mesh. For example with $\delta_x = \frac{\lambda}{40}$ the maximum of velocity change is about 0.05% [34].

The dispersion equation and the stability criterion are the same as those calculated without motion, for the problems considered in this paper (moving source, moving observer, and moving scatterers). Different dispersion equations and stability criteria would be required if the field is moved, but this problem is not considered here. The FDTD dispersion equation for a plane wave propagating in the x-axis can be written

$$\omega = \frac{2}{\delta_t}\arcsin\left(\frac{c\delta_t}{\delta_x}\sin\left(\frac{k\delta_x}{2}\right)\right), \tag{1}$$

where ω is pulsation frequency, δ_t is time step, c is the speed of light in vacuum, and k is the propagation constant. Figure 1 shows the dispersion diagram for different values of space mesh. In next subsection, the propriety of the dispersion diagram is used to make undesirable waves having high frequencies propagate with lower speed than desirable waves, for better differentiation.

C. Effect of discontinuous motion and its mitigation

Let us consider a plane wave source parallel to zoy plane and moving in x direction. The plane wave source is constituted of z-polarized electric current sources. Due to the discretization in the classical FDTD numerical

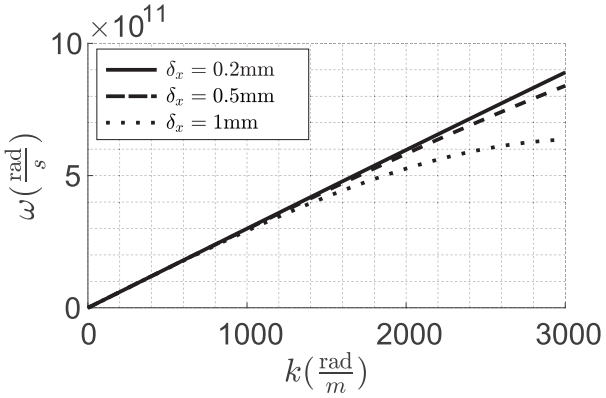

Fig. 1. Numerical dispersion for different values of δ_x.

method, the source location doesn't change continuously because it doesn't move inside a cell. Instead, in the FDTD code, for a specific value of source motion speed v, the position of the source is fixed for $n\delta_t$ with $n = \left\lfloor \frac{\delta_x}{v\delta_t} \right\rfloor$. $\lfloor\cdot\rfloor$ stands for floor function. δ_t and δ_x are the time step and space mesh. Then, after this time, the source moves one cell in the desired direction. Figure 2 illustrates the discontinuous movement of the source in FDTD, the ideal continuous motion, and an approximate model for the discontinuous movement. Without motion, the time-domain signal received from a plane wave can be written

$$E(t) = \exp(-j(kx + \omega t)). \tag{2}$$

As shown Fig. 2, the position of the source can be approximated by using a sine function

$$x_p(t) = x_0 + vt + a\sin(\omega_{\mathrm{d}} t), \tag{3}$$

where $a = \frac{\delta_x}{2}$ and $\omega_{\mathrm{d}} = \frac{2\pi}{\delta_t \left\lfloor \frac{\delta_x}{v\delta_t} \right\rfloor}$. Because of the additional term $a\sin(\omega_{\mathrm{d}} t)$, the time-domain signal received for the moving plane wave source can be written

$$E''(t) = E'(t)\exp(-j(ka\sin(\omega_{\mathrm{d}} t))), \tag{4}$$

where $E'(t)$ is the signal received by observer if the source moves continuously. We can expand (4) by using the Fourier series

$$E''(t) = E'(t)\sum_{n=-\infty}^{\infty} c_n \exp(jn\omega_{\mathrm{d}} t), \tag{5}$$

$$c_n = \frac{\omega_{\mathrm{d}}}{2\pi}\int_{-\frac{\pi}{\omega_{\mathrm{d}}}}^{\frac{\pi}{\omega_{\mathrm{d}}}} e^{-j(ka\sin(\omega_{\mathrm{d}} t))} e^{-jn\omega_{\mathrm{d}} t}\, dt. \tag{6}$$

With a change of variable $t' = \omega_{\mathrm{d}} t$, the coefficients c_n can be written

$$c_n = \frac{1}{2\pi}\int_{-\pi}^{\pi} e^{-j(ka\sin(t'))} e^{-jnt'}\, dt'. \tag{7}$$

By using the definition of the Bessel function of the first kind, equation (5) can be expressed as

$$E''(t) = E'(t)\sum_{n=-\infty}^{\infty} \mathrm{J}_n(ka)\exp(jn\omega_{\mathrm{d}} t). \tag{8}$$

This shows that the received signal contains $E'(t)$ and other waves that are made from the modulation of $E'(t)$ with center frequencies of $n\omega_{\mathrm{d}}$, $n = 1, 2, \ldots$.

The FDTD simulations confirm our analysis, as shown in Fig. 3 (a), where the windowed sine signal is the expected signal for continuous motion, and the high frequency modulated signal is due to the discontinuous

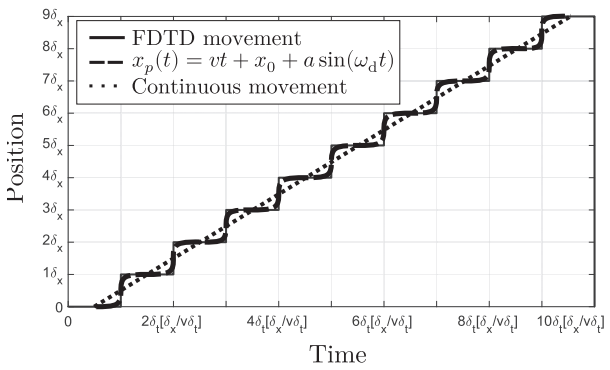

Fig. 2. Discontinuous movement of plane wave source.

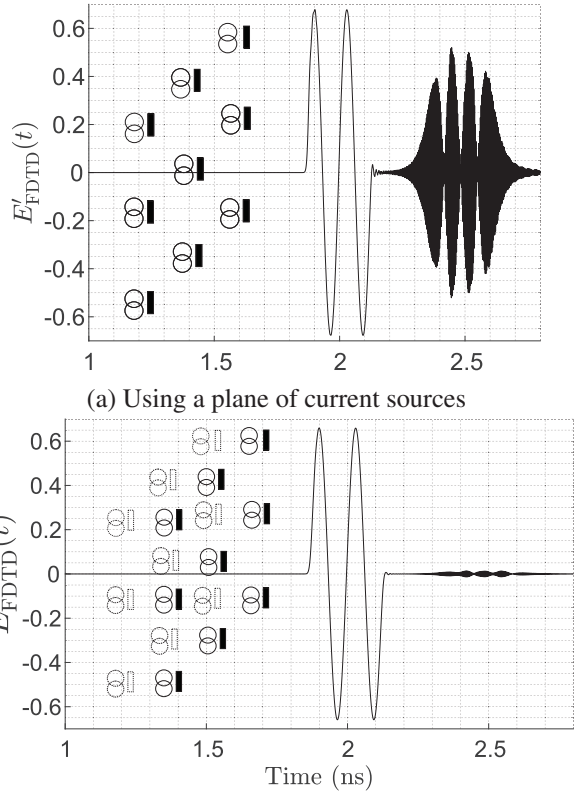

(a) Using a plane of current sources

(b) Using two layers of current sources

Fig. 3. Observed signal in time domain for a moving plane wave source in FDTD. Using two layers for the plane wave source can mitigate the undesirable effects due to discontinuous motion.

motion effect. In this figure, we were able to separate undesirable signals from the expected signal by using the FDTD dispersion equation such that the waves at higher frequencies propagate with less speed.

We propose now a technique to mitigate the undesirable effects. By using a second layer of current sources to make the plane wave source, we can show that the discontinuous motion adds the term $a\sin(\omega_d t)+a\sin(\omega_d t+\pi) = a\sin(\omega_d t)$ - $a\sin(\omega_d t) = 0$. Thus, this method can suppress the undesirable effects. FDTD simulations, as shown in Fig. 3 (b), confirm that by using two layers of current sources, the undesirable effects are mitigated. The same phenomena have been observed by using a moving PRS, whose thickness needs to be at least one cell in order to mitigate the undesirable effects.

D. Space mesh and time step

Because of the discontinuous motion in FDTD, as illustrated in Fig. 2, the space mesh needs to be sufficiently small to detect the smallest velocity considered in a problem. The pulsation frequency ω_d needs to be larger than the maximum pulsation frequency considered, ω_{max}. Based on empirical analysis,

$$\omega_d > 2\omega_{max}. \tag{9}$$

After simplification, we can show that the following condition is required:

$$\delta_x < 0.5\frac{v}{f_{max}}, \tag{10}$$

where f_{max} is the maximum frequency considered. From this equation, if the speed v is decreased, δ_x must be decreased. The time step needs also to be reduced because of the classical stability criterion $\delta_t < \frac{\delta_x}{c\sqrt{3}}$.

III. MOVING PLANE WAVE SOURCE

A. Structure and definitions of the analyzed parameters

A plane wave source that is moving in $+\hat{x}$ direction toward the observer with speed v, is considered, as shown in Fig. 4. Mur's absorbing boundary conditions (ABCs) [35] are used in boundaries parallel to *zoy* plane. Perfect magnetic conductors (PMCs) and perfect electric conductors (PECs) are used in other boundaries to model an infinite structure.

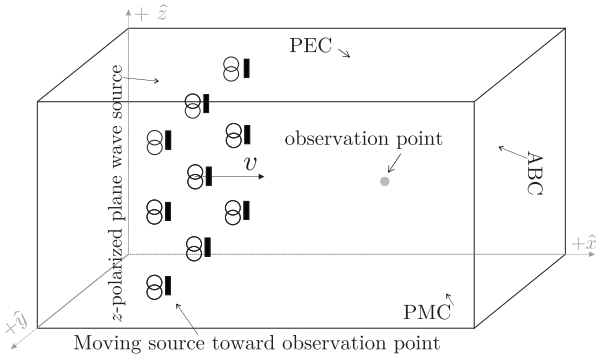

Fig. 4. Plane wave source moving toward the observer.

E'_z and E_z, are the electric field components in z-axis observed by the observation point for a moving source and for a source at rest, respectively. f' is the frequency of observed signals when the source is moving, and f is the frequency when the source is at rest. A'_f and A'_t are the amplitudes of observed signals in the frequency and time domains, respectively, when the source is moving. A_f and A_t are the same amplitudes when the source is at rest.

B. Model of the plane wave source

Figure 5 presents the model of a realistic plane wave source in FDTD. It is made of z-polarized electric current sources and resistors with resistance R. A similar model has been used in [36, 37] for analyzing a Fabry-Perot cavity excited from its inside.

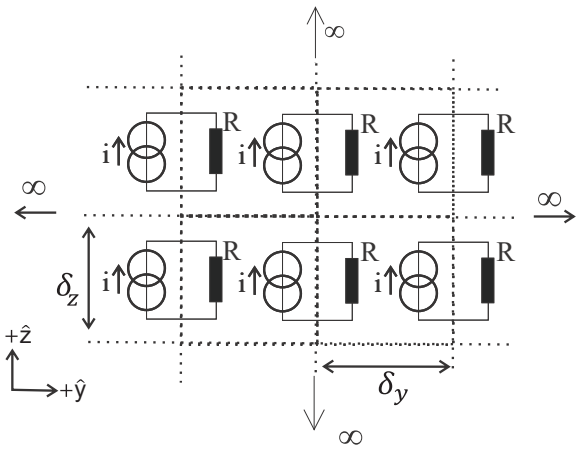

Fig. 5. Model of a plane wave source used in FDTD.

C. Speed of wave propagation independent of the speed of the source

By using two observation points, one can measure the speed of propagation of the plane wave for different values of the speed of the plane wave source. It is confirmed that the speed of wave propagation in FDTD does not change when the source is moving. This shows that the direct FDTD method is in agreement with the following postulate from the special theory of relativity: *"light is always propagated with a definite velocity c which is independent of the state of motion of the emitting body"*[38].

D. Doppler frequency shift and amplitude variation of electric field in frequency domain

An ideal source with low output impedance (R is small) is considered. Figure 6 (a) shows the signal

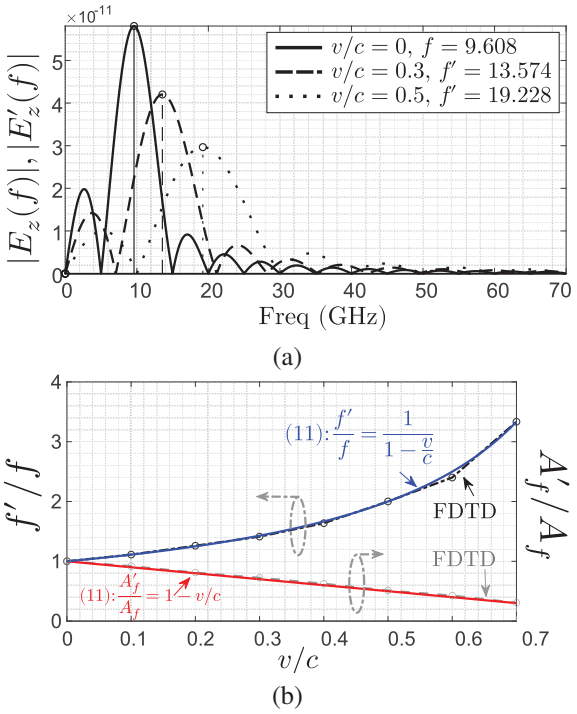

Fig. 6. Simulated results for an ideal plane wave source moving with speed v toward the observer: (a) Observed signal in the frequency domain for different values of $\frac{v}{c}$, (b) Doppler frequency shift and amplitude variation of the observed electric field in frequency domain versus $\frac{v}{c}$.

observed in the frequency domain at different normalized speeds of motion $\frac{v}{c}$. From these curves, the changes of the main frequency and of the amplitude at the main frequency due to motion are measured, as shown in Fig. 6 (b), and the curve-fitted results can be written as

$$\frac{f'}{f} = \frac{A_f}{A'_f} = \frac{1}{1-\frac{v}{c}}. \tag{11}$$

In special relativity, the Doppler effect formula for the moving source is given by $\frac{f'}{f} = \gamma^{-1}\frac{1}{1-\frac{v}{c}}$, where $\gamma = \frac{1}{\sqrt{1-(\frac{v}{c})^2}}$. A technique will be proposed later in order to take into account the relativistic effects.

E. Effect of the impedance of a plane wave source in motion

The amplitude of the signal in time domain does not change with the motion of the source if the output impedance of the source is small, as shown in Fig. 7 (a).

A high-impedance source can be modeled by using current sources without the resistors. For this case, Fig. 7 (b) shows that the amplitude of the signal in time domain increases with the speed of the source. The simulated results fit with the closed-form expression $\frac{A'_t}{A_t} = \frac{1}{1-\frac{v}{c}}$.

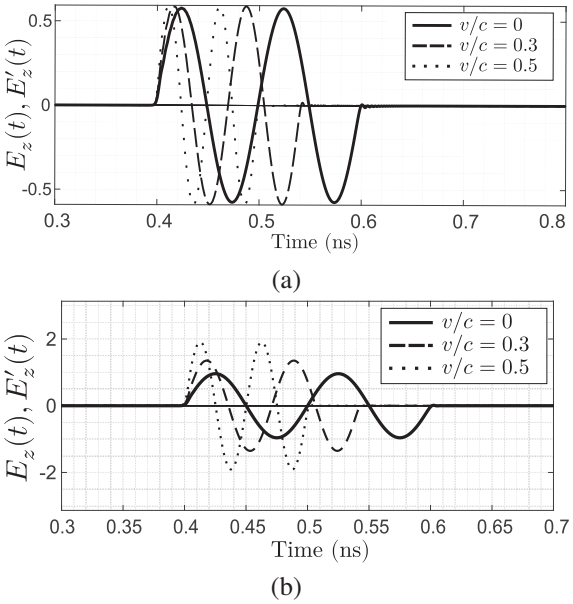

Fig. 7. Simulated signal in time domain for plane wave source moving with speed v toward observer, for different values of $\frac{v}{c}$: (a) Ideal plane wave source, (b) Plane wave source without resistors.

Based on the analysis presented in this subsection, it is suggested that previous studies on electromagnetism with moving objects should be revisited. For example, Heaviside derived from Maxwell's equations the electric field of a moving charge, and he found that the amplitude of this electric field grows without bounds with $\frac{v}{c}$ [39]. At Heaviside's time, this effect has been used as an argument against the possibility for a charge (or any object) to move at a speed greater than the speed of light. However, if the charge has a low output impedance, the amplitude of its electric field should not increase with the motion, as it has been shown in the present work.

F. Technique for implementing relativistic Doppler effect for moving source

The relativistic Doppler effect for the moving source can be obtained in the direct FDTD method, if the signal of the moving source is modified before its introduction in the FDTD time loop. This can be done by using the formula

$$E_{z,source\_modif}(t) = E_{z,source}(\gamma^{-1}t). \tag{12}$$

It is worth mentioning that, with the proposed approach, it is possible to consider multiple sources moving at different relativistic speeds.

IV. MOVING OBSERVATION POINT

A. Structure and definitions of the parameters

Let us consider an observation point moving in -x direction (toward the source) with the speed v as shown in Fig. 8.

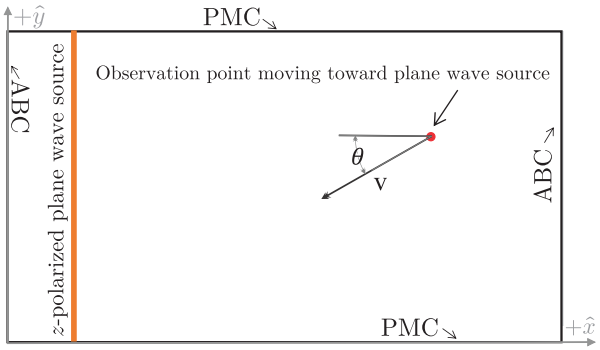

Fig. 8. Observation point moving toward a plane wave source, in normal or oblique direction.

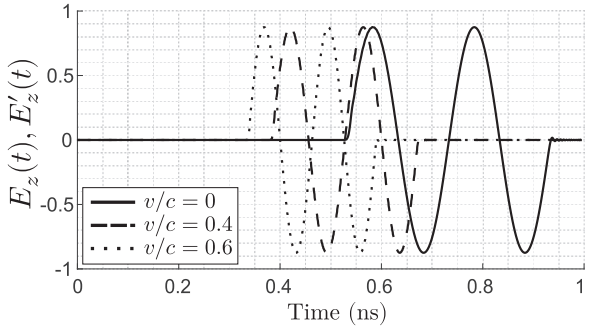

Fig. 9. Simulated signal in time domain for observation point moving in normal direction toward -x with speed v, for different values of $\frac{v}{c}$.

The observer measures E'_z and E_z, the electric field component in z-axis for moving observer and for observer at rest, respectively. We call f' the frequency of observed waves when the observation point is moving and f the frequency when the observer is at rest. A'_f and A'_t are the amplitudes of observed waves in the frequency and time domains, respectively, when observer is moving. A_f and A_t are the same amplitudes when observer is at rest.

B. Time domain signal and Lorentz local time

Figure 9 shows the signal received by the observer in FDTD, in the time domain. One can note that the amplitude of the signal does not change with the motion, i.e, $\frac{A'_t}{A_t} = 1$. We also observe that

$$E'_z(t) = E_z\left(t(1+\frac{v}{c})\right). \tag{13}$$

For example, for $t = 0.34ns$ and $v/c = 0.6$, we have $E'_z(0.34) = E_z(0.34(1+0.6)) = E_z(0.544)$. This has been verified for different values of t and for different values of v/c. Equation (13) can be explained by the fact that if we replace x with x-vt in the phase of a plane wave kx-ωt, we obtain $k(x$-$vt)$ - $\omega t = kx$-$\omega t(1+kv/\omega) = kx$-$\omega t(1+v/c)$, since $k/\omega = 1/c$ for a plane wave propagating in free space.

The parameter $t(1\pm v/c)$ of (13) has an analogy with Lorentz "local" time $t' = t \pm xv/c^2$. Indeed $t(1\pm v/c) = t \pm tv/c = t \pm xv/c^2$. The last calculation is obtained by replacing the second t with x/c.

The time parameter t' in Lorentz transformation is given by $t' = \gamma(t \pm xv/c^2)$ [38]. In special relativity, this parameter t', which is often written $t' = \gamma t(1\pm v/c)$, represents the true time for an observer in a moving frame. In the direct FDTD program, the term γ is missing, and the parameter $t(1\pm v/c)$ represents the Doppler effect in time domain. Thus, Lorentz local time is present in the direct FDTD method but with a different physical interpretation.

C. Doppler frequency shift and amplitude of the electric field in frequency domain

Figure 10 shows the signal received by the observer in FDTD, in frequency domain. As shown in Fig. 11, the center frequency and the amplitude in frequency domain vary according to

$$\frac{f'}{f} = \frac{A_f}{A'_f} = 1 + \frac{v}{c}. \tag{14}$$

In special relativity, the Doppler effect formula for the moving observer is given by $\frac{f'}{f} = \gamma(1+\frac{v}{c})$. Based on the time domain results in the previous subsection, the change of amplitude in frequency domain can be understood by the relation $\mathscr{F}(g(|a|t)) = \frac{1}{|a|}\mathscr{G}(\frac{f}{|a|})$, where $\mathscr{F}(\cdot)$ stands for Fourier transform operator, $\mathscr{G}(f)$ is Fourier transform function of a signal $g(t)$, and a is a constant. In our case $a = 1+\frac{v}{c}$.

From Fig. 10, it is interesting to note that $\int |E'_z(f)|df = \int |E_z(f)|df$ = Constant for any value of $\frac{v}{c}$.

For motion in $+x$ direction (observer moving away from the source), in (14), one should replace v with -v (these cases were validated numerically).

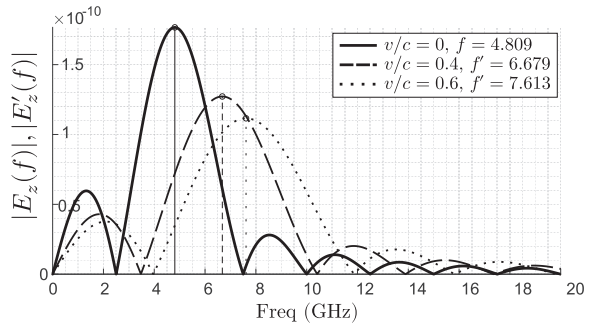

Fig. 10. Simulated signal in frequency domain for observation point moving with speed v toward -x in normal direction, for different values of $\frac{v}{c}$.

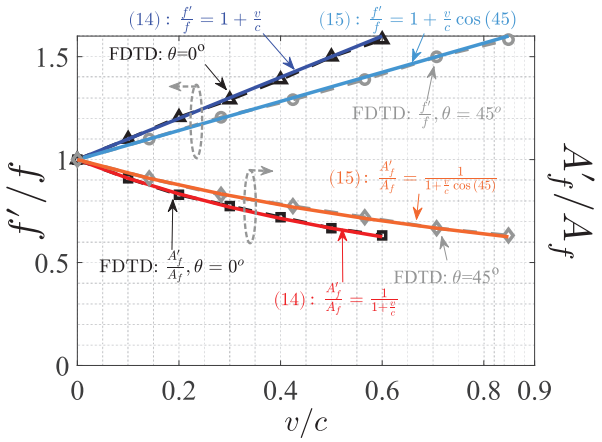

Fig. 11. Simulated Doppler frequency shift and amplitude of the electric field in frequency domain for observation point moving with speed v toward -x in normal direction or at 45°, versus $\frac{v}{c}$.

D. Motion in oblique direction

We consider now that the observer is moving obliquely with the angle θ toward the source. The results are presented in Fig. 11. The changes of the frequency and of amplitude in frequency domain agree now with

$$\frac{f'}{f} = \frac{A_f}{A'_f} = 1 + \frac{v}{c}\cos\theta. \tag{15}$$

According to special relativity, we should have $\frac{f'}{f} = \gamma(1+\frac{v}{c}\cos\theta)$. Again, the missing γ factor can be omitted for non-relativistic speeds.

E. Technique for implementing relativistic Doppler effects for moving observer

The relativistic Doppler effect for the moving observer can be obtained in the direct FDTD method, if the observed signal is modified (post-processing), by using the following formula:

$$E_{z,obs\_modif}(t) = E_{z,obs}(\gamma t). \tag{16}$$

V. MOVING PARTIALLY REFLECTING SURFACE

A. Straight PRS

A PRS that is parallel to the plane wave source is moving in -x direction (toward the source), with the speed v. The observation point is between the source and the PRS, as shown in Fig. 12. FDTD simulations (Fig. 13) show that frequency can be written

$$\frac{f'}{f} = \frac{1+\frac{v}{c}}{1-\frac{v}{c}}. \tag{17}$$

(17) can be understood as the combination of two Doppler effects: the frequency shift due to an observer (the PRS) moving toward the source (numerator part)

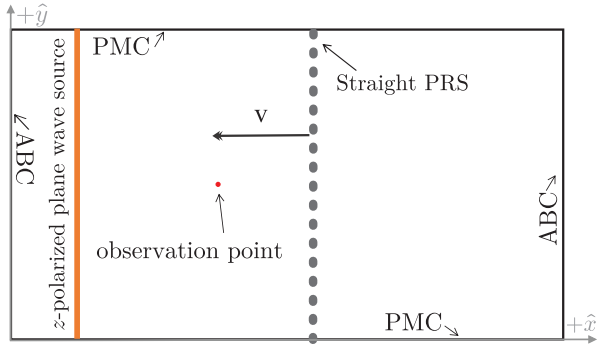

Fig. 12. Straight PRS moving toward a plane wave source.

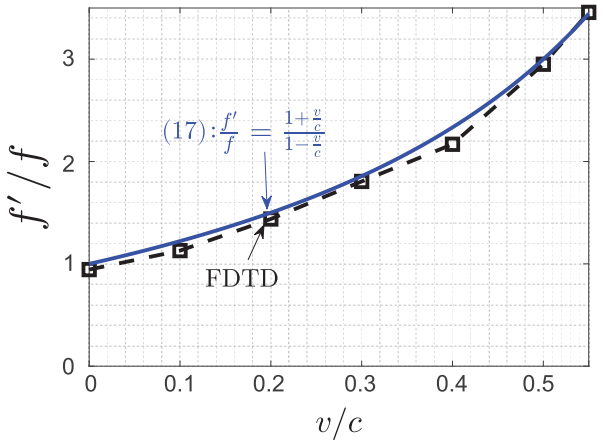

Fig. 13. Simulated Doppler frequency shift for straight PRS moving in -x direction (toward the source), versus $\frac{v}{c}$.

and the frequency shift due to a source (the PRS acts as a source after diffracting the received field) moving toward the observer (denominator part). This formula is well known by radar engineers.

It is interesting to note that special relativity predicts the same formula (17) for a moving plane reflector with normal incidence. Thus, the direct FDTD method could be used for some problems at relativistic speeds.

B. Inclined PRS

The PRS is now inclined with the angle θ_{PRS}, and it is moving in -x direction (toward the source), with the speed v (Fig. 14). First, it is worth noting that a wave propagating at an angle θ in a frame moving with the speed v will be seen in the stationary frame as propagating at the angle α_B, as given by Bradley's aberration formula [40] (this formula has been validated with FDTD)

$$\alpha_B = \arctan\left(\frac{\sin(\theta)}{\cos(\theta)+\frac{v}{c}}\right). \tag{18}$$

For inclined PRS, a graphical method can be used to derive the Doppler effect formula, as illustrated in

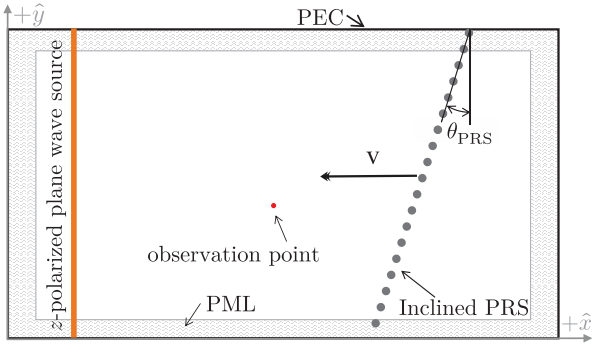

Fig. 14. Inclined PRS moving toward a plane wave source.

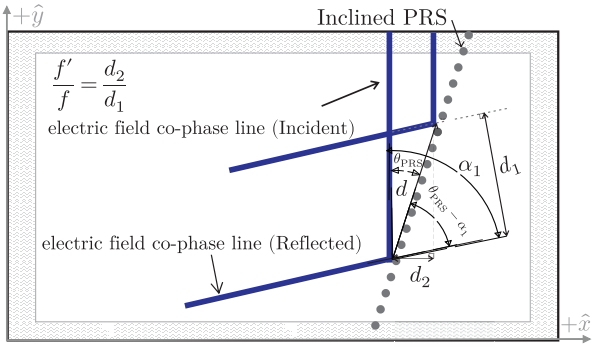

Fig. 15. Graphical method for deriving the frequency of reflected wave for a moving inclined PRS.

Fig. 15. From this figure, we obtain

$$\frac{f'}{f}=\frac{\sin(\theta_{PRS})}{\sin(\alpha_1\text{-}\theta_{PRS})}, \tag{19}$$

where α_1 is the angle of the reflected wave, and it can be written

$$\alpha_1 = 2\arctan\left(\frac{\tan(\theta_{PRS})}{1+\frac{v}{c}}\right). \tag{20}$$

For a PRS moving in $+x$ direction (away from the source), the same formula (19) can be obtained, except that α_1 should be replaced by

$$\alpha_2 = \pi - 2\arctan\left(\frac{\tan(\theta_{PRS})}{1-\frac{v}{c}}\right). \tag{21}$$

Good agreements are obtained between full-wave simulations and the proposed analytical formulas, as shown in Fig. 16. Numerical and analytical solutions for α_1 and α_2 are shown in Fig. 17, where we have also plotted α_B (for $\theta = 90°$) for comparison. Figure 18 shows how the different angles are measured accurately, with a numerical protractor.

Equation (19) is novel and simple to apply. The relativistic formula, which is given by $\frac{f'}{f}=\frac{1+2\frac{v}{c}\cos(\theta_{PRS})+(\frac{v}{c})^2}{1-(\frac{v}{c})^2}$, differs from the direct FDTD only for $\theta_{PRS}\neq 0°$ and relativistic speeds.

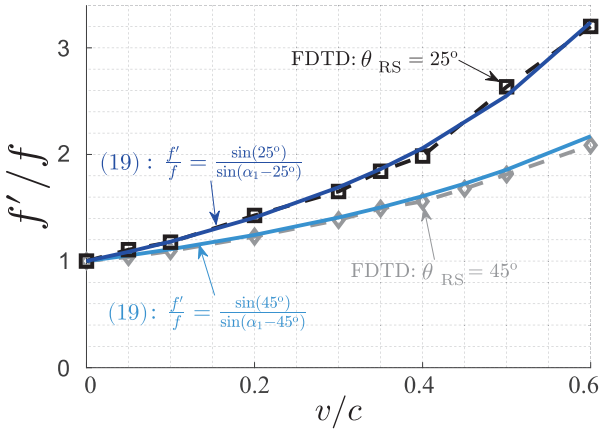

Fig. 16. Simulated Doppler frequency shift for inclined PRS moving toward the source, for $\theta_{PRS} = 45°$ and $25°$, versus $\frac{v}{c}$.

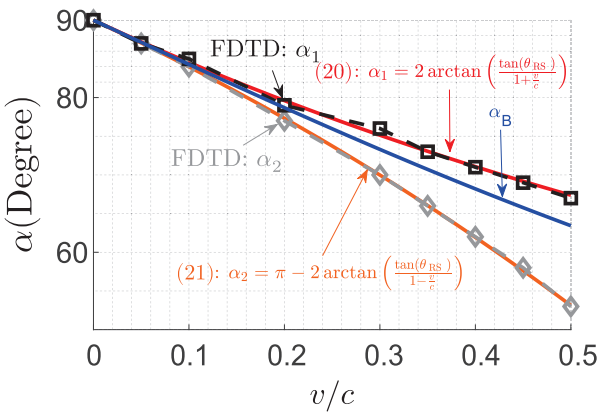

Fig. 17. Simulated reflection angles for inclined PRS moving with speed v toward $\pm x$ directions, with $\theta_{PRS} = 45°$. Bradley's aberration angle α_B is also plotted for comparison.

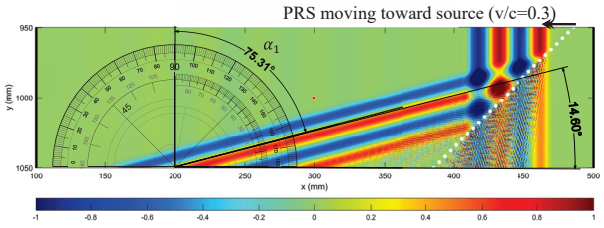

Fig. 18. Illustration of the method used to measure the angle of reflected wave in FDTD simulations for a moving inclined PRS, with a numerical protractor. In this example, the PRS moves toward the source in -x direction with $\frac{v}{c} = 0.3$ and $\theta_{PRS} = 45°$. The measured angle gives α_1 which is plotted versus v/c in Fig. 17. One region part of the computational volume is shown, for better visualization.

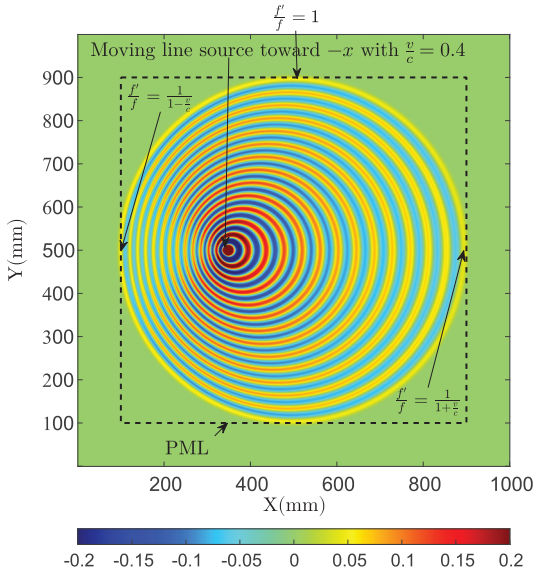

Fig. 19. Electric field distribution for a line source moving toward -x direction with $\frac{v}{c}=0.4$.

VI. MOVING LINE SOURCE AND METALLIC WIRE ILLUMINATED BY A PLANE WAVE

A. Moving line source

We consider a line source made of current sources and which generates a cylindrical wave when it is at rest. Figure 19 shows the electric field distribution at a time instant when the line source is in motion. By measuring the different wavelengths (i.e, distances between consecutive maxima) at the different directions, we obtain results for the Doppler effect that agree with the analysis of the plane wave source, as shown in Fig. 19.

B. Moving metallic wire illuminated by a plane wave

A metallic wire is moving in -x direction with speed v, and it is illuminated by a plane wave propagating in $+x$ direction, with speed c. Figure 20 shows the electric field distribution at a time instant. Based on the analysis of the wavelengths, the Doppler effect is indicated at different directions in Fig. 20. These results confirm the previous analysis on the plane reflector.

In Fig. 20, we can observe the presence of additional waves, which are highlighted in the back of the moving metallic wire in a region with triangular shape. Based on simulations not shown here, the time step and the cell size have no effect on these additional waves. We conclude that they are not due to numerical effects, but they are inherent to Maxwell's equations. They can be associated with shock waves, due to their similarities with these types of waves. These waves can also be observed if the metallic wire moves in a direction perpendicular to the plane wave, as shown in Fig. 21. It should

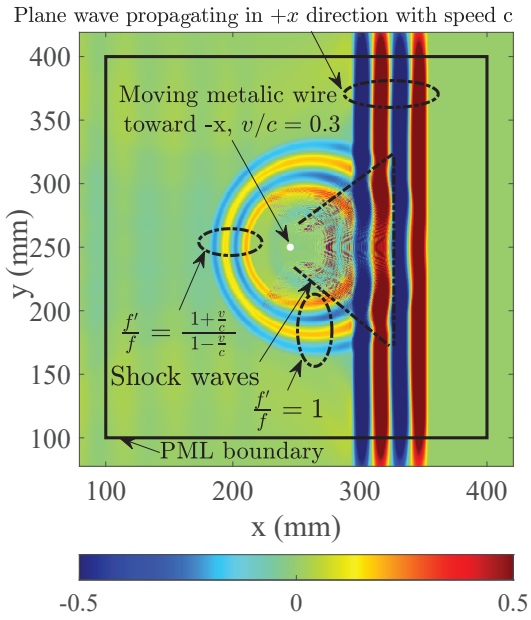

Fig. 20. Electric field distribution for a metallic wire moving toward a plane wave source in -x direction with $\frac{v}{c}=0.3$. The plane wave is propagating in $+x$ direction with speed c.

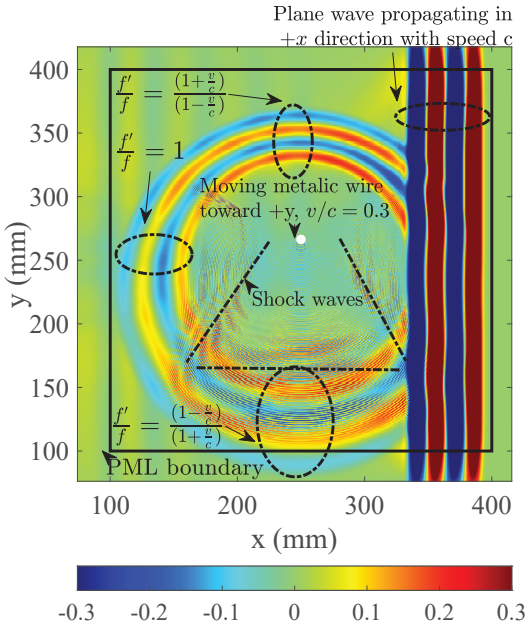

Fig. 21. Electric field distribution for a metallic wire moving in $+y$ direction with $\frac{v}{c}=0.3$, and a plane wave propagating in $+x$ direction with speed c.

be noted that electromagnetic shock waves have been already observed in the literature but with other contexts, such as gyromagnetic media and non-linear transmission lines [31-33].

VII. CONCLUSION

In this paper, we propose a non-relativistic finite difference time domain method, and we assess the effectiveness of this technique by analyzing electromagnetic problems with different bodies in motion: plane wave source, line source, observer, partially reflecting surface and metallic wire. In the proposed direct FDTD method, movements are implemented by changing positions of the objects at different time instants, through the classical FDTD time loop.

First, the numerical aspects are analyzed thoroughly. Then, several analytical formulas for the Doppler frequency shifts, amplitudes of electric field and angles of reflection are derived, validated with full-wave simulations and compared with relativistic formulas (reference formulas). These results show that the direct FDTD method is suitable for non-relativistic speeds.

Furthermore, some aspects of special relativity are present in the direct FDTD approach, such as the independence of the velocity of electromagnetic wave propagation with the speed of the source and Lorentz local time (with a different physical interpretation). The results obtained with our analysis give new physical insights into the propagation of waves with moving bodies. For instance, it is shown that the amplitude of the electric field for a moving plane wave source does not increase with the speed of motion, if the impedance of the source is small. Moreover, electromagnetic shock waves can be observed in FDTD simulations of a metallic wire illuminated by a plane wave.

The proposed technique has the advantage of being simple to implement, and it can be used to consider, for non-relativistic speeds, multiple objects moving at different speeds, accelerating objects, or rotating objects.

REFERENCES

[1] K. Yee, "Numerical solution of initial boundary value problems involving Maxwell's equations in isotropic media," *IEEE Transactions on Antennas and Propagation*, vol. 14, no. 3, pp. 302-307, 1966.

[2] A. Taflove and M. E. Brodwin, "Numerical solution of steady-state electromagnetic scattering problems using the time-dependent Maxwell's equations," *IEEE Transactions on Microwave Theory and Techniques*, vol. 23, no. 8, pp. 623-630, 1975.

[3] A. Reineix and B. Jecko, "Analysis of microstrip patch antennas using finite difference time domain method," *IEEE Transactions on Antennas and Propagation*, vol. 37, no. 11, pp. 1361-1369, 1989.

[4] D. M. Sheen, S. M. Ali, M. D. Abouzahra, and J.-A. Kong, "Application of the three-dimensional finite-difference time-domain method to the analysis of planar microstrip circuits," *IEEE Transactions on Microwave Theory and Techniques*, vol. 38, no. 7, pp. 849-857, 1990.

[5] K. S. Yee, D. Ingham, and K. Shlager, "Time-domain extrapolation to the far field based on FDTD calculations," *IEEE Transactions on Antennas and Propagation*, vol. 39, no. 3, pp. 410-413, 1991.

[6] M. S. Rabbani, J. Churm, and A. P. Feresidis, "Fabry–Pérot beam scanning antenna for remote vital sign detection at 60 GHz," *IEEE Transactions on Antennas and Propagation*, vol. 69, no. 6, pp. 3115-3124, 2021.

[7] L. Chioukh, H. Boutayeb, D. Deslandes, and K. Wu, "Noise and sensitivity of harmonic radar architecture for remote sensing and detection of vital signs," *IEEE Transactions on Microwave Theory and Techniques*, vol. 62, no. 9, pp. 1847-1855, 2014.

[8] S. Taravati and A. A. Kishk, "Space-time modulation: Principles and applications," *IEEE Microwave Magazine*, vol. 21, no. 4, pp. 30-56, 2020.

[9] A. Mock, D. Sounas, and A. Alù, "Magnet-free circulator based on spatiotemporal modulation of photonic crystal defect cavities," *ACS Photonics*, vol. 6, no. 8, pp. 2056-2066, 2019.

[10] H. Rajabalipanah, A. Abdolali, and K. Rouhi, "Reprogrammable spatiotemporally modulated graphene-based functional metasurfaces," *IEEE Journal on Emerging and Selected Topics in Circuits and Systems*, vol. 10, no. 1, pp. 75-87, 2020.

[11] A. Alù, "Beyond passivity and reciprocity with time-varying electromagnetic systems," pp. 1863-1864, 2020.

[12] L. Zhang, X. Q. Chen, R. W. Shao, J. Y. Dai, Q. Cheng, G. Castaldi, V. Galdi, and T. J. Cui, "Breaking reciprocity with space-time-coding digital metasurfaces," *Advanced Materials*, vol. 31, no. 41, p. 1904069, 2019.

[13] X. Wang, A. Diaz-Rubio, H. Li, S. A. Tretyakov, and A. Alu, "Theory and design of multifunctional space-time metasurfaces," *Physical Review Applied*, vol. 13, no. 4, p. 044040, 2020.

[14] A. Kashaninejad-Rad, A. Abdolali, and M. M. Salary, "Interaction of electromagnetic waves with a moving slab: fundamental dyadic method," *Progress in Electromagnetics Research B*, vol. 60, 2014.

[15] S. Stolyarov, "Reflection and transmission of electromagnetic waves incident on a moving dielectric slab," *Radiophysics and Quantum Electronics*, vol. 10, no. 2, pp. 151-153, 1967.

[16] C. Yeh and K. Casey, "Reflection and transmission of electromagnetic waves by a moving dielectric slab," *Physical Review*, vol. 144, no. 2, p. 665, 1966.

[17] C. Yeh, "Propagation along moving dielectric wave guides," *JOSA*, vol. 58, no. 6, pp. 767-770, 1968.

[18] C. Yeh, "Brewster angle for a dielectric medium moving at relativistic speed," *Journal of Applied Physics*, vol. 38, no. 13, pp. 5194-5200, 1967.

[19] G. Pelosi, R. Coccioli, and R. Graglia, "A finite-element analysis of electromagnetic scattering from a moving dielectric cylinder of arbitrary cross section," *Journal of Physics D: Applied Physics*, vol. 27, no. 10, p. 2013, 1994.

[20] F. Harfoush, A. Taflove, and G. A. Kriegsmann, "A numerical technique for analyzing electromagnetic wave scattering from moving surfaces in one and two dimensions," *IEEE Transactions on Antennas and Propagation*, vol. 37, no. 1, pp. 55-63, 1989.

[21] M. J. Inman, A. Z. Elsherbeni, and C. Smith, "Finite difference time domain simulation of moving objects," in *Proc. of IEEE Radar Conf.*, pp. 439-445, 2003.

[22] K. Zheng, X. Liu, Z. Mu, and G. Wei, "Analysis of scattering fields from moving multilayered dielectric slab illuminated by an impulse source," *IEEE Antennas and Wireless Propagation Letters*, vol. 16, pp. 2130-2133, 2017.

[23] K.-S. Zheng, J.-Z. Li, G. Wei, and J.-D. Xu, "Analysis of Doppler effect of moving conducting surfaces with Lorentz-FDTD method," *Journal of Electromagnetic Waves and Applications*, vol. 27, no. 2, pp. 149-159, 2013.

[24] Y. Liu, K. Zheng, Z. Mu, and X. Liu, "Reflection and transmission coefficients of moving dielectric in half space," in *2016 11th International Symposium on Antennas, Propagation and EM Theory (ISAPE)*, pp. 485-487, IEEE, 2016.

[25] K. Zheng, Z. Mu, H. Luo, and G. Wei, "Electromagnetic properties from moving dielectric in high speed with Lorentz-FDTD," *IEEE Antennas and Wireless Propagation Letters*, vol. 15, pp. 934-937, 2015.

[26] Y. Li, K. Zheng, Y. Liu, and L. Xu, "Radiated fields of a high-speed moving dipole at oblique incidence," in *2017 International Applied Computational Electromagnetics Society Symposium (ACES)*, pp. 1-2, IEEE, 2017.

[27] K. Zheng, Y. Li, X. Tu, and G. Wei, "Scattered fields from a three-dimensional complex target moving at high speed," in *2018 International Applied Computational Electromagnetics Society Symposium-China (ACES)*, pp. 1-2, IEEE, 2018.

[28] K. Zheng, Y. Li, L. Xu, J. Li, and G. Wei, "Electromagnetic properties of a complex pyramid-shaped target moving at high speed," *IEEE Transactions on Antennas and Propagation*, vol. 66, no. 12, pp. 7472-7476, 2018.

[29] K. Zheng, Y. Li, S. Qin, K. An, and G. Wei, "Analysis of micromotion characteristics from moving conical-shaped targets using the Lorentz-FDTD method," *IEEE Transactions on Antennas and Propagation*, vol. 67, no. 11, pp. 7174-7179, 2019.

[30] M. Marvasti and H. Boutayeb, "Analysis of moving dielectric half-space with oblique plane wave incidence using the finite difference time domain method," *Progress in Electromagnetics Research M*, vol. 115, pp. 119-128, 2023.

[31] W. B. Hatfield and B. Auld, "Electromagnetic shock waves in gyromagnetic media," *Journal of Applied Physics*, vol. 34, no. 10, pp. 2941-2946, 1963.

[32] R. Landauer, "Phase transition waves: Solitons versus shock waves," *Journal of Applied Physics*, vol. 51, no. 11, pp. 5594-5600, 1980.

[33] R. Landauer, "Shock waves in nonlinear transmission lines and their effect on parametric amplification," *IBM Journal of Research and Development*, vol. 4, no. 4, pp. 391-401, 1960.

[34] M. N. Sadiku, *Numerical Techniques in Electromagnetics*, CRC Press, 2000.

[35] G. Mur, "Absorbing boundary conditions for the finite-difference approximation of the time-domain electromagnetic-field equations," *IEEE Transactions on Electromagnetic Compatibility*, no. 4, pp. 377-382, 1981.

[36] H. Boutayeb, K. Mahdjoubi, and A.-C. Tarot, "Antenna inside PBG and Fabry-Perot cavities," in *Journées Internationales de Nice sur les Antennes, JINA 2002*, p. 4, Nov. 2002.

[37] H. Boutayeb, *Etude des structures périodiques planaires et conformes associées aux antennes. Application aux communications mobiles*, Ph.D. thesis, Université Rennes 1, 2003.

[38] A. Einstein, "On the electrodynamics of moving bodies," *Annalen der physik*, vol. 17, no. 10, pp. 891-921, 1905.

[39] O. Heaviside, "The electro-magnetic effects of a moving charge," *The Electrician*, vol. 22, pp. 147-148, 1888.

[40] J. Bradley, "A letter from the reverend Mr. James Bradley Savilian professor of astronomy at Oxford, and F. R. S to Dr. Edmond Halley Astronom. Reg. &c. giving an account of a new discovered motion of the fixed stars," *Philosophical Transactions of the Royal Society of London*, vol. 35, no. 406, pp. 637-661, 1729.

Mohammad Marvasti received his B.Sc. Diploma in electrical engineering major at the AmirKabir University of Technology, Tehran, Iran, in 2015. During his B.Sc. period, he received the 1st rank among all of his entrance colleagues. Therefore, he was awarded direct admission to M.Sc. of the Sharif University of Technology, Tehran, 1st ranked university in Iran. He received his M.Sc. degree in telecommunications focusing on applied electromagnetic from Sharif in 2017. He was working on designing, fabricating, and testing antenna systems and passive radio-frequency components in 3, 4, 5, 6, and 24 GHz frequency bands in a highly result-oriented company, Pionaria in Tehran, Iran (2017-2022). The main focus of his work was designing high-gain dual-polarization splash-plate feed parabolic antennas. He has started his Ph.D. research on developing novel ideas to achieve capacity growth of 5G and beyond mobile networks, and on computational electromagnetism at Université du Québec en Outaouais, Gatineau, Canada, since 2022.

Halim Boutayeb received the Diplôme d'Ingénieur (B.Sc.) degree in electrical engineering from the École Supérieur d'Ingénieur de Rennes, France, in 2000, and the French D.E.A. (M.Sc.) degree and Ph.D. degree in electrical engineering from the University of Rennes, France, in 2000 and 2003, respectively. From March 2004 to December 2006, he was with INRS-EMT, Montréal, QC, Canada. From Jan. 2007 to Dec, 2011, he was a researcher with the École Polytechnique de Montréal, Montréal, QC, Canada. He was also coordinator and a member of the Centre de Recherche en Électronique Radiofréquence (CREER), a strategic cluster on applied electromagnetics and RF technologies. From Jan. 2012 to June 2020, he was a research and development staff member with the Huawei Technologies Company Ltd., Ottawa, ON, Canada. Since July 2020, He has been a professor in electrical engineering at Université du Québec en Outaouais, Gatineau, Canada. He has authored or coauthored more than 100 journal and conference papers, and he holds 24 patents. Since 2003, he has been a reviewer for a number of scientific journals and conferences. His main fields of interest are antennas, microwaves circuits, the finite-difference time-domain (FDTD) method, artificial materials, radars, local positioning systems, biomedical engineering, and phased arrays. Dr. Boutayeb is a senior member of the Professional Engineers of Quebec. He has served as a technical program committee member of the IEEE Vehicular Technology Conference (VTC) 2006 and as a steering committee member of the IEEE Microwave Theory and Techniques Society (IEEE MTT-S) International Microwave Symposium (IMS) 2012. He was a recipient of the Natural Sciences and Engineering Research Council of Canada (NSERC) Postdoctoral Fellowship Grant (2004–2006), the Best Paper Award of the European Conference on Antennas and Propagation (2004), and five Gold Huawei Medal Awards (2013, 2015, 2017, 2018, and 2019).

Physics-informed Neural Networks for the Resolution of Analysis Problems in Electromagnetics

S. Barmada[1], P. Di Barba[2], A. Formisano[3], M. E. Mognaschi[2], and M. Tucci[1]

[1]DESTEC, University of Pisa, Pisa, Italy
sami.barmada@unipi.it, mauro.tucci@unipi.it

[2]Dept. of Electrical, Computer and Biomedical Engineering, University of Pavia, Pavia, Italy
paolo.dibarba@unipv.it, eve.mognaschi@unipv.it

[3]Dept. of Engineering, University of Campania "Luigi Vanvitelli," Aversa, Italy
alessandro.formisano@unicampania.it

Abstract – Learning from examples is the golden rule in the construction of behavioral models using neural networks (NN). When NN are trained to simulate physical equations, the tight enforcement of such laws is not guaranteed by the training process. In addition, there can be situations in which providing enough examples for a reliable training can be difficult, if not impossible. To alleviate these drawbacks of NN, recently a class of NN incorporating physical behavior has been proposed. Such NN are called "physics-informed neural networks" (PINN). In this contribution, their application to direct electromagnetic (EM) problems will be presented, and a formulation able to minimize an integral error will be introduced.

Index Terms – Direct and inverse electromagnetic problems, neural networks, physics informed neural networks.

I. INTRODUCTION

Machine learning or neural network (NN) approaches are frequently adopted to create models of physical relationships, starting from a set of input-output examples: we can refer, for instance, to the computation of the magnetic field created by known sources in a set of measurement points (e.g., currents in assigned coils); this is usually referred to as forward problem. Data-driven approaches are applicable also for solving inverse problems (loosely speaking, recovering the source originating the observed field) [1–3], although their nature, usually ill-posed or ill-conditioned, requires dedicated countermeasures. As a matter of fact, data-driven approaches usually converge, under suitable but quite relaxed hypotheses, to some solution tightly related to the selection of examples and of the training paradigm. On the other hand, in the case of NN mimicking the behavior of physical systems, it is expected not only that the model is able to generalize its response to cases not included in the learning dataset but also that the underlying equations are fully respected. A second relevant issue related to the use of NN to simulate physical phenomena is the difficulty in creating datasets populated enough to grant reliable training. This is particularly relevant in cases where the data must be gathered from experiments, or from demanding simulations.

Recently, the concept of "physics-informed" learning started to be considered as a powerful aid to the construction of data-driven models converging to solutions with known properties [3]. The underlying concept is to try using the governing equations of the physical system as a priori knowledge, able to regularize the learning process, driving it towards acceptable solutions. Such a priori knowledge also helps in reducing the need for large datasets for the learning and testing of NN.

As a matter of fact, in several areas of physics including EM, physics-informed neural networks (PINNs) [4], with their compelling ability of learning solutions of partial differential equations (PDEs) without the need for providing examples, have gained popularity. However, first contributions to the use of neural networks for EM field analyses date back to the beginning of the 2000s. For instance, in [5] a finite element neural network (FENN) that embeds finite element models into a neural network format for solving Poisson's equation was proposed. More recently, other relevant works [6, 7] dealing with electrostatic problems, made use of convolutional neural networks (CNNs). In particular, [6] highlighted the flexibility of CNNs in the case of complex distributions of excitation sources and dielectric constants. Since the introduction of PINNs, most applications in EM have involved optics [8–12];

Submitted On: July 26, 2023
Accepted On: December 12, 2023

https://doi.org/10.13052/2023.ACES.J.381102

more specifically, in [8] Maxwell's equations were solved in the frequency domain with several model simplifications. The architecture was similar to the one of a generative adversarial network (GAN): the first part is reminiscent of a generator since it maps the space distribution of permittivity to the electric field distribution. The second part, i.e., the discriminator, evaluates how physically sound the generator's outputs are. This enables, after training, the creation of a real-time field solver. This idea was re-introduced in [9] and put in a more general framework. In turn, [12] predicted the time evolution field in transient electrodynamics making use of an encoder-recurrent-decoder architecture. PINNs have also been used in magnetostatics and magneto-quasi-statics [13–16].

It can be noted that in most works (e.g., [2, 4, 10–14]), PINNs do not take system parameters (i.e., geometries, field sources, material properties) as an input and therefore they must be retrained, eventually taking advantage of transfer learning whenever the system parameters in the model must be changed. However, a few exceptions are reported in [8], [9], [15] where, once trained, PINNs could provide the solution of a class of direct field problems. This has been achieved by convolutional layers adopted in a GAN-like framework as in [8, 9]. More recently PINNs using dense layers and taking system parameters as input have been introduced [15], while in [16] an energy-based error function was used for training a PINN for the solution of magnetostatic problems.

Summing up, three mainstream methods could be categorized:

- *Data-driven networks*: Starting from the available observations, this approach generates a (nonlinear) model not only able to reproduce the observed data but also to generalize on data not included in training datasets [17]. As an example, [18] proposes a PDE-Net to identify the governing PDE models by data learning, able to approximate the unknown nonlinear responses.

- *Physics-constrained networks*: Within this further approach, physics constraints are introduced to strengthen the prediction ability of the NN, especially in the small data regime. Following the seminal paper [4], in [19] a physics-informed extreme learning machine (PIELM) to solve PDEs in complex domains was presented.

- *Algorithm optimization based on NN*: More recently, the NN approach has been used to optimize the performance of classical numerical methods. In [20], for instance, a NN has been utilized for accelerating the numerical resolution of PDEs; this way, a substantial gain in computational efficiency over standard numerical methods was achieved.

In this contribution, a brief description of possible schemes to introduce partial differential equations in the structure of NN is first presented; this basically transforms a NN into a PINN, capable of self learning and not needing any pre-calculated training set. Then a simple electromagnetic problem is presented to show the effectiveness of PINN in the resolution of (direct) EM field problems. Finally, a perspective on PINN based on integral rather than pointwise error functional is presented.

II. PHYSICS INFORMED NEURAL NETWORKS

A. Local residual approach

To clarify ideas, let us consider a simple non-dynamical problem in EM field computation, described by Poisson equation, with suitable boundary conditions:

$$\begin{cases} \nabla^2 \varphi(x,t) = f(x,t) \ \forall x \in \Omega \\ \varphi = \varphi^* \ on \ \partial\Omega_D \\ \partial_n \varphi = \psi^* \ on \ \partial\Omega_N \end{cases} . \tag{1}$$

In (1), the time t is a simple parameter, but the PINN approach is general enough to treat also dynamical cases. ∇^2 represents the Laplacian of the unknown (scalar) function $\varphi(x)$, Ω is the spatial definition domain, $\partial\Omega_D$ and $\partial\Omega_N$ are the Dirichlet and Neumann parts of the boundary, respectively.

A NN model of (1) receives as input the coordinates x of a point within Ω and yields as output the value of the approximated solution $\widehat{\varphi}(x, p_{NN})$, where p_{NN} represents the vector of weights and biases describing the NN. A possible approach to consider the a priori information about (1) is to define a representation error E, including a term related to the "residual" of the equation, and a second term related to boundary conditions:

$$\mathrm{E}(\mathrm{p}_{NN}) = \mathrm{E}_{\mathrm{bnd}}(p_{NN}) + \mathrm{E}_{\mathrm{eq}}(p_{NN}), \tag{2}$$

where

$$\begin{aligned} \mathrm{E}_{\mathrm{bnd}}(\mathrm{p}_{NN}) = &\left\| \tilde{\varphi}(\underline{x}, p_{NN}) - \varphi^*(\underline{x}) \right\|_{\underline{x} \in \partial\Omega_D} \\ &+ \left\| \partial_n \tilde{\varphi}(\underline{x}, p_{NN}) - \psi^*(\underline{x}) \right\|_{\underline{x} \in \partial\Omega_N} \end{aligned}, \tag{3}$$

and

$$\mathrm{E}_{\mathrm{eq}} = \left\| \nabla^2 \tilde{\varphi}(\underline{x}, p_{NN}) - f(\underline{x}) \right\|_{\underline{x} \in \Omega}, \tag{4}$$

where φ^* and ψ^* are the assigned conditions on the Dirichlet and Neumann parts of the boundary, respectively, while $\underline{x}$ represents the array of sampling points coordinate where error is evaluated; we note that the term E_{eq} can be computed using the automated differentiation (AD) approach described in [4, 21]. When eq.(4) is evaluated using a L_2 norm, it is often referred to as energy-like error.

Figure 1 shows a general view of the training process of a PINN inspired by (1)-(4).

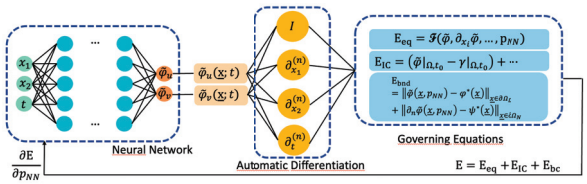

Fig. 1. General architecture of a PINN for solving a PDE. E_{IC} represents the error due to initial conditions in the case of dynamical problems, $x = (x_1, x_2)$ for the sake of simplicity.

B. Integral error approach

PINNs solving problems similar to (1) are usually trained based on the local residual of the governing equations [1, 2], and derivatives are typically evaluated by means of AD. Unfortunately, this approach could suffer from poor regularity. Domain decomposition represents a potential workaround [2], but only up to a certain degree. In this contribution, the authors propose an additional strategy, based on the minimization of an integral error instead of local quantities, much like the Rayleigh-Ritz method [22].

We start from the weighted residual form of (1):

$$\iiint_{\Omega} \left(k\nabla^2\varphi - f\right)\lambda\, d\Omega = 0 \;\; \forall\lambda \in H_0, \tag{5}$$

where k is the material constant (permeability μ in the case of magnetostatics and permittivity ε in the case of electrostatics), and H_0 is a suitable Sobolev space, defined according to the boundary conditions. The solution will be defined in H_g, the space of functions with correct boundary values on $\partial\Omega_D$ (which will be explicitly enforced at training time). Using standard calculus, eq.(5) can be reformulated as [22]:

$$\iint_{\partial\Omega_N} k\frac{\partial\varphi}{\partial n}\lambda\, d\Sigma - \iiint_{\Omega} (\nabla\varphi k\nabla\lambda) d\Omega + \iiint_{\Omega} (f\lambda) d\Omega = 0. \tag{6}$$

Equation (6) can be discretized following a Galerkin approach, in which the weighting functions are selected as coincident with the elements of the representation basis for the unknown function. More in detail the approximate solution is defined as

$$\tilde{\varphi} = \sum_{i=1,2,N\,\mathrm{out}} p_{NN_i}\lambda_i, \tag{7}$$

where p_{NN_i} are the coefficients of the expansion, usually named nodal potentials Φ_i in FEM-like expressions, λ_j is the j^{th} weighting function, and N_{out} is the number of output neurons. With this in mind, equations (6) and (7) lead to the following discretization.

$$\begin{aligned}\iiint_{\Omega} \left[\left(\sum_{i=1,2,Nout} p_{NN_i}\nabla\lambda_i\right) k\nabla\lambda_j\right] d\Omega \\ = \iiint_{\Omega} (f\lambda_k)\, d\Omega - \iint_{\partial\Omega_N} kg\lambda_j d\Sigma \\ \forall\lambda_j \in H_0.\end{aligned} \tag{8}$$

Note that for the sake of simplicity in (8) we have highlighted just the dependence on output layer weights, but the argument of the functions λ_i does contain all the weights (and activation functions) of the hidden and input layers.

It is now necessary to turn (8) into an error function for the PINN training, with the aim of obtaining, at the end of the training step, a network able to provide a reliable approximation $\widehat{\varphi}(x,\, p_{NN})$ also for points not included in the training data. In view of this, a possible approach inspired by the Ritz formulation is to generate a training dataset from N_{pnt} points in Ω (and as well as on the boundaries $\partial\Omega_D$ and $\partial\Omega_N$) and compute integrals as discrete summations. Accordingly, the left-hand side term in (8) modifies as

$$\begin{aligned}\iiint_{\Omega} \left[\left(\sum_{i=1,\,Nout} p_{NN\_i}\nabla\lambda_i\right) k\nabla\lambda_j\right] d\Omega \\ = \sum_{n=1,\,Npnt} \left(w_n \sum_{i=1,\,Nout} p_{NN\_i}\nabla\lambda_i(x_n)\, k\nabla\lambda_j(x_n)\right).\end{aligned} \tag{9}$$

We note that this approach corresponds to looking for the stationary points of the energy functional already defined in (4), the only difference, in this straightforward formulation, being that the training takes place only when all points have been processed (*batch* learning).

III. TEST CASES

A. Overall description

In this section, two test cases are shown. The first one presents the solution of a Poisson equation in a 1D domain. This simple problem serves as first validation relative to the use of PINNs for the solution of partial differential equations. It must be highlighted that in this implementation, the PINN does not need a training dataset: starting from a random guess solution, obtained by a random initialization of weights and biases, in a set of internal points (and on the boundary), the PINN evaluates the approximate solution $\widehat{\varphi}$, and at each epoch the physics-based error function (4) leads to an adjustment of the weights/biases. After the training is over, the PINN is capable of evaluating the function φ in points not necessarily coincident with the original set. This process can be referred to as self-training because no input-output pattern is externally supplied; furthermore the possibility of freely selecting the evaluation points makes the PINN

similar to a meshless method. In the following sections, the word "grid" is used to indicate the set of points $\underline{x}$. It is implicit that with this process a PINN trains itself on a specific set of points (grid); for this reason a change in the geometry necessarily leads to a new PINN, as it is for a new model in standard numerical methods.

A more complex 2D problem is then considered: this second example shows the accuracy of the method and its potential for the solution of general problems in presence of Neumann/Dirichlet boundary conditions. This problem is solved using the local residual approach; in addition, the quantities object of the integral error approach are also shown together with a perspective overview.

B. 1D problem

To show the performance of the PINN approach to electromagnetic analysis, we first considered a simple one-dimensional problem ruled by the Poisson's equation subject to Dirichlet boundary conditions. In particular, the problem to be solved is defined in $\Omega = [0,1]$ and described in equation (769)

$$\begin{cases} \frac{\partial^2 \varphi}{\partial x^2} = -10 \text{ in } \Omega \\ \varphi(0) = 0, \varphi(1) = 1 \end{cases} . \tag{10}$$

Following the methodological approach (1)-(4), a shallow NN composed of one input layer fed with sampling point coordinates, and one hidden layer with 4 neurons, was synthesized. Sigmoidal functions were selected as the activation function; stochastic gradient descent was the minimization algorithm, with random initialization of weights and biases and learning rate 5×10^{-3}. $N_{samp} = 21$ sampling points were considered to compute E on the grid discretizing the domain; in particular, the use of sigmoidal activation functions made it possible to analytically evaluate the second-order derivative in the Laplace operator. In Fig. 2 the training history of the network is shown in terms of error function against epochs, while in Fig. 3 the solution predicted by the trained PINN is represented.

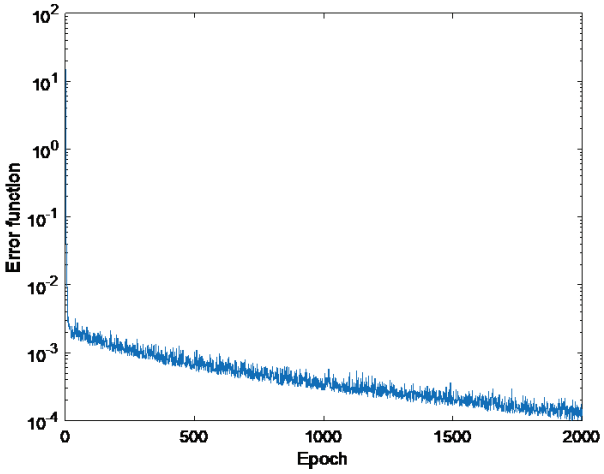

Fig. 2. Error function history during training (1D problem).

After several experiments, an excellent agreement between predicted solution and exact solution was observed.

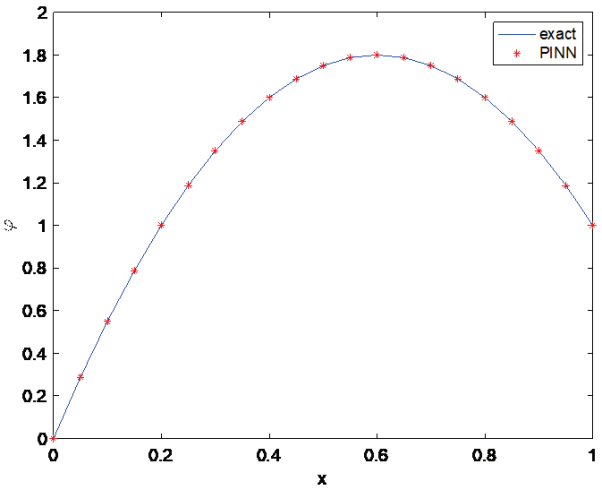

Fig. 3. Solution of the 1D problem. Arbitrary units are used for visualization.

C. 2D problem, local residual approach

As a less trivial test case, the following 2D problem has been considered:

$$\begin{cases} \frac{\partial^2 \varphi(x,y)}{\partial x^2} + \frac{\partial^2 \varphi(x,y)}{\partial y^2} = 0 \text{ in } \Omega \\ \varphi = 0, \partial\Omega_{D0} \\ \varphi = 1, \partial\Omega_{DV} \end{cases} . \tag{11}$$

The domain Ω is described in Fig. 4, in which $L =$ 1 m. Also in this case, a shallow NN with sigmoidal activation functions has been used. The details of the network are shown in Table 1.

Table 1: Neural network description

Input dimension	2
Output dimension	1
Number of hidden layers	5
Number of neurons in each hidden layer	15
Total number of parameters	1021

The hyper-parameters above described have been determined by using a 5-fold cross validation with the number of hidden layers varying from 1 to 7 and with the number of neurons in each hidden layer from 2 to 20. Due to the final number of parameters, the PINN can be classified as a deep network for regression purpose.

Stochastic gradient descent was the minimization algorithm, with random initialization of weights and

biases and a learning rate equal to $5 \cdot 10^{-3}$. $N_{samp} = 300$ sampling points were considered to compute the error function on the grid discretizing the domain. In particular, the adopted grid is composed by a set of 300 equally spaced point, in both the x_1 and x_2 directions, with $\Delta x_1 = \Delta x_2 = L/20$, as shown in Fig. 5.

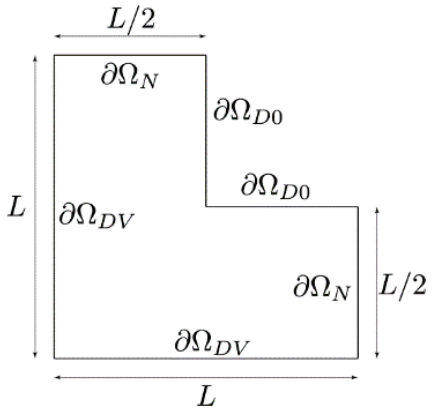

Fig. 4. Graphical description of the 2D test case. $\partial\Omega_N$ is the section of boundary where Neumann conditions hold, $\partial\Omega_{D0}$ and $\partial\Omega_{DV}$ the sections where vanishing and non-vanishing Dirichlet conditions hold, respectively.

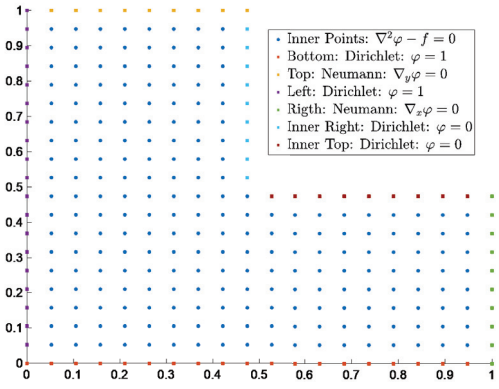

Fig. 5. Representation of the grid used to train the PINN or the 2D example.

In case the local residual approach (2)-(4) is followed, the solution obtained after training the PINN is depicted in Fig. 6, while Fig. 7 shows the field evaluated by AD.

The error function training history is shown in Fig. 8. The accuracy of the solution has been properly verified, comparing the obtained potential with the results obtained by a finite element method model implemented on Comsol Multiphysics [23]. For the sake of conciseness, a point-to-point comparison is not shown here, but an integral like comparison (between the energies calculated by both methods) is shown in the next section.

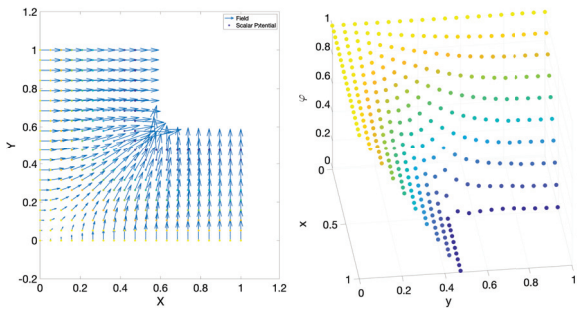

Fig. 6. Potential map obtained by the use of the PINN.

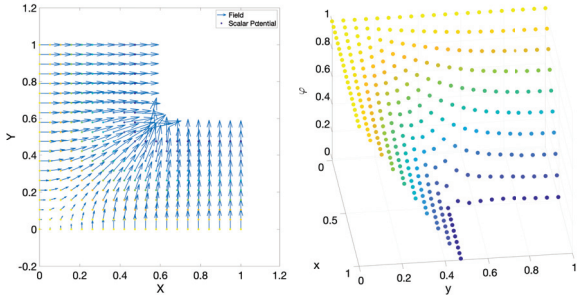

Fig. 7. Field as evaluated by the PINN and AD.

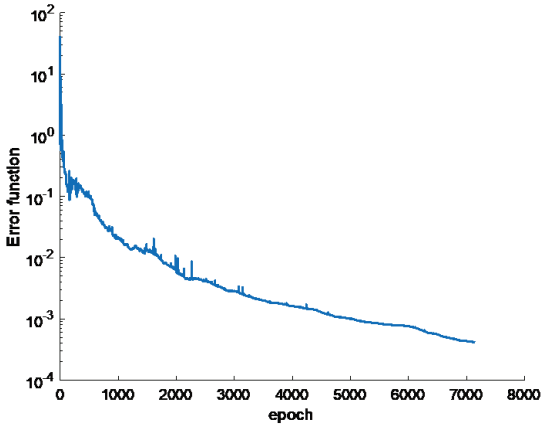

Fig. 8. Error function history during training (2D problem).

D. 2D problem, integral error approach

As an intermediate step between the local residual approach and the integral error approach, the behavior of the global energy as a function of the training epoch has been evaluated (Fig. 9). In this case, the "energy" is

calculated by using the point values of $\nabla\widehat{\varphi}$ (obtained by AD), integrated on the relevant support (< 1 in case of a grid point belonging to $\partial\Omega$). This shows that, in the considered case, the integral formulation leads to the same result, yet being able to treat prospectively also the case of internal discontinuities in the material properties like magnetic permeability. The graph shows that the energy

$$W_{PINN} = \mu \left(\sum_{i=1,2,N \text{ out}} p_{NN_i} \nabla \lambda_i \right)^2, \qquad (12)$$

(with μ being the magnetic permeability) reaches a value of $W_{PINN} = 1.68\ \mu J$ at the end of the training phase; the total energy independently obtained by means of the benchmark FEM is $W_{FEM} = 1.61\ \mu J$, showing again the good agreement between the PINN and the FEM analysis. It is noteworthy that, in case the integral approach is performed on delta-like expansion functions, the evaluation of the integral approach leads to the same point-wise evaluation as shown in Fig. 5 at the same time, eq. (12) can substitute eq. (4) in the definition of an integral error approach, which would take the meaning of an energy-based approach.

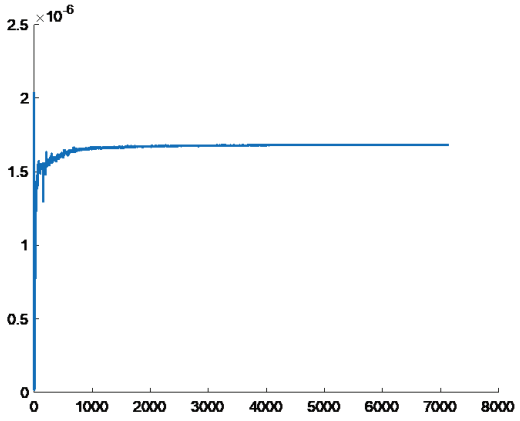

Fig. 9. Energy during training (2D problem).

IV. CONCLUSIONS AND OUTLOOK

In this paper, the use of PINN for the resolution of EM problems has been considered. Both local and integral errors, the latter being related to the value of the energy in the domain object of analysis, have been proposed as error functions for the NN training. In the considered examples, both approaches converged during the training phase.

The examples are aimed at showing the effectiveness of energy-based training; in particular, the latter is able to easily deal also with problems entailing discontinuities in the distribution of material properties. Moreover, when using a weighted residual formulation rather than the Ritz one, a different choice of the base functions and weight functions would be possible; this way, most numerical methods based on weighted residual could be revisited in terms of PINN.

REFERENCES

[1] A. Kovacs, L. Exl, A. Kornell, J. Fischbacher, M. Hovorka, M. Gusenbauer, L. Breth, H. Oezelt, D. Praetorius, D. Suess, and T. Schrefl, "Magnetostatic and micro magnetism with PINNs," *J. of Magnet. and Mag. Mat.*, vol. 548, 2022.

[2] A. Khan and D. A. Lowther, "Physics informed neural networks for electromagnetic analysis," *IEEE Transactions on Magnetics*, vol. 5, no. 9, 2022.

[3] S. Barmada, P. Di Barba, A. Formisano, M. E. Mognaschi, and M. Tucci, "Learning inverse models from electromagnetic measurements data," *Proc. of IGTE Symp. 2022*, Graz (Austria), Sep. 18-21, 2022.

[4] M. Raissi, P. Perdikaris, and G. E. Karniadakis, "PINNs: A deep learning framework for solving forward and inverse problems involving nonlinear partial differential equations," *J. Comput. Phys.*, vol. 378, pp. 686707, 2019.

[5] P. Rumuhalli, L. Udpa, and S. Udpa, "Finite element neural networks for elec. inverse problems," *Rev. Q. Nondestr. Eval.*, vol. 21, p. 28735, 2002.

[6] W. Tang, T. Shan, X. Dang, M. Li, F. Yang, S. Xu, and J. Wu, "Study on Poissons equation solver based on deep learning technique," *2017 IEEE El. Design of Adv. Pack. and Syst. Symp.*, Haining, China, 2018.

[7] Z. Zhang, L. Zhang, Z. Sun, N. Erickson, R. From, and J. Fan, "Study on a Poissons equation solver based on deep learning technique," *Proc. of J. Int. Symp. on Elect. Compat.*, Sapporo, p. 305308, 2019.

[8] B. Bartlett, "A generative model for computing electromagnetic field solutions," *Stanford CS229 Projects*, 233 Stanford, CA, 2018.

[9] J. Lim and D. Psaltis, "MaxwellNet: Physics-driven deep neural network training based on Maxwells equations," *APL Photonics*, vol. 7, 2022.

[10] Y. Chen, L. Lu, G. Karniadakis, and L. Negro, "Physics-informed neural net. for inv. problems in nano-optics and metamat," vol. 28, no. 8, 2020.

[11] L. Lu, R. Pestourie, W. Yao, Z. Wang, F. Verdugo, and S. Johnosn, "Physics-informed neural networks with hard constraints for inverse design," *J. Sci. Comput.*, vol. 43, no. 6, pp. B1105-B1132, 2021.

[12] S. Wang, Z. Pend, and C. Christodoulou, "Physics-informed deep neural networks for transient electromagnetic analysis," *Antennas and Propagation*, vol. 1, pp. 404-412, 2020.

[13] M. Baldan, G. Baldan, and B. Nacke, "Solving 1D non-linear magneto quasi-static Maxwells equations using neural networks," *IET Sci. Meas. Technol.*, vol. 15, pp. 204217, 2021.
[14] A. Kovacs, L. Exl, A. Kornell, J. Fischbacher, M. Hovorka, M. Gusenbauer, L. Breth, H. Oezelt, D. Praetorius, D. Suess, T. Schref, "Magnetost. and microm. with PINNs," *J. of Magnet. and Magnetic Materials*, vol. 548, 2022.
[15] A. Beltran-Pulido, I. Bilionis, and D. Aliprantis, "PINNs for Solving Parametric Magnetostatic Problems," *IEEE Trans. Energy Conversion*, 2022.
[16] M. Baldan, P. Di Barba, and D. A. Lowther, "Physics-informed neural networks for solving inverse electromagnetic problems," *IEEE Trans. Magnetics*, vol. 59, no. 5, 2023.
[17] S. H. Rudy, S. L. Brunton, J. L. Proctor, and J. N. Kutz, "Data-driven discovery of partial differential equations," *Sci. Adv.*, vol. 3, no. 4, Art. no. e1602614, 2017.
[18] Z. Long, Y. Lu, X. Ma, and B. Dong, "PDE-Net: Learning PDEs from data," in *Proc. 35th Int. Conf. Mach. Learn.*, pp. 3208-3216, 2018.
[19] V. Dwivedi and B. Srinivasan, "Physics informed extreme learning machine (PIELM)—A rapid method for the numerical solution of partial," *Neurocomputing*, vol. 391, pp. 96-118, 2020.
[20] S. Mishra, "A machine learning framework for data driven acceleration of computations of differential equations," *Math. Eng.*, vol. 1, no. 1, pp. 118-146, 2018.
[21] A. G. Baydin, B. A. Pearlmutter, A. A. Radul, and J. M. Siskind, "Automatic differentiation in machine learning: a survey," *J. of Machine Learning Res.*, vol. 18, no. 153, pp. 1-43, 2018.
[22] O. C. Zienkiewicz and R. Taylor, *The Finite Element Method* (4th ed.), New York: McGraw-Hill Book Co., 1989.
[23] COMSOL Multiphysics® v. 6.2. www.comsol.com. COMSOL AB, Stockholm, Sweden.

Sami Barmada received the M.S. and Ph.D. degrees in electrical engineering from the University of Pisa, Italy, in 1995 and 2001, respectively. He is currently a full professor with the Department of Energy and System Engineering, University of Pisa. He is author and co-author of more than 180 papers in international journals and indexed conferences. His research interests include applied electromagnetics, electromagnetic fields calculation, power line communications, wireless power transfer devices, and nondestructive testing.

Prof. Barmada is an Applied Computational Electromagnetics Society (ACES) Fellow, and he served as ACES president from 2015 to 2017. He is chairman of the International Steering Committee of the CEFC Conference and he has been the general chairman and technical program chairman of numerous international conferences.

Paolo Di Barba is a full professor of electrical engineering in the Department of Electrical, Computer, and Biomedical Engineering, University of Pavia, Pavia, Italy. His current research interests include the computer-aided design of electric and magnetic devices, with special emphasis on the methods for field synthesis and automated optimal design. He has authored or coauthored more than 240 papers, either presented to international conferences or published in international journals, the book *Field Models in Electricity and Magnetism* (Springer, 2008), the monograph *Multiobjective Shape Design in Electricity and Magnetism* (Springer, 2010) and the book *Optimal Design Exploiting 3D Printing and Metamaterials* (2022).

Alessandro Formisano is a full professor at Università della Campania "Luigi Vanvitelli." His scientific activity started in 1996, in cooperation with several research groups active in the fields of electromagnetic fields and devices (e.g., EdF Paris, TU-Graz, TU-Budapest, TU-Ilmenau, TU-Bucharest, Slovak Academy of Science, Grenoble Univ.), and thermonuclear controlled fusion (KIT, ITER, Fusion For Energy, EURATOM). His interests are electromagnetic fields computation, neural networks, robust design and tolerance analysis, thermonuclear plasmas identification, optimal design, and inverse problems in electromagnetism. He serves as editorial board member or reviewer for the most prestigious journals (*IEEE Trans. On Magn.*, *Compel*, *Sensors*, *ACES Journal)* in the field of numerical computation of electromagnetic fields.

Maria Evelina Mognaschi is associate professor at the University of Pavia (Italy), Department of Electrical, Computer and Biomedical Engineering. Her scientific interests are inverse problems, in particular multi-objective optimization and identification problems in electromagnetism and biological systems. Recently, she investigated the solution of forward and inverse problems in electromagnetics by means of deep learning techniques. She has authored or co-authored more than 120 ISI- or Scopus-indexed papers, either presented to international conferences or published in international journals.

Mauro Tucci received the Ph.D. degree in applied electromagnetism from the University of Pisa, Pisa, Italy, in 2008. Currently, he is a full professor with the Department of Energy and Systems Engineering, University of Pisa. His research interests are machine learning, data analysis, and optimization, with applications in electromagnetism, nondestructive testing, and forecasting.

A Parallel 3-D HIE-FDTD Method using the MPI Library

Qin Nan, Chunhui Mou, and Juan Chen

School of Electrical and Information Engineering
Xi'an Jiaotong University, Xi'an 710049, People's Republic of China
Chen.juan.0201@mail.xjtu.edu.cn

Abstract – This paper presents the implementation of the parallel hybrid implicit-explicit finite-difference time-domain (HIE-FDTD) method using the Message Passing Interface (MPI) library. The method proves to be very effective in simulating large-scale three-dimensional electromagnetic problems with fine structures in one direction. For the decomposition of the computational volume in the HIE-FDTD method, an MPI Cartesian 2D topology is implemented, allowing arbitrary division of the volume in two directions. Derived data types provided in the MPI library are employed to optimize inter-process communication. High accuracy and efficiency are subsequently demonstrated through a numerical example of a frequency-selected surface (FSS). It shows that the proposed method is very suitable for parallel computing, and the parallel efficiency maintains above 80% for different numbers of processes.

Index Terms – Electromagnetic scattering, finite-difference time-domain (FDTD), HIE-FDTD, parallel computing, thin layers.

I. INTRODUCTION

The finite-difference time-domain (FDTD) method is widely used due to its explicit leapfrog iterative scheme in the simulation of electromagnetic problems [1, 2]. Additionally, its regular data structures make it a top choice for parallelizing using domain-decomposition techniques to accelerate the solution of large-scale electromagnetic problems [3].

Two methods are widely used to achieve parallel computing of the FDTD method, using multi-core central processing units (CPUs) or using graphical processing units (GPUs). However, GPUs require additional hardware costs compared to multi-core CPUs, as they are separate hardware devices that are initialized and executed by a program running on a CPU. Besides that, it is hard to simulate the large-scale electromagnetic problems using a single GPU for its smaller memory size than CPU. Therefore, An MPI-based three dimensional parallel FDTD algorithm has been developed in [3].

Thin layers in electromagnetic devices are typically essential due to their significant impact on device performance, making the electromagnetic simulation of such structures valuable. However, in the FDTD method, which is constrained by the Courant-Friedrichs-Lewy (CFL) condition, the maximum time step size depends on the minimum mesh size in the computational volume, leading to inefficiencies in handling problems with fine structures.

Several unconditional stability FDTD methods, such as the alternating-direction implicit (ADI) FDTD method [4], Crank-Nicolson (CN) FDTD method [5] and the locally-one-dimensional (LOD) FDTD method [6], which introduce the implicit updating equations in the conventional FDTD method, have been proposed in order to eliminate the CFL bound. It should be noted that although the ADI-FDTD method is unconditionally stable, it has second-order truncation error terms that can reduce its accuracy [7]. The CN-FDTD and LOD-FDTD methods have high accuracy, but they both need to solve the large matrix which decreases the efficiency greatly. Furthermore, when applied to large-scale problems, issues such as augmented data traffic present challenges to the parallel implementation of the ADI-FDTD, CN-FDTD, and LOD-FDTD methods.

For some electromagnetic problems, such as the analysis of the degradation of shielding effectiveness with thin slots or frequency selective surfaces with thin layers, fine structures are present only in one direction [8]. Fine grids should be applied solely in the direction of the fine structure rather than in all three directions. In order to improve the efficiency of electromagnetic simulation for these structures, the HIE-FDTD method was proposed to eliminate the limitations of the fine grids on the time step size [9]. Apart from that, the error exists in semi-implicit processing rather than implicit processing, making HIE-FDTD more accurate than the ADI-FDTD method [10]. The computational volume in the HIE-FDTD cannot be directly divided in the direction of the fine structures as it is necessary for tridiagonal matrix equations solving, but it can be divided in both other directions. Due to its ability to directly divide the

Submitted On: November 20, 2023
Accepted On: January 21, 2024

https://doi.org/10.13052/2023.ACES.J.381103

computational domain into subdomains, HIE-FDTD is more suitable for parallelizing than the ADI-FDTD, CN-FDTD, and LOD-FDTD methods.

This paper describes the implementation of a parallel HIE-FDTD method based on the MPI library, which offers clear standardization benefits, especially in distributed storage communication environments. The computation volume can be decomposed using process topologies along the x- and z-directions. MPI communication functions and derived data types are used for transmitting field values between processes.

This paper is structured as follows. In Section II, the theory of the HIE-FDTD method is introduced. Section III demonstrates the implementation of the parallel HIE-FDTD method. Section IV presents a numerical example that confirms the high accuracy and efficiency of the proposed method. The conclusion is given in Section V.

II. THEORY OF THE HIE-FDTD METHOD

Assuming fine structures exist in the y-direction, the explicit equations for $E_y$and H_y components in the HIE-FDTD method are as follows:

$$\begin{aligned}
&E_y^{n+1}(i,j+1/2,k)\\
&=CA(i,j+1/2,k)E_y^n(i,j+1/2,k)\\
&+CB(i,j+1/2,k)/\Delta z\begin{bmatrix}H_x^n(i,j+1/2,k+1/2)\\-H_x^n(i,j+1/2,k-1/2)\end{bmatrix}\\
&-CB(i,j+1/2,k)/\Delta x\begin{bmatrix}H_z^n(i+1/2,j+1/2,k)\\-H_z^n(i-1/2,j+1/2,k)\end{bmatrix},
\end{aligned}\tag{1}$$

$$\begin{aligned}
&H_y^{n+1}(i+1/2,j,k+1/2)\\
&=CP(i+1/2,j,k+1/2)H_y^n(i+1/2,j,k+1/2)\\
&-CQ(i+1/2,j,k+1/2)/\Delta z\\
&\left[E_x^{n+1}(i+1/2,j,k+1)-E_x^{n+1}(i+1/2,j,k)\right]\\
&+CQ(i+1/2,j,k+1/2)/\Delta x\\
&\left[E_z^{n+1}(i+1,j,k+1/2)-E_z^{n+1}(i,j,k+1/2)\right],
\end{aligned}\tag{2}$$

where

$$\begin{aligned}
&CA(i,j+1/2,k)\\
&=\frac{\varepsilon(i,j+1/2,k)/\Delta t-\sigma(i,j+1/2,k)/2}{\varepsilon(i,j+1/2,k)/\Delta t+\sigma(i,j+1/2,k)/2},\\
&CB(i,j+1/2,k)\\
&=\frac{1}{\varepsilon(i,j+1/2,k)/\Delta t+\sigma(i,j+1/2,k)/2},\\
&CP(i+1/2,j,k+1/2)\\
&=\frac{\frac{\mu(i+1/2,j,k+1/2)}{\Delta t}-\frac{\sigma_m(i+1/2,j,k+1/2)}{2}}{\frac{\mu(i+1/2,j,k+1/2)}{\Delta t}+\frac{\sigma_m(i+1/2,j,k+1/2)}{2}},\\
&CQ(i+1/2,j,k+1/2)\\
&=\frac{1}{\frac{\mu(i+1/2,j,k+1/2)}{\Delta t}+\frac{\sigma_m(i+1/2,j,k+1/2)}{2}},
\end{aligned}\tag{3}$$

where Δt is the size of the time step. ε, σ, μ, and σ_m are the electrical permittivity, electric conductivity, magnetic permeability, and the equivalent magnetic loss of the media, respectively. n is the index of the time step. i, j, and k are the indices of spatial increments along the x-, y-, and z-directions.

The semi-implicit processing of the HIE-FDTD method can be found as follows:

$$\begin{aligned}
&E_x^{n+1}(i+1/2,j,k)\\
&=CA(i+1/2,j,k)E_x^n(i+1/2,j,k)\\
&-CB(i+1/2,j,k)/\Delta z\\
&\begin{bmatrix}H_y^n(i+1/2,j,k+1/2)\\-H_y^n(i+1/2,j,k-1/2)\end{bmatrix}\\
&+CB(i+1/2,j,k)/2\Delta y\\
&\begin{bmatrix}H_z^{n+1}(i+1/2,j+1/2,k)\\-H_z^{n+1}(i+1/2,j-1/2,k)\\+H_z^n(i+1/2,j+1/2,k)\\-H_z^n(i+1/2,j-1/2,k)\end{bmatrix},
\end{aligned}\tag{4}$$

$$\begin{aligned}
&E_z^{n+1}(i,j,k+1/2)\\
&=CA(i,j,k+1/2)E_z^n(i,j,k+1/2)\\
&+CB(i,j,k+1/2)/\Delta x\\
&\begin{bmatrix}H_y^n(i+1/2,j,k+1/2)\\-H_y^n(i-1/2,j,k+1/2)\end{bmatrix}\\
&-CB(i,j,k+1/2)/2\Delta y\\
&\begin{bmatrix}H_x^{n+1}(i,j+1/2,k+1/2)\\-H_x^{n+1}(i,j-1/2,k+1/2)\\+H_x^n(i,j+1/2,k+1/2)\\-H_x^n(i,j-1/2,k+1/2)\end{bmatrix},
\end{aligned}\tag{5}$$

$$\begin{aligned}
&H_z^{n+1}(i+1/2,j+1/2,k)\\
&=CP(i+1/2,j+1/2,k)H_z^n(i+1/2,j+1/2,k)\\
&-CQ(i+1/2,j+1/2,k)/\Delta z\\
&\left[E_y^{n+1}(i+1,j+1/2,k)-E_y^{n+1}(i,j+1/2,k)\right]\\
&+CQ(i+1/2,j+1/2,k)/2\Delta y\\
&\left[E_x^{n+1}(i+1/2,j+1,k)-E_x^{n+1}(i+1/2,j,k)\right.\\
&\left.+E_x^n(i+1/2,j+1,k)-E_x^n(i+1/2,j,k)\right],
\end{aligned}\tag{6}$$

$$\begin{aligned}
&H_x^{n+1}(i,j+1/2,k+1/2)\\
&=CP(i,j+1/2,k+1/2)H_x^n(i,j+1/2,k+1/2)\\
&+CQ(i,j+1/2,k+1/2)/\Delta z\\
&\left[E_y^{n+1}(i,j+1/2,k+1)-E_y^{n+1}(i,j+1/2,k)\right]\\
&-CQ(i,j+1/2,k+1/2)/2\Delta y\\
&\left[E_z^{n+1}(i,,j+1,k+1/2)-E_z^{n+1}(i,j,k+1/2)\right.\\
&\left.+E_z^n(i,j+1,k+1/2)-E_z^n(i,j,k+1/2)\right].
\end{aligned}\tag{7}$$

The formulations of the HIE-FDTD method are shown above with the field components arranged similarly to the FDTD method. According to (4), updating of E_x component requires H_z component at the same step. Thus, E_x component cannot be updated explicitly. Substituting (6) into (4) gives us the equation of E_x component that is given by

$$\begin{aligned} &a_i E_x^{n+1}(i+1/2,j-1,k)+b_i E_x^{n+1}(i+1/2,j,k)\\ &+c_i E_x^{n+1}(i+1/2,j+1,k)=d_i \end{aligned} \tag{8}$$

where

$$\begin{aligned} a_i &= -\frac{CB(i+1/2,j,k)CQ(i+1/2,j-1/2,k)}{4\Delta y^2},\\ b_i &= 1+\frac{CB(i+1/2,j,k)CQ(i+1/2,j+1/2,k)}{4\Delta y^2},\\ &+\frac{CB(i+1/2,j,k)CQ(i+1/2,j-1/2,k)}{4\Delta y^2}\\ c_i &= -\frac{CB(i+1/2,j,k)CQ(i+1/2,j+1/2,k)}{4\Delta y^2},\\ d_i &= [CA(i+1/2,j,k)+a_i+c_i]E_x^n(i+1/2,j,k)\\ &-a_i E_x^n(i+1/2,j-1,k)-c_i^n(i+1/2,j+1,k)\\ &-CB(i+1/2,j,k)/\Delta z\\ &\left[H_y^n(i+1/2,j,k+1/2)-H_y^n(i+1/2,j,k-1/2)\right]\\ &+CB(i+1/2,j,k)/2\Delta y\\ &\left\{[CP(i+1/2,j+1/2,k)+1]H_z^n(i+1/2,j+1/2,k)\right.\\ &-[CP(i+1/2,j-1/2,k)+1]H_z^n(i+1/2,j-1/2,k)\\ &-\frac{CQ(i+1/2,j+1/2,k)}{\Delta z}\begin{bmatrix}E_y^{n+1}(i+1,j+1/2,k)\\ -E_y^{n+1}(i,j+1/2,k)\end{bmatrix}\\ &\left.+\frac{CQ(i+1/2,j-1/2,k)}{\Delta z}\begin{bmatrix}E_y^{n+1}(i+1,j-1/2,k)\\ -E_y^{n+1}(i,j-1/2,k)\end{bmatrix}\right\}. \end{aligned} \tag{9}$$

Substituting (7) into (5) gives us the equation of E_z component that is given by

$$\begin{aligned} &a_k E_z^{n+1}(i,j-1,k+1/2)+b_k E_z^{n+1}(i,j,k+1/2)\\ &+c_k E_x^{n+1}(i,j+1,k+1/2)=d_k \end{aligned} \tag{10}$$

where

$$\begin{aligned} a_k &= -\frac{CB(i,j,k+1/2)\cdot CQ(i,j-1/2,k+1/2)}{4\Delta y^2},\\ b_k &= 1+\frac{CB(i,j,k+1/2)\cdot CQ(i,j+1/2,k+1/2)}{4\Delta y^2}\\ &+\frac{CB(i,j,k+1/2)\cdot CQ(i,j-1/2,k+1/2)}{4\Delta y^2},\\ c_k &= -\frac{CB(i,j,k+1/2)\cdot CQ(i,j+1/2,k+1/2)}{4\Delta y^2},\\ d_k &= [CA(i,j,k+1/2)+a_k+c_k]E_z^n(i,j,k+1/2)\\ &-a_k E_z^n(i,j-1,k+1/2)-c_k E_z^n(i,j+1,k+1/2)\\ &+CB(i,j,k+1/2)/\Delta x\\ &\left[H_y^n(i+1/2,j,k+1/2)-H_y^n(i-1/2,j,k+1/2)\right]\\ &-CB(i,j,k+1/2)/2\Delta y\\ &\left\{[CP(i,j+1/2,k+1/2)+1]H_x^n(i,j+1/2,k+1/2)\right.\\ &-[CP(i,j-1/2,k+1/2)+1]H_x^n(i,j-1/2,k+1/2)\\ &+\frac{CQ(i+1/2,j+1/2,k)}{\Delta x}\begin{bmatrix}E_y^{n+1}(i+1,j+1/2,k)\\ -E_y^{n+1}(i,j+1/2,k)\end{bmatrix}\\ &\left.-\frac{CQ(i+1/2,j-1/2,k)}{\Delta x}\begin{bmatrix}E_y^{n+1}(i+1,j-1/2,k)\\ -E_y^{n+1}(i,j-1/2,k)\end{bmatrix}\right\}. \end{aligned} \tag{11}$$

Thus, the process of updating field components entails the explicit update of E_y and H_y by using equations (1) and (2) first, followed by the implicit update of E_x and E_z via tridiagonal matrix equations (8) and (10). Finally, explicit updating is made to obtain the H_z and H_x components by using equations (6) and (7).

The time step size in the HIE-FDTD method can be calculated as follows [9]:

$$\Delta t \le 1 \Big/ c\sqrt{1/\Delta x^2+1/\Delta z^2}, \tag{12}$$

where $c=1/\sqrt{\varepsilon\mu}$ is the speed of light in the medium, and Δx, Δz are the minimum cell in the x- and z-directions.

It indicates that the stability condition for the HIE-FDTD method is not restricted by the cells in the fine structures, unlike the FDTD method. Therefore, if a model only has fine structures in one direction, using the HIE-FDTD method increases efficiency due to the much larger time step size than that of the FDTD method.

III. PARALLELISM WITH THE MPI LIBRARY

The first step of the parallel FDTD method is the computational volume division. The computational volume can be decomposed directly along three directions in the parallel FDTD method, but this is impossible in the parallel HIE-FDTD method, because it needs to solve the tridiagonal matrix equations in the direction of fine structures. As such, the proposed method in this paper divides the computational volume in the x- and z-directions, excluding the y-direction where the fine structures exist.

The computational volume is divided using a Cartesian topology in the MPI library. The procedure for creating a two-dimensional Cartesian topology of the three-dimensional problem space using the MPI library is described in [3]. Figure 1 shows the division of the computational volume into nine subspaces, each of which corresponds to a process located by its Cartesian

coordinates. The MPI function *MPI_Cart_shift* determines the ID numbers of processes surrounding a process, once the Cartesian topology has been created. These ID numbers are then used for implementing communications.

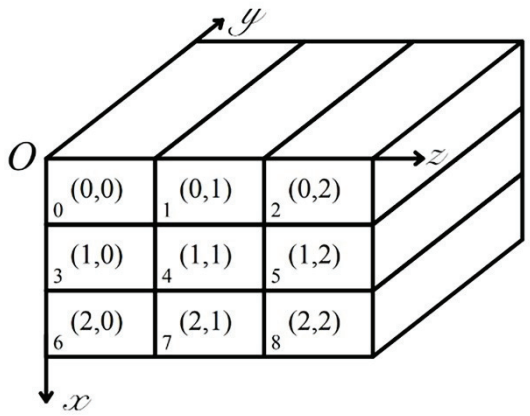

Fig. 1. The division of the computational volume using a two-dimensional Cartesian topology (x-z plane).

Both the HIE-FDTD method and the FDTD method must solve the boundary condition problem. Therefore, it is important to determine the necessary components to transmit after the equal distribution of the problem.

For the FDTD method, updating field components at (i,j,k) is dependent on the surrounding field components. To provide an example, as shown by Fig. 2, the iteration of E_x component at $(i+1/2,j,k)$ requires H_z at $(i+1/2,j+1/2,k)$, $(i+1/2,j-1/2,k)$ and H_y at $(i+1/2,j-1/2,k)$, $(i+1/2,j+1/2,k)$.

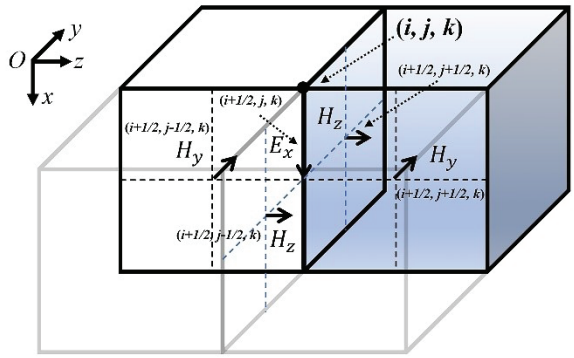

Fig. 2. The iteration of E_x component at $(i+1/2,j,k)$ using the conventional FDTD method and the surrounding field components.

Figure 3 shows that only the components encapsulated by the blue dotted contour designated to PROC4

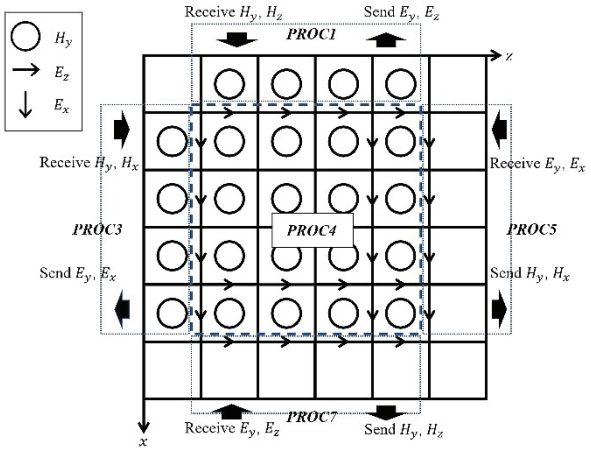

Fig. 3. The send-receive communications in PROC4 using the parallel FDTD method.

are assigned in the parallel FDTD method. So, to update E_x component in PROC4, H_y component from PROC3 is required. As there is no division along the y-direction, there is no need to transmit H_z component. Similarly, updating E_z component requires H_y component in PROC1, and updating E_y component requires both H_z and H_x components in PROC1 and PROC3. It should be noted that PROC4 fulfils the role of both an emitter and an addressee process, and therefore, must send the components to the surrounding processes. The send-receive communications of PROC4 are illustrated in Fig. 3.

Figure 4 shows the iteration of E_x at $(i+1/2,j,k)$ using the HIE-FDTD method. E_y at $(i+1,j+1/2,k)$ and $(i+1,j-1/2,k)$ are also essential, besides H_y and H_z components that are required in the FDTD method. Therefore, when implementing the parallel HIE-FDTD

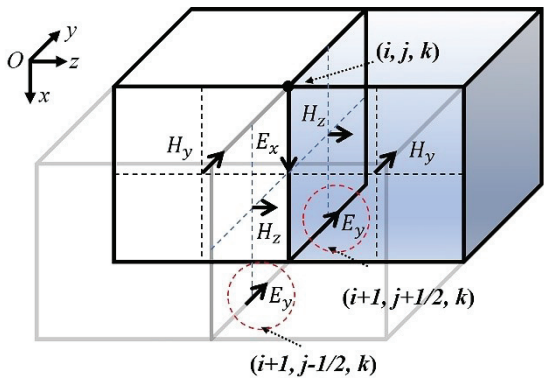

Fig. 4. The iteration of E_x component at $(i+1/2,j,k)$ using HIE-FDTD method and the surrounding field components.

method, it is important to note that updating E_x component requires E_y belonging to PROC7, with H_y component belonging to PROC3. To update E_z, it is necessary to receive E_y component belonging to PROC5, with H_y component from PROC1.

Figure 5 (a) shows the complete communications between PROC4 and other processes in the parallel HIE-FDTD method. Figure 5 (b) shows that the parallel HIE-FDTD method requires the communication of E_y component in the x- and z-directions when performing E_x and E_z iterations. It is the difference between it and the parallel FDTD method.

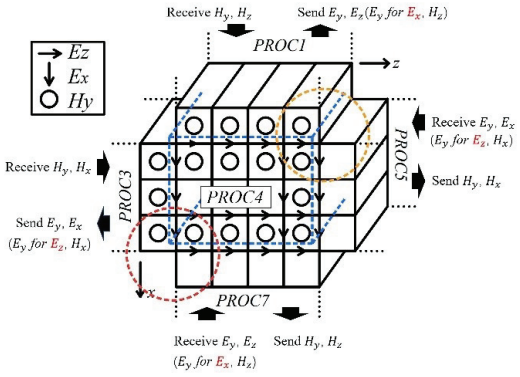

(a)

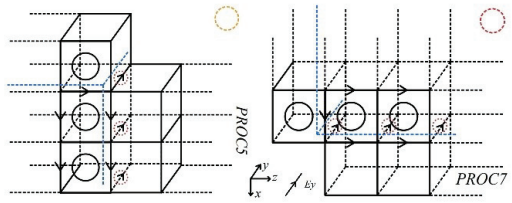

(b)

Fig. 5. The communications between PROC4 and its neighboring processes using the parallel HIE-FDTD method: (a) Overall view and (b) the communication of $E_y$component in the x- and z-directions.

Assuming that the size of the field components array is sizex × sizey × sizez, which needs to be augmented for the reception of the components from neighboring processes as follows,

$$A_i(\text{sizex},\text{sizey},\text{sizez}) \rightarrow A_i(\text{sizex}+1,\text{sizey},\text{sizez}+1),$$

where $A=[E,H]$ and $i=[x,y,z]$.

The details of the derived data types implementation, transmission, and reception of field components are documented in [3]. The procedure for the parallel HIE-FDTD method is provided here:

1) MPI initialization
2) Read parameters used in simulation
3) Create a two-dimensional Cartesian topology (no division along the y-direction)
4) Create the derived data types for communications
5) Start updating field components
Update E_y component
Communicate E_y component for updating of E_x and $E_z$components
Update E_x and E_z components
Communicate E_x and E_z components
Update the H-field components
Communicate the H-field components
6) End.

IV. NUMERICAL RESULTS

To verify the accuracy and efficiency of the implementation of the proposed parallel HIE-FDTD method based on the MPI library, a numerical example of a FSS is simulated. Figure 6 (a) shows the structure of the FSS.

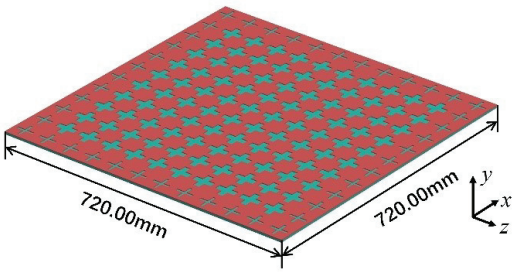

(a)

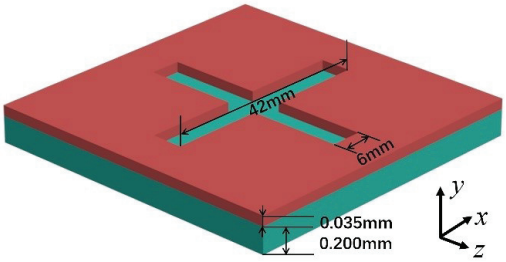

(b)

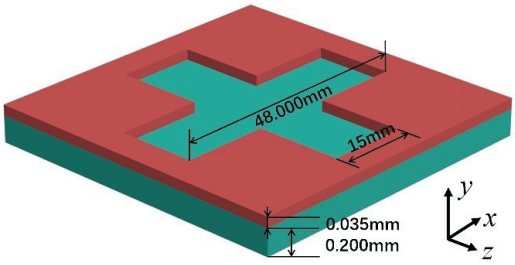

(c)

Fig. 6. The structure of the FSS: (a) overall view of the FSS, (b) the size of the narrow cross slot unit, and (c) the size of the wide cross slot unit.

Its length in both x- and z-directions is 720 mm. The surface comprises two different cross-slot units, as shown in Figs. 6 (b) and (c).

The narrow cross slot has a width of 6 mm and a length of 42 mm, and the wide cross slot has a width of 15 mm and a length of 48 mm. The thickness of the FSS is 0.235 mm, of which metal is 0.035 mm thick and the substrate is 0.2 mm thick. The ε_r of the substrate is 4.5 and σ is 0.004 S/m. The thickness of the metal is the fine structure of the FSS which greatly confines the computational efficiency. A plane wave polarized along the x-direction is incident perpendicular to the FSS. The excitation source is a modulated Gaussian pulse with a frequency range from 2.5 GHz to 4 GHz. The time dependence of the excitation function is given as follows:

$$E_x(t) = \cos(2\pi \cdot fre \cdot t) \exp\left(-4\pi \left((t-t_0)/\tau\right)^2\right), \tag{13}$$

where fre = 3.125 GHz, τ = 2.67 ns, and $t_0 = 0.9\tau$ = 2.4 ns.

One observation point is located at 120 mm behind the center of the surface. We use the serial FDTD, the serial HIE-FDTD method, and the parallel HIE-FDTD method to compute the electric field at the observation point and the transmission coefficient of the FSS. The minimum grids in the x- and z-directions are 1 mm. In the y-direction, the minimum grid is 0.035 mm. The total number of grids is 396×35×396. According to the time stability condition, the time step size in the FDTD method is

$\Delta t_f = 1\Big/c\sqrt{1/\Delta x^2 + 1/\Delta y^2 + 1/\Delta z^2}$ =0.0583 ps, while in the HIE-FDTD method, the time step is

$\Delta t = 1\Big/c\sqrt{1/\Delta x^2 + 1/\Delta z^2}$ =2.36 ps, which is 40.48 times larger than that in the FDTD method. The simulation history is 8 ns, which can ensure the complete convergence of time-domain signals. It corresponds to 323,842 time steps in the FDTD method and 8000 time steps in the HIE-FDTD method. The simulation is implemented on Intel(R) Xeon(R) Gold 6248R with 3.00 GHz CPU and 1 TB memory.

Figure 7 shows the value of E_x component at the observation point calculated by using the parallel HIE-FDTD method, the serial HIE-FDTD method, and the serial FDTD method. Figure 8 presents the calculated transmission coefficient of the FSS. From these figures, it is obvious that the calculated results of the parallel HIE-FDTD agree very well with those of the serial HIE-FDTD method and the serial FDTD method, whether in the time domain or frequency domain. The transmission coefficient of the FFS exceeds 0.9 within the range from 2.9 GHz to 3.65 GHz. Figures 7 and 8 validate the high computational accuracy of the parallel HIE-FDTD method.

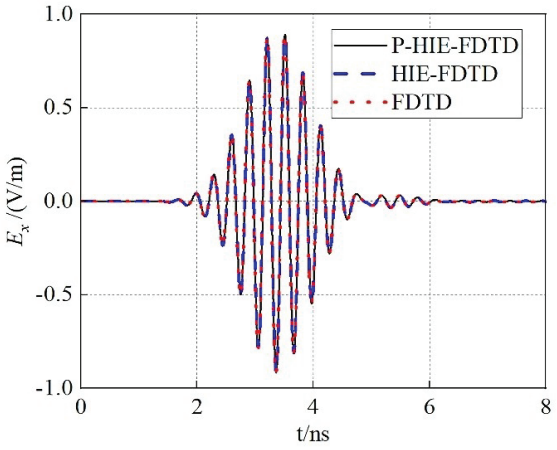

Fig. 7. The value of the E_x components at the observation point calculated by using the proposed parallel HIE-FDTD method, the serial HIE-FDTD method, and the serial FDTD method.

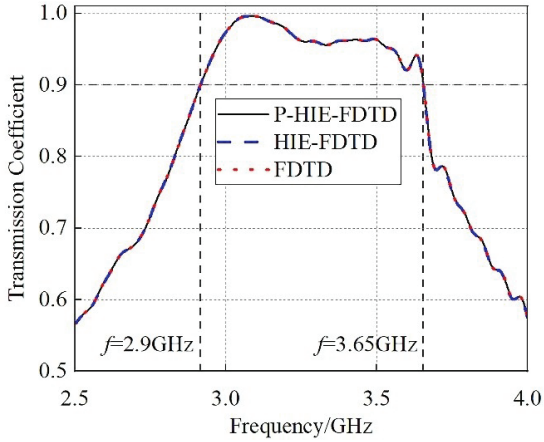

Fig. 8. The result of the transmission coefficient of the FSS calculated by using the proposed parallel HIE method, the serial HIE-FDTD method, and the serial FDTD method.

Table 1 displays the computation time of the serial FDTD method, the serial HIE-FDTD method, and the parallel HIE-FDTD method with 32 processes. We also introduce the speedup factors $S_p(k)$ with the following definition:

$$S_p(k) = \frac{p \times \text{Run time with } p \text{ cores}}{\text{Run time with } k \text{ cores}}, \tag{14}$$

where p is the reference number of processors and k is the number of processors used in calculation. $S_1(k)$of the proposed method is showed in Fig. 9.

The results demonstrate that the simulation speed of the serial HIE-FDTD method is 29.3 times faster than the serial FDTD, which is due to the larger time step in the HIE-FDTD method. Moreover, the simulation speed

Table 1: The time step size, total time steps, and computing time of different methods

Method	$\Delta t(ps)$	Total Steps	Computing Time (h)
FDTD	0.0583	323,842	901.40
HIE-FDTD	2.36	8000	30.77
P-HIE-FDTD	2.36	8000	1.18

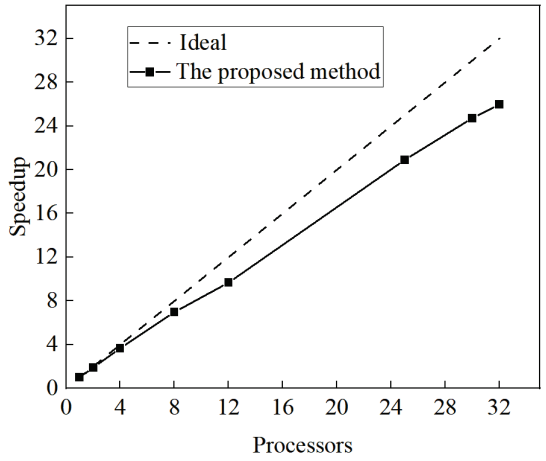

Fig. 9. $S_1(k)$ obtained for a space size of 396×35×396 in case of the proposed parallel HIE-FDTD method.

of the proposed parallel HIE-FDTD method with 32 processes is 25 times faster than the serial HIE-FDTD method. The parallel efficiency of the proposed method reaches 81.2 %. It can conclude that the proposed parallel HIE-FDTD method considerably reduces the runtime over the serial FDTD and the serial HIE-FDTD, while the accuracy of the proposed method is still maintained.

The parallel efficiency of the proposed method is defined as $\delta = T_1 / T_n n$. Here, T_1 represents the computing time of the HIE-FDTD method with a single process; n is the number of the processes and T_n is the computing time of the HIE-FDTD method with n processes. Table 2 presents the computing time and the parallel efficiency of the proposed parallel HIE-FDTD method. It can be observed that the efficiency maintains above 80% for different numbers of processes, which proves that this method is very suitable for parallel computing.

Table 2: Comparison of computation efficiency

Number of Processes	Number of Subdomains	Computing Time (s)	Parallel Efficiency δ
1	$1\times1\times1$	6652.02	100%
2	$2\times1\times1$	3496.58	95.1%
4	$2\times1\times2$	1812.13	91.8%
8	$4\times1\times2$	952.54	87.3%
12	$4\times1\times3$	687.61	80.6%
25	$5\times1\times5$	318.16	83.6%
30	$6\times1\times5$	268.99	82.4%
32	$8\times1\times4$	256.00	81.2%

V. CONCLUSION

This paper describes a parallel HIE-FDTD method implemented through the MPI library. Parallel computing is realized by creating a two-dimensional topology that divides the computational volume along two directions. The differences of the field components transmitted between the parallel HIE-FDTD method and parallel FDTD method are discussed. The function for communication and derived data types provided by the MPI library are employed to transmit HIE-FDTD field components. The numerical example indicates the high computational accuracy and excellent parallel efficiency of the proposed method. It shows that the parallel efficiency maintains above 80% for different numbers of processes, which proves that this method is very suitable for parallel computing.

ACKNOWLEDGMENT

This work was supported by the National Key Research and Development Program of China under No. 2020YFA0709800, and by the National Natural Science Foundations of China under No. 62122061, and also by the Shaanxi Natural Science Basic Research Project under No. 2023-JC-QN-0673.

REFERENCES

[1] K. S. Yee, "Numerical solution of initial boundary value problems involving Maxwell's equations in isotropic media," *IEEE Trans. Antennas Propagat.*, vol. AP-14, pp. 302-307, 1966.

[2] A. Taflove and S. C. Hagness, *Computational Electrodynamics: The Finite-Difference Time-Domain Method*, 3rd ed. Boston, MA, USA: Artech House, 2005.

[3] Guiffaut and K. Mahdjoubi, "A parallel FDTD algorithm using the MPI library," *IEEE Antennas Propag. Mag.*, vol. 43, no. 2, pp. 94-103, Apr. 2001.

[4] T. Namiki, "A new FDTD algorithm based on alternating-direction implicit method," *IEEE Trans. Microw. Theory Tech.*, vol. 47, no. 10, pp. 2003-2007, Oct. 1999.

[5] Y. Yang, R. S. Chen, and E. K. N. Yung, "The unconditionally stable Crank–Nicolson FDTD method for three-dimensional Maxwell's equations," *Microw. Opt. Tech. Lett.*, vol. 39, pp. 97-101, Oct. 2003.

[6] J. Shibayama, M. Muraki, J. Yamauchi, and H. Nakano, "Efficient implicit FDTD algorithm based on locally one-dimensional scheme," *Electron. Lett.*, vol. 41, no. 19, pp. 1046-1047, Sep. 2005.

[7] S. Garcia, T. Lee, and S. Hagness, "On the accuracy of the ADI-FDTD method," *IEEE Antennas Wireless Propag. Lett*., vol. 1, no. 1, pp. 31-34, Jan. 2002.

[8] M. Li, K. P. Ma, D. M. Hockanson, J. L. Drewniak, T. H. Hubing, and T. P. Van Doren, "Numerical and experimental corroboration of an FDTD thin slot model for slots near corners of shielding enclosures," *IEEE Trans. Electromagn. Compat*., vol. 39, no. 3, pp. 225-232, Aug. 1997.

[9] J. Chen and J. G. Wang, "A 3D hybrid implicit-explicit FDTD scheme with weakly conditional stability," *Microw. Opt. Technol. Lett*. 48, 2291-2294, 2006.

[10] J. Chen and J. Wang, "Comparison between HIE-FDTD method and ADI FDTD method," *Microw. Opti. Technol. Lett*., vol. 49, no. 5, pp. 1001-1005, Mar. 2007.

Qin Nan was born in Yan'an, China. He completed his B.S. in Northwest University, Xi'an, China, in 2022. He is currently working toward the Ph.D. degree in electromagnetic field and microwave technology at Xi'an Jiaotong University, Xi'an, China. His research interests include the fast FDTD method and parallel computing.

Chunhui Mou was born in Yantai, China. She received the B.S. and M.S. degrees from Xidian University, Xi'an, China, in 2012 and 2015, and the Ph.D. degree from Xi'an Jiaotong University, Xi'an, China, in 2023, all in electromagnetic field and microwave technology.

She is currently working in Xi'an Jiaotong University, Xi'an, China, as a postdoctoral researcher. Her research interests include the fast FDTD method, FDTD mesh generation method, and multi-physical field calculation.

Juan Chen was born in Chongqing, China. She received the Ph.D. degree from Xi'an Jiaotong University, Xi'an, China, in 2008, in electromagnetic field and microwave technology.

She is currently working in Xi'an Jiaotong University, Xi'an, China, as a professor. Her research interests include computational electromagnetics, microwave device design, etc.

Fractal Interpolation Function based Thin Wire Antennas

Gizem Kalender[1], Emine Yeşim Zoral[2], and Serkan Günel[2]

[1]The Graduate School of Natural and Applied Sciences

[2]Engineering Faculty, Dept. of Electrical & Electronics Engineering
Dokuz Eylül University, Izmir, 35800, Turkey
gizem.kalender@deu.edu.tr, yesim.zoral@deu.edu.tr, serkan.gunel@deu.edu.tr

Abstract – This paper presents an approach for the design of wire antennas based on fractal interpolation functions (FIFs). The interpolation points and the contraction factors of the FIFs are chosen as free parameters to modify the antenna geometry. The proposed structures' gain and radiation pattern can be optimized using FIF parameters. Producible prefractal antennas obtained in the intermediate iterations of fractal generation have compact sizes compared to classical counterparts. The error in prefractal geometry and the original fractal is bounded, and can be determined in terms of the finest producible detail's dimensions. The emerging structures have multiband behavior due to their self-similar and symmetric nature. To illustrate the approach, we have provided finite element based simulations for several prefractal antennas. $|S_{11}|$, the gain, the radiation efficiency, the radiation patterns, and feed point impedances for the demonstrated antennas are calculated numerically. The results indicate that produced antennas can be used in applications that require limited mechanical size, multiple operating bands, and controlled radiation patterns.

Index Terms – Fractal antenna, fractal interpolation functions, iterated function systems.

I. INTRODUCTION

Recent developments in wireless communications systems require more compact, wider bandwidth, multiband, and low-cost antennas. Fractal antennas can fulfill these requirements due to scale invariance, self-similarity, and space-filling properties of the fractals [1]. These properties enable the miniaturization of antenna structures [2–5]. The fractal structures can be designed to increase the effective physical length of the antennas to achieve multiband behavior in a limited space [6–8]. Basic fractal geometries such as Koch and Hilbert curves, and Sierpinski carpet have been studied for their radiation characteristics in the literature widely [9–15]. Comprehensive and up-to-date reviews can be found in [16, 17].

However, the studies rarely relate the mathematical properties of fractals to the antenna radiation characteristics. One approach is to optimize the antenna geometry over the fractal dimension using genetic algorithms [18, 19] directly. The authors present the relation between the resonant frequencies and the fractal dimension of the parameterized Koch curves in [20]. In general, the studies in the literature focus on predefined well-known fractal templates such as variants of the infamous Koch curve or the Sierpinski carpet. On the other hand, restricting the geometry a priori limits the practical applications.

As a novel approach, we present fractal wire antenna geometries based on the FIFs. In contrast to the literature, we don't assume a predefined topology in this study, and the designer is in full control of the antenna's shape by setting a few interpolation points and contraction factors. The interpolation points and the contraction factors of the FIFs can be used to optimize the antennas for a specific purpose. Then, we investigate the effects of fractal parameters on antenna radiation properties, namely the resonant frequencies, the bandwidth, the radiation patterns, gain, and input impedance.

Fractal interpolation is a technique used to construct continuous functions whose graphs are fractals based on iterated function systems (IFS) [21, 22]. Following the pioneering research, FIFs have been applied in geometric design, signal processing, and wavelet theory in the context of engineering, physics, and chemistry [23, 24]. FIFs provide non-smooth alternatives to traditional smooth interpolation techniques and are more suitable for irregular curves that display self-similarity.

Fractal interpolation is an iterative procedure, and each iteration can be considered a *prefractal*. The various antennas can be constructed associated with each of the prefractals. The skeleton of the antenna geometry can be determined by the given interpolation points. Additionally, the FIFs have free parameters that can be used to manipulate the geometry to alter the fractal dimension and the symmetry of the structure. The antenna can be

Submitted On: October 17, 2023
Accepted On: January 9, 2024

https://doi.org/10.13052/2023.ACES.J.381104

optimized by changing the interpolation points and the free parameters. Therefore, it can be constructed without a predefined fractal template in order to optimize the antenna performance. Note that several structures such as the Koch curve can also be obtained by specific choice of FIF parameters.

To demonstrate the proposed approach, we generated a simple curved wire dipole antenna using FIFs based on affine transformations. The parameters of affine transformations consist of contraction factors on the horizontal axis and scaling factors on the vertical axis, which simply controls the antenna geometry.

The scattering parameter $|S_{11}|$, the input impedance, the gain, and the bandwidth of the constructed structure are calculated via extensive numerical simulations.

We have observed that even the simple structure can show multiband behavior for prefractals obtained at each iteration. Using the proposed procedure, the designer has flexibility in the determination of the skeletal structure of the antenna first. Afterwards, the vertical scaling parameters that are particularly significant on fractal properties can be used to optimize the antenna for a specific application. By means of this flexibility, the technique can be extended to design effective antennas confined in a limited space especially.

II. FRACTAL INTERPOLATION

Let the set of interpolation points, $\{[x_i,y_i]^T \in \mathbb{R}^2 : i = 0,1,2,...,N\}$ where $x_0 < x_1 < \cdots < x_N$ be given, and the continuous function $h : [x_0,x_N] \mapsto \mathbb{R}$ that satisfies $h(x_i) = y_i$, be the interpolation function.

We can construct an IFS from a set of contractive shear transformations $w_i : \mathbb{R}^2 \to \mathbb{R}^2$, $i = 1,2,\ldots,N$, of the form

$$w_i\left(\begin{bmatrix}x\\y\end{bmatrix}\right) = \begin{bmatrix}\alpha_i & 0\\ \beta_i & \gamma_i\end{bmatrix}\begin{bmatrix}x\\y\end{bmatrix} + \begin{bmatrix}u_i\\v_i\end{bmatrix}, \tag{1}$$

such that its attractor is the graph of continuous function h. Clearly, $0 \le |\alpha_i|, |\gamma_i| < 1$, $\forall i$. The contraction factor of w_i is than $\sigma_i = \max\{|\alpha_i|, |\gamma_i|\}$, and the contraction factor of the IFS is $\sigma = \max_i \sigma_i$.

Following the steps in [23] and choosing γ_i's as free parameters, one can construct w_i's in such a way that the line segment between $[x_0,y_0]^T$ and $[x_N,y_N]^T$ is mapped to the line segment between $[x_{i-1},y_{i-1}]^T$ and $[x_i,y_i]^T$. Therefore, the parameters must be chosen to satisfy

$$\begin{aligned}\alpha_i &= \frac{x_i - x_{i-1}}{x_N - x_0}, \quad u_i = \frac{x_N x_{i-1} - x_0 x_i}{x_N - x_0},\\ \beta_i &= \frac{y_i - y_{i-1}}{x_N - x_0} - \gamma_i \frac{y_N - y_0}{x_N - x_0},\\ v_i &= \frac{x_N y_{i-1} - x_0 y_i}{x_N - x_0} - \gamma_i \frac{x_N y_0 - x_0 y_N}{x_N - x_0}.\end{aligned} \tag{2}$$

Denoting $\mathscr{F}$ as the space of continuous functions $h : [x_0,x_N] \to \mathbb{R}$ such that $h(x_0) = y_0$ and $h(x_N) = y_N$ with a metric $d(h,g) = \max\{|h(x) - g(x)|,\ h,g \in \mathscr{F}\}$, lets us define a transformation $T : \mathscr{F} \to \mathscr{F}$ that satisfies

$$\begin{aligned}(Th)(x) &= \beta_i l_i^{-1}(x) + \gamma_i h(l_i^{-1}(x)) + v_i,\\ l_i(x) &= \alpha_i x + u_i \qquad i = 1,2,\ldots,N,\end{aligned} \tag{3}$$

for $x \in [x_{i-1},x_i]$. T is a contraction in the metric space $\mathscr{F}$ with contraction factor $\sigma_T = \max\{|\gamma_i|\}$ and has a unique fixed point h^*, i.e. $(Th^*)(x) = h^*(x), \forall x \in [x_0,x_N]$ [22]. For any $h^{[0]} \in \mathscr{F}$, the sequence of functions for $k = 1,2,\ldots$

$$h^{[k]}(x) = (Th^{[k-1]})(x) \quad \forall x \in [x_0,x_N], \tag{4}$$

converges to h^*, i.e.,

$$\lim_{k\to\infty} h^{[k]}(x) = h^*(x), \quad \forall x \in [x_0,x_N]\,. \tag{5}$$

Furthermore, the points on the attractor of the IFS is determined by the function h^* since

$$(Th)(\alpha_i x + u_i) = \beta_i x + \gamma_i h(x) + v_i,\ \forall x \in [x_{i-1},x_i]. \tag{6}$$

We consider each set $\{[x,h^{[k]}(x)]^T \in \mathbb{R}^2, \forall x \in [x_0,x_N]\}$ associated with $h^{[k]}$ as a *prefractal* and a candidate antenna. Given the transformations w_i, and $h^{[0]}(x) \equiv 0$, we can construct the geometry of the antenna using (3) and the random iteration algorithm for IFS [22]. The convergence rate to final attractor depends on the contraction factor σ_T. Given $0 < \varepsilon \ll 1$, the convergence can be assumed if

$$\begin{aligned}&d(h^{[k]},h^{[k-1]}) \le \sigma_T^{k-1} d(Th^{[0]},h^{[0]})\\ &= \sigma_T^{k-1} \max_{x\in[x_0,x_N]} \left\{\left|\beta_i \frac{x-u_i}{\alpha_i} + v_i\right|\right\}_{i=1}^{N} \le \varepsilon,\end{aligned} \tag{7}$$

is satisfied. Clearly, σ_T depends on the number of interpolation points and chosen γ_i; hence the designer has two means of controlling how fast the convergence to h^* is. ε can be chosen according to the finest detail that can be manufactured in practice, and the necessary number of iterations, k, in (3) determined accordingly. We also have

$$d(h^*,h^{[k]}) \le \frac{\sigma_T}{1-\sigma_T} d(h^{[k-1]},h^{[k]}), \tag{8}$$

in order to measure how close the prefractal associated with $h^{[k]}$ is to the fractal associated with h^*.

Note that the selection γ_i's has a significant impact on the overall topology of the FIF, as depicted in Fig. 1.

The fractal dimension, D, of the final attractor of the associated IFS satisfies

$$D = 1 + \begin{cases}\frac{\log\left(\sum_{i=1}^{N}|\gamma_i|\right)}{\log(N)}, & \sum_{i=1}^{N}|\gamma_i| > 1\\ 0, & \text{otherwise.}\end{cases} \tag{9}$$

Hence $1 \le D < 2$ if the interpolation points are spaced equally. Clearly, we have absolute control of the fractal's dimension and the complexity [22].

If $\gamma_i = \gamma = 0, \forall i$, h^* corresponds to the linear interpolator. Besides, the small contraction factor ($\sigma_T \to 0$) yields 1D fractals without much detail, and associated prefractals are not of much interest. The choice of

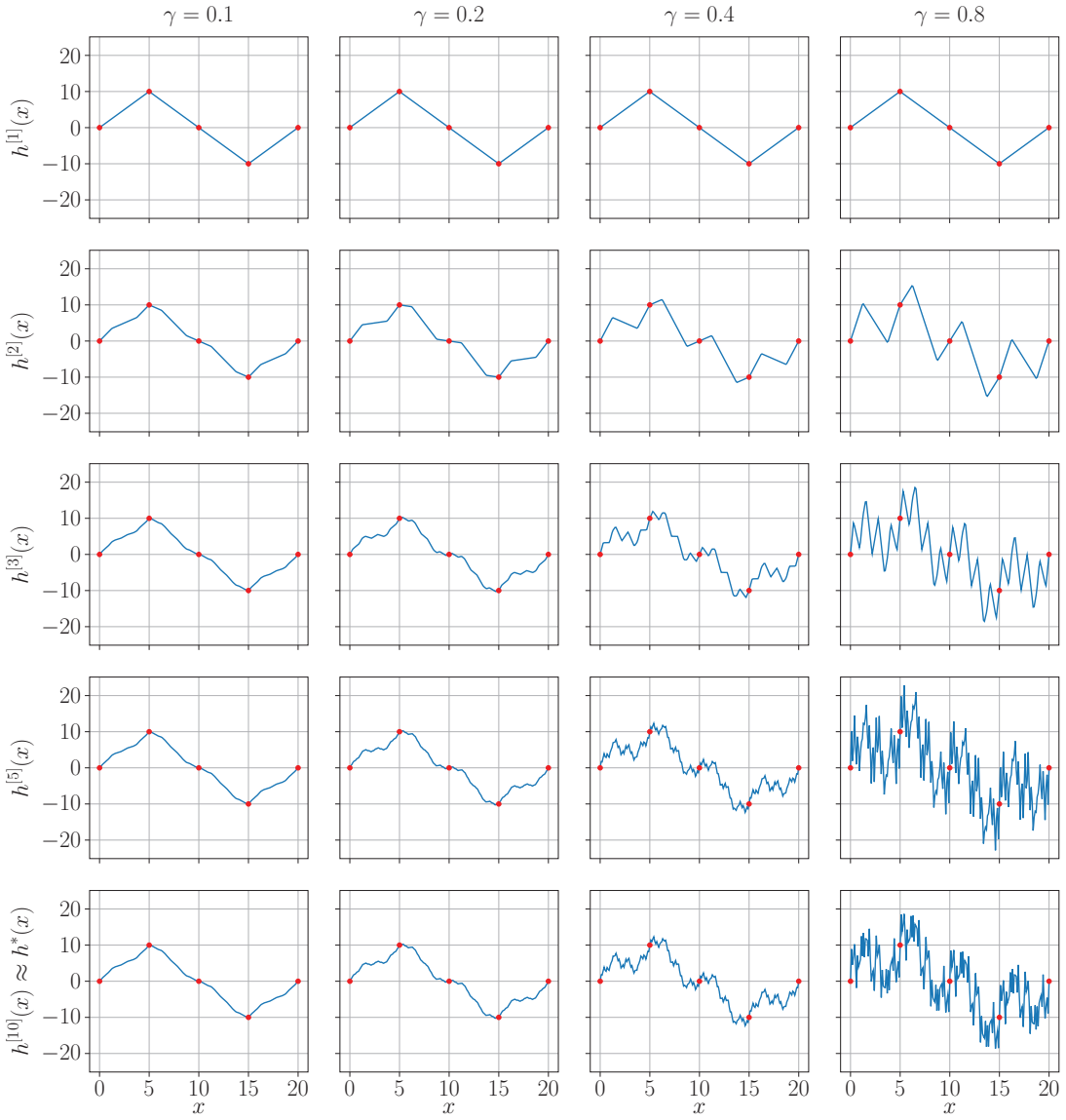

Fig. 1. FIF's corresponding to prefractals for the parameters in Table 1. The red dots indicate interpolation points. The fractal dimensions for $\gamma_i = \gamma \leq 0.25$, $\gamma = 0.4$, and $\gamma = 0.8$ are $D = 1$, $D \approx 1.34$, and $D \approx 1.84$ for the graph of $h^*(x)$ respectively.

Table 1: The parameters of FIF wire prefractal antennas for $\gamma = 0.2$ and 0.4 in Fig. 1

Parameter	Value	Description
N	5	Number of interpolation points
$\begin{bmatrix} z_i \\ y_i \end{bmatrix}, i = 1,2,...,5$	$\begin{bmatrix} 0.5 \\ 0 \end{bmatrix} + \begin{bmatrix} 0 & 5 & 10 & 15 & 20 \\ 0 & 10 & 0 & -10 & 0 \end{bmatrix}$	Interpolation points (mm), $y_i = h^{[k]}(z_i)$
$\alpha_i, i = 1,2,3,4$	0.25	z-scaling factor
$\beta_i, i = 1,2,3,4$	$\frac{y_i - y_{i-1}}{20}$	y-scaling factor
$u_i, i = 1,2,3,4$	z_{i-1}	z-translation
$v_i, i = 1,2,3,4$	y_{i-1}	y-translation
r_0	0.005	Radius of the antenna wire (mm)

$\sum_{i=1}^{N} |\gamma_i| > 1$ results in fractals with self similar and symmetric structures with fine details. On the other hand, $|\gamma_i| \to 1$ implies $\sum_{i=1}^{N} |\gamma_i| \to N$ and as a result $D \to 2$. The attractor associated with the underlying IFS has finer details in this case. However, the details of the associated prefractals may not be suitable for manufacturing for large k.

The parameter ε in (7) can be chosen with respect to the finest producible detail. Hence, k can be determined automatically. Then the error estimate between the prefractal at k^{th} iteration and the attractor can be estimated by (8). Although the fractal structures are more interesting in terms of radiation properties as $D \to 2$, the practical realization can be cumbersome for a given accuracy due to large number of required iterations, yielding extremely fine details.

The main advantage of using FIF as the basis for the structure of the antenna is its flexibility. The designer can optimize the structure by a few number of points on the structure ($\{x_i, h(x_i)\}_{i=1}^{N}$) and altering the free parameters ($\{\gamma_i\}_{i=1}^{N}$) for desired radiation properties.

III. ILLUSTRATIVE EXAMPLE

To illustrate the approach, we present FIF perfectly conducting thin wire prefractal antennas oriented along z-axis embedded in yz-plane as a proof of concept.

The simulations were carried out using Ansoft High Frequency Structural Simulator (HFSS)™, on an Intel Xeon based workstation with 32 physical cores and 256 Gb of memory.

The antennas have been fed through a gap of 1 mm located at the origin with a 50 Ω lumped port. The common parameters for the design are listed in Fig. 1. The prefractal curves that form the antennas are obtained by running iterations in (4) with Julia programming language [25]. The generated curves are imported to HFSS for further processing. A circle of radius $r_0 = 5\ \mu m$ has been extruded along the imported path to create the 3D model. The 3D model is simplified to exclude irrelevant details with respect to operating wave length. The 3D models are simulated using finite element method (FEM). The mesh used in FEM has been fine-tuned with adaptive meshing. Only half $z \geq 0$ plane is considered with an electric symmetry boundary at xy-plane (Fig. 2 (a)). The largest FEM model had 852,603 mixed order tetrahedral elements for the case with $\gamma = 0.4$ and $k = 10$ (Fig. 2 (b)).

The resonant frequencies, 10 dB bandwidths, peak gains, and feed point impedances are listed in Table 2. The radiation efficiencies have been confirmed to be unity in all cases listed, as the antennas have been assumed to be perfect electric conductors. The frequency sweep analysis in the range of $0.8\text{GHz} \leq f \leq 8\text{GHz}$ is shown in Fig. 3. Note that the case with $k = 1$ corresponds to linear interpolation over the set $\{x_i, h(x_i)\}_{i=1}^{N}$, and its shape is independent of the contraction factors $\{\gamma_i\}_{i=1^N}$. It is a simple bend wire dipole antenna. The decrease in the first mode's frequency and the emergence of several other modes is apparent with respect to the reference bend wire dipole.

When the contraction factor is close to 0, the prefractals in each iteration converge to a simple wire antenna with slight decrease in the resonant frequencies for increasing k (Table 2). This is expected since the

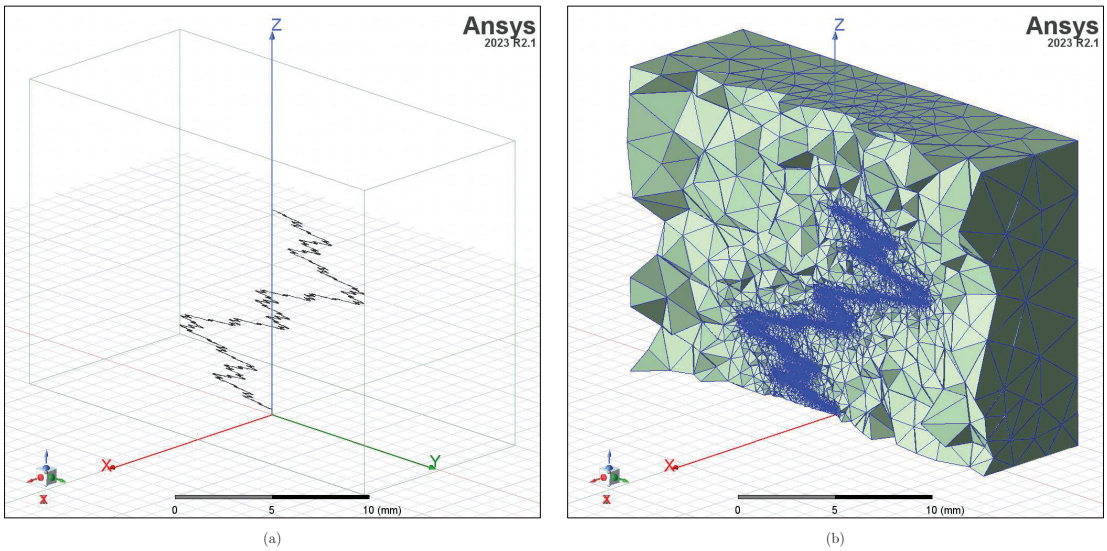

Fig. 2. HFSS 3D model for $\gamma = 0.4$, $k = 10$. (b) Corresponding mesh. yz-plane is set to be a perfect electric symmetry boundary to for a smaller FEM model. The other outer surfaces of the mesh region is set to be radiation boundaries.

Table 2: The properties of the simulated FIF wire prefractal antennas

γ	k	**Frequency**[GHz]	**Bandwidth** [MHz]	**Gain**	**Impedance** [Ω]
-	1	1.807	126	0.47	$67.2-j2.0$
		5.277	146	1.36	$53.3-j0.0$
0.2	3	1.653	108	0.40	$64.4-j1.4$
		4.838	115	1.27	$45.5-j0.1$
	10	1.602	90	0.38	$64.2-j0.5$
		4.636	94	1.01	$46.6-j0.1$
0.4	3	1.088	56	0.2	$57.4-j0.8$
		3.043	37	0.42	$34.4-j0.1$
		4.832	49	2.09	$78.9-j0.4$
		6.484	47	2.09	$83.5+j0.1$
	10	0.866	42	0.13	$55.2-j0.9$
		2.468	28	0.29	$35.4+j0.3$
		3.824	39	1.40	$62.3-j2.8$
		5.058	45	1.90	$46.8-j1.2$

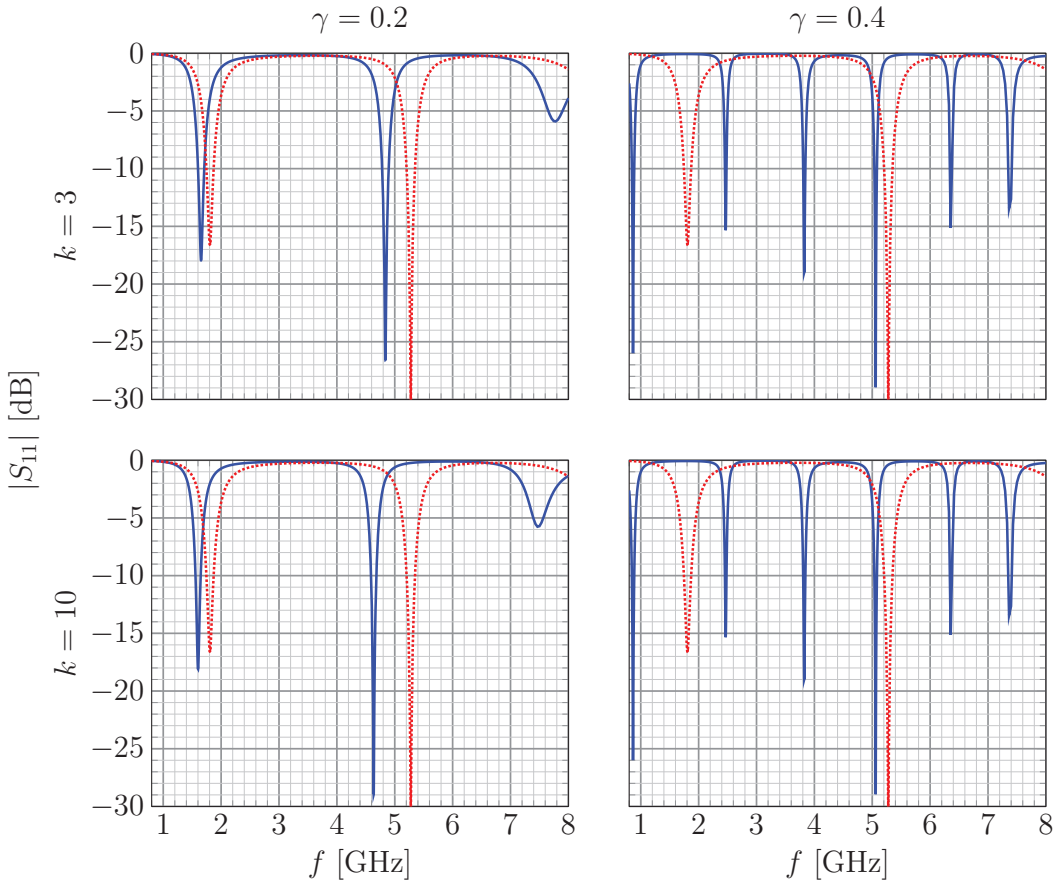

Fig. 3. $|S_{11}|$ versus the frequency f for varying k and γ. (——) and (·····) indicates the prefractal and the reference bend wire antenna corresponding to $k=1$ case, respectively.

physical length of the antenna increases with successive iterations of FIF as well. More interesting results are observed when $\gamma=0.4$. Several new bands of operation with excellent matching emerge as k increases. Besides, the deviation in resonant frequencies is more pronounced compared to $\gamma=0.2$. For larger contraction factors, the antenna is still confined to the same space compactly, although it is electrically longer.

The normalized radiation patterns for $\gamma=0.4$ are presented in Fig. 4. The multi-directional radiations

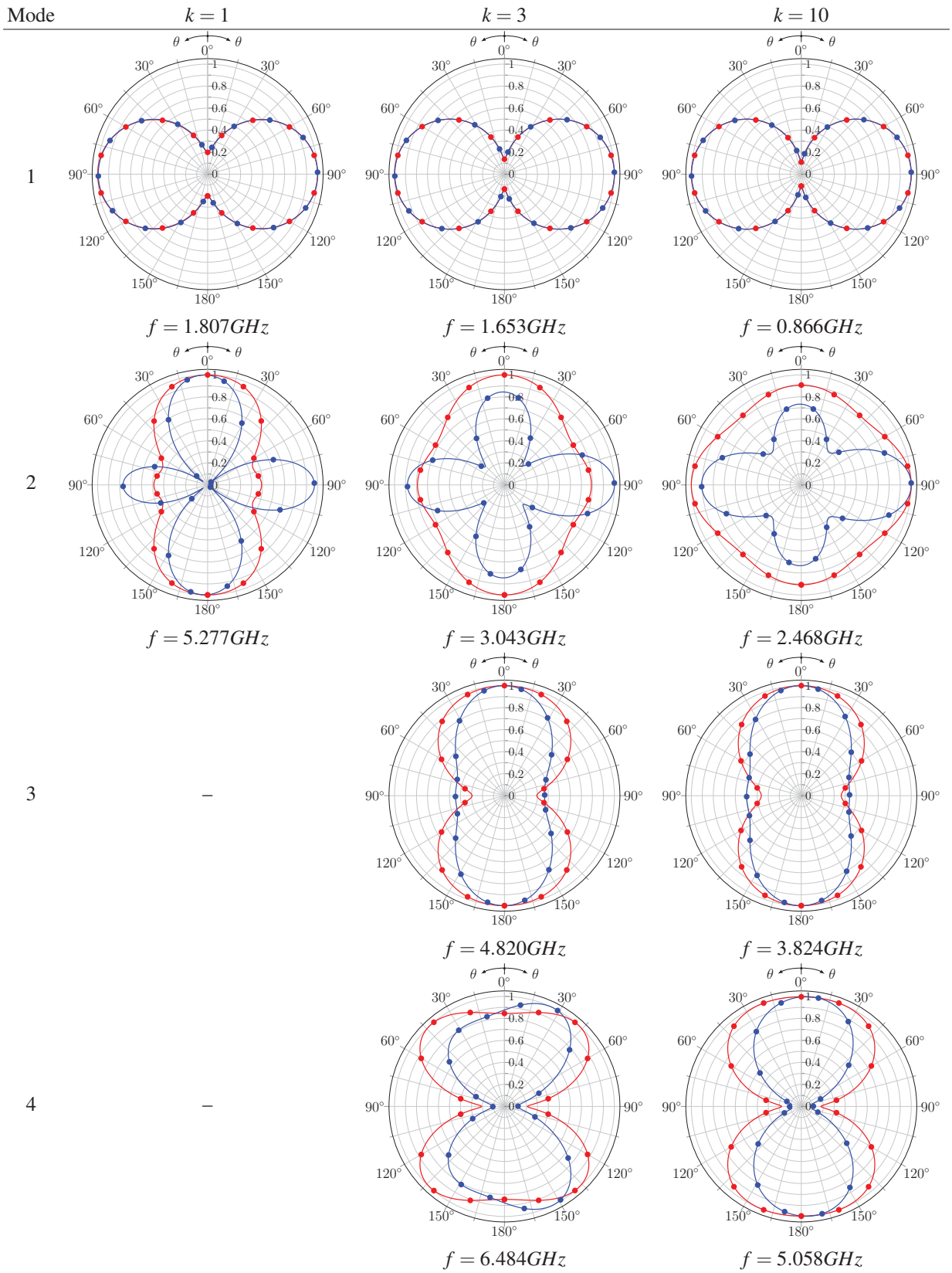

Fig. 4. The H-plane (—●—: $\phi = 0°$), and E-plane (—●—: $\phi = 90°$) normalized radiation patterns for the first four modes in frequency range $0.8GHz \leq f \leq 8GHz$ with $\gamma = 0.4$.

patterns emerge for various operating frequencies. Note that although the antenna's orientation was kept fixed along z-axis, the radiation patterns are almost perpendicular in mode 1 ($f = 0.866$ GHz) and mode 4 ($f = 5.058$ GHz) for $k = 10$ and $\gamma = 0.4$. The fractal structure allows such possibilities, which would not be available in classical wire antennas.

IV. CONCLUSION

In this article, we propose an approach based on FIFs to design fractal wire antennas. In this approach the geometry need not be predetermined, but can be altered flexibly, in contrast to the fractal antenna studies in the literature. The geometry of the antenna can be controlled by the free parameters, i.e., the interpolation points and the contraction factors of the FIF. Therefore, the antenna's radiation properties can be controlled directly. The FIF parameters can be adjusted to optimize the performance for the desired antenna properties in terms of gain, radiation pattern, and matching. Furthermore, the optimization can be carried out for multiple bands of operation under spatial constraints.

One of the advantages of the proposed approach is the possibility to bound errors between the prefactals obtained in the intermediate iterations of fractal generation and ideal fractals. This is particularly important because it is impossible to manufacture the infinite details of the ideal fractal. We can determine the required number of iterations a priori for a given manufacturing tolerance based on the constructiveness of the underlying transformations leading to FIF for given antenna performance measures.

The fractal nature of the designed geometries allows the apparent electrical length of the antenna to be larger than the equivalent dipole fitted to the same limited space. In other words, the antenna size can be miniaturized relative to classical structures while operating at low frequencies. Additionally, the self-similarity of the generated fractals results in multiband behavior. These properties render proposed antennas suitable for mobile and wearable wireless applications that require long-range communication especially.

ACKNOWLEDGMENT

This study has been fully supported by Dokuz Eylül University, Scientific Research Fund under project 2021.KB.FEN.004 and partially supported under project 2021.KB.FEN.007.

REFERENCES

[1] B. B. Mandelbrot, *The Fractal Geometry of Nature*, vol. 1, WH Freeman New York, 1982.

[2] D. H. Werner and S. Ganguly, "An overview of fractal antenna engineering research," *IEEE Antennas and Propagation Magazine*, vol. 45, no. 1, pp. 38-57, 2003.

[3] W. J. Krzysztofik, "Fractal geometry in electromagnetics applications from antenna to metamaterials," *Microwave Review*, vol. 19, no. 2, 2013.

[4] N. Sharma and V. Sharma, "A journey of antenna from dipole to fractal: A review," *J. Eng. Tech.*, vol. 6, no. 2, pp. 317-351, 2017.

[5] P. Prabhu and S. Malarvizhi, "Compact dual-band hybrid-fractal MIMO system for UMTS and LTE mobile applications," *Applied Computational Electromagnetics Society (ACES) Journal*, pp. 135-140, 2019.

[6] D. H. Werner, R. L. Haupt, and P. L. Werner, "Fractal antenna engineering: The theory and design of fractal antenna arrays," *IEEE Antennas and Propagation Magazine*, vol. 41, no. 5, pp. 37-58, 1999.

[7] D. Werner and P. Werner, "Frequency-independent features of self-similar fractal antennas," *Radio Science*, vol. 31, no. 6, pp. 1331-1343, 1996.

[8] J. Anguera, C. Puente, C. Borja, and J. Soler, "Fractal shaped antennas: A review," *Encyclopedia of RF and Microwave Engineering*, 2005.

[9] H. Sagan, *Space-filling Curves*, Springer Science & Business Media, 2012.

[10] A. Ismahayati, P. J. Soh, R. Hadibah, and G. Vandenbosch, "Design and analysis of a multiband koch fractal monopole antenna," in *2011 IEEE International RF & Microwave Conference*, pp. 58-62, IEEE, 2011.

[11] C. P. Baliarda, J. Romeu, and A. Cardama, "The Koch monopole: A small fractal antenna," *IEEE Trans. on Antennas and Propagation*, vol. 48, no. 11, pp. 1773-1781, 2000.

[12] C. Puente-Baliarda, J. Romeu, R. Pous, and A. Cardama, "On the behavior of the Sierpinski multiband fractal antenna," *IEEE Trans. on Antennas and Propagation*, vol. 46, no. 4, pp. 517-524, 1998.

[13] A. Bhattacharya, B. Roy, S. K. Chowdhury, and A. K. Bhattacharjee, "Design and analysis of a Koch snowflake fractal monopole antenna for wideband communication," *Applied Computational Electromagnetics Society (ACES) Journal*, pp. 548-554, 2017.

[14] P. Chowdary, A. M. Prasad, P. M. Rao, and J. Anguera, "Design and performance study of Sierpinski fractal based patch antennas for multiband and miniaturization characteristics," *Wireless Personal Communications*, vol. 83, no. 3, pp. 1713-1730, 2015.

[15] K. Vinoy, K. Jose, V. Varadan, and V. Varadan, "Hilbert curve fractal antenna: A small resonant antenna for VHF/UHF applications," *Microwave and Optical Technology Letters*, vol. 29, no. 4, pp. 215-219, 2001.

[16] J. Anguera, A. Andújar, J. Jayasinghe, V. V. S. S. S. Chakravarthy, P. S. R. Chowdary, J. L. Pijoan, T. Ali, and C. Cattani, "Fractal antennas: An historical perspective," *Fractal and Fractional*, vol. 4, no. 1, 2020.

[17] A. Karmakar, "Fractal antennas and arrays: A review and recent developments," *Int. J. of Microwave and Wireless Tech.*, vol. 13, no. 2, pp. 173-197, Mar. 2021.

[18] H. Oraizi and S. Hedayati, "Miniaturized UWB monopole microstrip antenna design by the combination of Giusepe Peano and Sierpinski carpet fractals," *IEEE Antennas and Wireless Propagation Letters*, vol. 10, pp. 67-70, 2011.

[19] D. H. Werner, P. L. Werner, and K. Church, "Genetically engineered multiband fractal antennas," *Electronics Letters*, vol. 37, no. 19, pp. 1150-1151, 2001.

[20] K. Vinoy, K. Jose, V. Varadan, and V. Varadan, "Resonant frequency of Hilbert curve fractal antennas," in *IEEE Antennas and Propagation Society Int. Symp. 2001 Digest. Held in conjunction with: USNC/URSI National Radio Science Meeting (Cat. No. 01CH37229)*, vol. 3, pp. 648-651, IEEE, 2001.

[21] K. Vinoy, J. K. Abraham, and V. K. Varadan, "On the relationship between fractal dimension and the performance of multi-resonant dipole antennas using Koch curves," *IEEE Trans. on Antennas and Propagation*, vol. 51, no. 9, pp. 2296-2303, 2003.

[22] M. F. Barnsley, *Fractals Everywhere*, Academic Press, 2014.

[23] M. F. Barnsley, "Fractal functions and interpolation," *Constructive Approximation*, vol. 2, no. 1, pp. 303-329, 1986.

[24] M. A. Navascués, A. K. B. Chand, V. P. Veedu, and M. V. Sebastián, "Fractal interpolation functions: A short survey," *Applied Mathematics*, vol. 2014, 2014.

[25] J. Bezanson, A. Edelman, S. Karpinski, and V. B. Shah, "Julia: A fresh approach to numerical computing," *SIAM Review*, vol. 59, no. 1, pp. 65-98, 2017.

Gizem Kalender received a degree in electrical and electronics eng. from Çukurova University, Turkiye, in 2013 and her M.Sc. degree from Dokuz Eylül University in 2015. She is a Ph.D. candidate and holds a research assistant position at Dokuz Eylül University. Her main research interests are antennas, fractal theory, and metamaterials.

Emine Yeşim Zoral graduated from Dokuz Eylül University, Izmir, Turkiye, in 1990. She received the Ph.D. from the Illinois Inst. of Tech., Chicago, USA, in 1999, in electrical and electronics eng. She has been working as a professor at the Department of Electrical and Electronics Eng. at Dokuz Eylül University since 2000. Her main research interests are perturbation techniques in electromagnetic theory, microwave circuits, dielectric resonators, and antennas.

Serkan Günel completed his Ph.D. at Dokuz Eylül University, Inst. of Natural Sciences, Dept. of electrical and electronics eng., in 2006. His main research areas include nonlinear system analysis, information theory, and electromagnetic theory. His current research topics cover analysis of nonlinear dynamics via entropy measures, design of fractal antennas based on iterated function systems, analysis of resonant electromagnetic structures via perturbation of matrices, and the applications of cluster synchronization of chaotic systems. Currently, he is employed as an associate professor in Dokuz Eylül University.

Composite Scattering Study of Layered Rough Surface with Target based on CCIA

Jiaguo Zhang and Huan Wei

School of Mathematics and Computer Science
Yichun University, Yichun, 336000, China
ycu_zjg2022@126.com, wbsf2019@126.com

***Abstract* –** In this paper, a fast Cross Coupling iterative Approach (CCIA) is proposed for studying the composite scattering of the layered rough surfaces with buried target, which uses forward backward method (FBM) to solve the electric field integral equations (EFIE) of the layered rough surface and bi-conjugate gradient method (BI-CG) to solve the EFIE of the target, and the interaction between the rough surface and the target is achieved by updating the excitation term. The algorithm is applied to calculate the composite scattering coefficients of the rough surface with a buried target, the results match with those of the traditional numerical algorithm MOM while the error can be reduced to 10^{-3} by 6 iterations, and the convergence speed and calculation accuracy meet the requirements. The composite scattering coefficients and Angular Correlation Function (ACF) amplitudes of layered rough surface and dielectric targets with different conditions are calculated, and the effects of various factors such as target size and burial depth on the composite scattering characteristics are discussed. It is found that the buried targets will have a great influence on the scattering characteristics, weakening or neglecting the coupling between them will lead to larger errors. Moreover, the results show that ACF can suppress scattering from rough surfaces well, making the scattering characteristics of the target more obvious, which is important for detecting underground targets.

***Index Terms* –** Cross Coupling iterative Approach (CCIA), Electric Field Integral Equations (EFIE), Angular Correlation Function (ACF), composite scattering characteristics.

I. INTRODUCTION

The study of electromagnetic characteristics [1–5] of targets and environment has a very important role in the field of remote sensing information processing and target identification: in the field of remote sensing information processing [6–9], it is necessary to analyze and study the electromagnetic characteristics of remote sensing environment and targets, and to design and manufacture sensors to match them in order to obtain the best target remote sensing information. Radar is one of the most commonly used sensors for target remote sensing, which uses electromagnetic signals to sense targets and has the ability to work around the clock. Therefore, analyzing and acquiring target and environment features, and establishing a database of target and environment features are very important for remote sensing information processing. On the other hand, target and environment feature extraction and identification [10–13] is the basic technology to realize battlefield precision perception, precision strike and missile attack and defense confrontation, so target feature signal extraction and identification technology is the advanced stage of target and environment feature research, target and environment electromagnetic scattering feature analysis is the basis of target identification, and the model-based target identification method depends largely on the target and environment electromagnetic scattering feature modeling accuracy. There are usually two methods to obtain environmental and target characteristics: real measurements and simulations. Although the results of real measurements are highly reliable, the cost of real measurements is high and it is difficult to obtain complete scattering characteristics data due to many practical conditions. With the rapid development of computer technology, it is becoming easier and easier to realize 3D reconstruction of complex targets and high accuracy of electromagnetic calculation problems by using its powerful computing power.

Zou [14] introduced the single integral equation-Kirchhoff approximation (SIE-KA) hybrid method with a multilevel fast multipole algorithm (MLFMA) to accelerate the computation to solve complex scattering problems in coastal environments containing conductor and dielectric targets, and presented many practical ideas in remote sensing. Liang [15] established a composite scattering model based on the propagation-inside-layer expansion + generalized forward-backward method (EPILE+GFBM), studied the coupling mechanism between sea surface-missile-ship, and discussed the

Submitted On: June 5, 2023
Accepted On: November 27, 2023

https://doi.org/10.13052/2023.ACES.J.381105

effects of different states of the target (such as attitude, position, and rotation angle) on the composite scattering characteristics. The results of the study are instructive for target detection, identification, and imaging in the marine environment. Zou [16] established a natural valley model, simulated the cavity structure of the valley, and proposed the SBR-EEC method to solve the compound scattering problem existing in ultra-low altitude targets in the valley. It is found that the cavity in the valley has a great influence on the composite scattering, which will affect the detection and identification accuracy of targets in the environment. Based on the traditional FBAM and GO/PO hybrid methods, Li [17] proposed an acceleration algorithm that can effectively reduce the occlusion judgment. Experiments prove that the algorithm is effective for SAR imaging of ships in the marine environment, and the electromagnetic scattering characteristics of multi-ship targets in the marine environment are studied based on the algorithm. Wang [18] proposed an algorithmic model for composite scattering of environment with target, derived the integral equations for each computational domain in the complex model, solved them one by one using a hybrid method of CFIE and EFIE, and accelerated the matrix computation using the multilevel fast multipole algorithm (MLFMA) in the computation process.

In this paper, we focus on the composite scattering problem of layered rough surface with target. Firstly, in order to solve the problem of low computational efficiency of traditional algorithms, the CCIA algorithm is proposed, which uses FBM to solve the EFIE of the layered rough surface and BI-CG to solve the EFIE of the target, and the interaction between the rough surface and the target is achieved by updating the excitation term. And the effectiveness of the proposed algorithm is demonstrated by computational examples. Then the coupling effect between the rough surface and the target is studied by this algorithm, and their composite scattering coefficients are calculated, it is found that the coupling effect has a great influence on the composite scattering. Finally, the ACF of the composite environment is investigated, and the results show that the ACF is greatly influenced by the target size, and the ACF can well suppress the scattering from rough surfaces, which is important for detecting subsurface targets.

II. COMPOSITE SCATTERING CALCULATION MODEL

A. Coupled boundary integral equations of layered rough surface and dielectric target

A typical spherical medium target is located in zone II, the second layer of the medium, as shown in Fig. 1. Zone O denotes free space, usually air; Zone I denotes rough surface 1 and Zone II denotes rough surface 2, which usually have different dielectric constants.

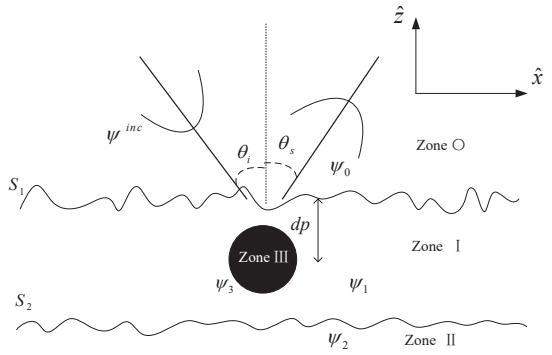

Fig. 1. Graphics of dielectric target and rough surfaces.

When the size of the target is infinitely small (which can be considered as no target), the boundary integral equation of the stratified rough surface is:

$$\frac{1}{2}\psi_0(r) = \psi^{inc}(r) + \int_{f_1(x)} \left[\psi_0(r)\hat{n}_1 \cdot \nabla g_0\left(r,r'\right) - g_0\left(r,r'\right)\hat{n}_1 \cdot \nabla\psi_0(r)\right] ds, \quad (1)$$

$$\frac{1}{2}\psi_1(r) = \int_{f_2(x)} \left[\psi_1(r)\hat{n}_2 \cdot \nabla g_1\left(r,r'\right) - g_1\left(r,r'\right)\hat{n}_2 \cdot \nabla\psi_1(r)\right] ds - \int_{f_1(x)} \left[\psi_1(r)\hat{n}_1 \cdot \nabla g_1\left(r,r'\right) - g_1\left(r,r'\right)\hat{n}_1 \cdot \nabla\psi_1(r)\right] ds, \quad (2)$$

$$\frac{1}{2}\psi_1(r) = \int_{f_2(x)} \left[\psi_1(r)\hat{n}_2 \cdot \nabla g_1\left(r,r'\right) - g_1\left(r,r'\right)\hat{n}_2 \cdot \nabla\psi_1(r)\right] ds. \quad (3)$$

In the above equation, $\hat{n}_i$ is the normal vector in zone i with the direction vertically upward, $\boldsymbol{r}$ represents the field point, $\boldsymbol{r'}$ represents the source point, $g_i(r,r')$is the Green's function in zone i, and there is

$$r = x\hat{x} + z\hat{z}, \quad (4)$$

$$r' = x'\hat{x} + z'\hat{z}, \quad (5)$$

$$g_i(r,r') = \frac{i}{4}H_0^{(1)}(k_i\left|r-r'\right|). \quad (6)$$

The target surface is denoted by f_c and the rough surface is denoted by $f_i(x)(i = 2,3$ denotes the upper and lower rough surfaces, respectively). ψ^{inc} denotes the incident wave and ψ_i is the total field in the i region.

And when there is a non-negligible target (sphere) on the stratified rough surface, Eq. (2) can be rewritten as

$$\frac{1}{2}\psi_1(r) = \int_{f_2(x)} \left[\psi_1(r)\hat{n}_2 \cdot \nabla g_1\left(r,r'\right) - g_1\left(r,r'\right)\hat{n}_2 \cdot \nabla\psi_1(r)\right] ds - \int_{f_1(x)} \left[\psi_1(r)\hat{n}_1 \cdot \nabla g_1\left(r,r'\right) - g_1\left(r,r'\right)\hat{n}_1 \cdot \nabla\psi_1(r)\right] ds + \int_{f_0} \left[\psi_1(r)\hat{n}_{op} \cdot \nabla g_1\left(r,r'\right) - g_1\left(r,r'\right)\hat{n}_{op} \cdot \nabla\psi_1(r)\right] ds. \quad (7)$$

where $\hat{n}_{op}$ is the normal vector of the target surface with the direction perpendicular to the target surface outward,

and this partial integral in Eq. (7) represents the target's contribution to the total field.

The scattered field within the target is:

$$\frac{1}{2}\psi_3(r) = -\int_{f_0}[\psi_3(r)\hat{n}_{op}\cdot\nabla g_3(r,r') - g_3(r,r')\hat{n}_{op}\cdot\nabla\psi_3(r)]ds. \tag{8}$$

Then we obtained the surface integral equations for the stratified rough surface and the medium target. Their boundary conditions under TM and TE waves are as follows, respectively. TE:

$$\psi_i(r) = \psi_{i+1}(r)\ \frac{\partial\psi_i(r)}{\partial n_i} = \frac{\mu_i}{\mu_{i+1}}\frac{\partial\psi_{i+1}(r)}{\partial n_{i+1}}, \tag{9}$$

TM:

$$\psi_i(r) = \psi_{i+1}(r)\ \frac{\partial\psi_i(r)}{\partial n_i} = \frac{\varepsilon_i}{\varepsilon_0}\frac{\partial\psi_{i+1}(r)}{\partial n_{i+1}}. \tag{10}$$

Using the basis function to discrete the above set of equations, let the length of the rough surface is L, the discrete density is Δx, and the total discrete number is N; the dielectric target surface discrete density is Δx_0, and the total discrete number is M. The following matrix equation can be obtained:

$$A^{(0,1,1)}U_1 + B^{(0,1,1)}\psi_1 = \psi^{inc}, \tag{11}$$

$$\rho_1 A^{(1,2,1)}U_1 + B^{(1,2,1)}\psi_1 + A^{(1,2,2)}U_1 + B^{(1,2,2)}\psi_1, + C\cdot U_0 + D\cdot\psi_0 = 0, \tag{12}$$

$$\rho_1 A^{(1,2,1)}U_1 + B^{(1,2,1)}\psi_1 + A^{(1,2,2)}U_1 + B^{(1,2,2)}\psi_1, + E\cdot U_0 + F\cdot\psi_0 = 0, \tag{13}$$

$$\rho_2 A^{(2,2,2)}U_1 + B^{(2,2,2)}\psi_1 = 0, \tag{14}$$

$$G\cdot U_1 + H\cdot\psi_1 + I\cdot U_2 + J\cdot\psi_2 + K\cdot U_0 + L\cdot\psi_0 = 0, \tag{15}$$

$$\rho_3 P\cdot U_0 + Q\cdot U_0 = 0. \tag{16}$$

Where the expressions of the matrix elements $A_{mn}^{(a,b,c)}$, $B_{mn}^{(a,b,c)}$ are

$$A_m^{(a,b,c)} = \begin{cases} w^{(a,c)}\frac{i\Delta x}{4}H_0^{(1)}\left(k_a \mid r_{m,b} - r_{n,c}\right)\Delta l_{m,b} \\ (\text{for}(b=c, m\neq n) \text{ or } b\neq c) \\ w^{(a,c)}\frac{i\Delta x}{4}\left[1 + \frac{i2}{\pi}\ln\left(\frac{e^{\gamma}k_a\Delta x\Delta l_{m,b}}{4e}\right)\right] \\ (\text{for}(b=c, m=n)) \end{cases}, \tag{17}$$

$$B_{mn}^{(a,b,c)} = \begin{cases} -w^{(a,c)}\frac{ik_a\Delta x}{4}\frac{H_1^{(1)}\left(k_a\left|r_{m,b}-r_{n,c}\right|\right)}{\left\|r_{m,b}-r_{n,c}\right\|}\times \\ \left(f_c'(x_n)(x_n - x_m) - (f_c(x_n) - f_b(x_m))\right) \\ (\text{for}(b=c, m\neq n) \text{ or } b\neq c) \\ \frac{1}{2} - w^{(a,c)}\frac{f_b''(x_m)}{4\pi}\frac{\Delta x}{1+f_b'(x_m)^2} \\ (\text{for}(b=c, m=n)) \end{cases}. \tag{18}$$

Where when $a = c$, $w^{(a,c)} = 1$; when $a \neq c$, $w^{(a,c)} = -1$. And $\rho_l = \mu_l/\mu_{l-1}$ for TE wave, $\rho_l = \varepsilon_l/\varepsilon_{l-1}$ for TE wave, $U_i(x) = \frac{\partial\psi_i(r)}{\partial n'}\sqrt{1+(\partial S_l/\partial x)^2}\Big|_{r\in S_i}$, $\psi_i(x) = \psi_i(r)|_{r\in S_i}$. The three superscripts in the upper right corner of the matrix elements represent: the first number indicates the region, the second number indicates the rough surface where the field point is located, and the third number indicates the rough surface where the source point is located. The specific meaning of each parameter can be found in the literature (19), which is not repeated here considering the length of the article.

Solving the above matrix equations yields composite electromagnetic scattering results for rough surfaces and targets, and it should be noted that computational accuracy and computational time should be considered when solving. However, since the MoM numerical method [20-22] is based on strict Maxwell equations and boundary conditions, it includes various interactions between electromagnetic waves and rough surfaces (especially multiple scattering between cells on rough surfaces), and is theoretically an accurate solution method that has been widely used in scattering calculations. However, numerical simulations of scattering from rough surfaces often need to consider taking a sufficiently long rough surface for the calculation, especially under the conditions of low grazing angle incidence and moderate rough surface, where a large unknown quantity is generated after the dissection, making the conventional MoM a great challenge. For this reason, relevant fast algorithms must be used to accelerate the calculation.

B. Cross coupling iterative approach (CCIA)

Therefore, in order to solve this problem and improve the practicality of the algorithm, Cross Coupling iterative Approach (CCIA) is proposed in this paper, which overcomes the limitations of the traditional MoM by considering both the computational accuracy and the computational speed in solving the composite scattering of the layered rough surface and the medium target. The basic principle is that while considering the interaction between the layered rough surface and the dielectric target, the surface integral equation of the layered rough surface is solved by FBM and the surface integral equation of the target is solved by Bi-CG, and then the set of equations is solved by iteration. the computational volume and memory required by the CCIA method is only $O(N^2)$, which greatly improves the computational efficiency.

Rectifying Eqs. (11-16), the following matrix equation can be obtained:

$$\begin{bmatrix} A^{(0,1,1)} & B^{(0,1,1)} & 0 & 0 \\ \rho_1 A^{(1,1,1)} & B^{(1,1,1)} & A^{(1,1,2)} & B^{(1,1,2)} \\ \rho_1 A^{(1,2,1)} & B^{(1,2,1)} & A^{(1,2,2)} & B^{(1,2,2)} \\ 0 & 0 & \rho_2 A^{(2,2,2)} & B^{(2,2,2)} \end{bmatrix}\cdot\begin{bmatrix} U_1 \\ \psi_1 \\ U_2 \\ \psi_2 \end{bmatrix} = \begin{bmatrix} \psi^{inc} \\ \psi_{Tar}^1 \\ \psi_{Tar}^2 \\ 0 \end{bmatrix}, \tag{19}$$

$$\begin{bmatrix} K & L \\ \rho_3 P & Q \end{bmatrix}\begin{bmatrix} U_0 \\ \psi_0 \end{bmatrix} = \begin{bmatrix} \psi^{sur} \\ 0 \end{bmatrix}. \tag{20}$$

Where

$$\psi_{Tar}^I = -C^I\cdot U_0 - D^I\cdot\psi_0, \tag{21}$$

$$\psi_{Tar}^2 = -E\cdot U_0 - F\cdot\psi_0, \tag{22}$$

$$\psi^{Sur} = -F^{(1)} \cdot U_1 - H^{(1)} \cdot \psi_1 - I^{(2)} \cdot U_2 - J^{(2)} \cdot \psi_2. \quad (23)$$

In the above equations, the surface current distributions of the stratified rough surface and the target can be obtained by solving the matrix Eqs. (19) and (20), respectively. ψ^i_{Tar} denotes the scattering effect of the target on the rough surface, superscript i=1 denotes the upper rough surface, superscript i=2 denotes the lower rough surface; ψ^{Sur} denotes the scattering effect of the layered rough surface on the target. Thus, the rough surface and the target do not exist in isolation, they are not only irradiated by the incident waves, but also influence each other.

During the iteration, the excitation term on the right-hand side of the matrix Eqs. (19-20) are continuously updated and Eqs. (19-20) become:

$$Z^0 \cdot I_0^{(i)} = \begin{bmatrix} A^{(0,1,1)} & B^{(0,1,1)} & 0 & 0 \\ \rho_1 A^{(1,1,1)} & B^{(1,1,1)} & A^{(1,1,2)} & B^{(1,1,2)} \\ \rho_1 A^{(1,2,1)} & B^{(1,2,1)} & A^{(1,2,2)} & B^{(1,2,2)} \\ 0 & 0 & \rho_2 A^{(2,2,2)} & B^{(2,2,2)} \end{bmatrix} \cdot \begin{bmatrix} U_1^{(i)} \\ \psi_1^{(i)} \\ U_2^{(i)} \\ \psi_2^{(i)} \end{bmatrix} = \begin{bmatrix} \psi^{inc} \\ \psi^1_{Tar}(i) \\ \psi^2_{Tar}(i) \\ 0 \end{bmatrix} = V_0^{(i)}, \quad (24)$$

$$Z^1 \cdot I_1^{(i)} = \begin{bmatrix} K & L \\ \rho_3 P & Q \end{bmatrix} \begin{bmatrix} U_0^{(i)} \\ \psi_0^{(i)} \end{bmatrix} = \begin{bmatrix} \psi^{sur}(i) \\ 0 \end{bmatrix}. \quad (25)$$

Where the upper corner marker i denotes the number of iteration steps, $I_0^{(i)}$ denotes the current distribution on the rough surface, $I_1^{(i)}$ denotes the current distribution on the target surface, $\psi^1_{Tar}(i)$ denotes the target excitation on the upper rough surface, $\psi^2_{Tar}(i)$ denotes the target excitation on the lower rough surface, and $\psi^{sur}(i)$ denotes the target excitation on the layered rough surface.

Then, each matrix is decomposed into three parts, namely the upper matrix $\boldsymbol{U}$, the lower matrix $\boldsymbol{D}$ and the diagonal matrix $\boldsymbol{L}$, and the forward backward method (FBM) method is used to solve Eq.(24), and the equations for the forward current are:

$$A^{L,(0,1,1)}U_1^f + B^{L,(0,1,1)}\psi_1^f = \psi^{inc} - \psi^{Tar} - A^{D,(0,1,1)}(U_1^f + U_1^b) - B^{D,(0,1,1)}(\psi_1^f + \psi_1^b), \quad (26)$$

$$\rho_1 A^{L,(1,1,1)}U_1^f + B^{L,(1,1,1)}\psi_1^f + A^{L,(1,1,2)}U_2^f + B^{L,(1,1,2)}\psi_2^f = \psi^1_{Tar} - \rho_1 A^{D,(1,1,1)}(U_1^f + U_1^b) - B^{D,(1,1,1)}(\psi_1^f + \psi_1^b) - A^{D,(1,1,2)}(U_2^f + U_2^b) - B^{D,(1,1,2)}(\psi_2^f + \psi_2^b), \quad (27)$$

$$\rho_1 A^{L,(1,2,1)}U_1^f + B^{L,(1,2,1)}\psi_1^f + A^{L,(1,2,2)}U_2^f + B^{L,(1,2,2)}\psi_2^f = \psi^2_{Tar} - \rho_1 A^{D,(1,2,1)}(U_1^f + U_1^b) - B^{D,(1,2,1)}(\psi_1^f + \psi_1^b) - A^{D,(1,2,2)}(U_2^f + U_2^b) - B^{D,(1,2,2)}(\psi_2^f + \psi_2^b), \quad (28)$$

$$\rho_2 A^{L,(2,2,2)}U_1^f + B^{L,(2,2,2)}\psi_1^f = -\rho_2 A^{D,(2,2,2)}(U_2^f + U_2^b) - B^{D,(2,2,2)}(\psi_2^f + \psi_2^b). \quad (29)$$

Where $U_l = U_l{}^f + U_l{}^b$, $\psi_l = \psi_l{}^f + \psi_l{}^b$, f and b denote the forward and backward components obtained after decomposition of the unknown components, respectively.

The initial values of the iteration are $U_1^{b,(0)} = 0$, $\psi_1^{b,(0)} = 0$, $U_2^{b,(0)} = 0$, $\psi_2^{b,(0)} = 0$, the initial values are substituted into Eq. (24) to update the solution to obtain U_1, ψ_1, U_2 and ψ_2. Then U_1, ψ_1, U_2, ψ_2 are substituted into Eq. (25) to obtain U_0, and the updated ψ^1_{Tar} and ψ^2_{Tar} are calculated and then substituted into Eq. (24). Repeat this iterative process until the specified convergence accuracy is reached. Eq. (24) can be solved by the FBM method, while Eq. (25) needs to be solved by the bi-conjugate gradient method (Bi-CG). The iteration error of step i is:

$$\tau(i) = \left| \frac{Z^1 \cdot [I_1^{(i)} - I_1^{(i-1)}]}{V_1^{(i)}} \right|. \quad (30)$$

The calculation achieves multiple scattering calculations of the layered rough surface and the target by continuously updating the excitation terms of the two equations until the iterative error meets the specified convergence accuracy.

C. Conical incident wave

In order to apply the numerical algorithm, the area calculated by the rough surface is bounded in a certain range. For the two-dimensional scattering problem, in order to limit the rough surface to L, i.e., $|x| \le L/2$, the surface current is artificially specified to be zero when $|x| > L/2$. In this way, the surface current has a sudden change at $x = \pm L/2$, and if a plane wave is used, this will cause artificial reflections at both endpoints.

In order to solve this problem, one of the methods is to set the edge as a periodic boundary, but this method has a certain approximation, and the error is not easy to determine, so it is generally not desirable; the second method is to select the incident wave as a conical wave, that is, the incident wave has Gaussian characteristics, when close to the boundary, the incident wave tends to zero, so as to avoid the abrupt change of the surface current. Using the widely used Thorsos conical wave, which can well satisfy the Helmholtz fluctuation equation, the one-dimensional conical wave is [23]

$$\psi^{inc}(r) = \exp[ik(x\sin\theta_i - z\cos\theta_i)\cdot(1+w(r))] \cdot \exp[-\frac{(x + z\tan\theta_i)^2}{g^2}], \quad (31)$$

where θ_i is the angle of incidence (labeled in Fig. 1) and g is the beamwidth factor, which determines the width of the window function.

Figure 2 represents the distribution of the amplitude of the incident wave on the surface.

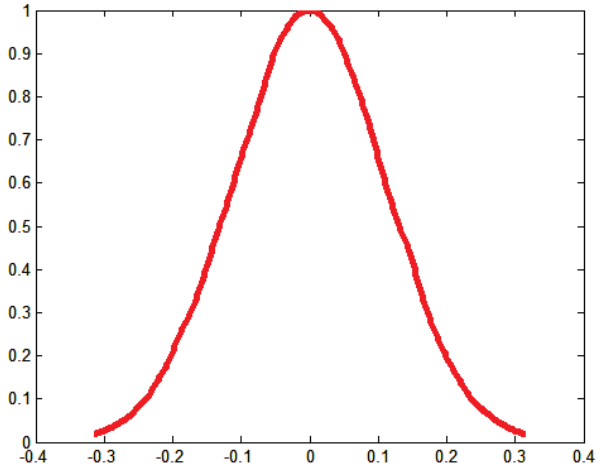

Fig. 2. Amplitude distribution of one-dimensional conical incident waves.

In Eq. (31), the wave vector of the incident wave is

$$k_i = k\left(\hat{x}\sin\theta_i - \hat{z}\cos\theta_i\right), \tag{32}$$

$$w(x,z) = \frac{1}{(kg\cos\theta_i)^2}\left[2\frac{(x+z\tan\theta_i)^2}{g^2} - 1\right]. \tag{33}$$

The width g is an important physical quantity that determines the incident width of the incident wave and the length of the rough surface. The larger the value of g, the greater the incident width of the incident wave and the greater the length of the rough surface. The larger the value of g, the more the numerical calculation can reflect the average scattering characteristics of the rough surface, and the more accurate the numerical calculation is, but it needs to consume more storage and calculation time. Therefore, the choice of g should consider both the accuracy of the calculation results and the calculation efficiency: the conical width g is determined by the incident angle, while the rough surface length L is determined by g. The expression is

$$g \geq \frac{6}{(\cos\theta_i)^{1.5}} L = 4g. \tag{34}$$

III. ALGORITHM VALIDATION

In this subsection, the parameters of the rough surface and the target are: $h_1 = 0.13\lambda$, $L_1 = 40\lambda$, $l_1 = 1.0\lambda$, $\varepsilon_{r1} = 4.0 + 0.01i$, $d = 6.0\lambda$, $h_2 = 0.08\lambda$, $L_2 = 40\lambda$, $l_2 = 1.0\lambda$, $\varepsilon_{r2} = 7.0$, $\theta_i = 20^o$, $g = L/6$, $dp = 3.0\lambda$, $R = 1.0\lambda$, $\varepsilon_c = 2.25$. Where h_i is the root mean square height of the rough surface, L_i is the length of the rough surface, l_i is the correlation length, ε_{ri} is the dielectric constant of the rough surface, where i=1 represents the upper rough surface and i=2 represents the lower rough surface, ε_c is the dielectric constant of the target, dp is the burial depth of the target, R is the radius of the sphere, and d is the thickness of the rough surface.

This subsection focuses on verifying the effectiveness of the CCIA algorithm proposed in this paper in terms of both computational efficiency and computational accuracy.

The MOM numerical algorithm is a solution method with high accuracy, and although it is relatively slow, it is undoubtedly suitable and more convincing as a validation algorithm due to its accurate calculation. In this subsection, both the algorithm of this paper and the MOM method are used to calculate the composite bistatic scattering coefficients for the layered rough surface and the dielectric target, and the calculation results are shown in Fig. 3.

Figure 3 (a) shows the calculation results of TE waves, and Fig. 3 (b) shows the calculation results of TM waves. From these two figures, it can be seen that the calculation curves of CCIA and MOM almost overlap for both TE incident wave and TM incident wave, indicat-

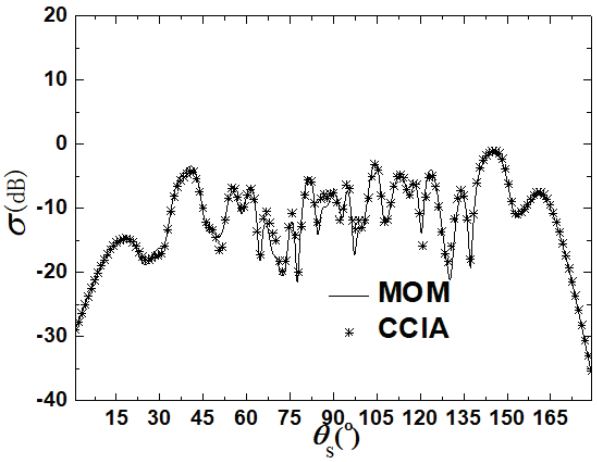

(a) TE incident wave

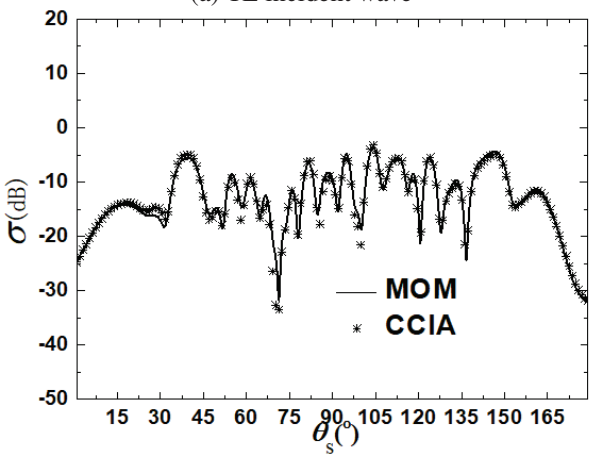

(b) TM incident wave

Fig. 3. Comparison of calculation results of different methods.

ing that their calculation results are extremely close, thus verifying the correctness of the method.

Table 1: Comparison of time consumed

Method	Time Consumption (sec)
CCIA	357
MoM	2109

Table 1 shows the time consumed for two different methods. It is evident that CCIA requires only 357 seconds of computation time, while MoM takes 2109 seconds. The CCIA method greatly reduces the computational time and significantly improves computational efficiency.

Figure 4 shows the variation of the iteration error $\tau(i)$ with the number of iteration steps i during the calculation. When CCIA is used to calculate the composite scattering of rough surfaces and targets, the iteration error in both cases can be reduced to 10^{-3} after 6 iterations, and the convergence speed is relatively fast, which can meet the calculation requirements. It indicates that the algorithm improves the computational speed while ensuring the computational accuracy, which is consistent with the expectation.

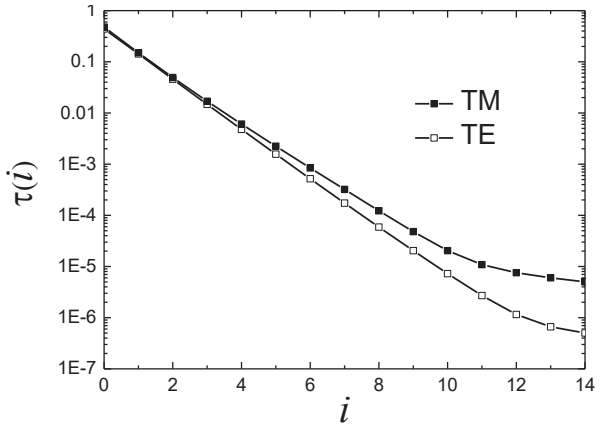

Fig. 4. Iterative error curve.

IV. CALCULATION RESULTS AND ANALYSIS

A. Effect of target on compound scattering

In this subsection, the parameters of the rough surface and the target are: $h_1 = 0.13\lambda$, $L_1 = 40\lambda$, $l_1 = 0.16\lambda$, $\varepsilon_{r1} = 4.0 + 0.01i$, $d = 6.0\lambda$, $h_2 = 0.08\lambda$, $L_2 = 40\lambda$, $l_2 = 0.16\lambda$, $\varepsilon_{r2} = 7.0$, $\theta_i = 20°$, $g = L/6$, $dp = 3.0\lambda$, $R = 1.0\lambda$, $\varepsilon_c = 2.25$.

In the study, the radii of the spheres are set as $R = 1.0\lambda$ and $R = 2.0\lambda$, respectively, and other parameters are kept constant to study the effects of different sizes of spheres on the composite scattering, and the results are shown in Fig. 5. Observing Fig. 5, it can be found that the scattering coefficient increases significantly after the introduction of the medium target relative to the rough surface without a target, which is caused by the mutual coupling effect between the target and the rough surface, and as the target volume increases, the distance between the target and the upper and lower rough surfaces shortens, the mutual coupling effect becomes stronger, and the scattering coefficient shows an enhanced trend, and the influence on the scattering characteristics of the layered rough surface becomes more and more obvious. Therefore, when studying the problems related to the target and the environment, the coupling effect between them must be taken into account.

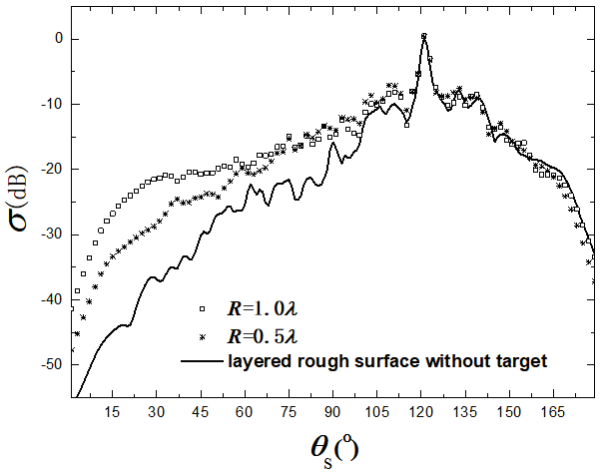

(a) TE incident wave

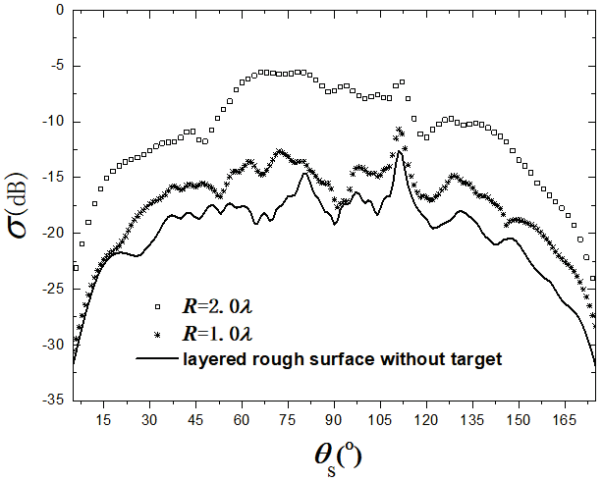

(b) TM incident wave

Fig. 5. Effect of target on compound scattering.

B. Effect of target depth on compound scattering

The target depths are set as $dp = 1.0\lambda$, $dp = 2.0\lambda$, $dp = 3.0\lambda$, respectively, and the effects of different

target depths on the target-environment scattering characteristics are investigated. Figure 6 shows that the composite scattering is almost unaffected by the target depth. While keeping the target volume constant, the target depth increases, its coupling with the upper rough surface decreases, and the coupling with the lower rough surface increases, so no big difference appears in general. In contrast, this variation is more pronounced at TM wave incidence.

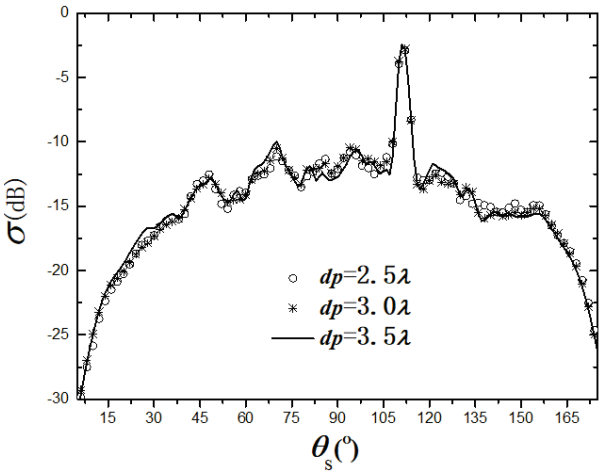

(a) TE incident wave

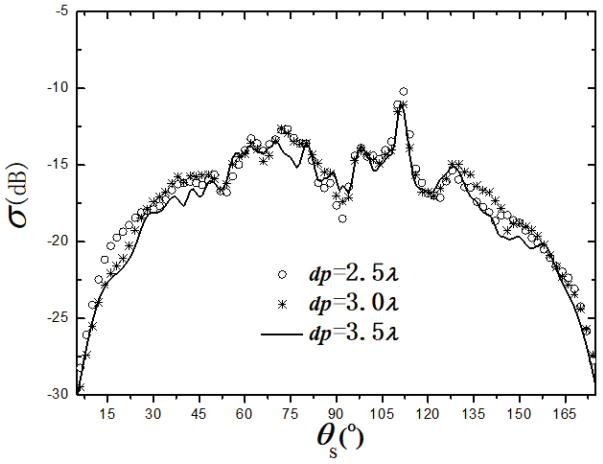

(b) TM incident wave

Fig. 6. Effect of target on compound scattering.

C. The effect of coupling on compound scattering

In this subsection, the coupling effects of the upper and lower rough surfaces and the rough surface-target coupling are mainly discussed. First, the scattering characteristics of a monolayered rough surface with dielectric constant $\varepsilon_{r1} = 4.0 + 0.01i$ are investigated, and the scattering coefficients are calculated for no rough surface-rough surface coupling and no rough surface-target coupling; then, keeping other parameters constant, a second layer of rough surface with dielectric constant $\varepsilon_{r2} = 4.0 + 0.01i$ is set at depth $d = 6.0\lambda$, and the scattering coefficients are calculated for only the rough surface-rough surface coupling action. Keeping the parameters unchanged, a dielectric target is next introduced in the upper rough surface with target depth $dp = 3.0\lambda$, $R = 1.0\lambda$, and dielectric constant $\varepsilon_c = 4$. The scattering coefficient is calculated again when multiple coupling exists. The scattering characteristic curves of the above three cases are shown in Fig. 7.

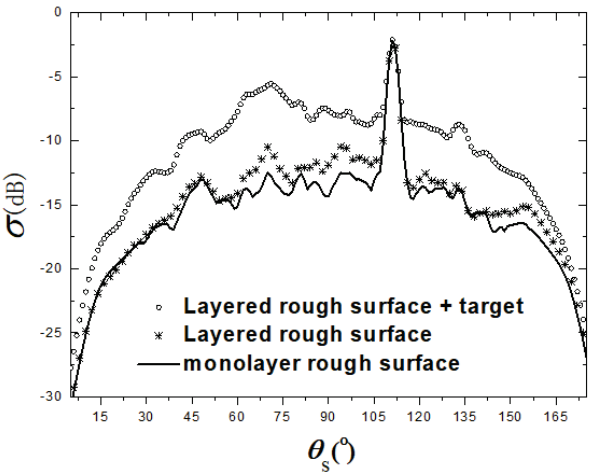

Fig. 7. The effect of coupling on compound scattering.

Figure 7 illustrates that the scattering coefficient of the layered rough surface increases significantly (compared to the single-layer rough surface) due to the coupling between the layers. This indicates that the coupling between the upper and lower layers is also an important component of the layered rough surface. The scattering coefficient continues to increase after the target is buried in the rough surface. It can be seen that the second magnitude is significantly stronger than the first one, indicating a strong coupling effect between the rough surface and the target. When studying electromagnetic scattering in complex environments, ignoring this coupling effect will lead to large errors.

D. ACF (Angular Correlation Function) characteristics for composite environments

The study of ACF is also an important part of the study of scattering in a composite environment. Its expression is [24]

$$\begin{aligned}&\Gamma(\theta_{s1},\theta_{i1},\theta_{s2},\theta_{i2})\\&= \langle \psi_s(\theta_{s1},\theta_{i1})\cdot\psi_s^*(\theta_{s2},\theta_{i2})\rangle / \sqrt{W_1 W_2}\\&= \frac{1}{N_r}\sum_{q=1}^{N_r}\psi_s(\theta_{s1},\theta_{i1},q)\cdot\psi_s^*(\theta_{s2},\theta_{i2},q)/\sqrt{W_1 W_2}. \quad (35)\end{aligned}$$

Where

$$W_1 = \sqrt{\frac{\pi}{2}} g \cos\theta_{i1} \left(1 - \frac{1 + 2\tan^2\theta_{i1}}{2k_0^2 g^2 \cos^2\theta_{i1}}\right), \quad (36)$$

$$W_2 = \sqrt{\frac{\pi}{2}} g \cos\theta_{i2} \left(1 - \frac{1 + 2\tan^2\theta_{i2}}{2k_0^2 g^2 \cos^2\theta_{i2}}\right). \quad (37)$$

Finally, the ACFs of the layered rough surface and the buried target layered rough surface were calculated and plotted in Fig. 8. Figure 8 illustrates that when there is no target, the ACF amplitude of the rough surface is relatively small (less than 0.05). After the target is buried in the rough surface, the scattering at this time consists of both the rough surface and the target, and the ACF amplitude increases significantly and is positively correlated with the size of the target. While changing the burial depth of the target with the same size of the target, the ACF amplitude gradually decreases with the increase of the target depth, which is due to the increase of the target depth and the decrease of his interaction with the rough surface. The graphical results show that the target size is an important factor affecting the ACF, and the ACF can well suppress the scattering from the rough surface and make the scattering characteristics of the target more significant, which is important for the detection of subsurface targets.

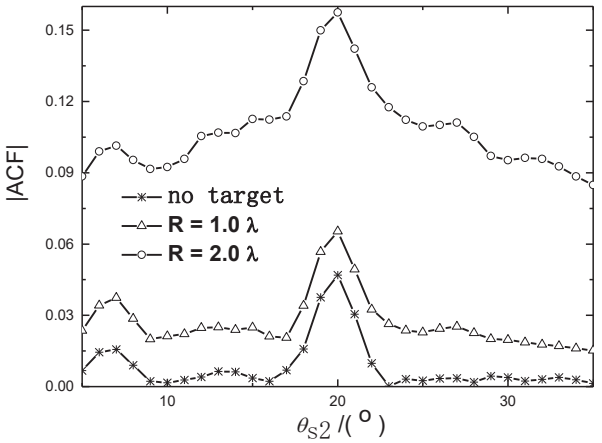

(a) TM incident wave

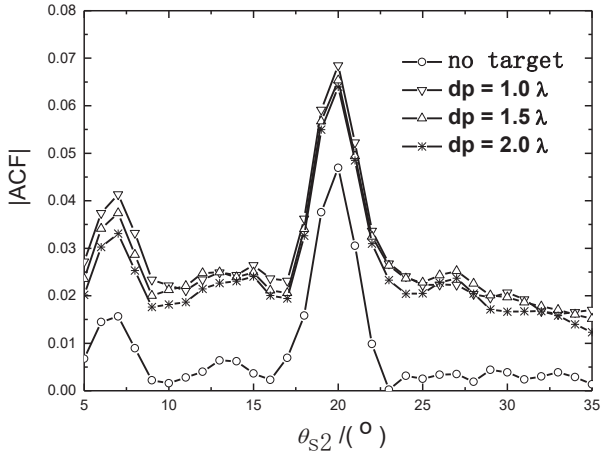

(b) TM incident wave

Fig. 8. ACF characteristics for different conditions.

V. CONCLUSION

This paper focuses on the composite scattering characteristics of layered rough surfaces and buried targets. Firstly, the CCIA algorithm model is established, the EEIF of the rough surface with the target are calculated by FBM and BI-CG respectively, and the coupling effect is realized by continuously updating the excitation term. By comparing the results with those of MOM, it is proved that the computational accuracy and computational speed of CCIA meet the requirements of practical calculations. Then the compound scattering coefficients of the rough surface with the target are calculated by this algorithm, it is found that the coupling effect between them has a great influence on the compound scattering and is positively correlated with the size of the target. It is also found that the burial depth of the target has little effect on the composite scattering characteristics due to the coupling effect between the target with the upper-lower rough surfaces. Finally, its ACF is studied, it is found that the target size is an important factor affecting the ACF, and the ACF can well suppress the scattering from the rough surface and make the scattering characteristics of the target more significant, which is important for detecting subsurface targets.

ADDITIONAL STATEMENTS

There are no conflicts of interest to disclose for all the authors.

REFERENCES

[1] S. Dey, W. G. Szymczak, A. Sarkissian, and J. A. Bucaro, "Scattering from targets in three-dimensional littoral and surf-zone environments with multi-layered elastic sediments based on an interior-transmission formulation," *Computer Methods in Applied Mechanics and Engineering*, vol. 260, 2013.

[2] X. W. Liu, J. Z. Li, Y. Zhu, and S. J. Zhang, "Scattering characteristic extraction and recovery for multiple targets based on time frequency analysis," *Applied Computational Electromagnetics Society (ACES) Journal*, vol. 35, no. 8, 2020.

[3] J. Li, H. G. Bao, and D. Z. Ding, "Analysis for scattering of non-homogeneous medium by time domain volume shooting and bouncing rays," *Applied Computational Electromagnetics Society (ACES) Journal*, vol. 36, no. 3, 2020.

[4] K. Williams, A. Espana, S. Kargl, and M. Zampolli, "Submerged target scattering: comparison of combined finite element/simplified acoustics models to data," *The Journal of the Acoustical Society of America,* vol. 131, no. 4, 2012.

[5] A. Edirisinghe, G. E. Chapman, and J. P. Louis, "A simplified method for retrieval of ground level reflectance of targets from airborne video imagery," *International Journal of Remote Sensing,* vol. 22, no. 6, 2001.

[6] Remote Sensing, "New remote sensing data have been reported by researchers at Fudan university (an analytical method for high-frequency electromagnetic scattering of arbitrary undulating rough surfaces)," *Electronics Newsweekly*, 2020.

[7] P. P. Huang, Q. Shi, W. X. Tan, W. Xu, and C. F. Hu, "Research on modelling and calculation method of river ice electromagnetic scattering," *The Journal of Engineering,* vol. 2019, no. 21, 2019.

[8] Earth Observations and Remote Sensing, "Studies from Xidian university in the area of earth observations and remote sensing reported (spectral decomposition modeling method and its application to EM scattering calculation of large rough surface with SSA method)," *Journal of Technology & Science,* 2015.

[9] E. Bahar and P. E. Crittenden, "Electromagnetic wave scattering from a rough interface above a chiral medium: Generalized telegraphists' equations," *Journal of the Optical Society of America. A, Optics, Image Science, and Vision,* vol. 30, no. 3, 2013.

[10] W. Kong, X. Yang, F. Zhou, J. Xie, C. Chen, N. Li, and W. Yang, "Fast analysis of broadband electromagnetic scattering characteristics of electrically large targets using precorrected fast fourier transform algorithm based on near field matrix interpolation method," *Applied Computational Electromagnetics Society (ACES) Journal*, vol. 36, no. 7, 2021.

[11] D. Sevket, K. Ozkan, and O. Caner, "Interpretation and analysis of target scattering from fully-polarized ISAR images using Pauli decomposition scheme for target recognition," *IEEE Access,* vol. 8, 2020.

[12] P. J. Li and A. W. Wood, "Electromagnetic Scattering by Multiple Cavities Embedded in the Infinite 2D Ground Plane," *Applied Computational Electromagnetics Society (ACES) Journal*, vol. 29, no. 7, 2014.

[13] B. Y. Ding, G. J. Wen, X. H. Huang, C. H. Ma, and X. L. Yang, "Target recognition in synthetic aperture radar images via matching of attributed scattering centers," *IEEE Journal of Selected Topics in Applied Earth Observations and Remote Sensing,* vol. 10, no. 7, 2017.

[14] G. X. Zou, C. M. Tong, H. L. Sun, and P. Peng, "Research on electromagnetic scattering characteristics of combined conducting and dielectric target above coastal environment," *IEEE Access,* vol. 8, 2020.

[15] Y. Liang and L. X. Guo, "A study of composite scattering characteristics of movable/rotatable targets and a rough sea surface using an efficient numerical algorithm," *IEEE Transactions on Antennas and Propagation,* vol. 69, no. 7, 2021.

[16] G. X. Zou, C. M. Tong, J. Zhu, H. L. Sun, and P. Peng, "Study on composite electromagnetic scattering characteristics of low-altitude target above valley composite rough surface using hybrid SBR-EEC method," *IEEE Access,* vol. 8, 2020.

[17] J. X. Li, M. Zhang, W. Q. Jiang, and P. B. Wei, "Improved FBAM and GO/PO method for EM scattering analyses of ship targets in a marine environment," *Sensors,* vol. 20, no. 17, 2020.

[18] M. Wang, J. Chen, and Y. Cao, "An efficient scheme for analysis of electromagnetic scattering from target and environment composite model," *Progress in Electromagnetics Research M.,* vol. 32, 2013.

[19] C. D. Moss, T. M. Grzegorczyk, H. C. Han H, and J. A. Kong, "Forward-backward method with spectral acceleration for scattering from layered rough surfaces," *IEEE Trans Antennas Propagation,* vol. 54, no. 3, 2006.

[20] K. C. Wang, Z. He, D. Z. Ding, and R. S. Chen, "Uncertainty scattering analysis of 3-D objects with varying shape based on method of moments," *IEEE Transactions on Antennas and Propagation,* vol. 67, no. 4, 2019.

[21] M. A. Mojtaba, S. S. H. Hesamedin, and D. Mojtaba, "A method of moments for analysis of electromagnetic scattering from inhomogeneous anisotropic bodies of revolution," *IEEE Transactions on Antennas and Propagation,* vol. 66, no. 6, 2018.

[22] J. Y. Li and L. W. Li, "Electromagnetic scattering by a mixture of conducting and dielectric objects: Analysis using method of moments," *IEEE Transactions on Vehicular Technology,* vol. 53, no. 2, 2004.

[23] A. Thorsos, "The validity of the Kirchhoff approximation for toygh surface scattering using a Guassian roughness spectrum," *Journal of the Acoustical Society of America,* vol. 83, no. 1, 1988.

Jiaguo Zhang was born in Jiangxi, China. He received a bachelor's degree from Yichun University in 2011 and a master's degree of computer technology from Yunnan University in 2016. Her research interests include network technology and computer communication.

Huan Wei was born in Jiangxi, China. He received a bachelor's degree from Zhejiang University in 2005 and a master's degree of computer technology from Yunnan University in 2015. Her research interests include network technology and computer communication.

Simulation Analysis of Electromagnetic Environment Effect and Shielding Effectiveness for VPX Chassis under Plane Wave Radiation

Hongkun Ni[1], Hong Jiang[1]*, Xinbo Li[1], Qian Jia[2], and Xiaohui Wang[2]

[1]College of Communication Engineering
Jilin University, Changchun, 130012 China
jiangh@jlu.edu.cn
*Corresponding Author

[2]Research and Development Department
China Academy of Launch Vehicle Technology, Beijing 100076, China

Abstract – The chassis based on the VPX bus standard structure has been widely applied to the fields of vehicle, missile, radar, etc. In this paper, we analyze the electromagnetic environment effect on VPX chassis via the CST software, and investigate the electromagnetic coupling characteristics of VPX chassis under 20 v/m plane wave radiation according to the RS103 test defined in the MIL-STD-461G standard. By simulation, we analyze the electromagnetic coupling paths of the VPX chassis, find the key positions of the electromagnetic protection such as the air intake, air outlet, trapdoor, and panel gaps, and we propose the electromagnetic protective measures for the weak parts of the VPX chassis. The electromagnetic shielding effectiveness before and after protection design is evaluated. Finally, the simulation results are verified by the experiments. It has guiding significance for the electromagnetic protection design of VPX chassis.

Index Terms – VPX chassis, shielding effectiveness, electromagnetic environment effect, electromagnetic protection.

I. INTRODUCTION

In recent years, aerospace electronic technology is developing rapidly, and its applications are becoming increasingly extensive. With the emergence of various types of electronic devices, the requirements for their performance and response speed in aerospace and other fields are becoming higher [1-4]. With the rapid development of electronic equipment with different functions, the structure and performance of the traditional chassis cannot meet the load-bearing requirements of the new generation of electronic equipment [5, 6]. VPX is a new generation high-speed serial bus standard Versa Module European (VME) proposed by the International Trade Association (VITA) [7]. The VPX chassis based on VITA46 standard is a new type of chassis, which has strong shock resistance and impact resistance through reinforcement technology [8, 9]. Its internal space design is compact, and the position and routing planning of each module are clear, so that it has the smallest volume as far as possible under the premise of ensuring the normal work of each piece of equipment, which is convenient for installation, maintenance, handling, and replacement. At present, the chassis and electronic equipment based on VPX bus standard structure have been successfully applied to the fields of vehicle, missile, aircraft, radar, etc. [10-14]. The stability and environmental adaptability of the VPX chassis under plane wave radiation need to be further verified. It is a prerequisite and a necessary requirement to analyze the electromagnetic environmental effects of the VPX chassis and propose protective measures in order for the chassis and its internal electronic equipment to work normally in complex electromagnetic environments [15-20]. However, in the existing literature, the electromagnetic environment effect of the VPX chassis has not been well investigated, whether with theoretical calculation or simulation methods. In addition, the existing electromagnetic protection design for VPX chassis was completed via experimental measurements, which has greatly increased the cost of the electromagnetic protection design.

In this paper, considering that the shape of the VPX chassis is irregular, the electromagnetic environment effect of the VPX chassis is analyzed via the Computer Simulation Technology (CST) software [21], which is based on the transmission line method (TLM). The electromagnetic coupling characteristics of VPX chassis under 20 v/m plane wave radiation is investigated according to the RS103 test defined in the MIL-STD-461G standard [22]. The electric field energy density distribution and surface current distribution of the VPX chassis at different frequencies are obtained by CST simulations. The electromagnetic coupling paths of the VPX

Submitted On: May 24, 2023
Accepted On: November 27, 2023

https://doi.org/10.13052/2023.ACES.J.381106

chassis are analyzed, the key positions of the electromagnetic protection of the VPX chassis such as the air intake, air outlet, trapdoor, and panel gaps are determined, and the protective measures for the weak parts are proposed. The electromagnetic shielding effectiveness before and after protection design is evaluated, and the simulation results are verified by the experiments.

II. PERFORMANCE METRICS OF ELECTROMAGNETIC COUPLING CHARACTERISTICS

A. Energy density of electric field intensity

The energy density of an electric field is the energy of the electric field per unit volume, which is expressed as

$$w = k \cdot E^2, \tag{1}$$

where E is the electric field intensity and k is a half of the permittivity.

In the CST electromagnetic simulation software, the electric field energy density monitor can be set to monitor the electric field energy density at different frequency points under plane wave radiation. The larger the electric field energy density is, the greater the amount of electromagnetic coupling is. Therefore, the electric field energy density can be used as an important performance metric to analyze the electromagnetic coupling path of a shielding enclosure [23-26].

B. Shielding effectiveness

Generally, shielding effectiveness is used to evaluate the shielding performance of a shield body, denoted as

$$SE_E = 20 lg \frac{E_1}{E_2}. \tag{2}$$

E_1 refers to the electric field intensity at the position of interest inside the shield body under the radiation of plane wave, and E_2 refers to the electric field intensity at the location of interest without the shield body under plane wave radiation.

III. SIMULATION SETTINGS

According to the standard of RS103 electric field radiation sensitivity in MIL-STD-461G, the CST electromagnetic simulation software is used to numerically model and analog the test conditions. According to the simulation requirements, basic settings are first carried out in the CST studio suite, including the operating frequency band selection, and excitation source settings.

A. VPX chassis model

The units of physical quantities are set as dimensions (mm), frequency (GHz), temperature (Kelvin), and time (ns). We set the chassis material as PEC (ideal conductor), the background material as normal, and the boundary condition as open. A typical VPX chassis model 1:1 is imported into CST microwave studio. The VPX chassis model is shown in Fig. 1.

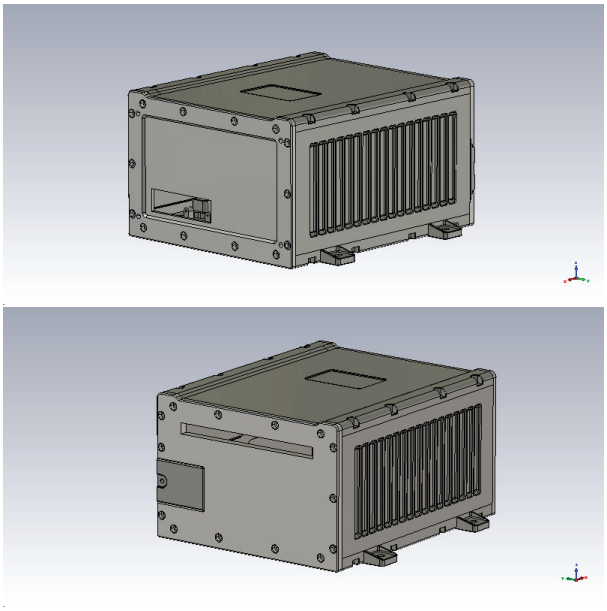

Fig. 1. The VPX chassis model.

B. Frequency range and excitation signal

In the experiment of RS103 electric field radiation sensitivity in MIL-STD-461G, the frequency range and corresponding applications are given in Table 1.

We analyze the electromagnetic environment effect and shielding effectiveness of the VPX chassis via the CST simulation. Assume a plane wave with a frequency domain value of 20 v/m to radiate the VPX chassis. The type of excitation signal is impulse, whose approximate expression is

$$f(t) = \frac{dA}{\pi(t-c)} \sin\left(\frac{(B_H - B_L)(t-c)}{2}\right) e^{j\frac{(B_H+B_L)(t-c)}{2}}, \tag{3}$$

where d is the amplitude coefficient, A is the frequency domain value, B_H and B_L are the maximum and minimum angular frequencies, respectively, and c is the

Table 1: Applicable frequency range

No.	Frequency Range	Applications
1	10 kHz-2 MHz	Army aircraft applicable, other options
2	2 MHz-30 MHz	For army ships, army aircraft and navy, the others shall be selected by the purchaser
3	30 MHz-100 MHz	All applicable
4	100 MHz-1 GHz	All applicable
5	1 GHz-18 GHz	All applicable
6	18 GHz-40 GHz	Selected by the purchaser

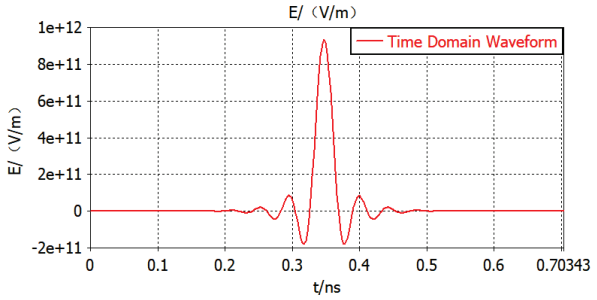

(a)

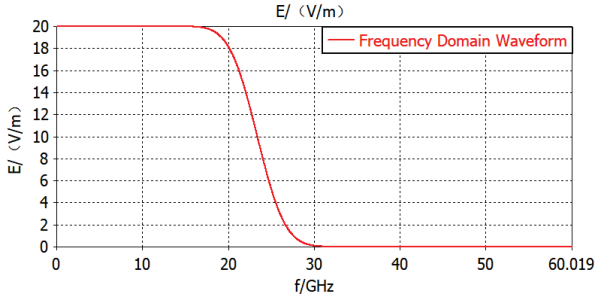

(b)

Fig. 2. Excitation signal: (a) Time domain and (b) frequency domain.

time offset. The excitation signal in time and frequency domains is shown in Fig. 2.

In the CST simulation, the external high-frequency electromagnetic environment is simulated. Assume that the excitation source is linear polarization mode. The vertical and horizontal polarizations are respectively set to examine the coupling characteristics of the chassis for different polarization modes, as shown in Fig. 3.

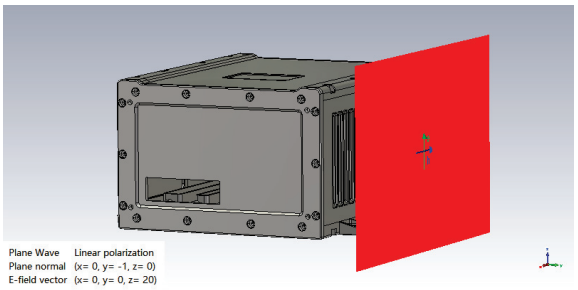

(a)

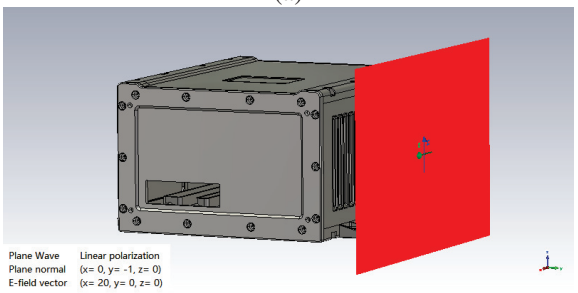

(b)

Fig. 3. Polarization modes of excitation source: (a) Vertical polarization and (b) horizontal polarization.

C. Electric field probes

From the preliminary analysis of the chassis structure, it is found that the key positions of the chassis vulnerable to electromagnetic interference are the air intake, air outlet, trapdoor, and panel gaps. Thus, the electric field probes are set at these three key positions to monitor the electric field intensity, as shown in Fig. 4.

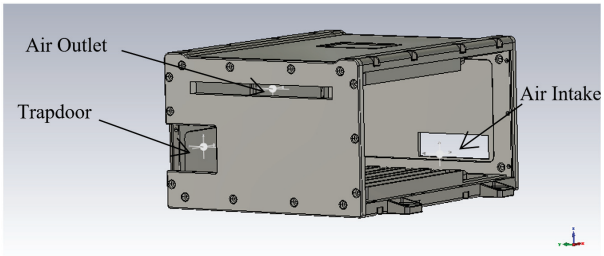

Fig. 4. Electric field probes.

IV. ELECTROMAGNETIC COUPLING PATH ANALYSIS OF VPX CHASSIS

The electric field intensity monitor and electric field energy density monitor at different frequency points are set with the CST simulation software, and the frequency points are selected as 1 GHz, 3 GHz, 5 GHz, 7 GHz, 9 GHz, 11 GHz, 13 GHz, 15 GHz, 17 GHz, 18 GHz under plane wave radiation. The electric field energy density distribution and surface current distribution of the air intake, air outlet, trapdoor, and panel gaps of the VPX chassis are obtained, as shown in Figs. 5-10, from which we can analyze the electromagnetic coupling paths of the VPX chassis.

It can be seen from Figs. 5-10 that, the electromagnetic coupling paths of the front panel of the VPX chassis come from the air intake and the panel gap. The maximum coupling values of the air intake appear at 7 GHz, 9 GHz, and 11 GHz, and the panel gap at 1 GHz, 3 GHz, and 5 GHz. The electromagnetic coupling paths of the back panel of the VPX chassis come from the air outlet, trapdoor, and panel gap. The maximum coupling values of the air outlet and trapdoor appear at 7 GHz, 9 GHz, and 11 GHz, and the panel gap at 1 GHz, 3 GHz, and 5 GHz. The VPX fan chassis needs to dissipate heat through the air intake and air outlet, where there is a large amount of electromagnetic coupling and a great impact on the electromagnetic shielding performance of the VPX chassis.

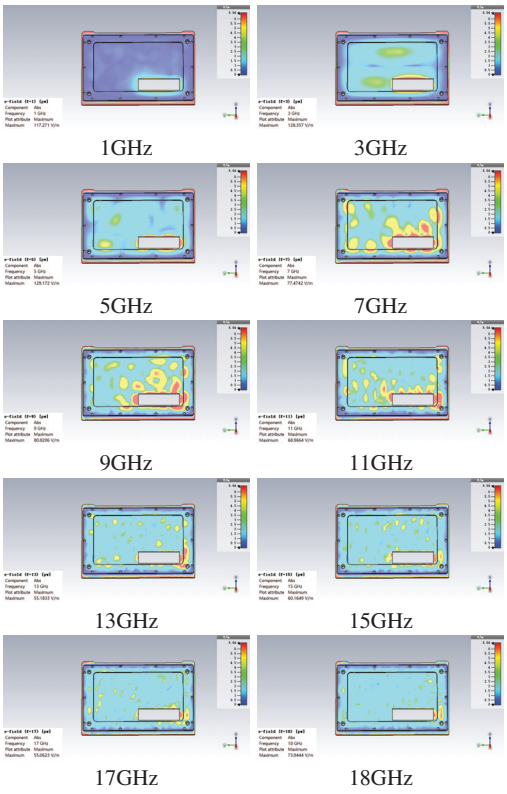

Fig. 5. Electric field energy distribution of the air intake.

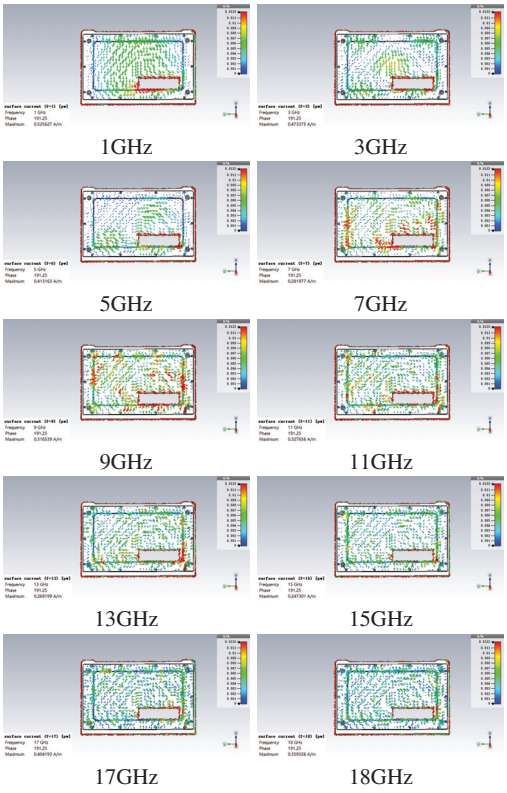

Fig. 6. Surface current distribution of the air intake.

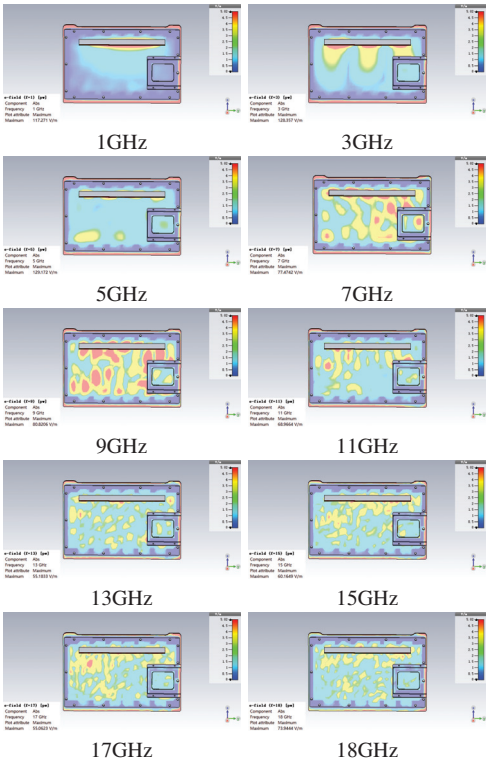

Fig. 7. Electric field energy distribution of the air outlet and trapdoor.

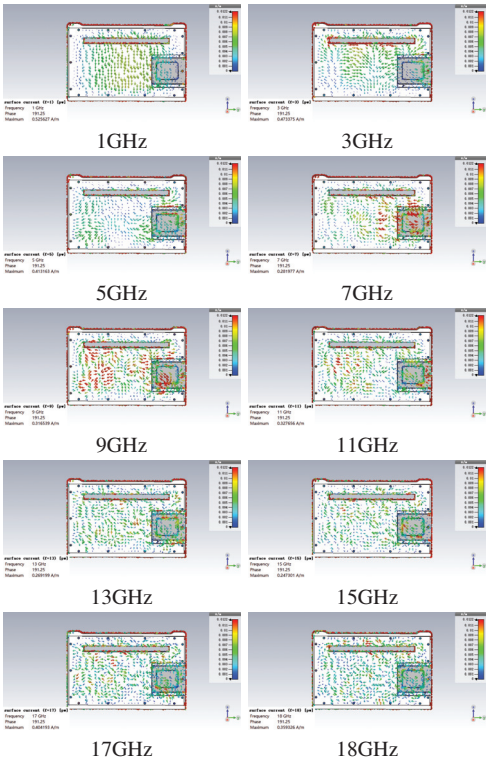

Fig. 8. Surface current distribution of the air outlet and trapdoor.

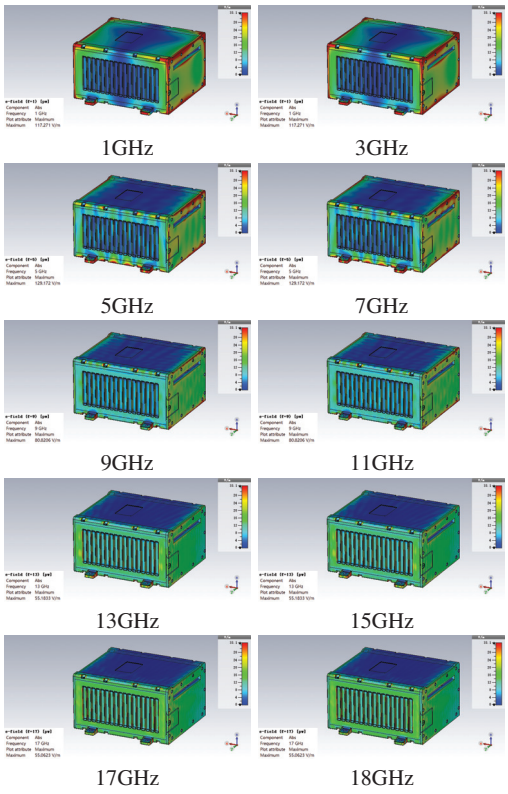

Fig. 9. Electric field energy distribution of the panel gaps.

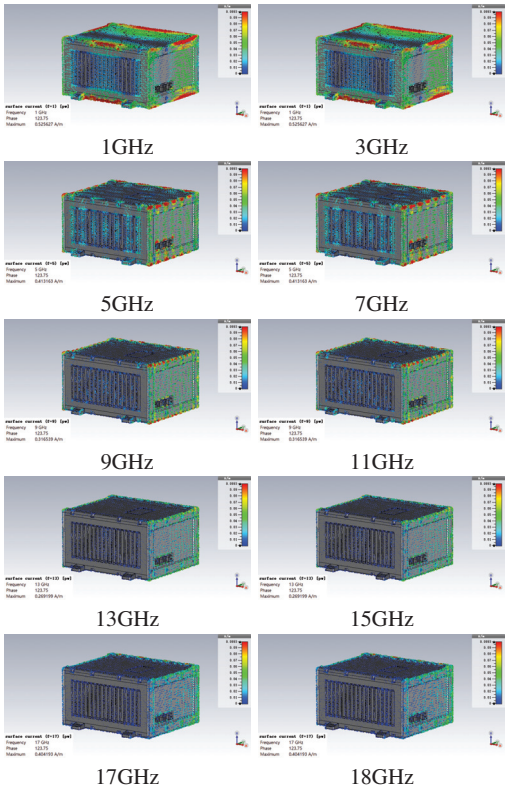

Fig. 10. Surface current distribution of the panel gaps.

V. PROTECTION DESIGN OF AIR INTAKE, AIR OUTLET, AND TRAPDOOR

Electric field intensities are calculated via simulation by setting electric field probes in the key positions of the VPX chassis, then the shielding effectiveness before and after protection design is evaluated.

A. Electric field intensity of the air intake, air outlet, and trapdoor

For the key positions such as the air intake, air outlet, and trapdoor, the electric field intensity in the horizontal and vertical polarization modes in the frequency domain are calculated. The simulation result of the air intake, the air outlet, and the trapdoor are shown in Figs. 11, 12, and 13, respectively.

It can be seen that the electric field intensity of vertical polarization is higher than that of horizontal polarization in the above three key positions. For the air intake, the maximum coupling value of 17.224 v/m is obtained at 1.9561 GHz for vertical polarization, and 7.5602 v/m is obtained at 7.2929 GHz for horizontal polarization. For the air outlet, the maximum coupling is 36.162 v/m at 1.0956 GHz for vertical polarization and 11.762 v/m for horizontal polarization. For the trapdoor, the maximum coupling volume is 11.213 v/m at 5.2357 GHz for vertical polarization, and 6.4445 v/m at 6.1296 GHz for

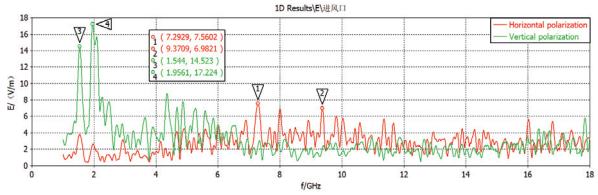

Fig. 11. Electric field intensity of the air intake.

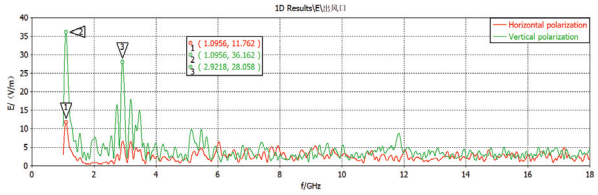

Fig. 12. Electric field intensity of the air outlet.

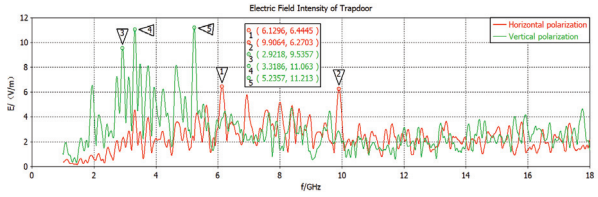

Fig. 13. Electric field intensity of the trapdoor.

horizontal polarization.

B. Shielding effectiveness of the air intake, air outlet, and trapdoor

According to (2), we respectively calculate the shielding effectiveness of the intake, outlet, and trapdoor before protection design. The calculation results of the air intake, air outlet and trapdoor are shown in Figs. 14-16.

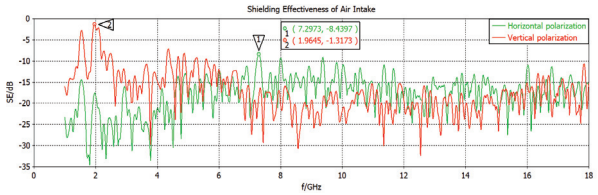

Fig. 14. Shielding effectiveness of the air intake.

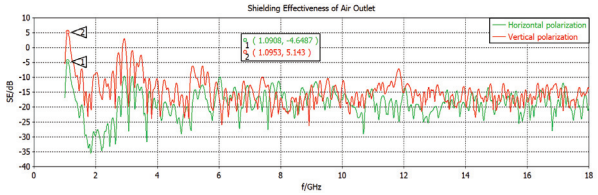

Fig. 15. Shielding effectiveness of the air outlet.

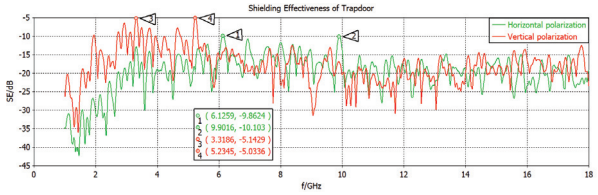

Fig. 16. Shielding effectiveness of the trapdoor.

It can be seen from Figs. 14-16 that the shielding effectiveness of the fan-type VPX chassis is greatly affected by the coupling between the air intake and the air outlet, so it is of great significance to design the protection of the air intake and the air outlet.

C. Evaluation of shielding effectiveness after protection design

To protect the VPX chassis, we install the metal shielding nets at the air intake and air outlet, as shown in Fig. 17.

Through the simulation analysis of the VPX chassis after installing the metal shielding nets, the electric field intensities at the air intake and the air outlet can

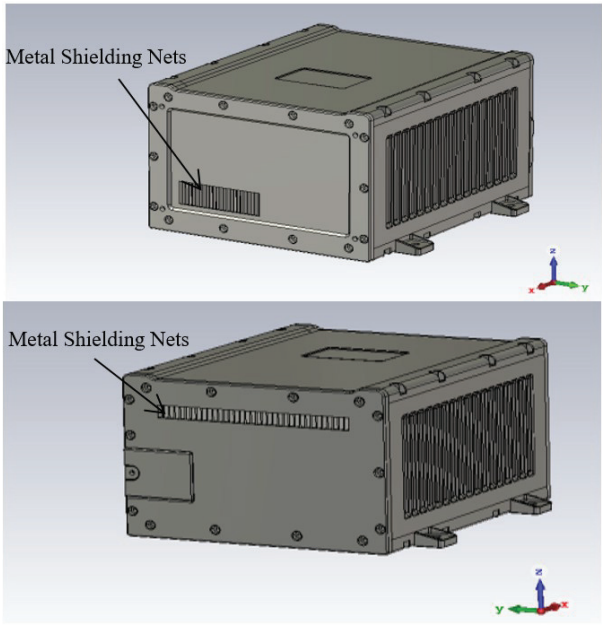

Fig. 17. Installation of metal shielding nets at the air intake and the air outlet.

be obtained. Despite that there is no protection design at the trapdoor, its electric field intensity has also reduced. Vertical polarization as an example, according to (2), the shielding effectiveness of the intake, outlet, and trapdoor after protection design is respectively calculated. The results of the above three key positions are shown in Figs. 18, 19, and 20, respectively.

Compared with the results before protection design, it is revealed that through the protection design, the VPX chassis can obtain higher shielding effectiveness in the

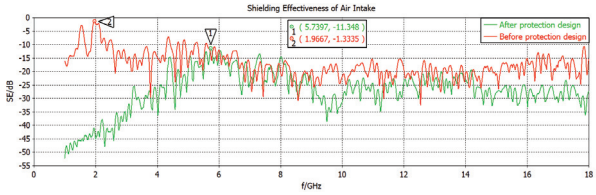

Fig. 18. Shielding effectiveness of the air intake after protection design.

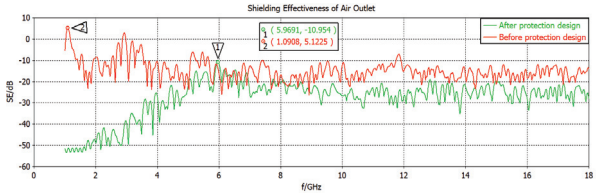

Fig. 19. Shielding effectiveness of the air outlet after protection design.

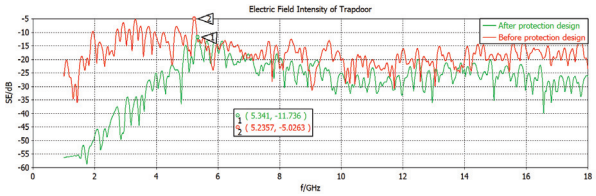

Fig. 20. Shielding effectiveness of the trapdoor after protection design.

three key positions. It increases to 11.348 dB at the air intake, 10.954 dB at the air outlet, and 11.736 dB at the trapdoor.

VI. PROTECTION DESIGN OF PANEL GAPS

Besides the intake, outlet and trapdoor, the protection design of the panel gaps is also important for the VPX chassis. In this case, we use absorbing sticky paper to cover the panel gaps to reduce the electromagnetic leakage. Assume that the probe is set in the geometric center of the VPX chassis, as shown in Fig. 21, and the placement of the absorbing sticky paper as shown in Fig. 22. Vertical polarization as an example, the electric field intensity, and shielding effectiveness of the VPX chassis before and after protection design are simulated, and the results are shown in Figs. 23 and 24, respectively.

As seen in Figs. 23 and 24, by the protection design of panel gaps, the electric field intensity after protection design has much reduced, and the shielding effectiveness

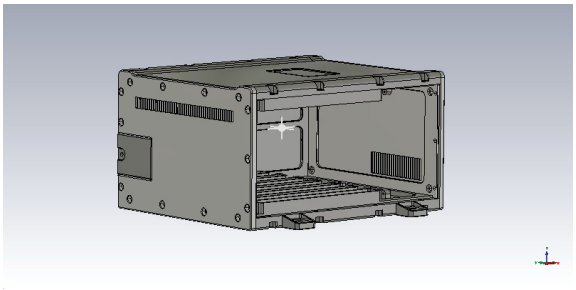

Fig. 21. The probe position inside the VPX chassis.

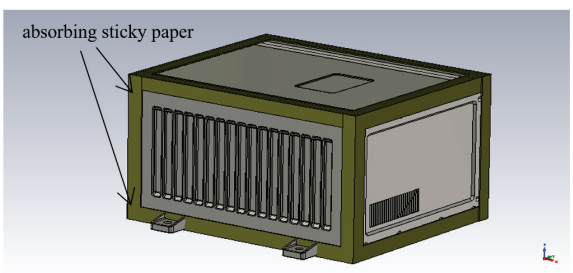

Fig. 22. Protection of panel gaps with absorbing sticky paper.

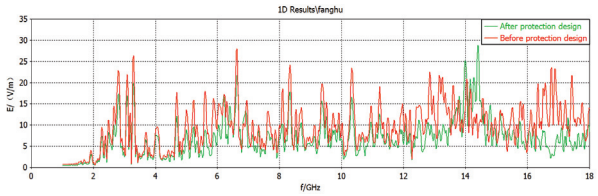

Fig. 23. Electric field intensity at the probe position.

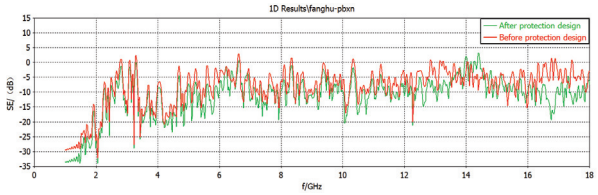

Fig. 24. Shielding effectiveness at the probe position.

has greatly increased compared with that before protection design.

VII. EXPERIMENTAL VERIFICATION OF PROTECTION DESIGN

The electromagnetic experiment for the VPX chassis is performed to validate the simulation results. The experiment scene is shown in Fig. 25. The VPX chassis with protection design is placed in the electromagnetic

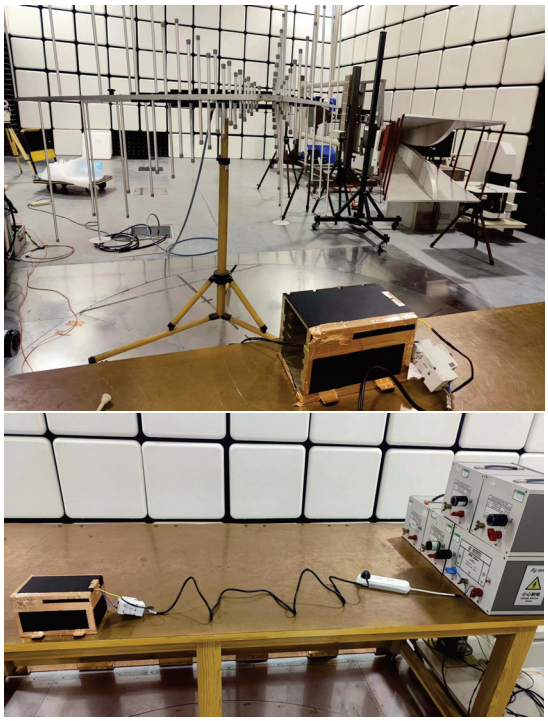

Fig. 25. The experiment scene.

Table 2: Measurement results of the electric field intensity of the VPX chassis

Operating Frequency	Excitation Signal Radiated Power (dBm)	External Electric Field Intensity of the Chassis (v/m)	Interior Electric Field Intensity of the Chassis (v/m)
300 MHz	-24.7	20	1.0
400 MHz	-24.6		1.0
500 MHz	-23.0		6.0
600 MHz	-23.6		3.0
800 MHz	-23.3		4.0
1000 MHz	-24.4		2.0

test environment. Limited to the actual experimental platform, the operating frequencies of electric field intensity test are lower than 1 GHz. The type of excitation signal is sinc. The radiation antenna is in the vertical polarization mode. The external electric field intensity of the VPX chassis is set to 20 v/m, and the radiated power values of the source signal at different frequency points of 300 MHz, 400 MHz, 500 MHz, 600 MHz, 800 MHz, and 1000 MHz are measured, which are fixed in the subsequent experiment. Then, the sensor probe is placed inside the chassis and the electric field intensities at different operating frequencies are measured. The measurement results of the electric field intensity of the VPX chassis are recorded in Table 2.

For comparison, the electromagnetic simulations with CST are performed to obtain the interior electric field intensity of the VPX chassis under the same conditions of operating frequencies and excitation signal. At different frequency points of 300 MHz, 400 MHz, 500 MHz, 600 MHz, 800 MHz, and 1000 MHz, the simulation curves of the interior electric field intensity in time-domain are shown in Fig. 26.

The accuracy of the electromagnetic simulation model can be calculated as

$$Accuracy = -20\lg \frac{|E_{sim} - E_{\exp}|}{E_{\exp}} \ (dB), \qquad (4)$$

where $E_{\exp}$ indicates the experimental value of the interior electric field intensity of the VPX chassis, and E_{sim} indicates the simulation value of the interior electric field intensity of the VPX chassis. With the simulation result and experimental result, the accuracy calculation of the simulation model under such plane wave radiation is listed in Table 3.

Table 3 shows that the simulation result is consistent with the experimental result at different operating frequencies, and the accuracies of electromagnetic compatibility simulation model are higher than 9.90 dB, which can verify the simulation results and further

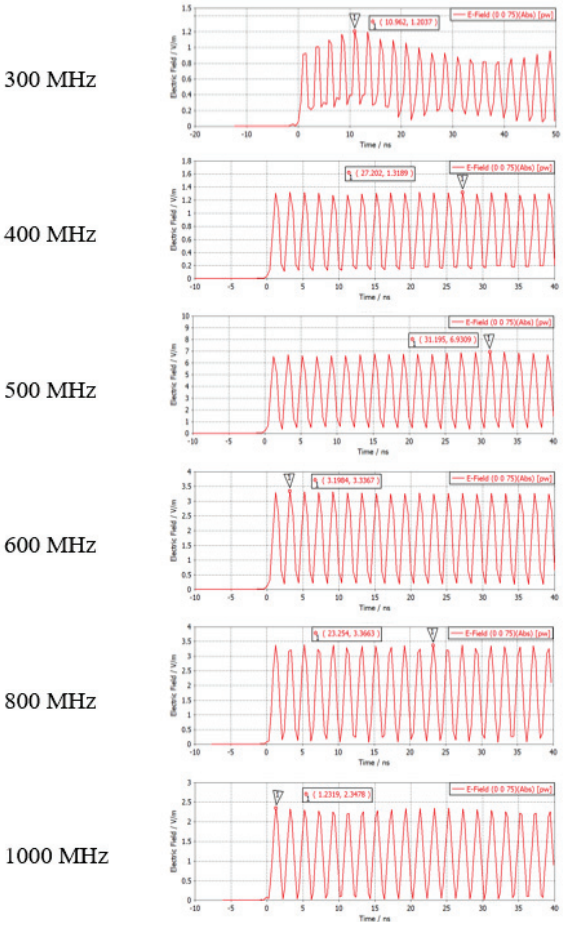

Fig. 26. Simulation results of the interior electric field intensity of the VPX chassis.

demonstrate the feasibility and effectiveness of the protection design. To sum up, by adding protective measures on the air intake, air outlet, and trapdoor, as well as the gaps of the VPX chassis panels, the shielded VPX chassis has higher shielding effectiveness and can greatly reduce the electromagnetic coupling amounts of the important components in the VPX chassis. This is of great significance for the devices inside the VPX chassis to work normally under radiation electromagnetic environment.

VIII. CONCLUSION

Electromagnetic compatibility should be considered as early as possible in the product design process to reduce the cost and cycle investment caused by later rectification. In this paper, the electromagnetic environment effects of the VPX chassis are analyzed via the CST simulation. The electromagnetic coupling characteristics are investigated under 20 v/m plane wave radiation. The coupling paths and the key positions of the electromagnetic protection in the VPX chassis are found, and the

Table 3: Accuracy of electromagnetic simulation model under plane wave radiation

Operating Frequency	Interior Electric Field Intensity of VPX Chassis		Accuracy of Simulation Model (dB)
	Experiment Result (v/m)	Simulation Result(v/m)	
300 MHz	1.0	1.20	13.98
400 MHz	1.0	1.32	9.90
500 MHz	6.0	6.93	16.19
600 MHz	3.0	3.34	18.91
800 MHz	4.0	3.37	16.05
1000 MHz	2.0	2.35	15.14

electromagnetic shielding effectiveness of the VPX chassis before and after protection design is evaluated. The simulation results are verified by the experiments. It provides guidance for the design of electromagnetic protective measures, and is helpful for reducing the cost of the actual electromagnetic protection design.

ACKNOWLEDGMENT

This work is supported by the Natural Science Foundation of Jilin Province under Grant 20220101100JC. The authors would like to thank the reviewers for their useful comments and suggestions.

REFERENCES

[1] I. Zheng and G. Wei, "New development of electromagnetic compatibility in the future: Cognitive electromagnetic environment adaptation," *2021 13th Global Symposium on Millimeter-Waves & Terahertz* (*GSMM*), Nanjing, China, pp. 1-3, 2021.

[2] Y. Wang, H. Sun, Q. Zhao, Y. Mao, and Q. Hou, "Study on capability verification test of electromagnetic pulse protection for aircraft," *2022 Asia-Pacific International Symposium on Electromagnetic Compatibility (APEMC)*, Beijing, China, pp. 391-439, 2022.

[3] Q. F. Liu, S. Q. Zheng, Y. Zuo, H. Q. Zhang, and J. W. Liu, "Electromagnetic environment effects and protection of complex electronic information systems," *2020 IEEE MTT-S International Conference on Numerical Electromagnetic and Multiphysics Modeling and Optimization (NEMO)*, Hangzhou, China, pp. 1-4, 2020.

[4] J. Jin, H. Xie, J. Hu, and W. Y. Yin, "Characterization of anti-jamming effect on the joint tactical information distribution system (JTIDS) operating in complicated electromagnetic environment," *2014 International Symposium on Electromagnetic Compatibility*, Gothenburg, Sweden, pp. 997-1000, 2014.

[5] Q. Li, W. Cao, J. Ding, J. Fang, J. Sun, and C. Guo, "Research on high-power electromagnetic effect and protective technology of electronic equipments," *2022 IEEE 9th International Symposium on Microwave, Antenna, Propagation and EMC Technologies for Wireless Communications (MAPE)*, Chengdu, China, pp. 333-337, 2022.

[6] I. Xiao, Z. Song, J. Wang, and L. Wang, "Simulation analysis of electromagnetic shielding of electronic device chassis," *2019 12th International Workshop on the Electromagnetic Compatibility of Integrated Circuits (EMC Compo), Hangzhou, China*, pp. 91-93, 2019.

[7] Z. Jingchao, Q. Liyan, and C. Liqun, "Development of serial RapidIO high-speed data transmission based on VPX bus," *2019 14th IEEE International Conference on Electronic Measurement & Instruments (ICEMI)*, Changsha, China, pp. 65-71, 2019.

[8] N. K. Singh, C. Fouziya, V. Kumar, and T. Venkatamuni, "A programmable, multimode operational 3U-VPX based digital transceiver & processing module for CIT-MKXIIA IFF," *2023 International Conference for Advancement in Technology (ICONAT)*, Goa, India, pp. 1-5, 2023.

[9] M. Hua, N. Minxi, T. Anju, and M. Jianghong, "Power and signal integrity analysis of high-speed mixed-signal backplanes based on VPX," *2018 IEEE Symposium on Electromagnetic Compatibility, Signal Integrity and Power Integrity (EMC, SI & PI)*, Long Beach, CA, USA, pp. 577-581, 2018.

[10] N. Wu, D. G. Xie, D. E. Wen, and C. Wang, "Research on simulation and analysis of electromagnetic environment of cabinet in cabin," *2011 4th IEEE International Symposium on Microwave, Antenna, Propagation and EMC Technologies for Wireless Communications*, Beijing, China, pp. 524-527, 2011.

[11] Y. S. Wang, W. Q. Guo, W. Li, and Y. L Bian, "Research on strong electromagnetic protection technology of radar vehicle cockpit," *2020 6th Global Electromagnetic Compatibility Conference (GEMCCON)*, XI'AN, China, pp. 1-8, 2020.

[12] Q. Q. Zheng, D. D. Wang, B. Xiong, and H. Y. Yan, "Investigation on ship LEMP protection design and test," *2018 12th International Symposium on Antennas, Propagation and EM Theory (ISAPE)*, Hangzhou, China, pp. 1-4, 2018.

[13] Y. Yang, F. Zhu, N. Lu, and Y. Xiao, "Study on the electromagnetic interference of shielded cable in rail weighbridge," *Applied Computational Electromagnetics Society (ACES) Journal*, vol. 37, no. 2, pp. 215-221, 2022.

[14] X. Hao, X. Meng, and X. Chen, "Effects mechanism of strong electromagnetic environment to equipment," *2016 IEEE MTT-S International Microwave Workshop Series on Advanced Materials and Processes for RF and THz Applications (IMWS-AMP)*, Chengdu, China, pp. 1-4, 2016.

[15] Z. Yu and J. Wang, "Electromagnetic interference prediction in transient electromagnetic environment," *2007 International Symposium on Electromagnetic Compatibility*, Qingdao, China, pp. 221-224, 2007.

[16] H. Z. Zhao, G. H. Wei, and X. D. Pan, "Evaluation method of noise electromagnetic radiation interference effect," *IEEE Transactions on Electromagnetic Compatibility*, vol. 65, no. 1, pp. 69-78, Feb. 2023.

[17] J. C. Zhou and X. T. Wang, "An efficient method for predicting the shielding effectiveness of an apertured enclosure with an interior enclosure based on electromagnetic topology," *Applied Computational Electromagnetics Society (ACES) Journal*, vol. 37, no. 10, pp. 1014-1020, 2022.

[18] Z. Xu, Z. Zhang, B. Wu, H. Wang, X. Kong, and M. Wang, "A study of enclosed magnetic shielding room by simulation," *IEEE Transactions on Applied Superconductivity*, vol. 31, no. 8, pp. 1-4, Art no. 2500404, Nov. 2021.

[19] A. Keshtkar, A. Maghoul, A. Kalantarnia, and A. Asad, "Design considerations to affect on shielding effectiveness for conductive enclosure," *IEICE Electronics Express*, vol. 813388, no. 13, pp. 1047-1055, 2011.

[20] A. M. Dagamseh, Q. M. Al-Zoubi, and Q. Qananwah, "Modeling of electromagnetic fields for shielding purposes applied in instrumentation systems," *Applied Computational Electromagnetics Society (ACES) Journal*, vol. 36, no. 8, pp. 1075-1082, 2021.

[21] Computer Simulation Technology (CST), http://www.cst.com.

[22] *American National Standard Dictionary of Electromagnetic Compatibility (EMC) including Electromagnetic Environmental Effects (E3)*, ANSI C63.14-2014 (Revision of ANSI C63.14-2009) *IEEE*, 2014.

[23] M. Z. M. Jenu and F. A. Po'ad, "Electric and magnetic shielding effectiveness of metallic enclosures with apertures," *2006 Asia-Pacific Microwave Conference*, Yokohama, Japan, pp. 536-539, 2006.

[24] K. Cui, D. Shi, C. Sun, and X. Liu, "A compact and high-performance shielding enclosure by using metamaterial design," *Applied Computational Electromagnetics Society (ACES) Journal*, vol. 36, no. 11, pp. 1484-1491, 2021.

[25] A. Keshtkar, A. Maghoul, A. Kalantarnia, and H. Hashempour, "Simulation of shielding effectiveness in low frequencies for conductive enclosure," *2009 Second International Conference on Computer and Electrical Engineering*, Dubai, United Arab Emirates, pp. 372-377, 2009.

[26] Z. Dou, J. Zhang, G. Wang, D. He, C. Liu, and T. Wang, "Electromagnetic shielding effectiveness of an absorber-like Carbonyl iron-FeNi double-layer composite," *Journal of Materials Engineering and Performance*, vol. 31, no. 1, pp. 643-650, 2022.

Hongkun Ni received the B.S. degree in communication engineering from Jilin University, Changchun, China, in 2020. He is currently pursuing the M.S. degree in communication engineering with Jilin University, Changchun, China. His current research interests include simulation analysis of electromagnetic environment effect, electromagnetic compatibility, and protection for electronic equipment.

Hong Jiang (corresponding author) received the B.S. degree in radio technology from Tianjin University, Tianjin, China, in 1989, the M.S. degree in communication and electronic system from Jilin University of Technology, Changchun, China, in 1996, and the Ph.D. degree in communication and information system from Jilin University, Changchun, China, in 2005. From 2010 to 2011, she had worked as a visiting research fellow at McMaster University, Canada. Currently, she is a professor at the College of Communication Engineering, Jilin University, China. Her research fields focus on electromagnetic compatibility, and signal processing for radar and wireless communications.

Xinbo Li received the B.S. degree in automation from Jilin University, Changchun, China, in 2002, the M.S. and Ph.D. degrees in control theory and control engineering from Jilin University, Changchun, China, in 2005 and 2009, respectively. Currently, he is a professor at the College of Communication Engineering, Jilin University, China. His research interests focus on electromagnetic protection, electromagnetic environment perception, intelligent signal recognition, and processing.

Qian Jia received the M.S. degree in electronic information engineering from North China Electric Power University, China. She is currently a senior engineer in Research and Development Department, China Academy of Launch Vehicle Technology, Beijing, China. She is engaged in integrated electronic system design of spacecraft. Her main research field is knowledge-based EMC design.

Xiaohui Wang received the M.S. degree in China. He is currently a researcher in Research and Development Department, China Academy of Launch Vehicle Technology, Beijing, China. He is engaged in long-term research on advanced integrated electronic optimization design.

Design of a New Balanced Side Slotted Vivaldi Antenna with Director using Genetic Algorithm

Xiaoyan Zhang[1,2], Yuxu Hu[1*], and Aiyun Zhan[1]

[1]School of Information Engineering
East China Jiaotong University, Nanchang, 330013, China
xy_zhang3129@ecjtu.edu.cn, huyuxu_2021@163.com, 707290432@qq.com

[2]State Key Laboratory of Millimeter Waves, Nanjing, China

Abstract – Generally, side slotting and directional techniques can improve the performance of a conventional Vivaldi antenna (CVA), but the optimal structure and distribution of slots and directors may be irregular or even complex, requiring significant manual effort, thus limiting the design possibilities. In this paper, a genetic algorithm (GA) is introduced to assist in designing and optimizing a new type of balanced side slotted Vivaldi antenna with director (SSVAD). The methods of artificial intelligence make the process of searching for the optimal structure of such a multi-objective and multi-dimensional problem simpler and more diverse. The GA-generated SSVAD antenna consists of a CVA and 34 slots with varying lengths, as well as 5 metal strips. It has a compact size of $38.2\times49\times0.8$ mm^3 (or $0.32\lambda_L\times0.41\lambda_L\times0.007\lambda_L$, where λ_L is the lowest operating frequency of 2.48 GHz). The measured results show that the antenna has a peak gain >0 dBi over 2.48-10.88 GHz and >5 dBi over 4.6-10.88 GHz with S_{11}<-10 dB standard, and exhibits directional characteristics at most of the operating frequencies. Since the measured results are basically consistent with the simulation ones, the effectiveness of the designed scheme has been proven.

Index Terms – Balanced side slotted Vivaldi antenna, director, genetic algorithm optimization, ultra-wide band.

I. INTRODUCTION

Due to the characteristics such as stable directional radiation pattern, ultra-wideband, high gain, and low profile, the Vivaldi antenna has aroused the researchers' intense interest. Miniaturization and high gain are its main design difficulties [1]. To solve these issues, a method of side slotting has been introduced into conventional Vivaldi antenna (CVA) designs [2–5]. For example, in 2017, sparse irregular slots were etched on the radiators of a CVA, achieving a compact design with bandwidth of 3.9-9.15 GHz [2]; in the same year, dense comb-shaped slits with identical spacing and length were applied to a conventional antipodal antenna (CAVA) design, expanding its bandwidth from 1.8-4 GHz to 1.65-18 GHz and improving low-frequency gain as well [3]; in 2021, a new balanced side-slotted Vivaldi antenna (SSVA) with three pairs of triangular shaped slots was proposed, realizing a bandwidth of 3.05-12.2 GHz and a peak gain of 8.2 dBi [4]. In 2019, a Vivaldi antenna array was proposed for underwater communication. A linear conical array slot structure was applied to the traditional Vivaldi antenna, achieving an impedance bandwidth of over 55% with a return loss of 10 dB and a peak gain of 10.75 dBi [5]. Obviously, the side slotting technology can effectively improve the performance of the CVA/CAVA, but the shape features of the slots may be very complex and may need a long time to find a suitable one. Therefore, in order to improve design efficiency, the slots are usually assumed to have regular features and are uniformly distributed, which may result in the inability to obtain the optimal structure and limit the more possibilities of design.

To further improve the performance of the SSVA, a lens or a director is loaded at the front of its radiation patch, which can guide the energy distribution of the antenna along the end-fire direction, thereby enhancing its directivity. Specifically, the lens includes a protruding substrate [6, 7], as well as single-layer or multi-layer phase compensation metal strips [8, 9], increasing the size of the antenna. For example, in 2016, the substrate at the front end of the antenna was protruded into a semicircle, which reduced the phase error on the antenna aperture, but increased its size by 20×70 mm^2 [6]; in 2017, a three-layer phase correcting lens (PCL) was introduced into a CVA. Although it increased the antenna's gain by 1.1-6.1 dB, it also resulted in an additional size of 52×16.5 mm^2 and a thickness of 15 mm [8]. In contrast, the director only occupies the clearance area of the antenna, so that the antenna can remain compact.

Submitted On: August 20, 2023
Accepted On: December 20, 2023

https://doi.org/10.13052/2023.ACES.J.381107

Generally, the director can be formed by adding higher permittivity dielectric elements [10], metal parasitic patches [1, 7, 9, 11], and conductor gratings [12–14]. For example, an elliptical metal director was loaded into SSVA, increasing its fractional bandwidth by 13% and gain by 0.2 dB in [11]; several rectangular gratings were used in a SSVA, resulting in a gain improvement of nearly 1 dB in [13]; some epsilon negative metamaterial cells are arranged in two flares of a CAVA in [14], enhancing the gain of the antenna by 3 dB in the 24-30 GHz frequency range. Similar to grooving technology, the size, shape, and position distribution of the director have an impact on the directivity of the antenna, so they also need to be carefully designed.

In order to shorten the time for manual design, intelligent search technologies, such as swarm intelligence algorithm [15–17] and genetic algorithm (GA) [18–19], have been applied to optimize antenna parameters. For example, a frequency selective surface (FSS)-loaded CAVA was optimized using honeybee mating optimization (HBMO) algorithm in [15], but the structure of the antenna itself has not been optimized; in [16], the optimal size of the slots of a notch band UWB antenna was obtained through a particle swarm optimization (PSO) algorithm. However, only the voltage standing wave ratio (VSWR) was tested, and its gain and co-polarization radiation patterns were given through simulation, so the algorithm's performance has not been fully demonstrated; in [18], the heights of the rings of a lens antenna were optimized using GA. Compared with the swarm intelligence algorithms, GA is more widely used because it is less likely to fall into local optima prematurely, which reveals the enormous potential of GA in complex antenna design.

In this work, considering that SMA joint welding may cause a relatively large error in the antipodal antenna, as well as the research needs of the group in flexible antennas in the future, planar Vivaldi was selected as a reference in this design. The side slots and director of the SSVAD are jointly optimized and generated through GA, so their shapes and scales exhibit symmetric and random characteristics, making it difficult to achieve through manual design, as it requires extensive multi-objective and multi-dimensional simulation experiments. The measured results indicate that the antenna has a compact size, a bandwidth of 125.6%, and a peak gain of 8.47 dBi. Compared with published literatures, the proposed antenna has the advantages of miniaturization, relatively large fractional bandwidth, and high gain. Although the structure of the antenna appears complex, the GA approach make the process of searching for the optimal structure of such a multi-objective and multi-dimensional problem simpler and more diverse.

This manuscript is arranged as following. First, the design and optimization methods of the antenna are described in Section II. Then, the GA-generated SSVAD was fabricated and tested in Section III, and the measured results were compared with the simulation ones, all of which were presented. Finally, a conclusion is made in Section IV.

II. METHODS FOR ANTENNA DESIGN AND OPTIMIZATION

A. Basic structure of the CVA

The proposed antenna is designed based on a traditional structure, as shown in Fig. 1. It is printed on a FR4 substrate with relative dielectric constant (ε_r) of 4.4, loss tangent of 0.025, and thickness (t) of 0.8 mm. The length (L_t) and width (W_t) of the substrate are 49 mm and 38.2 mm, respectively. This CVA consists of a coupler (as shown in Fig. 1 (a) and two radiating fins (as shown in Fig. 1 (b)). They are etched on two opposite sides of the substrate.

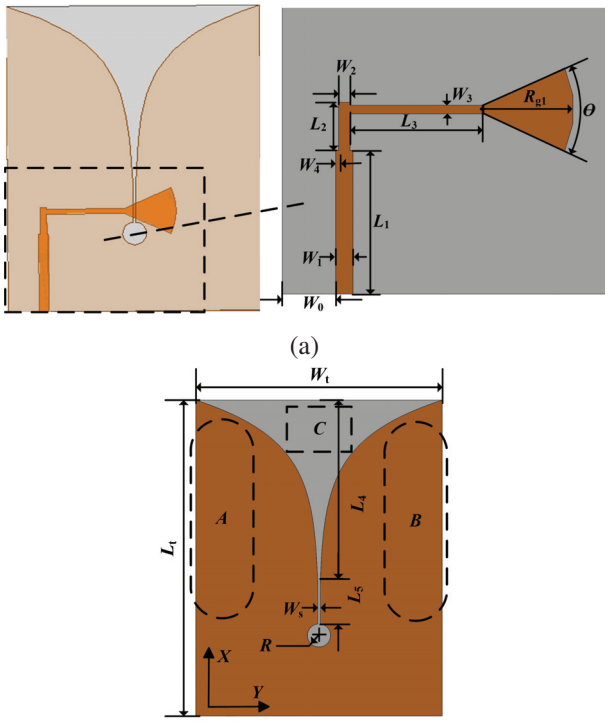

Fig. 1. Basic structure of the Vivaldi antenna: (a) Its top view and (b) its bottom view.

The coupler includes a microstrip feed line, a microstrip-to-slot-line transition, and a fan-shaped stub. They are cascaded to match the impedance between the feeding and the tapered slot structure, thus enabling the antenna to maintain good impedance matching over

a wide frequency band. Their parameters are represented by L_1, W_1, L_2, W_2, L_3, W_3, R_{g1}. The width of the microstrip feed line that matches the characteristic impedance of 50 ohms can be calculated through following formulas [20]:

$$Z_0 = \frac{120pi}{\sqrt{\varepsilon_e}\left[\frac{w_1}{t} + 1.393 + 0.667\ln(\frac{w_1}{t} + 1.444)\right]}, \quad (1)$$

with

$$\varepsilon_e = \frac{\varepsilon_r + 1}{2} + \frac{\varepsilon_r - 1}{2\sqrt{1 + (12t/w_1)}}, \quad (2)$$

where t is the thickness of FR4 substrate and W_1 is the width of the microstrip feeder .

The fins have exponential curves and a circular resonant cavity (with a radius of R) slotted at their intersection. The exponential curves of the fins are given as

$$y(x) = C\ \exp(kx), \quad (3)$$

where x and y represent the coordinates of the curve. The constant C and opening rate k are given by:

$$C = W_s/2 \text{ and } \mathrm{k} = \ln(W_t/W_s)/L_4, \quad (4)$$

where L_4, W_t, and W_s are the length, width, and throat width of the aperture respectively. The distance between the aperture and the top of the circular cavity is L_5. Radiation occurs along the exponential curves. The circular cavity serves as an open circuit to minimize the reflections from the microstrip line to the microstrip-to-slotline transition [12].

The regions A, B, and C shown in Fig. 1 (b) were selected for optimization. Specifically, side slotting technique is applied to the A and B regions, while the conductor gratings as the director have been introduced into the C region. The slots in region B are symmetrical and identical to A.

B. The proposed SSVAD design and optimization

Before optimization, the specific location of the slots and the total area they will occupy cannot be determined. Therefore, the A/B region is initialized as 36 evenly spaced etched slots along the X direction. Similarly, the region C is initialized with 6 metal strips. For ease of fabricating, each slot and strip are rectangular in shape. The specific optimization methods based on GA are as follows.

Considering the large number of the slots, their widths and the distance between adjacent slots are fixed as 0.5 mm, and only their lengths (numbered as L_{cn}, n=1, 2, …, 36) are generated by GA. While, the director is only composed of 6 metal strips, so both their length (L_{gn}, n=1, 2, …, 6) and width (W_{gn}) can be optimized. These elements are arranged in parallel and the distance between the bottom edges of two adjacent elements is fixed as g_0. To avoid overlapping and excessive length of metal strips, L_{gn} is set to <1.2 mm and W_{gn} <7 mm. In contrast, the size range limitations of L_c require more consideration. Firstly, the resonant wavelength λ_0 caused by a slot with a length of L_c can be estimated as [21]

$$\lambda_0 = 4L_c/\sqrt{(1+\varepsilon_r)/2}. \quad (5)$$

According to (5), the estimated length of the slots is 12.3-41 mm (corresponding to 3-10 GHz). Next, considering that the half width of CVA is W_t = 19.1 mm, and to avoid damaging the current distribution of the exponential curves, the length of the slots L_{c12} - L_{c29} needs to be shortened. Ultimately, they are controlled between 0 mm and 15 mm. The determination of the range for other L_{cn} is also for the same reason.

The GA and a high frequency simulation software (HFSS) V15.1 are combined through an application programming interface (API). The former is used to search for the optimal parameters, while the latter attempts to apply them in antenna simulation. In order to minimize the reflection of the antenna within the frequency range of 3-10 GHz and ensure a higher gain, the fitness function is defined as the average return loss of the antenna at the sampling frequency:

$$\text{Fitness} = \frac{1}{n}\sum_{n=1}^{N} F(f_\mathrm{n}), \quad (6)$$

with

$$F(\mathrm{f}_n) = \begin{cases} 10, & |S_{11}(\mathrm{f}_n)| \geq 10 \\ |S_{11}(\mathrm{f}_n)|, & |S_{11}(\mathrm{f}_n)| < 10 \end{cases}, \quad (7)$$

and constraints:

$$\mathrm{A} = \frac{1}{n}\sum_{n=1}^{N} A_n, \quad (8)$$

where

$$A_n = \begin{cases} 1, & Gain(f_n) \geq Gain0(fn) \\ 0, & Gain(fn) < Gain_0(fn) \end{cases}. \quad (9)$$

Here, N refers to the number of discrete frequencies f_n; $|\mathrm{S}_{11}(f_n)|$ refers to the return loss of the antenna at f_n, and its standard is $|S_{11}| \geq 10$ dB. The average return loss of the antenna is calculated using formula (6). When Fitness = 10, it indicates that the return loss of the target frequency band is larger than 10 dB; Gain(f_n) and $\mathrm{Gain}_0(f_n)$ are the peak gains of the GA generated antenna and the CVA (as shown in Fig. 1), respectively. Literature research [9, 22] has found that adding gratings can improve some of the high-frequency gain but has little effect on the low-frequency gain. The frequency at which the gain can be increased accounts for approximately 70-80% of the total frequency. Therefore, in order to reduce optimization time, A $\geq$ 0.8 is used as the standard for determining the optimal parameter, which means that the antenna gain of over 80% of frequencies is higher than that of CVA.

The flowchart of GA assisted antenna design is shown in Fig. 2. The parameters optimized using GA and their corresponding limiting ranges are listed in Table 1. Table 2 presents the main parameters of GA, such as

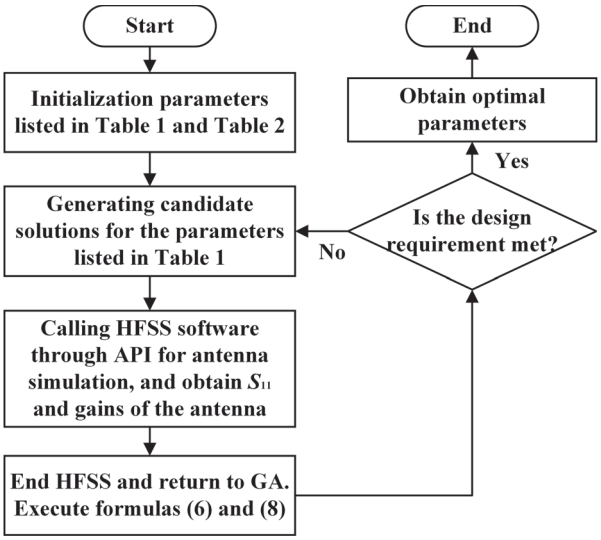

Fig. 2. Design process of the GA-generated antenna.

Table 1: Parameters and their constraints

Region	Parameter	Constraint (mm)
A/B	L_{c1}-L_{c11}, L_{c34}-L_{c36}	0-3
A/B	L_{c12}- L_{c29}	0-15
A/B	L_{c30}- L_{c33}	0-9
C	L_{g1}-L_{g6}	0-7
C	W_{g1}-W_{g6}	0.5-1.2

Table 2: Main parameters of the GA

Parameter	Value
Maximum iteration number	100
Crossover rate	0.9
Mutation rate	0.05
Deadline iterations	62
Gene length	8
Population number	150

population number, crossover rate, mutation rate, and maximum iteration number.

The optimization process is performed on a PC with Intel Core i7 (3.4 GHz, 8-core) CPU and 32 GB RAM. After about 18 days of calculation, the structure of the proposed balanced GA-generated SSVAD antenna is shown in Fig. 3. After optimization, L_{c8}, L_{c25}, and L_{g6} are 0, so the number of slots and metal strips are 34 and 5, respectively. The optimized parameters are shown in Table 3.

C. Antenna analysis

The current distribution on the radiation fins of the CVA, balanced SSVA and the proposed SSVAD at frequencies of 3.2, 7.2, and 9.2 GHz, is simulated and compared in Fig. 4. By comparing the current intensities in the D, E, and F regions, it can be clearly observed that the current of the CVA shown in Fig. 4 (a) is mainly distributed at the edges of the antenna radiation fins. In contrast, guided by the side slotting and the director, the surface currents of SSVA and SSVAD shown in Figs. 4 (b) and (c) diffuse toward the interior of the fins, thereby increasing the effective radiation area; and the director gathers the high-frequency radiation field of the antenna, thereby increasing the directionality of the antenna at high frequencies.

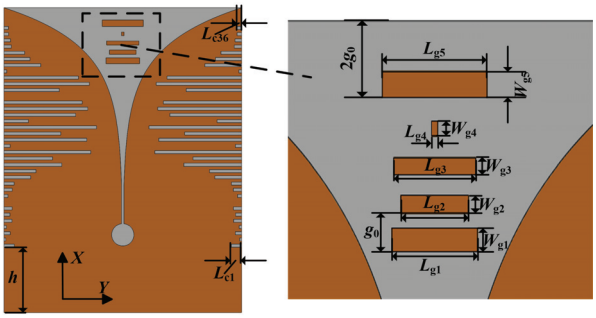

Fig. 3. The structure of the proposed SSVAD.

Table 3: Optimized parameters of the proposed SSVAD (unit: mm)

Symbol	Value	Symbol	Value	Symbol	Value
W_t	38.2	W_0	4.65	W_1	1.5
W_2	1	W_3	0.75	W_4	0.25
Lc_1	1.65	Lc_2	0.29	Lc_3	0.99
Lc_4	0.38	Lc_5	1.27	Lc_6	0.95
Lc_7	1.3	Lc_8	0	Lc_9	0.63
Lc_{10}	1.31	Lc_{11}	1.62	Lc_{12}	4.29
Lc_{13}	5.14	Lc_{14}	9.28	Lc_{15}	7.81
Lc_{16}	13.95	Lc_{17}	0.98	Lc_{18}	13.31
Lc_{19}	9.14	Lc_{20}	14.88	Lc_{21}	3.92
Lc_{22}	11.52	Lc_{23}	13.47	Lc_{24}	12.57
Lc_{25}	0	Lc_{26}	8.89	Lc_{27}	13.72
Lc_{28}	11.97	Lc_{29}	0.43	Lc_{30}	5.9
Lc_{31}	4.18	Lc_{32}	3.31	Lc_{33}	1.17
Lc_{34}	1.04	Lc_{35}	0.72	Lc_{36}	0.7
Ws	0.4	L_t	49	L_1	12.5
L_2	4.2	L_3	12.25	L_4	28.5
L_5	6.2	h	10.5	Wg_1	0.5
Wg_2	0.93	Wg_3	0.7	Wg_4	0.65
Wg_5	0.58	Wg_6	0	g_0	1.5
Lg_1	5.39	Lg_2	4.26	Lg_3	5.17
Lg_4	0.39	Lg_5	6.61	Lg_6	0
R	1.8	Θ	50°	Rg_1	8.6

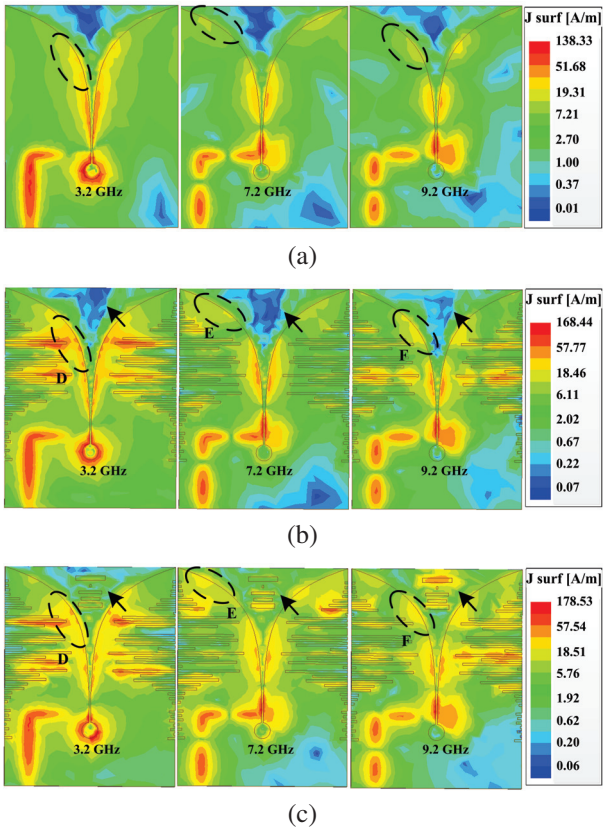

Fig. 4. Comparison of simulated surface current distribution of (a) CVA, (b) balanced SSVA, and (c) SSVAD at different frequencies (3.2, 7.2, and 9.2 GHz).

Figure 5 compares the simulated return loss of the CVA, balanced SSVA, and proposed SSVAD respectively. It can be seen that the operating frequency range of CVA is 3.1-10 GHz (or a fractional bandwidth of 105%). After side slotting and loading director, S_{11} decreased by 6.63 dB, 6.32 dB, 12.44 dB, 11.12 dB, and 10.33 dB at 3.1 GHz, 4.51 GHz, 7.24 GHz, 9.03 GHz, and 10.82 GHz, respectively, so its operating frequency is expanded to 2.79-11.17 GHz (up to 122%).

The realized gains of the three antennas at 2.79-11.17 GHz are compared in Fig. 6, which verifies that after loading director and applying side slotting technology, the antenna gains become higher.

Comparison of performance between the proposed SSVAD and other antennas listed in [4, 11, 13, 15, 17, 22, 23] is presented in Table 4. Through comparison, it can be seen that the design of artificial intelligence assisted Vivaldi antennas is still limited. Although the structure of the antenna appears complex, the process of designing with GA approach is relatively simple. The proposed antenna has a size of 0.32×0.4×0.007, a bandwidth of 8.4 GHz, and a peak gain of 8.47 dBi. It can be inferred that the proposed antenna achieves a wide impedance bandwidth and a high gain with a relatively compact size.

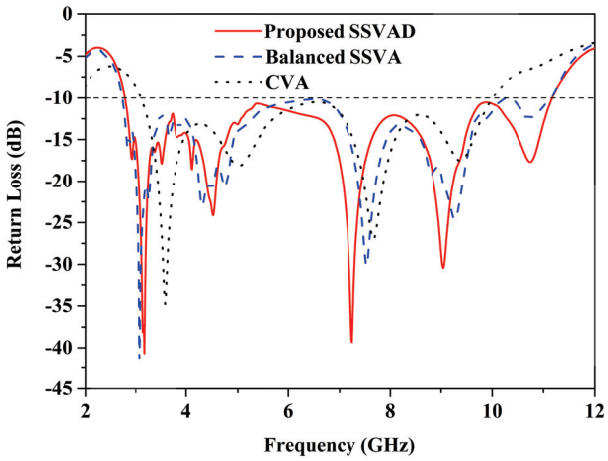

Fig. 5. Comparison of the simulated return loss for CVA, balanced SSVA, and proposed SSVAD.

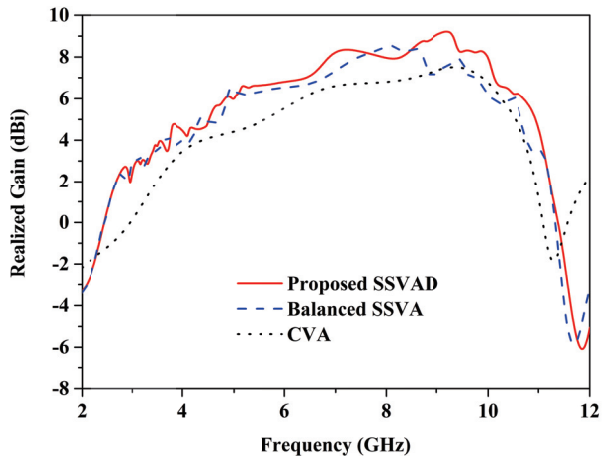

Fig. 6. Comparison of the simulated realized gains of CVA, balanced SSVA, and proposed SSVAD.

Table 4: Specification and performance comparison between reference antennas and the proposed antenna

Ref. (Years)	Intelligent Optimization Technology	Optimization Methods	Size (λ_L^3)	Bandwidth / Fractional Bandwidth (GHz/%)	Peak Gain (dBi)
[4] (2021)	–	Diagonal slot	0.36 × 0.36 × 0.016	3.05 – 12.2/120	8.2
[11] (2021)	-	Rectangular strip	0.49 × 0.45 × 0.008	2.5 – 11/126	7.2
[13] (2022)	–	Bottle-shaped slots+ Rectangular strip	1.1 × 0.96 × 0.008	3 – 8/91	8.8
[15] (2021)	HBMO	Multi layer FSS	0.83 × 0.97 × 0.03	5 – 12/82	10.1
[17] (2021)	HBMO + GA	FSS	0.92 × 1.07 × 0.01	2.1 – 3.1; 3.5 – 6.5 7.4 – 8.1; 8.2 – 9/116	10
[22] (2021)	–	Star-shaped slot + Artificial material lens + Dielectric lens	0.53 × 0.60 × 0.011	4 – 13/105	9.2
[23] (2021)	-	Rectangular slot	0.38 × 0.52 × 0.023	4.74 – 20/123	5.43
This work	GA	Rectangular slot+ irregular Rectangular strip	0.32 × 0.41 × 0.007	2.48 – 10.88/125.6	8.47

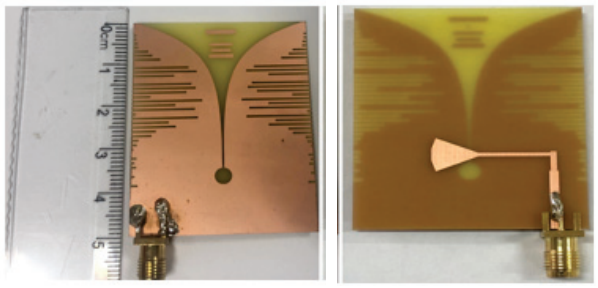

(a) (b)

Fig. 7. Photographs of the fabricated proposed antenna: (a) Top view and (b) bottom view.

III. MEASURED RESULTS

The proposed antenna has been fabricated, and its photographic images are shown in Fig. 7. Its return loss is tested by the Agilent Network Analyzer (Keysight E5071C) and compares with the simulated ones, which are shown in Fig. 8. Measured results show that the proposed antenna has a -10 dB impedance bandwidth of 2.48-10.88 GHz (>125%). Although there are some differences between the test results and simulated results (as ultra-wideband (UWB) antennas are very sensitive to fabrication tolerance), the overall trend is consistent.

The measured 2-D radiation patterns in the XY-plane and 3-D far-field radiation pattern of the proposed antenna at frequencies of 5.2, 6.2, 7.2, 9.2, and 10.2 GHz are shown in Figs. 9 (a), (b), (c), (d), and (e), respectively. Their co-polarization to cross-polarization ratios at 5.2 GHz, 6.2 GHz, 7.2 GHz, and 9.2 GHz are 27.8 dB, 27.51 dB, 26.2 dB, 23.2 dB, and 17.1 dB. They are all greater than 10 dB, indicating that the polarization interference of this antenna is small.

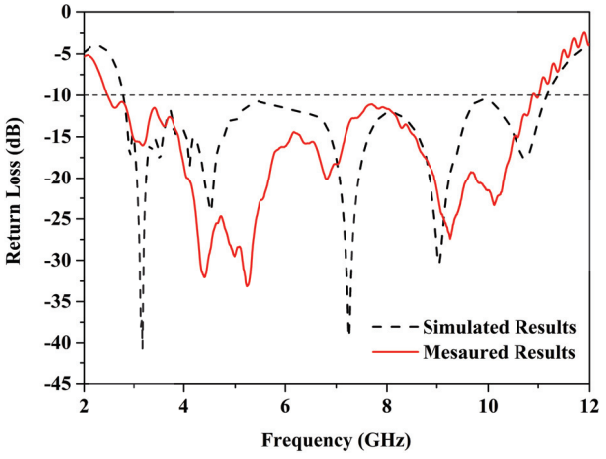

Fig. 8. Simulated and measured return loss of the proposed antenna.

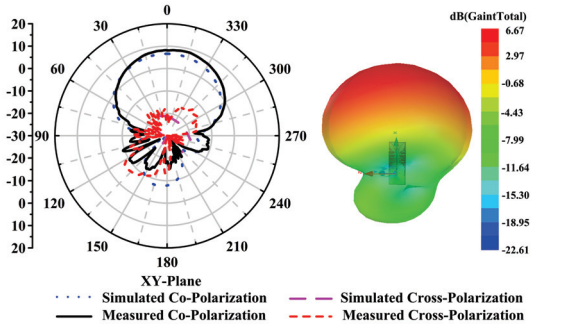

(a)

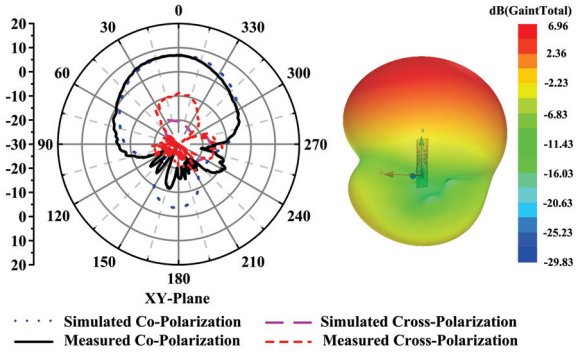

(b)

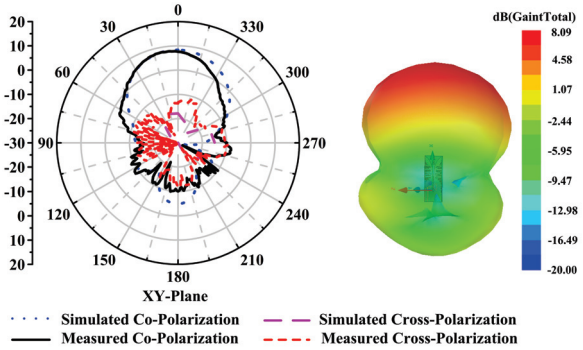

(c)

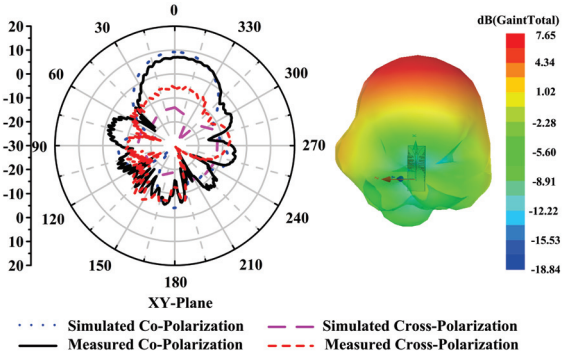

(d)

Fig. 9. *Continued*

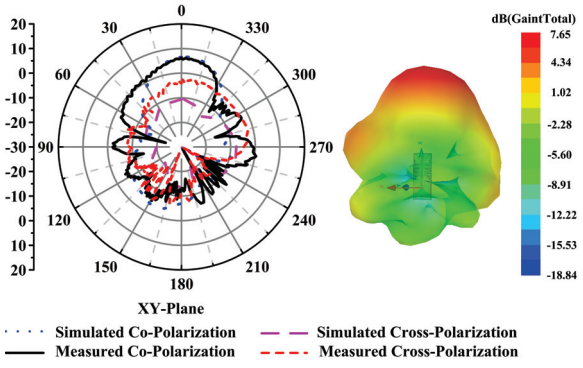

(e)

Fig. 9. Simulated and measured radiation patterns of the proposed antenna in the XY-plane and 3D far-field radiation pattern: (a) 5.2 GHz, (b) 6.2 GHz, (c) 7.2 GHz, (d) 9.2GHz, and (e) 10.2 GHz.

The variation of the peak gains of the designed antenna over 2-12 GHz is shown in Fig. 10. The maximum value of the test results is 8.47 dBi, which appears at 5.2 GHz and deviates from the simulation (the peak gain is 9.2 dBi at 9.2 GHz), which may be due to fabrication tolerance.

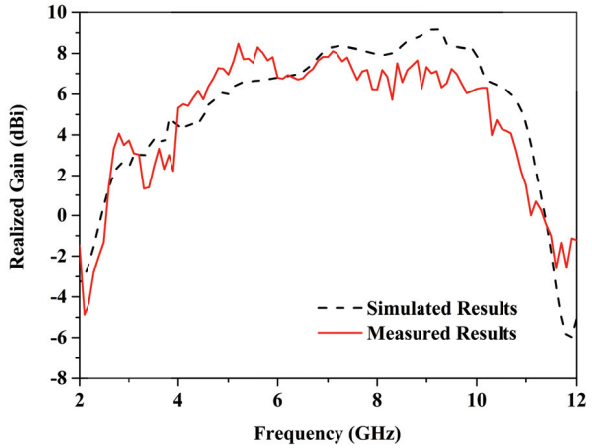

Fig. 10. Simulated and measured realized gains of the proposed antenna.

IV. CONCLUSION

In this paper, the GA approach is applied in generating edge slots of the SSVAD and determining the positions and scales of the slots and director elements. The proposed antenna has a compact size of $0.32\lambda_L \times 0.41\lambda_L \times 0.007\lambda_L$. It can operate at 2.48-10.88 GHz. The peak gain within this frequency range is 8.47 dBi. Compared with the traditional manually designed antennas, the proposed antenna has a more complex structure and a better performance. The design process of these structures can be separated from manual participation, reflecting the advantages of intelligent design. In the future, we will continue to seek a more efficient artificial intelligence algorithm to accelerate search speed. And, constraints such as directionality and cross polarization ratio will be introduced into the fitness function. These research approaches will be further applied to the design of flexible antennas.

ACKNOWLEDGMENT

The authors wish to acknowledge the support of the Jiangxi Provincial Department of Education Project (GJJ2200622), Open Project of Millimeter Wave Key Laboratory (K202431).

REFERENCES

[1] H. Zhu, X. Li, L. Yao, and J. Xiao, "A novel dielectric loaded Vivaldi antenna with improved radiation characteristics for UWB application," *Applied Computational Electromagnetics Society (ACES) Journal*, vol. 33, no. 4, pp. 394-399, Apr. 2018.

[2] M. Z. Mahmud, M. T. Islam, M. Samsuzzaman, S. Kibria, and N. Misran, "Design and aarametric investigation of directional antenna for microwave imaging application," *IET Microwaves, Antennas & Propagation*, vol. 11, no. 6, pp. 770-778, May 2017.

[3] M. Moosazadeh, S. Kharkovsky, J. T. Case, and B. Samali, "Antipodal Vivaldi antenna with improved radiation characteristics for civil engineering applications," *IET Microwaves, Antennas & Propagation*, vol. 11, no. 6, pp. 796-803, May 2017.

[4] H. Özmen and M. B. Kurt, "Radar-based microwave breast cancer detection system with a high-performance ultrawide band antipodal Vivaldi antenna," *Turkish Journal of Electrical Engineering and Computer Sciences*, vol. 29, no. 5, pp. 2324-2345, Sep. 2021.

[5] P. Soothar, H. Wang, B. Muneer, Z. A. Dayo, and B. S. Chowdhry, "A broadband high gain tapered slot antenna for underwater communication in microwave band," *Wireless Personal Communications*, vol. 116, no. 2, pp. 1025-1042, Aug. 2019.

[6] Y. Zhang, E. Li, C. Wang, and G. Guo, "Radiation enhanced Vivaldi antenna with double-antipodal structure," *IEEE Antennas and Wireless Propagation Letters*, vol. 16, pp. 561-564, Mar. 2017.

[7] X. Zhang, Y. Chen, M. Tian, J. Liu, and H. Liu, "A compact wide-band antipodal Vivaldi antenna design," *International Journal of RF And Microwave Computer-aided Engineering*, vol. 29, no. 4, pp. 1-6, Oct. 2018.

[8] X. Li, G. Liu, Y. Zhang, L. Sang, and G. Lv, "A compact multi-layer phase correcting lens to improve directive radiation of Vivaldi antenna," *International Journal of RF and Microwave Computer-aided Engineering*, vol. 27, no. 7, pp. 1-12, Apr. 2017.

[9] A. S. Dixit and S. Kumar, "The enhanced gain and cost-effective antipodal Vivaldi antenna for 5G communication applications," *Microwave and Optical Technology Letters*, vol. 62, no. 6, pp. 2365-2374, Feb. 2020.

[10] J. Bourqui, M. Okoniewski, and E. C. Fear, "Balanced antipodal Vivaldi antenna with dielectric director for near-field microwave imaging," *IEEE Transactions on Antennas and Propagation,* vol. 58, no. 7, pp. 2318-2326, July 2010.

[11] M. Samsuzzaman, M. T. Islam, M. T. Islam, A. A. S. Shovon, R. I. Faruque, and N. Misran, "A 16-modified antipodal Vivaldi antenna array for microwave-based breast tumor imaging applications," *Microwave and Optical Technology Letters,* vol. 61, no. 9, pp. 2110-2118, Sep. 2019.

[12] S. Guruswamy, R. Chinniah, and K. Thangavelu, "Design and implementation of compact ultra-wideband Vivaldi antenna with directors for microwave-based imaging of breast cancer," *Analog Integrated Circuits and Signal Processing*, vol. 108, pp. 45-47, May 2021.

[13] J. J. Wang, J. W. Liu, Y. C. Fan, and Y. X. Bai, "A novel Vivaldi antenna for UWB detection," *Microwave and Optical Technology Letters*, vol. 65, no. 3, pp. 826-843, Dec. 2023.

[14] A. S. Dixit and S. Kumar, "Gain enhancement of antipodal Vivaldi antenna for 5G applications using metamaterial," *Wireless Personal Communications*, vol. 121, pp. 2667-2679, Dec. 2021.

[15] P. Mahouti, A. Klzllay, O. Tari, A. Belen, M. A. Belen, and A. Caliskan, "Design optimization of ultra-wideband Vivaldi antenna using artificial intelligence," *Applied Computational Electromagnetics Society (ACES) Journal*, vol. 36, no. 12, pp. 1594-1601, Dec. 2021.

[16] Y. Li, W. Shao, L. You, and B. Wang, "An improved PSO algorithm and its application to UWB antenna design," *IEEE Antennas and Wireless Propagation Letters*, vol. 12, pp. 1236-1239, Oct. 2013.

[17] F. Güneş, İ. Ö. Evranos, M. A. Belen, P. Mahouti, and M. Palandökenb, "A compact triband antipodal Vivaldi antenna with frequency elective surface inspired director for IoT/WLAN applications," *Wireless Networks*, vol. 27, no. 5, pp. 3195-3205, June 2021.

[18] W. Yu, L. Peng, Y. Liu, Q. Zhao, X. Jiang, and S. Li, "An ultrawideband and high-aperture-efficiency all-dielectric lens antenna," *IEEE Antennas and Wireless Propagation Letters*, vol. 20, no. 12, pp. 2442-2446, Dec. 2021.

[19] K. Kayalvizhi and S. Ramesh, "Design and analysis of reactive load dipole antenna using genetic algorithm optimization," *Applied Computational Electromagnetics Society (ACES) Journal*, vol. 35, no. 3, pp. 279-287, Mar. 2020.

[20] D. M. Pozar, *Microwave Engineering* (3rd edition), New York, John Wiley & Sons, pp. 143-144, 2005.

[21] J. Bai, S. Shi, and D. W. Prather, "Modified compact antipodal Vivaldi antenna for 4–50-Ghz UWB application," *IEEE Transactions on Microwave Theory and Techniques*, vol. 59, no. 4, pp. 1051-1057, Apr. 2011.

[22] V. Binzlekar, A. Sharma, and S. Agarwal, "A high gain and wide bandwidth grooved AML loaded Vivaldi antenna design for imaging and communication applications," *Microwave and Optical Technology Letters*, vol. 64, no. 7, pp. 1217-1223, Apr. 2022.

[23] P. Soothar, H. Wang, C. Xu, Y. Quan, ZA. Dayo, M. Aamir, and B. Muneer, "A miniaturized broadband and high gain planar Vivaldi antenna for future wireless communication applications," *International Journal of Antennas and Propagation*, vol. 116, no. 2, pp. 1025-1042, Aug. 2021.

Xianyan Zhang received the B.S. degree in applied physics and the M.S. degree in physical electronics from Yunnan University, Kunming, China, in 2001 and 2004, respectively, and the Ph.D. degree in electromagnetic field and microwave technology from Institute of Electronics, Chinese Academy of Sciences in 2007. Her research interests include electromagnetic computation, antenna design, and wireless power transmission structure design.

Yuxu Hu was born in 1998 in Gao'an City, Jiangxi Province, China. He obtained a bachelor's degree in engineering from the School of Science and Technology of East China Jiaotong University and is currently studying at the School of Information Engineering of East China Jiaotong University. His main research direction is antenna design.

Aiyun Zhan was born in Nantong, Jiangsu, China in 1973. She received B.S. degree from Southwest Jiaotong University in 1997 and the M.S. degree in East China Jiaotong University in 2008. She is currently working at rhe School of Information Engineering, East China Jiaotong University. Her research interests focus on channel coding and optical communication.

Design of a Reconfigurable Band-notched Wideband Antenna using EBG Structures

Xiaoyan Zhang, Ziao Li, Aiyun Zhan*, and Yan Mei

School of Information Engineering
East China Jiaotong University, Nanchang, 330013, China
xy_zhang3129@ecjtu.edu.cn, lza_2017@163.com, 707290432@qq.com, 360291931@qq.com

Abstract – A compact WLAN band-notched reconfigurable wideband antenna using two mushroom-like electromagnetic band-gap (EBG) structures is proposed in this paper. It is designed based on a dual wideband microstrip feed patch antenna with operating frequency bands of 2.2-3.7 GHz and 4.8-6 GHz. One of the EBG cells is positioned alongside the feed line, while the other EBG cell is laid on the back of the substrate. The patch or ground of the two EBG units are fed with a stronger current through a ground slot and a parasitic stub respectively, and the connections between the EBG structures and the antenna are controlled by loading a PIN diode with two 56 pF DC blocking capacitors. The advantage of this proposed design is that the antenna and the EBG unit can be designed independently. The proposed antenna has an overall size of $35\times46\times1.6$ mm^3. When testing the S_{11} of the antenna, the influence of the bias circuit on the antenna is also considered. The measured results show that the proposed antenna can generate two notched bands of 2.3-2.49 GHz and 5.11-5.51 GHz of WLAN, and the realized gain in the notch bands can be reduced to -2.65 dBi and -4.55 dBi, respectively, demonstrating its anti-interference characteristics, and can be applied in band notch broadband communication systems or anti-interference communication equipments such as unmanned aerial vehicles and radars.

Index Terms – Anti-interference, electromagnetic band-gap (EBG), PIN diodes, reconfigurable band notched antenna, WLAN.

I. INTRODUCTION

The frequency bands of WLAN (2.4-2.4835 GHz, 5.15-5.825 GHz) are widely used in wireless communication systems. In order to prevent its interference, some wideband antennas need to own a single or a dual band-rejected filtering characteristic in the WLAN band. The main approaches used by these researches can be mainly divided into two categories [1]. The first category is to generate radiation perturbation through etching slots on the ground/ patches or loading parasitic stubs [2, 3] and stepped impedance resonators [1, 4] on the patches. The disadvantage of these methods is that they will change the radiation pattern of the antenna itself [1]. Moreover, due to the limited area that can be cleared, it is hard to load switch components on the patches, making it difficult to achieve reconfigurable band notch design. The second category is to integrate filters at the feed port of the antennas to reject the interfering sources [5–6]. By controlling the filters or their connections, the notch band can be tuned. While the filters increase the complexity of antenna design. In [7–8], the methods of adding an open loop resonator near to a feed line were proposed, which can generate a stopband in the signal source through coupling resonance. Although the frequency band can be adjusted by changing the on-off state of the resonator, its coupling effect is difficult to eliminate [9].

In recent years, electromagnetic band-gap (EBG) technology has been introduced into the single-, dual-, and multi-band-rejected antennas design [10–14] In these studies, the EBGs are mainly divided into two types: uniplanar EBG [10, 11] and high impedance electromagnetic surface (HIS) [12–15]. For example, two spiral uniplanar EBGs are symmetrically placed on both sides of a dual notch antenna's feed line in [10], and asymmetrically placed on the upper and lower sides of the microstrip feed line in [11], resulting in two additional notch bands; simpler structures of conventional mushroom-type HIS-EBG (CMT-HIS-EBG) [1, 12] or edge-located vias HIS-EBG (ELV-HIS-EBG) [12–15] were placed next to or in the middle of the antenna feed line [14], or even on the back of the antenna (with the patch as the ground) [15] to create the notch bands. The principle of loading uniplanar EBG is similar to the methods of positioning resonators next to the feed line, so the same problem is faced when realizing notch reconfigurability. In contrast, the essence of using HIS-EBG to design band-notched antennas belongs to the second category, as the HIS-EBG unit has a bandstop property, so it can be used as a bandstop filter without affecting the behavior of the antenna itself.

Submitted On: November 1, 2023
Accepted On: December 15, 2023

https://doi.org/10.13052/2023.ACES.J.381108

Based on the above reasons, the design of reconfigurable band-notched antennas using HIS-EBG structures has attracted research interest [16–18]. For example, in 2015, the concept of six band-notched reconfigurable antenna using six ELV-HIS-EBG units was proposed, but the bias circuit was not considered in this design. Therefore, the EBG units and the switches were printed separately in an intermediate layer and placed underneath the transmission line of the antenna [16]; in 2016, the copper strips of two ELV-HIS-EBGs are connected with a PIN diode, achieving a single reconfigurable band-rejected function, but its realized gain in the notch band at 4 GHz is about -1.5 dBi, which is not significantly decreased [17]; In 2020, two CMT-HIS-EBGs are surrounded by a square copper ring and connected to the ring using a varactor diode. By controlling the ON/OFF state of the varactor diodes, the reconfigurability in the notch band of 5.3 GHz was realized. However, the gain in the rejected band only reaches 0 dBi [18].

The patch of the HIS-EBG is connected to the ground through punching a copper via into the substrate, forming a complete circuit. The challenge of designing HIS-EBG-based band-notched reconfigurable antennas is that the PIN diodes cannot be directly loaded on the vias to control the ON/OFF of the circuit. In addition, the electronic components of the switches will occupy a certain clearance area, leading to changes in the antenna structure.

In this paper, a novel WLAN band-notched reconfigurable wideband monopole antenna based on two HIS-EBG was designed, fabricated, and tested. The impact of switches (it is composed of a PIN diode and two capacitors) on antenna performance is considered in testing. The switches are not directly loaded in the EBG unit but are loaded in its ground slot and the parasitic stubs. By extending the parasitic stubs and the ground slots into the areas with stronger currents, more surface waves will be directed into the EBG unit. The proposed method can enable the antenna and the HIS-EBG unit to be designed independently, and can sharply decrease the gain within the notch band, providing a new approach for the design of band-notched reconfigurable antennas.

II. DESIGN CONFIGURATION AND APPROACH

A. Overall design of the antenna

To verify the design scheme, a square microstrip patch antenna is used as the basic structure. It is fabricated on a FR4 substrate, with a dielectric constant of 4.4 and a loss tangent of 0.02. The prototype of the proposed antenna is shown in Fig. 1. As shown in Fig. 1 (a), the overall size of the antenna is $35\times46\times0.8$ mm^3, and the parameters of the patch antenna are L_p = 22 mm, W_p = 16 mm, L_f = 26.4 mm, and W_f =2 mm.

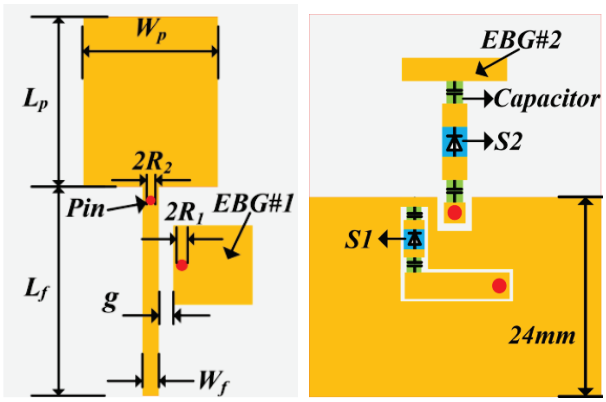

(a) (b)

Fig. 1. Geometry of the proposed antenna includes (a) top view and (b) bottom view.

Two square patch mushroom-like HIS-EBG units EBG #1 and EBG #2 are placed on the right side of the microstrip line (see Fig. 1 (a)) and on the back of the patch (see Fig. 1 (b)), fully utilizing the available space of the antenna. The connections between the EBGs and the patch antenna are controlled by two RF switches (represented as *S1* and *S2*). These switches are composed of a BAR50-02V PIN diode and two C_{bias} = 56 pF DC blocking capacitors. Figure 2 shows the equivalent bias circuit for the antenna. The bias voltage is 1 V, and a L_{bias} = 51 nH inductor is used to stabilize the bias current.

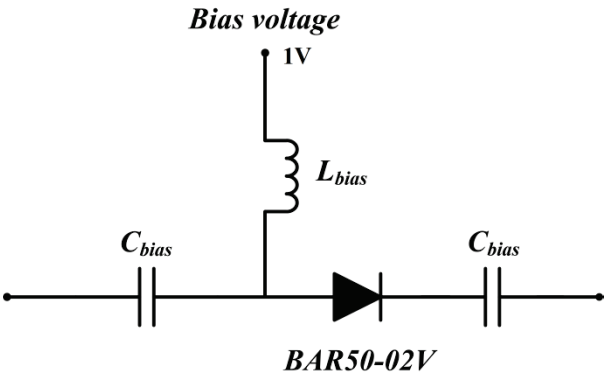

Fig. 2. Antenna bias circuit.

B. Antenna design by loading EBG #1

As Fig. 3 (a) shows, a microstrip-line-based method [12] is used to study the stopband characteristics of the EBG #1. Specifically, without considering the radiator of the patch antenna, the EBG #1 is placed on the right side of the microstrip line with a distance of *g*.

The equivalent circuit of this model is shown in Fig. 3 (b). C_0 is the fringing capacitance between the

EBG #1 and the microstrip line, C_1 and L_1 are the capacitance and inductance generated by the mushroom-shaped EBG #1 itself. They are simply estimated using the formula [19] for estimating periodic EBG parameters as

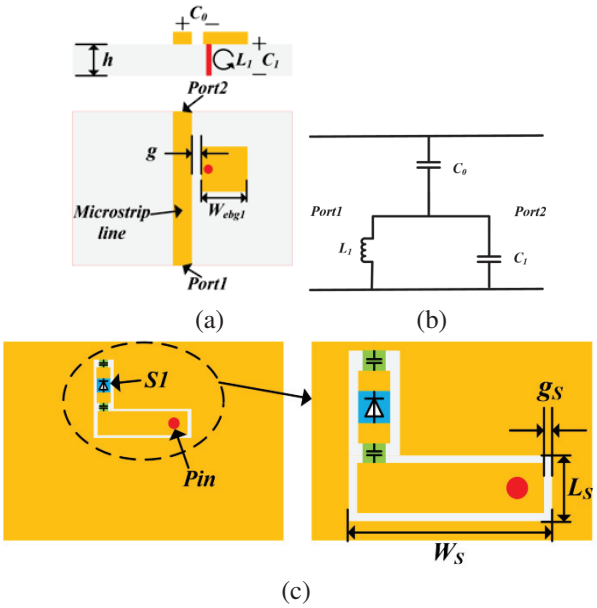

Fig. 3. Microstrip-line-based model: (a) Configuration diagram, (b) equivalent circuit model, (c) back view of the circuit.

$$C_0 = \frac{W_{ebg1}\varepsilon_0(1+\varepsilon_r)}{\pi}\cosh^{-1}\left(\frac{W_f+W_{ebg1}+g}{g}\right), \quad (1)$$

$$C_1 = \varepsilon_0\varepsilon_r W_{ebg1}^2/h, \quad (2)$$

$$L_1 = \mu_0 h, \quad (3)$$

where W_{ebg1} is the width of the patch for the square EBG #1 cell,ε_r= 4.4, is the relative dielectric constant of FR4, and h = 0.8 mm is the thickness of the substrate. Usually, g is much smaller than W_{ebg1}, so C_0 is mainly influenced by W_{ebg1}.

The resonant frequency(f_r) of this model can be derived as

$$f_r = 1/2\pi\sqrt{L_1(C_0+C_1)}. \quad (4)$$

Obviously, once g is fixed, the approximate value of W_{ebg1} can be inferred from the selected band-notch frequency f_r. Therefore, further optimization can be carried out based on this value. During this process, g can be determined simultaneously.

Figure 3 (c) shows the back of the model. It can be seen that an L-shaped slot has been etched on the ground around the pin of EBG #1, which separates the connection between the EBG #1 and the ground, preventing the EBG #1 from forming a complete circuit. Then, a BAR50-02V PIN diode and two DC blocking capacitors are embedded at the end of the slot, so the connection state between the EBG #1 and the microstrip line can be controlled by controlling the ON/OFF state of *S1*. Due to the extended length of the L-shaped slot being much longer than the width of the slot, it allows sufficient area for the loading of diodes and capacitors. In addition, by controlling the extension direction of the slot, the amount of current fed into the EBG #1 can be controlled.

In order to observe the effect of W_{ebg1} on the microstrip line's reflection, the state of *S1* is set to ON with g = 0.2 mm. According to Eq. (4), the W_{ebg1} corresponding to 2.45 GHz is predicted to be approximately 8 mm. Therefore, the scanning range of W_{ebg1} is selected to be 4-10 mm. As shown in Fig. 4, when W_{ebg1} = 5 mm, the antenna can generate the rejected frequency of 2.45 GHz. Due to the neglect of edge effects in formulas (1) and (2), the estimated W_{ebg1} is larger than the actual one. Then, the state of *S1* is switched to OFF to observe whether the EBG #1 is still coupled to the microstrip line when the circuit is open. Obviously, in this case, the impact of EBG #1 can be ignored.

Figures 5 (a) and (b) compare the current distribution on the back of the antenna before and after etching the L-shaped slot. It can be observed that as the current converges toward the L-shaped slot, it does indeed serve to guide the current.

C. Antenna design by loading EBG #2

Considering that the EBG cell needs to be coupled with sufficient current to better achieve frequency rejecting, it is hard to achieve high-frequency of WLAN filtering by reducing the size of the EBG # 1 further. And it is necessary to consider the welding interval and difficulty issues between the processed SMA connector and

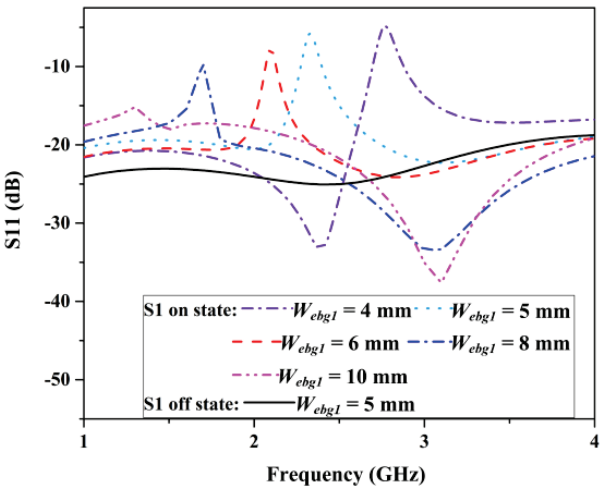

Fig. 4. S_{11} changes of the patch antenna with or without EBG #1 at different W_{ebg1}.

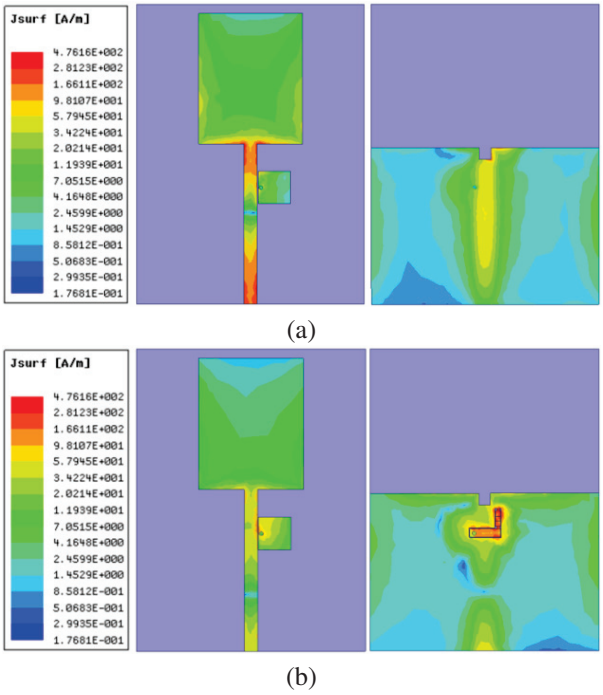

Fig. 5. The current distribution on the back of the antenna before and after etching the L-shaped slot at a resonant frequency of 2.45 GHz: (a) before grooving and (b) after grooving.

EBG and capacitor components. Therefore, the EBG # 2 is placed on the back of the antenna patch, as shown in Fig. 6. It is connected to the feeder through *S2* and uses the conductivity of the microstrip line as a ground.

Figure 7 shows the effect of EBG #2 size parameters W_{ebg2} and L_{ebg2} (with d_1 = 2.8 mm and a_1 = 1.8 mm) on the antenna's notch frequency. When L_{ebg2} = 0.5 mm, it can be observed that the filtered frequency

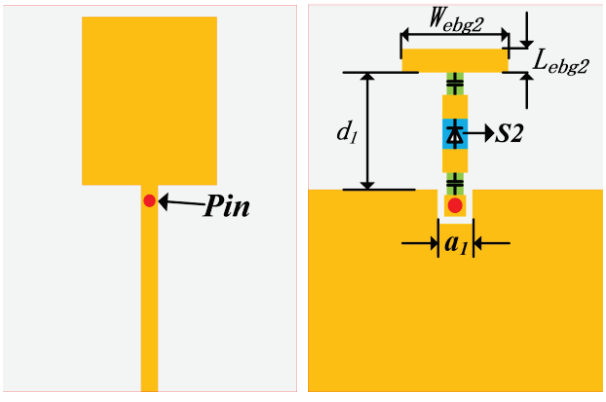

Fig. 6. The structural diagram of the antenna loaded EBG #2 from (a) top view and (b) back view.

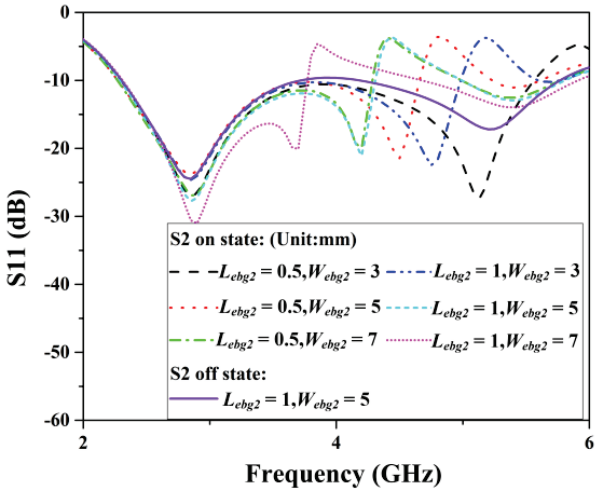

Fig. 7. S_{11} changes of the patch antenna with or without EBG #2 at different W_{ebg2} and L_{ebg2}.

will shift toward lower frequencies as W_{ebg2} increases. A similar phenomenon also occurs when L_{ebg2} increases. When *S2* is in the OFF state, it can be seen that the antenna operates in the high-frequency range of 4.2-5.76 GHz. Like the EBG #1, the EBG #2 will not interfere with the operation of the antenna itself in this state.

Figure 8 shows the influence of d_1 on the S_{11} of the monopole antenna with EBG #2. It can be observed that when d_1 increases from 2.8 mm to 3.2 mm, the center frequency of the notch band decreases from 5.15 GHz to 5 GHz, with a slight change, indicating that d_1 has little effect on the antenna.

The optimized parameters are shown in Table 1.

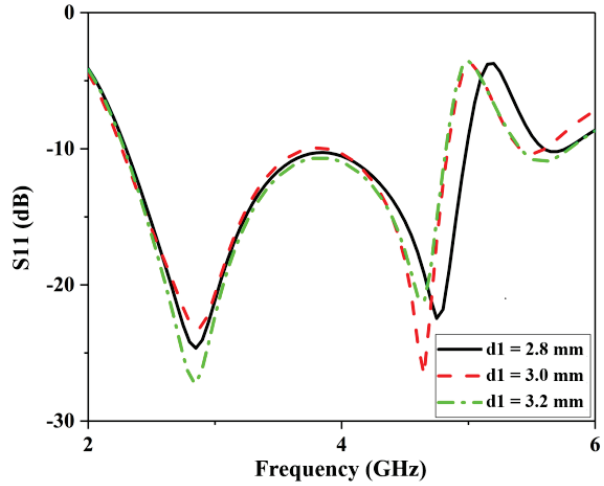

Fig. 8. S_{11} of the patch antenna with EBG #2 at different d_1.

Table 1: Optimized parameters of the EBG units (unit: mm)

Parameter	Value	Parameter	Value
W_{ebg1}	5	a_1	1.8
W_{ebg2}	3	R_1	0.25
L_{ebg2}	1	R_2	0.3
g_s	0.1	L_s	1.45
W_s	4.9	d_1	2.8

For convenience, the different state combinations of *S1* and *S2* are represented by F1, F2, and F3, which are listed in Table 2.

Table 2: Symbols of switches in different states

Symbols	Diode Status	
	S1	S2
F1	OFF	OFF
F2	OFF	ON
F3	ON	OFF

III. MEASURED RESULTS AND DISCUSSION

The proposed antenna is fabricated and measured as shown in Fig. 9. Considering that DC regulated power supply is an existing equipment in the laboratory, it has the function of a switching power supply and can provide stable and adjustable voltage. Therefore, for ease of testing, we use DC instead of batteries to power the bias circuit. Due to the fact that the diodes of the proposed antenna will not be in the ON-ON states in the experiment, only one DC is needed to power two PIN diodes separately to test the performance of the antenna in three states. When testing S_{11}, a 1 V stabilized power supply was connected to the bias circuit of the antenna, so the impact of the bias circuit on the antenna performance was tested.

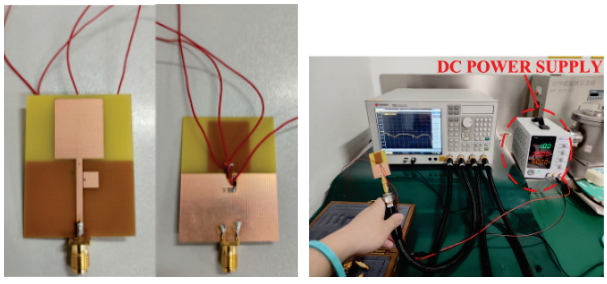

(a) (b)

Fig. 9. Photograph of the fabricated antenna: (a) Physical photos of the antenna and (b) photos of the testing environment.

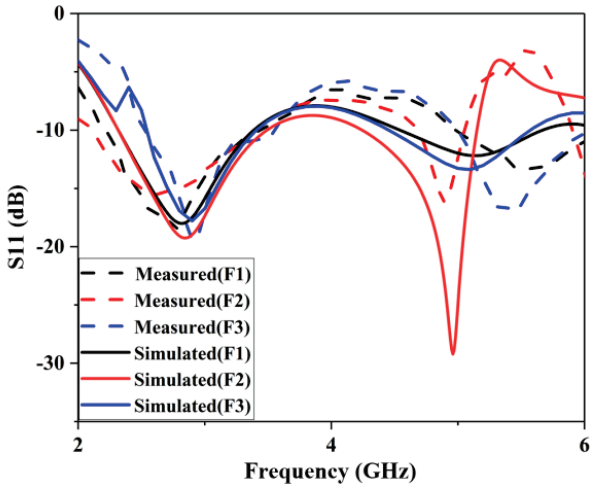

Fig. 10. Comparisons between the simulated and measured S_{11} of the proposed antenna in different switching states.

The comparisons of the simulated and measured S_{11} in F1, F2, and F3 states are shown in Fig. 10. The measured results show that in F1 state (the diodes in OFF-OFF state), the antenna operates in two frequency bands: 2.2-3.7 GHz and 4.8-6 GHz; In F2 state, the antenna can generate a notch band of 5.11-5.51 GHz, which belongs to the high-frequency of the WLAN; In F3 state, the antenna can generate a notch of 2.3-2.49 GHz, covering the low-frequency of the WLAN. Although there are some differences between the simulation and test results, which may be due to the fabrication tolerance and welding of the switch, they are generally consistent.

The simulated and measured peak gains of the antenna in different switching states are shown in Fig. 11. It can be seen that the low-frequency peak gain and high-frequency peak gain of the antenna in F1 state are 2.5 dBi and 3.3 dBi, respectively. The gain of the antenna within the two WLAN filtering frequencies is as low as -2.65 dBi and -4.65 dBi, respectively, indicating that the antenna can effectively suppress the gain in the notch frequency bands.

Figures 12, 13, and 14 show the two-dimensional radiation patterns of the proposed antenna at resonance frequencies of 2.8 GHz and 5.25 GHz, 2.8 GHz and 4.8 GHz, and 2.8 GHz and 5.25 GHz in different switching states. In these three states, the co-polarization and cross-polarization ratios exceed 21 dB, 27 dB, and 21 dB, respectively. As the figures show, the omnidirectional radiation characteristics are observed in the E and H planes.

The performance comparison between the proposed antenna and other antennas in references [15–18] is

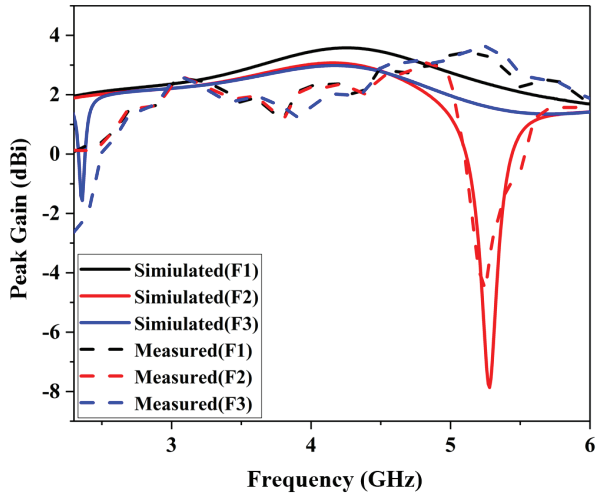

Fig. 11. Comparisons between the simulated and measured peak gains of the proposed antenna in different switching states.

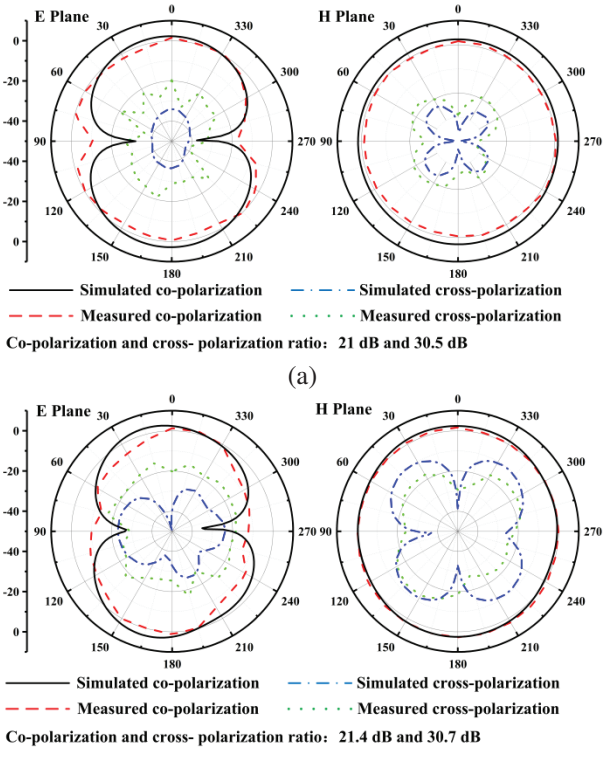

Fig. 12. Simulated and measured radiation patterns at frequencies of (a) 2.8 GHz (with status F1) and (b) 5.25 GHz (with status F1).

listed in Table 3. The results show that the filtering frequency of the antenna covers the two frequency bands of WLAN, and has a relatively small size and low gain in the notch band, demonstrating a better performance.

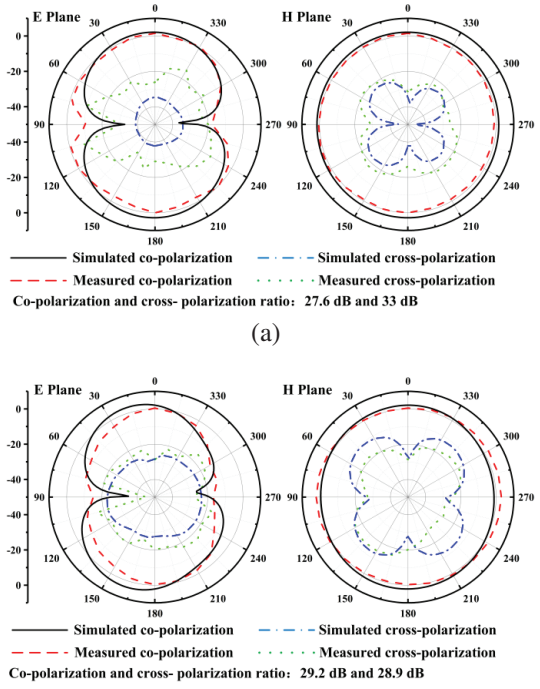

Fig. 13. Simulated and measured radiation patterns at frequencies of (a) 2.8 GHz (with status F2) and (b) 4.8 GHz (with status F2).

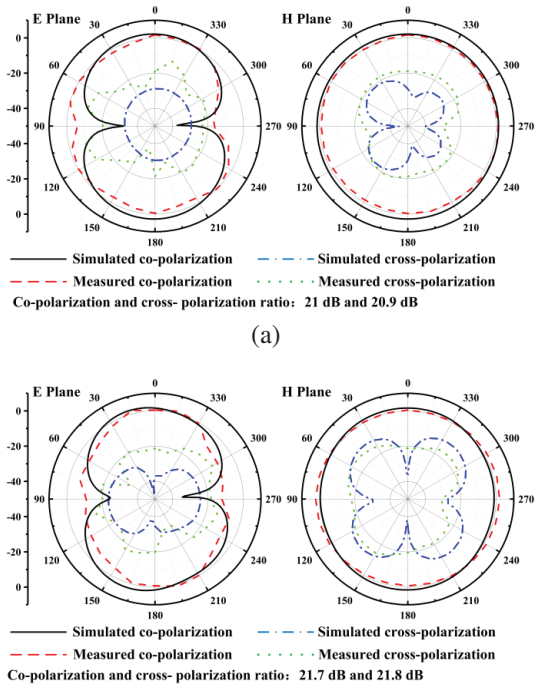

Fig. 14. Simulated and measured radiation patterns at frequencies of (a) 2.8 GHz (with status F3) and (b) 5.25 GHz (with status F3).

Table 3: Comparisons with the other EBG notch-band antennas

Ref.	Size (mm^3)	Notch Band Controllability	No. of EBGs	Notched Band (GHz)	Realized Gain (dBi)
15	$62.5 \times 100 \times 1.52$	YES	6	1.1, 1.59, 2.17, 2 .76, 3.25, 3.88	$-20, -19$
16	$50 \times 80 \times 1.6$	YES	2	$3.625 - 4.2$	-0.9
17	$42 \times 50 \times 1.6$	YES	2	4	-2.9
18	$38 \times 47 \times 0.8$	No	2	3.3, 5.72, 8.32	$-0.9, -3, -0.1$
Proposed Antenna	$35 \times 46 \times 0.8$	YES	2	$2.3 - 2.49, 5.11 - 5.51$	$-2.65, -4.55$

IV. CONCLUSION

A dual broadband monopole antenna with a bias circuit and PIN diode based on EBG structure and a notch reconfigurable function is proposed. The two mushroom-shaped EBGs are placed at the edge of the feeder and behind the radiation patch, making full use of the available space of the antenna. By controlling the ON/OFF state of the diodes through the paranoid circuit, the band-notched reconfigurable function of the two bands can be realized. The measured results show that the proposed antenna can operate in three states: OFF–OFF, OFF–ON, and ON–ON. When PIN diodes are in the OFF–OFF states, the antenna can operate at frequencies of 2.2-3.7 GHz and 4.8-6 GHz, with a peak gain of 2.5 dBi and 3.3 dBi, respectively. When PIN diodes are in the OFF–ON states, a notched band of 5.11-5.51 GHz is generated with a realized gain as low as -4.55 dBi. When PIN diodes are in the ON–ON states, a notched band of 2.3-2.49 GHz is generated, and the realized gain of the antenna in the notched band is -2.65 dBi. This antenna is applicable for band notch broadband communication systems.

ACKNOWLEDGMENT

The authors wish to acknowledge the support of the Jiangxi Provincial Department of Education Project (GJJ2200622).

REFERENCES

[1] M. Yazdi and N. Komjani, "Design of a band-notched UWB monopole antenna by means of an EBG structure," *IEEE Antennas And Wireless Propagation Letters*, vol. 10, pp. 170-173, Mar. 2011.

[2] X. Zhang, H. Xu, Y. Xie, and Q. Wu, "A dual band-notched antenna for UWB applications," *Progress in Electromagnetics Research Letters*, vol. 96, pp. 105-111, Feb. 2021.

[3] J. Liu, Z. Tang, and Y. Yin, "A differential CPW-fed ultra-wideband antenna with dual notched bands," *Applied Computational Electromagnetics Society (ACES) Journal*, vol. 33, no. 6, pp. 610-615, June 2018.

[4] S. Palanisamy and B. Thangaraju, "Design and analysis of clover leaf-shaped fractal antenna integrated with stepped impedance resonator for wireless applications," *International Journal of Communication Systems*, vo. 35, no. 11, pp. 1-18, July 2022.

[5] C. G. Hynes and R. G. Vaughan, "Conical monopole antenna with integrated tunable notch filters," *IEEE Antennas And Wireless Propagation Letters*, vol. 19, no. 12, pp. 2398-2402, Dec. 2020.

[6] H. Su, L. L. Wu, Y. Zhang, J. Zhang, H. L. Xu, and X. Y. Zhang, "Circuit modeling and parameter extracting of a filtering series-fed antenna," *IEEE Transactions on Microwave Theory and Techniques*, vol. 71, no. 4, pp. 1640-1653, Apr. 2023.

[7] Y. J. Guo, K. D. Xu, and X. H. Tang, "Multi-functional ultra-wideband monopole antenna with high frequency selectivity," *Applied Computational Electromagnetics Society (ACES) Journal*, vol. 33, no. 1, pp. 37-42, Jan. 2018.

[8] W. A. E. Ali and A. A. Ibrahim, "Tunable band-notched UWB antenna from WLAN to WiMAX with open loop resonators using lumped capacitors," *Applied Computational Electromagnetics Society (ACES) Journal*, vol. 33, no. 6, pp. 603-609, June 2018.

[9] A. V. Golliwar and M. S. Narlawar, "Multiple controllable band notch antenna for UWB cognitive radio application," *International Conference on Signal Processing and Integrated Networks*, Noida, pp. 694-697, Feb. 2016.

[10] S. Peddakrishna, V. Kollipara, J. Kumar, and T. Khan, "Slot and EBG-loaded compact quad band-notched UWB antenna," *Iranian Journal of Science and Technology, Transactions of Electrical Engineering*, vol. 46, pp. 205-212, Oct. 2022.

[11] S. Modak, T. Khan, and R. H. Laskar, "Penta-notched UWB monopole antenna using EBG structures and fork-shaped slots," *Radio Science*, vol. 55, issue. 9, pp. 1-11, Sep. 2020.

[12] L. Peng and C. Ruan, "UWB Band-notched monopole antenna design using electromagnetic-bandgap structures," *IEEE Transactions on Microwave Theory and Techniques*, vol. 59, no. 4, pp. 1074-1081, Apr. 2011.

[13] P. P. Bhavarthe, S. S. Rathod, and K. T. V. Reddy, "A compact dual band gap electromagnetic band gap structure," *IEEE Transactions on Antennas and Propagation*, vol. 67, no. 1, pp. 596-600, Jan. 2019.

[14] L. Peng, B. Wen, X. Li, X. Jiang, and S. Li, "CPW fed UWB antenna by EBGs with wide rectangular notched-band," *IEEE Access*, vol. 4, pp. 9545-9552, Dec. 2016.

[15] A. Abbas, N. Hussain, J. Lee, S. G. Park, and N. Kim, "Triple rectangular notch UWB antenna using

EBG and SRR," *IEEE Access*, vol. 9, pp. 2508-2515, Jan. 2021.

[16] H. A. Majid, A. Rahim, M. R. Hamid, N. A. Murad, N. A. Samsuri, M. F. M. Yusof, and O. Ayop, "Reconfigurable notched wideband antenna using EBG structure," *Microwave and Optical Technology Letters*, vol. 57, pp. 497-501, Feb. 2015.

[17] H. A. Majid, M. K. A. Rahim, M. R. Hamid, N. A. Murad, N. A. Samsuri, M. F. M. Yusof, and M. R. Kamarudin, "Band-notched reconfigurable CPW-fed UWB antenna," *Applied Physics A*, vol. 122, no. 347, pp. 1-6, Mar. 2016.

[18] A. S. Elkorany, H. A. Mohamed, Z. F. Elsharkawy, and D. A. Saleeb, "Heart shaped reconfigurable band-notched ultra-wide band antenna using electromagnetic band-gap structure and varactor diodes," *Analog Integrated Circuits and Signal Processing*, vol. 105, pp. 385-393, Aug. 2020.

[19] V. R. Kapure and S. S. Rathod, "A two element EBG-inspired UWB MIMO antenna with triple band notched characteristics and high isolation," *Sadhana-Academy Proceedings in Engineering Sciences*, vol. 48, no. 7, pp. 1-16, Jan. 2023.

[20] D. F. Sievenpiper, "High-impedence electromagnetics surfaces," Ph.D. dissertation, UCLA, 1999.

Xianyan Zhang received the B.S. degree in applied physics and M.S. degree in physical electronics from Yunnan University, Kunming, China, in 2001 and 2004, respectively, and the Ph.D. degree in electromagnetic field and microwave technology from Institute of Electronics, Chinese Academy of Sciences in 2007. Her research interests include electromagnetic computation, antenna design, and wireless power transmission structure design.

Ziao Li was born in 2000 in Guixi City, Jiangxi Province, China. He obtained a bachelor's degree in engineering from the School of Science and Technology of East China Jiaotong University and is currently studying at the School of Information Engineering of East China Jiao Tong University. His main research direction is antenna design

Aiyun Zhan was born in Nantong, Jiangsu, China in 1973. She received the B.S. degree from Southwest Jiaotong University in 1997, and rhe M.S. degree in East China Jiaotong University in 2008. She is currently working at the School of Information Engineering, East China Jiaotong University. Her research interests focus on channel coding and optical communication.

Yan Mei obtained a bachelor's degree in communication engineering from the School of Information and Communication, National Defense University of the People's Liberation Army of China in 2002, and a master's degree in computer science and technology from East China Jiaotong University in 2009. Research interests include wireless communication and deep learning.

CPW-Fed UWB-MIMO Antenna with Triple-band Notched and High Isolation using Double Y-shaped Decoupling Structure

Chenzhu Du and Huanchen Peng

Department of Electronics and Information Engineering
Shanghai University of Electric Power, Shanghai 200090, China
duchengzhu@163.com, 1106492100@qq.com

Abstract **–** A ultra-wideband (UWB) multiple-input-multiple-output (MIMO) antenna using double Y-shaped decoupling structure with high isolation and triple notched-band is presented. The designed antenna composed of two orthogonally placed monopole elements, coplanar ground and double Y-shaped branch. The defected substrate structure is used to achieve miniaturization. By slotting successively C-shaped slot, semicircular slot and rectangular slot on the radiation patch and the ground, achieved three notched bands at 3.5 GHz WiMAX, 5.25 GHz WLAN, and 7.5 GHz X-band. The proposed antenna can operate in range of 2.56-12 GHz with triple notched bands of 3.31-3.96 GHz, 4.58-5.67 GHz and 6.57-8.16 GHz. Considering all the results, it can be concluded that the antenna presented has a great performance in terms of good radiation, high isolation ($>$24 dB), a low level ECC ($<$0.01) and a high DG level ($>$9.99), which proves the presented antenna has good prospect in UWB-MIMO systems.

Index Terms **–** band-notched, DGS, defected substrate structure, high isolation, MIMO, SRR.

I. INTRODUCTION

Many scholars have studied ultra-wideband (UWB) technology for many years because by using this technology, wireless communication can be greatly improved in channel capacity and quality without having to increase the transmission power or spectrum. Although UWB technology has the advantages mentioned above, the application of UWB technology in other fields is limited because of its short transmission distance and limited signal transmission rate. Integration of UWB technology and multiple-input-multiple-output (MIMO) technology can overcome these shortcomings. MIMO antenna integrates at least two antenna elements on a dielectric substrate. Due to the limitation of substrate size, the two elements will be coupled with each other when they are close.

UWB covers the working bands of systems including WiMAX (3.3-3.7 GHz), WLAN (5.15-5.35 GHz), X-band (7.25-7.75 GHz) and so on. When UWB antenna works, it is easy to interfere with the above-mentioned systems, so suppressing overlapping band signals has become a research hotspot. The most effective method is to fabricate a UWB antenna with notched functions. [1–5] all achieve ultra-wide band. However, it is difficult and challenging to design an UWB-MIMO antenna that is small, has good anti-interference capabilities, a low coupling, and multiple notch characteristics.

Recently, MIMO technology has received a great attention. When MIMO technology is used in antenna design, it can help antennas achieve a high transmission rate and a stable transmission reliability. With MIMO technology, the signal is transmitted in multiple channels, thereby reducing multipath fading and increasing transmission capacity [6]. Many UWB-MIMO antennas are proposed in [6–22]. A circularly polarized MIMO antenna is designed in [6]. Although the impedance bandwidth is from 3.1-13.5 GHz, the antenna has a narrow axial ratio bandwidth from 4.7-6.1 GHz and is susceptible to be interfered by other useful bands. The slit slot is etched to improve isolation. In [7], a novel decoupling is used to improve isolation, which inter-element isolation is over 25 dB, but the function of notch is not realized. In [8], to get the notched-band characteristic a T-shaped slot is added; but it only realizes a notched band at 5.2 GHz, and the isolation just blow -15 dB. [9] proposed a MIMO antenna with the isolation higher than 20 dB. Loading a complementary CSRR produces two notched bands. [10] proposed a UWB-MIMO antenna which has two notch bands in 3.1-4.8 GHz and 5.1-6.3 GHz. The isolation which is enhanced by T-shape stubs is all better than 20 dB in the whole bands. [11] proposed an asymmetric coplanar strip fed MIMO antenna with two notched bands at WiMAX band and WLAN band. In [12], an increased level of isolation is achieved by introducing a defected ground structure. In order to generate triple notched bands, a C-shaped slot is introduced in the antenna, but the isolation is only less than 15 dB at working bands. Moreover, some three-notched bands antennas with microstrip feed are proposed in literatures

Submitted On: June 4, 2023
Accepted On: November 26, 2023
https://doi.org/10.13052/2023.ACES.J.381109

[23–28]. The different EBG structures are used to realize three notched bands at WiMAX, X Band, and WLAN in [23, 24]. In [25], a novel 4-element UWB antenna was presented with three notch-band characteristics, and the orthogonal separated trapezoidal structure is used to enhance isolation. In [26], A MIMO antenna with three notches is designed, three notched bands are at 4.56, 7.25, and 9.08 GHz with great isolation of -22 dB. In [27], a UWB-MIMO antenna with three L-shaped slots is presented. In [28], a 4×4 UWB-MIMO antenna is designed with three notch frequencies at 3.72, 5.53 and 8.2 GHz.

This paper presents a CPW-fed UWB-MIMO antenna with a triple notched band and a double Y-shaped decoupling structure. There are two orthogonally placed monopole elements and a Y-shaped branch in this antenna. In summary, the innovations of the proposed antenna are as follows:(1) The defected substrate structure helps to achieve miniaturization;(2) The antenna has a filtering performance. The simulation and experiment results indicated that the antenna proposed in this paper could operate form 2.56-12 GHz except three notched bands from 3.31-3.96 GHz, 4.58-5.67 GHz, and 6.57-8.16 GHz;(3) The double Y-shaped stub is introduced to improve the isolation between the antenna ports better than 24 dB;(4) The coplanar waveguide (CPW) feeder is easy to be integrated in applications.

II. ANTENNA DESIGN AND ANALYSIS

A. Antenna Structure

The MIMO antenna design structure and physical photograph are shown in Fig. 1, it composed of two orthogonal circular monopole elements with tapered feed line, coplanar ground and Y-shaped branch. Firstly, the proposed antenna is fabricated on a 50×50×0.8 mm^3 FR-4 square substrate, with a dielectric constant = 4.4, and loss tangent = 0.02. Then, the substrate is cut to minimize the size of antenna (the reduced size is 31.04 % of the original size). By etching slots on the radiation patch and ground, triple notched bands are achieved. The slot length of L is usually $\lambda/2$ or $\lambda/4$, the formula is as follows in [30, 31]:

$$L = \frac{C}{2f_{center}\sqrt{\varepsilon_{eff}}}, \tag{1}$$

$$\varepsilon_{eff} = \frac{\varepsilon_r + 1}{2} + \frac{\varepsilon_r - 1}{2}\left(1 + \frac{12h}{w_f}\right)^{-0.5}, \tag{2}$$

where C means the light speed, *fcenter* denotes the center frequency of the notch band, and εeff represents the effective value of the dielectric constant. h is the thickness of the substrate. Wf and εr are the width of feeder and relative dielectric constant of substrate. Detailed dimensions of designed MIMO antenna can be seen in Table 1.

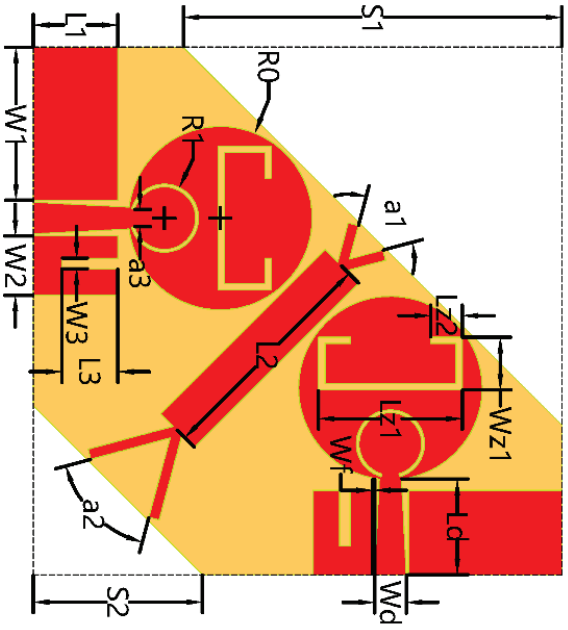

(a)

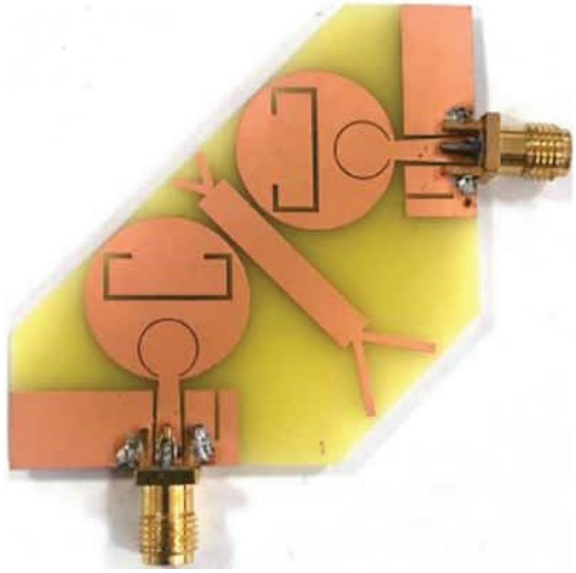

(b)

Fig. 1. Structure of the antenna: (a) Geometry of the antenna, (b) physical photograph of the antenna.

Table 1: Detailed dimensions of proposed antenna(mm)

L 1	***L 2***	***L3***	***L d***	***S1***
8	22	5.3	9.1	36
S2	***LZ1***	***LZ2***	***W1***	***W2***
16	13.6	3	14.5	5.6
W3	***WF***	***WD***	***WZ1***	***WZ2***
0.5	0.2	3	5	0.6
R0	***R1***	***a1***	***a2***	***a3***
8.7	3	60	57	1.6

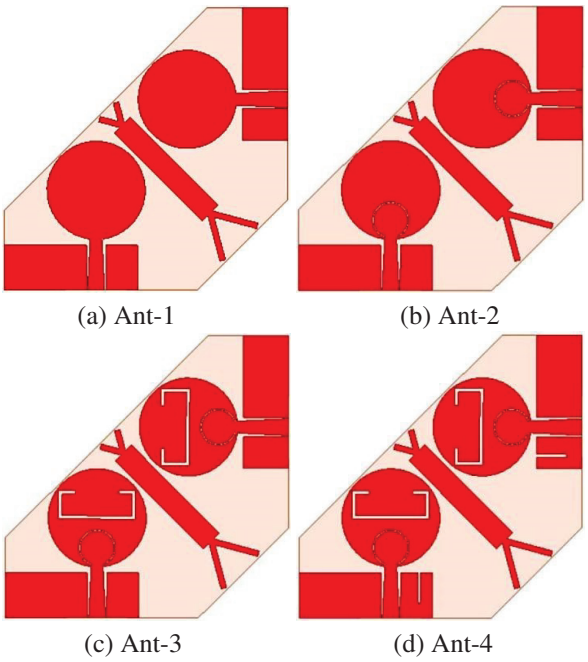

(a) Ant-1 (b) Ant-2

(c) Ant-3 (d) Ant-4

Fig. 2. Design process of notched band MIMO antenna.

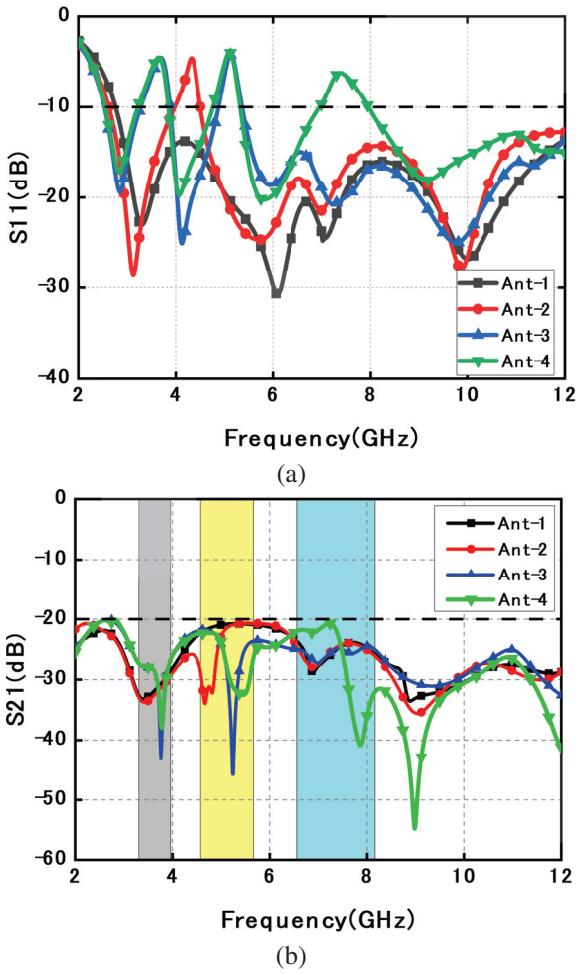

(a) (b)

Fig. 3. Effects of different slots on S-parameters: (a) S_{11}, (b) S_{21}.

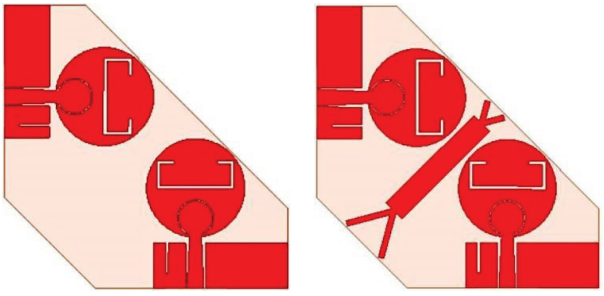

(a) (b)

Fig. 4. Diagram of the schematic: (a) Without branch, (b) with branch.

B. Design process

HFSS-18 is used to design the proposed antenna. Figure 2 depicts the designed triple notched-band antenna. By adding slots on the ultra-bandwidth MIMO antenna, three notched bands are generated. The simulated S_{11} and S_{21} of four different antennas were shown in Fig. 3.

The S_{11} of Ant-1 without slot is from 2.6 -12 GHz. In Ant-2, a notched band is generated from 3.98-4.70 GHz by adding an annular slot on the radiation patch. The notch frequency is set at 4.5 GHz. According to the formula (1) and (2), the approximate length of the annular slot is 40 mm. In Ant-3, another notch frequency is set at 3.3 GHz and the approximate length of the rectangular slot is 60 mm. Two slots interact with each other. Finally, two notched bands are generated from 3.11-3.79 GHz and 4.97-5.02 GHz by introducing C-shaped slot and rectangular slot on the radiation patch. By adding a rectangular slot on the ground of Ant-3, Ant-4 generates three notch frequencies from 3.11-3.79 GHz, 4.97-5.15 GHz and 6.80-7.97 GHz. At the same time, the S_{21} of all four antennas is less than -20 dB from 2.6 -12 GHz, which show all antennas have good performance.

C. Analysis of decoupling structure

A double Y-shaped branch is designed as an isolator in this paper. The antenna with and without double Y-shaped branch are shown in Fig. 4, and the influence of double Y-shaped structure on simulated S-parameter is shown in Fig. 5. The S_{21} of antenna without branch is less than -17 dB at all working bands, and the S_{21} of antenna with branch is below than -20 dB from 3-12 GHz, which show the branch is useful to enhance isolation.

To understand the decoupling mechanism of the Y-shaped structure, Fig. 6 indicates the current distribution

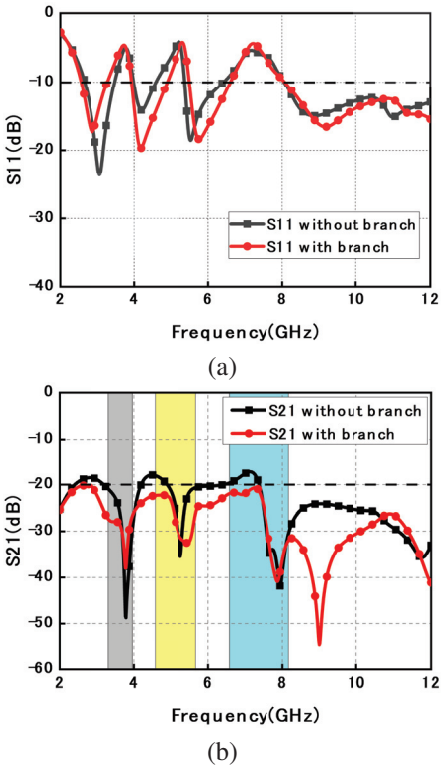

Fig. 5. Effects of branch on S-parameters: (a) S_{11} and (b) S_{21}.

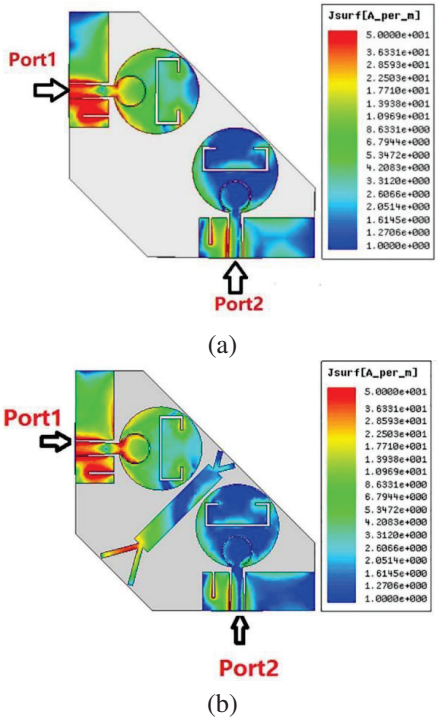

Fig. 6. Surface current distributions at 7 GHz when Port 1 acts as the exciter and Port 2 connects 50 Ω load: (a) Antenna with branch and (b) antenna without branch.

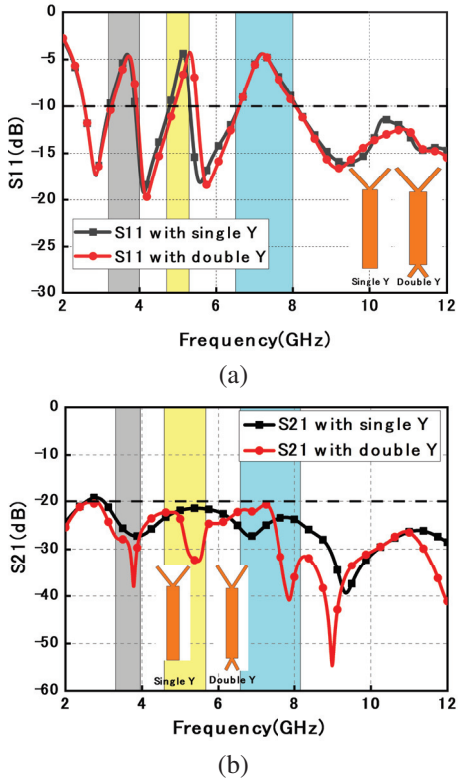

Fig. 7. The S-parameters with single and double Y-shaped branch: (a) S_{11}, (b) S_{21}.

of antenna with branch and without branch at 7 GHz. In Fig. 6 (a), the current flows directly from one port to another, which leads to poor independence between antenna units. The coupling current of another antenna element can be reduced effectively, when the double Y-shaped structure is added in Fig. 6 (b).

Figure 7 shows simulated S-parameters of the antenna with single and double Y-shaped branch. In terms of S_{11}, the middle notch band is more accurate to filter 5.25 GHz WLAN. The S_{21} of antenna with single Y-shaped branch is less than -20 dB except the band of 2.24-3.06 GHz. In addition, the S_{21} of the antenna with double Y-shaped branch is less than -20 dB at all working bands, and the decoupling effect is more obvious with S_{21} less than -30 dB within 7.45-9.25 GHz.

Simulated results of S_{11} and S_{21} with different lengths of *L2* can be known in Fig. 8. *L2* means the length of double Y-shaped structure, the change of *L2* mainly affects the intermediate notched band. When the value of *L2* is 22 mm, the intermediate notched band is wider than others, and S_{21} is less than -20 dB from 2-12 GHz.

D. The influence of slots

To further understand the influence of slots on antennas, Fig. 9 indicates the current distribution of the

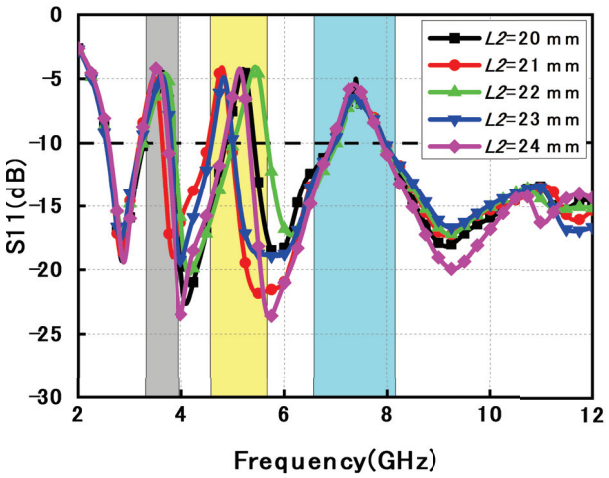

(a)

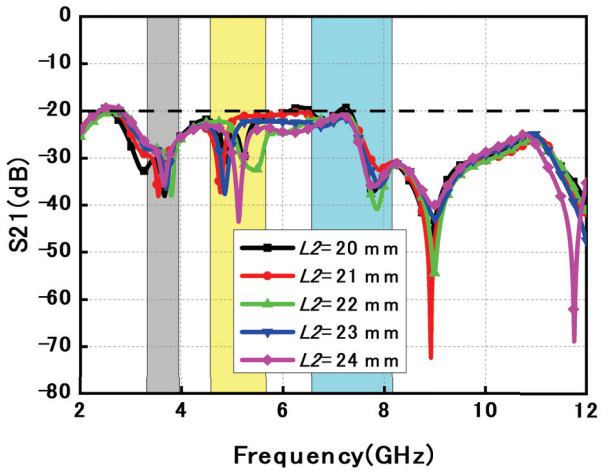

(b)

Fig. 8. Simulated of different parameters: (a) S_{11} and (b) S_{21}.

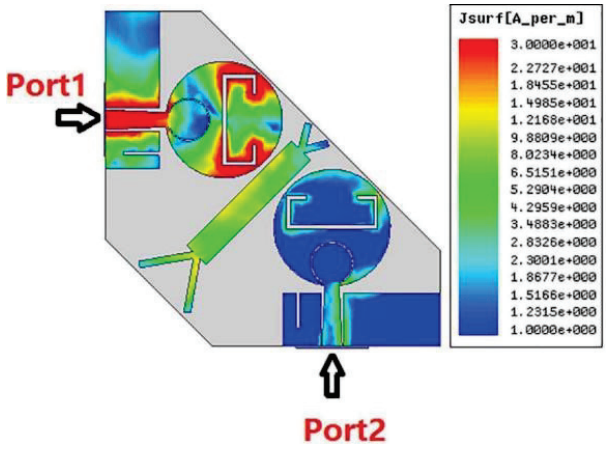

(a)

Fig. 9. *Continued.*

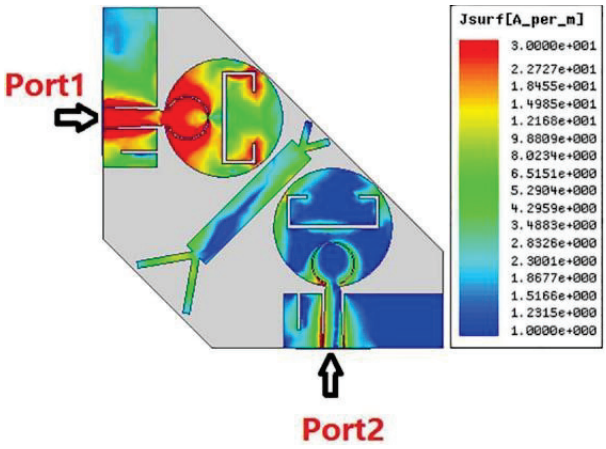

(b)

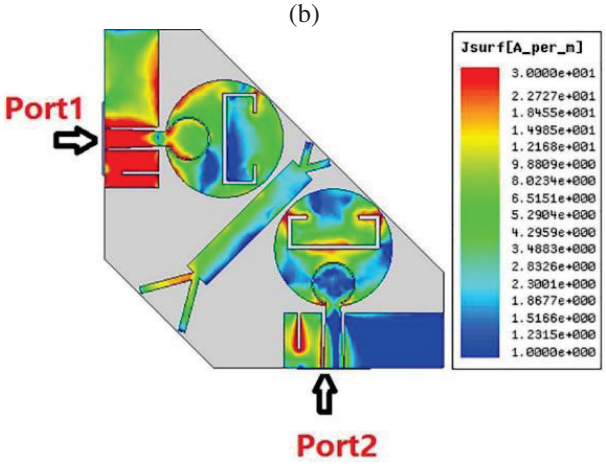

(c)

Fig. 9. Simulated surface current distribution when Port 1 acts as the exciter: (a) 3.4 GHz, (b) 5.25 GHz, and (c) 7.5 GHz.

antenna at notched band center frequencies of 3.4, 5.25 and 7.5 GHz. In Fig. 9 (a), lots of current accumulates on the C-shaped slot which is added to generate a 3.4 GHz notch band. From Figs. 9 (b) and (c), annular slot and rectangular slot have the same effect as the C-shaped slot and produce 5.25 GHz notch band and 7.5 GHz notch band respectively.

III. RESULTS AND DISCUSSIONS

A. S-parameter

S-parameters were measured by an Agilent E8362B network analyzer. One port is excited during the measurement, while the other port is connected to 50-ohm load.

In Fig. 10, the measured S_{11} < -10 dB (or VSWR < 2) is from 2.56 to 12 GHz, except notched frequencies of 3.31-3.96 GHz, 4.58-5.67 GHz, and 6.57-8.16 GHz. Moreover, the measured S_{21} is lower than -24 dB in working band.

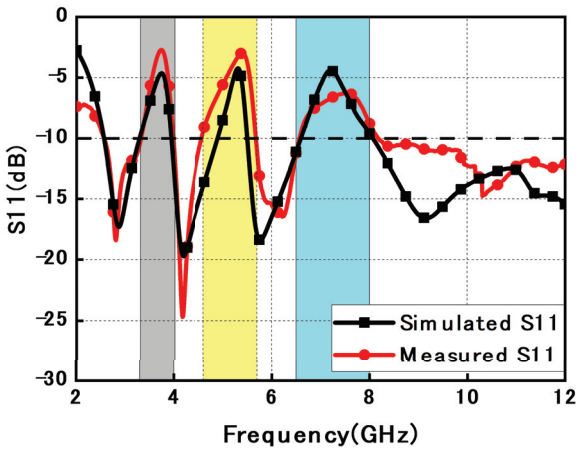

(a)

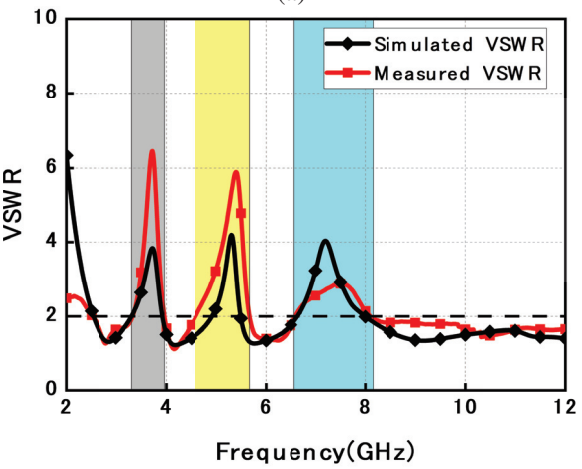

(b)

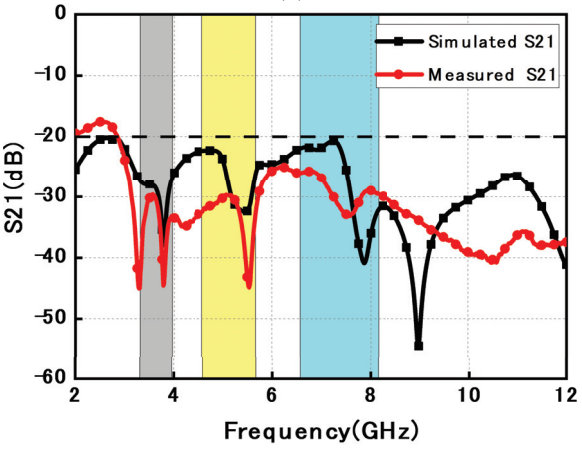

(c)

Fig. 10. Comparisons between simulated and measured values of S-parameters: (a) S_{11}, (b) VSWR, (c) S_{21}.

B. Radiation pattern

The antenna radiation pattern measurement of far field is shown in Fig. 11. Radiation patterns at 2.8 GHz, 4.1 GHz, 5.9 GHz, and 9.1 GHz are depicted in

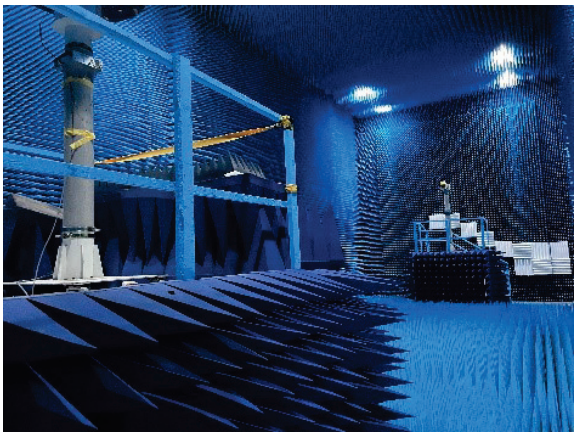

Fig. 11. Antenna far field measurement setup.

Fig. 12. The antenna exhibits omnidirectional radiation in H-plane and bidirectional radiation in the E-plane. At 9.1 GHz, the antenna's asymmetric ground produces a

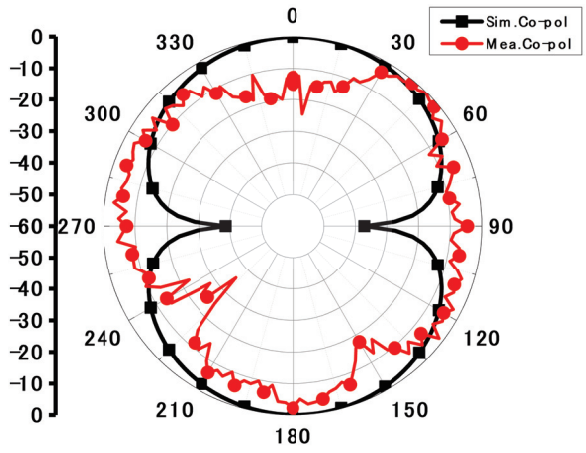

(a) E-plane at 2.8 GHz

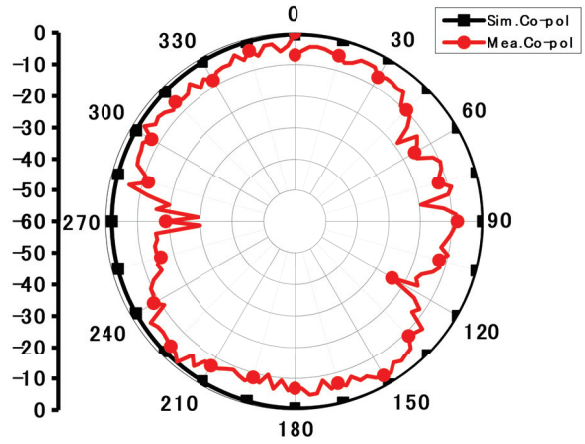

(b) H-plane at 2.8 GHz

Fig. 12. *continued*.

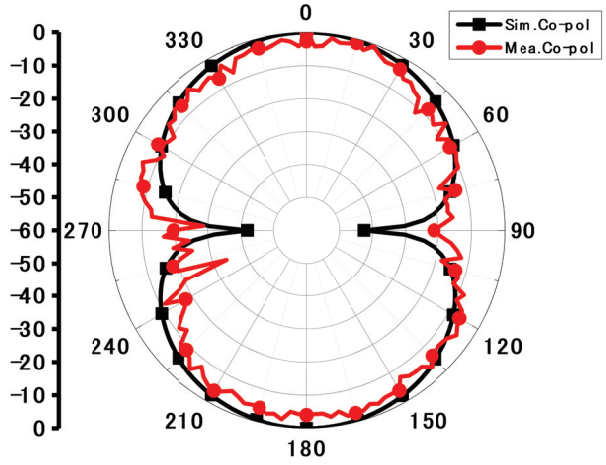

(c) E-plane at 4.1 GHz

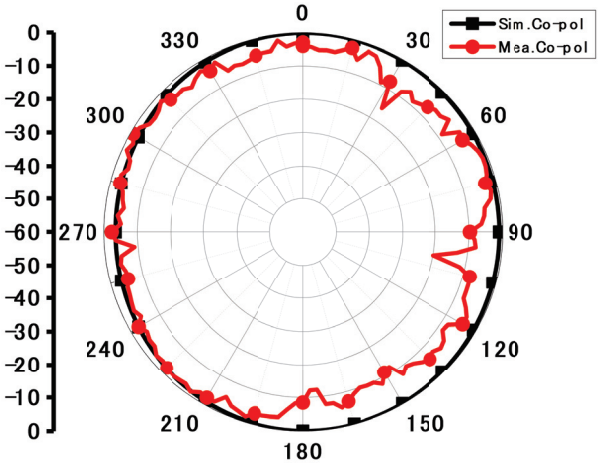

(d) H-plane at 4.1 GHz

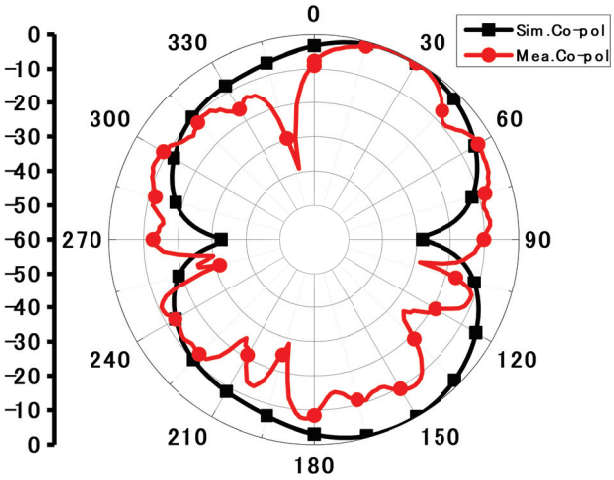

(e) E-plane at 5.9 GHz

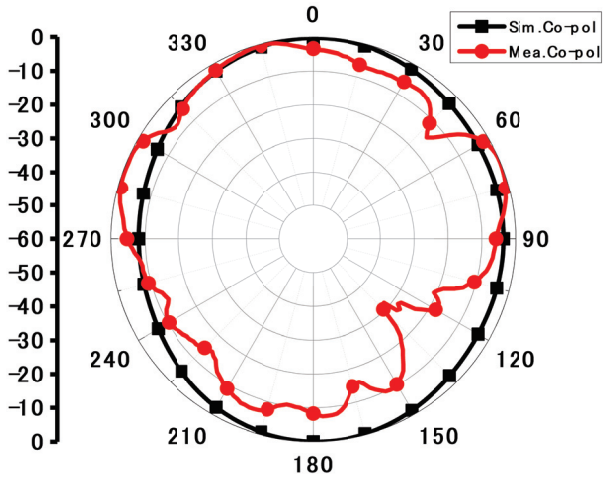

(f) H-plane at 5.9 GHz

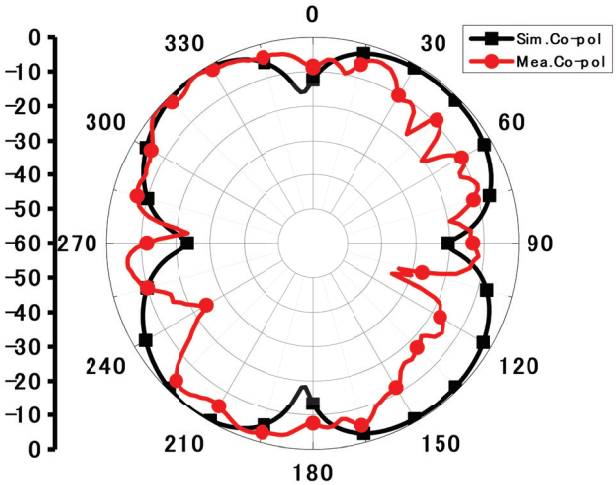

(g) E-plane at 9.1 GHz

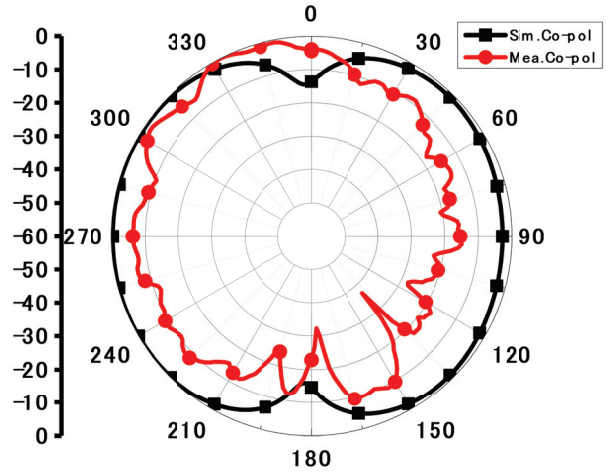

(h) H-plane at 9.1 GHz

Fig. 12. Radiation patterns.

slight distortion of the radiation pattern, but it does not influence its radiation performance.

C. Diversity Performance

The diversity characteristic is mainly determined by envelope correlation coefficient (ECC). ECC can effectively reflect the coupling degree between radiation patterns of different elements of the MIMO antenna. According to [12], a formula for ECC based on the S-parameter can be found in equation (3).

$$ECC = \left| \frac{S_{11}{}^{*}S_{12} + S_{21}{}^{*}S_{22}}{(\sqrt{1-|S_{11}|^2-|S_{21}|^2}) \cdot (\sqrt{1-|S_{22}|^2-|S_{12}|^2})} \right|. \quad (3)$$

The ECC is shown in Fig. 13 (a), which meets the requirement of port isolation for UWB MIMO antenna.

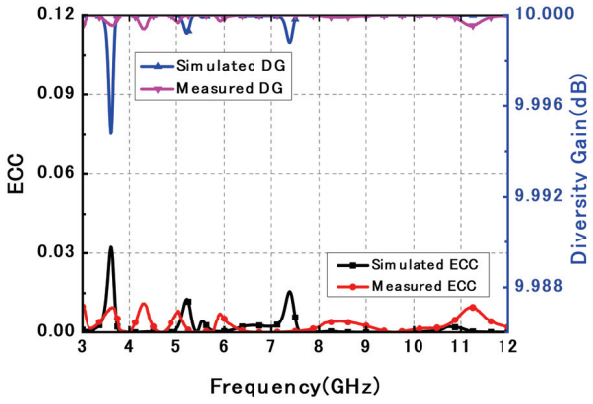

(a)

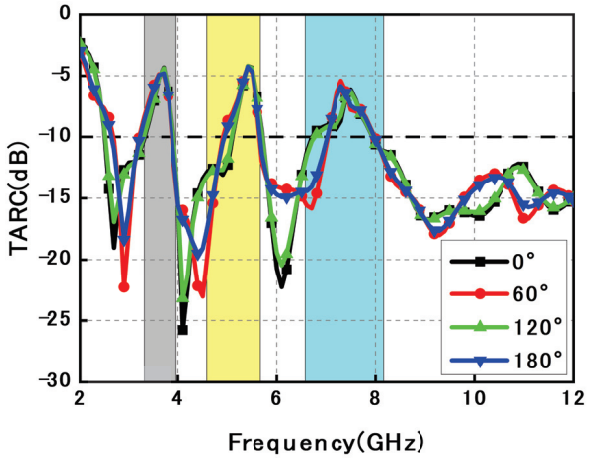

(b)

Fig. 13. Simulated or measured results. (a)ECC and DG. (b) TARC.

A closely related parameter to ECC is the diversity gain (DG). It is also a vital parameter. The formula is as follows:

$$DG = 10\sqrt{1-ECC^2}. \quad (4)$$

Figure 13 (a) depicts that the presented MIMO antenna has a great DG characteristic, which is greater than 9.99.

To predict the behavior of MIMO antenna systems, the total active reflection coefficient (TARC) is introduced. The simulated TARC is shown at Fig. 13 (b). The formula is expressed as:

$$TARC = \sqrt{\frac{(S_{11}+S_{12}e^{j\theta})^2+(S_{21}+S_{22}e^{j\theta})^2}{2}}. \quad (5)$$

D. Gain

Figure 14 indicates the gains of the MIMO antenna. The gain keeps stable from 2.5-12 GHz. Additionally, the gains at three rejected bands decrease dramatically.

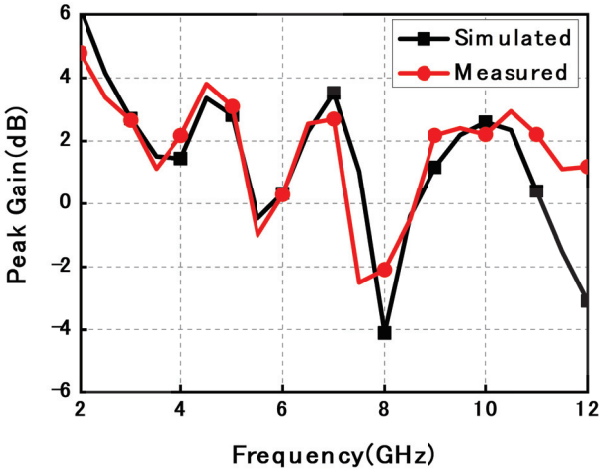

Fig. 14. Simulated and measured gain of MIMO antenna.

E. Comparison

Table 2 compares performance between proposed antenna and previous ones. Although [5–7] are designed with MIMO technology, they cannot filter interference band. And the presented antenna has more notched bands compared with references [8–11]. In comparison to other similar antennas reported in references [12 ,23–28], the presented antenna has a better isolation, wider bandwidth, lower ECC level and CPW feed.

Table 2: Performance comparison with previous antennas

Paper	Electrical Size (λ_0 is Calculated at lower band)	Antenna Size (mm^3)	Band-width (GHz)	Mutual Coupling (dB)	The Detailed Bands Notched (GHz)	Bands Notched	ECC	DG	Feeder Method
[5]	0.38×0.38	$38\times38\times1.6$	$3-20$	<-17	–	0	<0.08	9.97	CPW feed
[6]	0.26×0.52	$25\times51\times0.8$	$3.1-13.5$	<-18	-	0	<0.01	9.9	CPW feed
[7]	0.50×0.35	$50\times35\times1$	$3.0-11$	<-25	-	0	<0.004	-	Microstrip feed
[8]	0.33×0.26	$33\times26\times1.6$	$3-11$	<-15	$4.5-5.5$	1	<0.03	-	Microstrip feed
[9]	0.25×0.38	$24\times36\times1.6$	$3.1-13.4$	<-15	$5.15-5.8$ $8-12$	2	–	-	Microstrip feed
[10]	0.18×0.35	$18\times35\times1.6$	$2.3-12$	<-20	$3.1-4.8$ $5.1-6.3$	2	<0.035	-	CPW feed
[11]	0.35×0.35	$37\times37\times1.6$	$2.9-10.6$	<-15	$3.3-3.8$ $5.15-5.825$	2	<0.02	-	CPW feed
[12]	0.27×0.43	$27\times42\times1.6$	$3.1-11.5$	<-15	$3.3-3.7$ $3.7-4.2$ $5.15-5.85$	3	<0.015	9.99	CPW feed
[23]	0.14×0.24	$21\times36\times1.6$	$2-11$	<-15	$3.3-3.6$ $5-6$ $7.9-8.6$	3	<0.015	9.95	Microstrip feed
[26]	0.39×0.39	$39\times39\times1.57$	$3.1-10.6$	<-22	4.52-4.6, 7.02-7.49, $8.78-9.338$	3	<0.02	9.99	Microstrip feed
[27]	0.24×0.31	$21\times27\times0.8$	$3.1-11$	<-20	$3.3-3.75$ $5.07-5.95$ $7.6-8.6$	3	<0.04	-	Microstrip feed
[28]	0.58×0.58	$44\times44\times0.8$	$3.5-11$	<-23	3.72, 5.53 8.2	3	<0.008	-	Microstrip feed
This paper	0.42×0.30	$50\times36\times0.8$	$2.56-12$	<-24	$3.31-3.96$ $4.58-5.67$, $6.57-8.16$	3	<0.01	9.99	CPW feed

IV. CONCLUSION

Using a double Y-shaped decoupling structure, this paper introduces a CPW-fed UWB-MIMO antenna that exhibits triple notching characteristics and high isolation. Three notched bands of the antenna are realized by etching slots on the patch and coplanar ground. The proposed MIMO antenna has an ultra-wide band from 2.56-12 GHz with three notched bands which are from 3.31-3.96 GHz, 4.58-5.67 GHz and 6.57-8.16 GHz, and the measured isolation is all higher than 24 dB in whole bands. In addition, ECC are below 0.01 and DG is above 9.99. All the simulated and experiment results indicated that presented antenna is suitable in UWB field.

REFERENCES

[1] M. M. H. Mahfuz, M. R. Islam, M. H. Habaebi, N. Sakib, and A. K. M. Z. Hossain, "A notched UWB microstrip patch antenna for 5G lower and FSS bands," *Microwave and Optical Technology Letters*, pp. 796-802, Apr. 2022.

[2] M. Koohestani, N. Azadi-Tinat, and A. K. Skrivervik, "Compact slit-loaded ACS-fed monopole antenna for Bluetooth and UWB systems with WLAN band-stop capability," *IEEE Access*, pp. 7540-7550, Jan. 2023.

[3] D. Aissaoui, A. Chaabane, N. Boukli-Hacene, and T. A. Denidni, "Bandwidth enhancement of slot antenna using fractal shaped isosceles for UWB applications," *Applied Computational Electromagnetics Society (ACES) Journal*, Feb. 2023.

[4] M. B. Tayel, T. G. Abouelnaga, and N. M. Badran, "Localization of breast tumor using four elements UWB wearable antenna," *Applied Computational Electromagnetics Society (ACES) Journal*, vol. 37, no. 10, pp. 1021-1030, Mar. 2023.

[5] W. Yin, S. Chen, J. Chang, C. Li, and S. K. Khamas, "CPW fed compact UWB 4-element MIMO antenna with high isolation," *Sensors*, vol. 21, no. 8, p. 2688, Apr. 2021.

[6] L. Zhang, Q. Feng, and M. K. Khan, "Design of a novel circularly polarized MIMO antenna with

enhanced isolation for ultra-wideband communication," *Applied Computational Electromagnetics Society (ACES) Journal*, Nov. 2022.

[7] L. Wang, Z. Du, H. Yang, R. Ma, Y. Zhao, X. Cui and X. Xi, "Compact UWB MIMO antenna with high isolation using fence-type decoupling structure," *IEEE Antennas and Wireless Propagation Letters*, vol. 18, no. 8, pp. 1641-1645, Aug. 2019.

[8] G. Liu, Y. Liu, and S. Gong, "Compact uniplanar UWB MIMO antenna with band-notched characteristic," *Microwave and Optical Technology Letters*, vol. 59, no. 9, pp. 2207-2212, Sep. 2017.

[9] B. R. Rao, K. S. Chakradhar, and D. Nataraj, "Design, optimization and experimental verification of UWB-MIMO antenna with WLAN and complete X-band notched characteristics, checked with characteristic mode analysis (CMA)," *Analog Integrated Circuits and Signal Processing*, Feb. 2023.

[10] F. Bahmanzadeh and F. Mohajeri, "Simulation and fabrication of a high-isolation very compact MIMO antenna for ultra-wide band applications with dual band-notched characteristics," *AEU - International Journal of Electronics and Communications*, vol. 128, p. 153505, Jan. 2021.

[11] Q. Li, Y. Sun, and H. Fang, "Compact ACS-fed UWB MIMO antenna with dual band notches," *Applied Computational Electromagnetics Society (ACES) Journal*, vol. 36, no. 1, pp. 55-60, Feb. 2021.

[12] J. Banerjee, A. Karmakar, R. Ghatak, and D. R. Poddar, "Compact CPW-fed UWB MIMO antenna with a novel modified Minkowski fractal defected ground structure (DGS) for high isolation and triple band-notch characteristic," *Journal of Electromagnetic Waves and Applications*, vol. 31, no. 15, pp. 1550-1565, Oct. 2017.

[13] S. Jayant and G. Srivastava, "Close-packed Quad-element Triple-band-notched UWB MIMO antenna with upgrading capability," in *IEEE Transactions on Antennas and Propagation*, vol. 71, no. 1, pp. 353-360, Jan. 2023.

[14] O. P. Kumar, P. Kumar, and T. Ali, "A compact dual-band notched UWB antenna for wireless applications," *Micromachines*, vol. 13, no. 1, p. 12, Dec. 2021.

[15] X. Li, Y. Li, J. T. Huang and O. Yang Du, "A cross-slot loaded miniaturized UWB Vivaldi dual-polarized antenna," *2021 International Conference on Microwave and Millimeter Wave Technology (ICMMT)*, Nanjing, China, pp. 1-3, May 2021.

[16] P. Kumari, R. K. Gangwar, and R. K. Chaudhary, "An aperture-coupled stepped dielectric resonator UWB MIMO antenna with AMC," *IEEE Antennas and Wireless Propagation Letters*, vol. 21, no. 10, pp. 2040-2044, Oct. 2022.

[17] H. Li and N. Gong, "An SRR and CSRR based UWB-MIMO antenna," *2020 IEEE International Symposium on Antennas and Propagation and North American Radio Science Meeting*, Montreal, QC, Canada, pp. 679-680, July 2020.

[18] Z. Yang, F. Li, and F. Li, "A compact slot MIMO antenna with band-notched characteristic for UWB application," *2018 International Conference on Microwave and Millimeter Wave Technology (ICMMT)*, Chengdu, May 2018.

[19] Z. Li, C. Yin, and X. Zhu, "Compact UWB MIMO Vivaldi antenna with dual band-notched characteristics," *IEEE Access*, vol. 7, pp. 38696-38701, Jan. 2019.

[20] Z. He, Z. Yang, and J. Lv, "Design of a novel band-notched antenna for UWB MIMO communication system," *2018 International Conference on Microwave and Millimeter Wave Technology (ICMMT)*, Chengdu, May 2018.

[21] A. K. Gautam, S. Yadav, and K. Rambabu, "Design of ultra-compact UWB antenna with band-notched characteristics for MIMO applications," *IET Microwaves, Antennas & Propagation*, vol. 12, no. 12, pp. 1895-1900, Oct. 2018.

[22] Z. Tang, X. Wu, J. Zhan, S. Hu, Z. Xi, and Y. Liu, "Compact UWB-MIMO antenna with high isolation and triple band-notched characteristics," *IEEE Access*, vol. 7, pp. 19856-19865, Jan. 2019.

[23] E. Thakur, N. Jaglan, and S. D. Gupta, "Design of compact triple band-notched UWB MIMO antenna with TVC-EBG structure," *Journal of Electromagnetic Waves and Applications*, vol. 34, no. 11, pp. 1601-1615, July 2020.

[24] N. Jaglan, S. D. Gupta, B. K. Kanaujia, S. Srivastava, and E. Thakur, "Triple band notched DG-CEBG structure based UWB MIMO/Diversity antenna," *Progress in Electromagnetics Research C*, vol. 80, pp. 21-37, Jan. 2018.

[25] Z. Tang, X. Wu, J. Zhan, S. Hu, Z. Xi, and Y. Liu, "Compact UWB-MIMO antenna with high isolation and triple band-notched characteristics," *IEEE Access*, pp. 19856-19865, Jan. 2019.

[26] M. Agarwal, J. K. Dhanoa, and M. K. Khandelwal, "Ultrawide band two-port MIMO diversity antenna with triple notch bands, stable gain and suppressed mutual coupling," *AEU - International Journal of Electronics and Communications*, vol. 120, p. 153225, June 2020.

[27] L. Wu, Y. Xia, and X. Cao, "A compact triple-band notched MIMO antenna for UWB systems," *Applied Computational Electromagnetics Society (ACES) Journal*, Jan. 2018.

[28] S. Jayant and G. Srivastava, "Compact 4 × 4 proximity coupled microstrip fed UWB stepped slot MIMO antenna having triple band rejection," *Wireless Personal Communications*, vol. 119, no. 4, pp. 3719-3734, Aug. 2021.

[29] S. Rahim, A. A. Elobied, W. Huang, and X. Yang, "Super-UWB MIMO antenna with dual band-notched and high gain," *Radio Science*, vol. 57, no. 11, Nov. 2022.

[30] P. Jha, A. Kumar, A. De, and R. K. Jain, "Design of UWB antenna based on CSRR and EBG notch for prevention of undesired band," *2021 8th International Conference on Signal Processing and Integrated Networks (SPIN)*, IEEE, pp. 982-986, 2021.

[31] L. Pei, C. Du, C. Shi, and H. Peng, "A gain enhanced low SAR dual-band MIMO antenna integrated with AMC for wearable ISM applications," *2022 7th International Conference on Communication, Image and Signal Processing (CCISP)*, Chengdu, China, 2022.

Chenzhu Du was born in Haikou, Hainan Province, China. She received the B.S. degree from the Xidian University, M.S. degree from Nanjing University of Posts and Telecommunications and PhD degree from Shanghai University, in 1995, 2003 and 2012, respectively, all in electromagnetic wave and microwave technology. She is currently an associate professor of Shanghai University of Electric Power. Her research interests include flexible antennas, multiband and wideband antennas, and MIMO technologies.

Huanchen Peng was born in Shanghai, China in 1999. He received the B.S. degree from the Shanghai University of Electric Power in 2021. He is currently pursuing the M.S degree in College of Electronics and Information Engineering, Shanghai University of Electric Power. His research interests include circular polarization antennas, flexible antennas, and multiband MIMO antennas.

Analytical Model of an E-core Driver-pickup Coils Probe Applied to Eddy Current Testing of Multilayer Conductor

Siquan Zhang

Department of Electrical and Automation
Shanghai Maritime University, Shanghai, 201306, China
sqzhang@shmtu.edu.cn

***Abstract* –** An analytical model of an E-core driver-pickup coils probe located above a multilayer conductor containing a hidden cylindrical conductor is presented. The truncated region eigenfunction expansion (TREE) method is used to deal with the axial symmetry problem, and the closed-form final expression of the induced voltage in the pickup coil is derived. The changes of the induced voltage in the pickup coil due to the hidden cylindrical conductor are examined and calculated in Mathematica. Experiments and finite element simulations are performed and the results are compared with the analytical results, and they are in good agreement.

***Index Terms* –** Analytical model, cylindrical conductor, E-core driver-pickup coils probe, eddy current testing, induced voltage.

I. INTRODUCTION

In the aviation, petrochemical, nuclear power, and other industries, nondestructive testing and evaluation (NDT&E) methods are extensively used to acquire information about important components and structures, which is of great significance to ensure the normal operation of equipment and prevent accidents. Eddy current testing (ECT) is a widely used NDT method for detecting conductor defects due to its distinct advantages, such as non-contact, high sensitivity, and low cost. If the ECT probe is an absolute coil probe, the information obtained is the coil impedance or coil impedance change [1–3]. If the probe consists of a driver coil and a pickup coil, an induced voltage will be generated in the pickup coil.

The purpose of many practical ECT is to find the characteristics of conductive materials or reconstruct the shape of defect in the conductor by measuring changes of the coil impedance or changes of the induced voltage in pickup coils [4–6]. In the defect inversion operation [7–8], a lot of time is consumed in the forward model for repeated computations. Therefore, a fast and accurate forward model is very important for conductive defect evaluation. In general, the analytical model has the advantages of fast calculation speed and high accuracy compared with the finite element method. The traditional ECT analytical models proposed by Dodd and Deeds, whose final expressions are in integral form, have been widely used in ECT for more than fifty years [9]. Later, Theodoulidis proposed the truncated region eigenfunction expansion (TREE) method, which can obtain the expression of response in the form of series [10]. Compared with traditional integral model, one of the most important advantages of the TREE method is its fast calculation speed.

Coils are usually combined with ferrite cores to form a magnetic core probe, such as I-core, E-core, and T-core probes. The magnetic core has the function of concentrating the magnetic field, reducing flux leakage and shielding external electromagnetic interference. Therefore, in ECT, the sensitivity of a ferrite core coil is higher than that of an air core coil [11–12]. Among various magnetic cores, E-core has been widely used due to its superior performance.

In this paper, as shown in Fig. 1, the analytical model of an E-core probe placed over a layered conductor is investigated. The probe consists of two coils, an inner coil and an outer coil, both surrounding the column of the E-core with a circular air gap. If one of the coils is selected as the excitation coil and the other as the pickup coil, an E-core driver-pickup probe is formed. If the inner and outer coils are connected in series, they can also form an absolute E-core probe. For the case of an absolute cored coil probe located above an infinite layered conductor, on a multilayer conductor containing air hole, or on a multilayer conductive disk, many scholars have conducted extensive research on their analytical models and derived expressions of the coil impedance of the E-core probe with air gap in various cases [12–15]. However, the analytical model of an E-core probe consisting of an excitation coil and a pickup coil above a multilayer conductor containing a hidden cylindrical conductor has not been examined. In some special applications, driver-pickup coils probes have advantages over

Submitted On: August 30, 2023
Accepted On: December 20, 2023

https://doi.org/10.13052/2023.ACES.J.381110

absolute coil probes, and the solution method for a multilayer half-space conductor containing a hidden cylindrical conductor is different from that for a multilayer conductor with air hole, so it is necessary to further investigate its analytical model.

II. SOLUTION

The analytical model shown in Fig. 2 (a) is first analyzed, a filamentary driver coil c_d and a filamentary pickup coil c_p. The two filamentary coils are on the same plane, but have different radii, and are both wound around the column of an E-core with a circular air gap. The probe is located above four layers of nonmagnetic conductors, the second layer is a hidden cylindrical conductor with radius c, and the remaining layers are half-space conductors. From top to bottom, the conductivities of each layer of conductors are σ_6, σ_7, σ_8, and σ_9, respectively. The plane $z = 0$ coincides with the upper surface of the conductor. The whole problem region is truncated into a cylinder with radius b in the radial direction, and the homogeneous Dirichlet condition is applied to the magnetic vector potential on the truncation boundary.

According to the problem geometry, nine regions are formed along the z-axis in Fig. 2 (a). The cylindrical conductor is hidden in region 7. For other regions, the eigenvalues of each region can be defined and calculated in a similar way as discussed for E-core coil in the references [12–14], and will not be repeated here.

Region 7 consists of two subregions: cylindrical conductor ($0 \le r \le c$) and air space ($c \le r \le b$). The magnetic vector potentials of these subregions can be expressed in general form as

$$A_c = A_E J_1(v_i r) F_1(u_i c) \quad 0 \le r \le c \quad , \tag{1}$$

$$A_a = A_E J_1(v_i c) F_1(u_i r) \quad c \le r \le b \quad , \tag{2}$$

where

$$F_n(u_i r) = J_n(u_i r) Y_1(u_i b) - J_1(u_i b) Y_n(u_i r), \tag{3}$$

where J_n and Y_n are first kind Bessel functions of n order. A_E is the unknown coefficient, and u_i and v_i are the corresponding discrete eigenvalues. The eigenvalues u_i and related values v_i can be computed from the roots of the following equation obtained from the interface conditions in the radial direction at $r = c$.

$$\frac{1}{\mu_7} v_i F_1(u_i c) J_0(v_i c) = u_i J_1(v_i c) F_0(u_i c). \tag{4}$$

Finding all eigenvalues accurately is crucial for the correctness of the final analytical calculation results. The Newton-Raphson iteration scheme is a reliable method for calculating eigenvalues [10]. In recent years, some more accurate methods have been proposed to ensure that all eigenvalues are found [16–18].

The relationship between u_i and v_i is as follows:

$$u_i = \sqrt{v_i^2 + j\omega\mu_0\mu_7\sigma_7}. \tag{5}$$

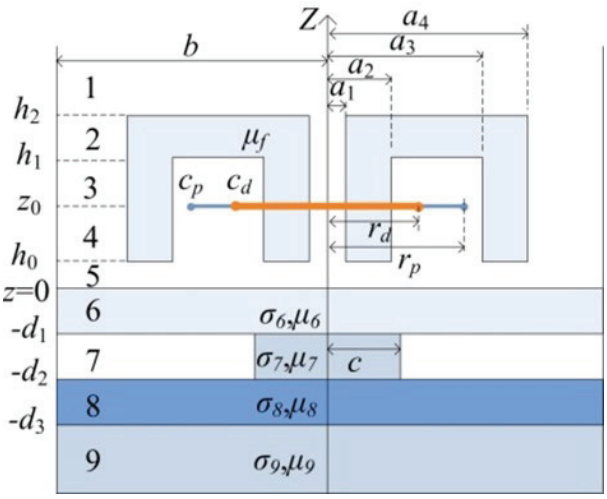

(a)

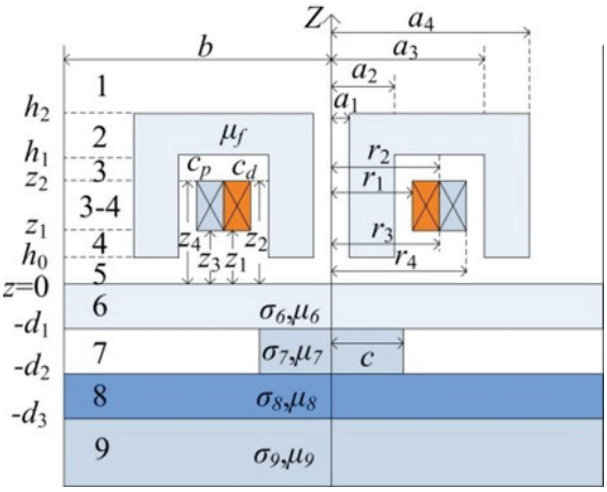

(b)

Fig. 2. Axially symmetric E-core (a) filamentary and (b) rectangular cross-section driver and pickup coils probe located above a layered conductor containing a cylindrical conductor.

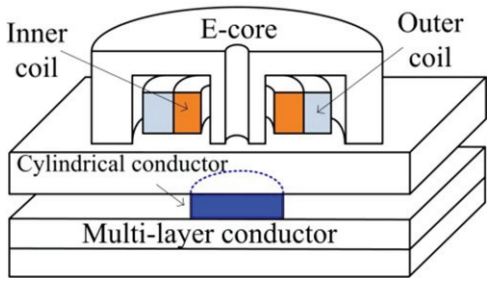

Fig. 1. E-core driver and pickup coils probe located above layered conductor containing a hidden cylindrical conductor.

The general expressions of the magnetic vector potential in the nine regions in Fig. 2 (a) can be expressed in matrix form as follows:

$$\mathbf{A}_1(r,z) = J_1(\mathbf{q}r)\mathbf{q}^{-1}e^{-\mathbf{q}z}\mathbf{C}_1, \tag{6}$$

$$\mathbf{A}_2(r,z) = \begin{cases} J_1(\mathbf{m}r) & 0 \le r \le a_1 \\ R_1(\mathbf{m}r)\mathbf{m}^{-1}\left(e^{-\mathbf{m}z}\mathbf{C}_2 - e^{\mathbf{m}z}\mathbf{B}_2\right) & a_1 \le r \le a_4 \\ R_1'(\mathbf{m}r) & a_4 \le r \le b \end{cases}, \tag{7}$$

$$\mathbf{A}_3(r,z) = \begin{cases} J_1(\mathbf{p}r) & 0 \le r \le a_1 \\ L_1(\mathbf{p}r) & a_1 \le r \le a_2 \\ L_1'(\mathbf{p}r)\mathbf{p}^{-1}\left(e^{-\mathbf{p}z}\mathbf{C}_3 - e^{\mathbf{p}z}\mathbf{B}_3\right) & a_2 \le r \le a_3 \\ L''(\mathbf{p}r) & a_3 \le r \le a_4 \\ L'''(\mathbf{p}r) & a_4 \le r \le b \end{cases}, \tag{8}$$

$$\mathbf{A}_4(r,z) = \begin{cases} J_1(\mathbf{p}r) & 0 \le r \le a_1 \\ L_1(\mathbf{p}r) & a_1 \le r \le a_2 \\ L_1'(\mathbf{p}r)\mathbf{p}^{-1}\left(e^{-\mathbf{p}z}\mathbf{C}_4 - e^{\mathbf{p}z}\mathbf{B}_4\right) & a_2 \le r \le a_3 \\ L''(\mathbf{p}r) & a_3 \le r \le a_4 \\ L'''(\mathbf{p}r) & a_4 \le r \le b \end{cases}, \tag{9}$$

$$\mathbf{A}_5(r,z) = J_1(\mathbf{q}r)\mathbf{q}^{-1}\left(e^{-\mathbf{q}z}\mathbf{C}_5 - e^{\mathbf{q}z}\mathbf{B}_5\right), \tag{10}$$

$$\mathbf{A}_6(r,z) = J_1(\mathbf{q}r)\mathbf{s}_6^{-1}\left(e^{-\mathbf{s}_6 z}\mathbf{C}_6 - e^{\mathbf{s}_6 z}\mathbf{B}_6\right), \tag{11}$$

$$\mathbf{A}_7(r,z) = \begin{cases} J_1(\mathbf{v}r)F_1(\mathbf{u}c) \\ F_1(\mathbf{u}r)J_1(\mathbf{v}c) \end{cases}\mathbf{u}^{-1}\left(e^{-\mathbf{u}z}\mathbf{C}_7 - e^{\mathbf{u}z}\mathbf{B}_7\right) \begin{matrix} 0 \leqslant r \leqslant c \\ c \leqslant r \leqslant b \end{matrix}, \tag{12}$$

$$\mathbf{A}_8(r,z) = J_1(\mathbf{q}r)\mathbf{s}_8^{-1}(e^{-\mathbf{s}_8 z}\mathbf{C}_8 - e^{\mathbf{s}_8 z}\mathbf{B}_8), \tag{13}$$

$$\mathbf{A}_9(r,z) = -J_1(\mathbf{q}r)\mathbf{s}_9^{-1}e^{\mathbf{s}_9 z}\mathbf{B}_9, \tag{14}$$

where

$$\mathbf{s}_6 = \sqrt{\mathbf{q}^2 + j\omega\mu_0\mu_6\sigma_6}, \tag{15}$$

$$\mathbf{s}_8 = \sqrt{\mathbf{q}^2 + j\omega\mu_0\mu_8\sigma_8}, \tag{16}$$

$$\mathbf{s}_9 = \sqrt{\mathbf{q}^2 + j\omega\mu_0\mu_9\sigma_9}. \tag{17}$$

The magnetic vector potential of each region in Fig. 2 (a) can be obtained by solving equations (6) to (14) using the interface conditions. The magnetic vector potential between region 3 and region 4 in Fig. 2 (b) can be derived by replacing z_2 with z in $\mathbf{A}_3$ and z_1 with z in $\mathbf{A}_4$, and then adding them together.

In Fig. 2 (b), the magnetic induction in z direction generated by the N_d turns excitation coil in region 3-4 can be expressed as follows:

$$\begin{aligned} \mathbf{B}_{z(3-4)} = {} & \frac{\mu N_d I}{2(r_2-r_1)(z_2-z_1)}\mathbf{D}^{-1}\mathbf{p}L_0'(\mathbf{p}r) \\ & \times [\mathbf{p}^{-4}\int_{\mathbf{p}r_1}^{\mathbf{p}r_2}\mathbf{p}r_d L_1'(\mathbf{p}r_d)d(\mathbf{p}r_d)] \\ & \cdot \Big\langle \quad (e^{-\mathbf{p}z}\mathbf{C}_{49} - e^{\mathbf{p}z}\mathbf{B}_{49}) \\ & \times \frac{\lambda_2[e^{\mathbf{p}(h_1-z_1)} - e^{\mathbf{p}(h_1-z_2)}] - \lambda_1[e^{\mathbf{p}(z_2-h_1)} - e^{\mathbf{p}(z_1-h_1)}]}{\lambda_1 e^{-\mathbf{p}h_1}\mathbf{C}_{49} - \lambda_2 e^{\mathbf{p}h_1}\mathbf{B}_{49}} \\ & + [2 - e^{\mathbf{p}(z_1-z)} - e^{\mathbf{p}(z-z_1)}] \quad \Big\rangle \end{aligned} \tag{18}$$

where I is the excitation current flowing in the driver coil.

When the z-direction magnetic induction intensity generated by the excitation coil passes through the pickup coil, the magnetic flux penetrating the N_p turns of pickup coil can be obtained as:

$$\begin{aligned} \phi = {} & \frac{\pi\mu N_d N_p I}{(r_2-r_1)(z_2-z_1)(r_4-r_3)(z_4-z_3)} \\ & \times \mathbf{D}^{-1}[\mathbf{p}^{-4}\int_{\mathbf{p}r_1}^{\mathbf{p}r_2}\mathbf{p}r_d L_1'(\mathbf{p}r_d)d(\mathbf{p}r_d)] \\ & \cdot \langle [(e^{-\mathbf{p}z_3} - e^{-\mathbf{p}z_4})\mathbf{C}_{49} + (e^{\mathbf{p}z_3} - e^{\mathbf{p}z_4})\mathbf{B}_{49}] \\ & \times \frac{\lambda_2[e^{\mathbf{p}(h_1-z_1)} - e^{\mathbf{p}(h_1-z_2)}] - \lambda_1[e^{\mathbf{p}(z_2-h_1)} - e^{\mathbf{p}(z_1-h_1)}]}{\lambda_1 e^{-\mathbf{p}h_1}\mathbf{C}_{49} - \lambda_2 e^{\mathbf{p}h_1}\mathbf{B}_{49}} \\ & + [2\mathbf{p}(z_4-z_3) + e^{\mathbf{p}(z_1-z_4)} - e^{\mathbf{p}(z_1-z_3)} - e^{\mathbf{p}(z_4-z_1)} + e^{\mathbf{p}(z_3-z_1)}] \rangle \\ & \cdot \mathbf{p}^{-3}\int_{pr_3}^{pr_4}\mathbf{p}r_p L_1'(\mathbf{p}r_p)d(\mathbf{p}r_p) \end{aligned} \tag{19}$$

The induced voltage generated in the pickup coil of rectangular cross section is derived as follows:

$$\begin{aligned} V = {} & V_{co}\cdot\mathbf{D}^{-1}\cdot\mathbf{p}^{-4}\chi'(\mathbf{p}r_1,\mathbf{p}r_2)\cdot(\mathbf{W}_1\mathbf{W}_2^{-1}\mathbf{W}_3 + \mathbf{W}_4) \\ & \cdot\mathbf{p}^{-3}\chi'(\mathbf{p}r_3,\mathbf{p}r_4), \end{aligned} \tag{20}$$

where

$$V_{co} = \frac{j\omega\pi\mu N_d N_p I}{(r_2-r_1)(z_2-z_1)(r_4-r_3)(z_4-z_3)}, \tag{21}$$

$$\chi'(x_1,x_2) = \int_{x_1}^{x_2} x L_1'(x)dx, \tag{22}$$

$$\mathbf{W}_1 = (e^{-\mathbf{p}z_3} - e^{-\mathbf{p}z_4})\mathbf{C}_{49} + (e^{\mathbf{p}z_3} - e^{\mathbf{p}z_4})\mathbf{B}_{49}, \tag{23}$$

$$\mathbf{W}_2 = \lambda_1 e^{-\mathbf{p}h_1}\mathbf{C}_{49} - \lambda_2 e^{\mathbf{p}h_1}\mathbf{B}_{49}, \tag{24}$$

$$\mathbf{W}_3 = \lambda_2[e^{\mathbf{p}(h_1-z_1)} - e^{\mathbf{p}(h_1-z_2)}] - \lambda_1[e^{\mathbf{p}(z_2-h_1)} - e^{\mathbf{p}(z_1-h_1)}], \tag{25}$$

$$\begin{aligned} \mathbf{W}_4 = {} & 2\mathbf{p}(z_4-z_3) + e^{\mathbf{p}(z_1-z_4)} - e^{\mathbf{p}(z_1-z_3)} \\ & - e^{\mathbf{p}(z_4-z_1)} + e^{\mathbf{p}(z_3-z_1)} \end{aligned}, \tag{26}$$

$$\begin{aligned} \lambda_1 = {} & (\mathbf{T}-\mathbf{U})e^{\mathbf{m}(h_1-h_2)}\mathbf{F}^{-1}(\mathbf{H}+\mathbf{G}) \\ & -(\mathbf{T}+\mathbf{U})e^{\mathbf{m}(h_2-h_1)}\mathbf{F}^{-1}(\mathbf{H}-\mathbf{G}) \end{aligned}, \tag{27}$$

$$\begin{aligned} \lambda_2 = {} & [(\mathbf{T}+\mathbf{U})e^{\mathbf{m}(h_2-h_1)}\mathbf{F}^{-1}(\mathbf{H}+\mathbf{G}) \\ & -(\mathbf{T}-\mathbf{U})e^{\mathbf{m}(h_1-h2)}\mathbf{F}^{-1}(\mathbf{H}-\mathbf{G})] \end{aligned}, \tag{28}$$

$$\begin{matrix} \mathbf{C}_{89} \\ \mathbf{B}_{89} \end{matrix} = \frac{1}{2}e^{\mp\mathbf{s}_8 d_3}(1 \mp \mathbf{s}_8\mathbf{s}_9^{-1})e^{-\mathbf{s}_9 d_3}, \tag{29}$$

$$\begin{aligned} \begin{matrix} \mathbf{C}_{79} \\ \mathbf{B}_{79} \end{matrix} = {} & \frac{1}{2}e^{\mp\mathbf{u}d_2}[(\mathbf{N}^{*-1}\mathbf{E} \pm \mathbf{N}^{-1}\mathbf{E}\mathbf{q}\mathbf{s}_8^{-1})e^{\mathbf{s}_8 d_2}\mathbf{C}_{89} \\ & + (\mathbf{N}^{*-1}\mathbf{E} \mp \mathbf{N}^{-1}\mathbf{E}\mathbf{q}\mathbf{s}_8^{-1})e^{-\mathbf{s}_8 d_2}\mathbf{B}_{89}] \end{aligned}, \tag{30}$$

$$\begin{aligned} \begin{matrix} \mathbf{C}_{69} \\ \mathbf{B}_{69} \end{matrix} = {} & \frac{1}{2}e^{\mp\mathbf{s}_6 d_1}[(\mathbf{E}^{-1}\mathbf{N}^* \pm \mathbf{s}_6\mathbf{q}^{-1}\mathbf{E}^{-1}\mathbf{N})e^{\mathbf{u}d_1}\mathbf{C}_{79} \\ & + (\mathbf{E}^{-1}\mathbf{N}^* \mp \mathbf{s}_6\mathbf{q}^{-1}\mathbf{E}^{-1}\mathbf{N})e^{-\mathbf{u}d_1}\mathbf{B}_{79}] \end{aligned}, \tag{31}$$

$$\begin{matrix} \mathbf{C}_{59} \\ \mathbf{B}_{59} \end{matrix} = \frac{1}{2}[(\mu_6^{-1} \pm \mathbf{q}\mathbf{s}_6^{-1})\mathbf{C}_{69} + (\mu_6^{-1} \mp \mathbf{q}\mathbf{s}_6^{-1})\mathbf{B}_{69}], \tag{32}$$

$$\begin{aligned} \begin{matrix} \mathbf{C}_{49} \\ \mathbf{B}_{49} \end{matrix} = {} & \frac{1}{2}e^{\pm\mathbf{p}h_0}\mathbf{D}^{-1} \\ & \times [(\mathbf{H}^* \pm \mathbf{G}^*)e^{-\mathbf{q}h_0}\mathbf{C}_{59} + (\mathbf{H}^* \mp \mathbf{G}^*)e^{\mathbf{q}h_0}\mathbf{B}_{59}]. \end{aligned} \tag{33}$$

The definitions of T, U, F, D, H, G, N, $\mathbf{N}^*$, $\mathbf{H}^*$ and $\mathbf{G}^*$ can be found in the APPENDIX.

III. SPECIAL CASES

When the radius of the hidden cylindrical conductor in the second layer is infinite, the general expression of the magnetic vector potential for region 7 in Fig. 2 (a) becomes

$$A_7(r,z) = J_1(\mathbf{q}r)\mathbf{s}_7^{-1}(e^{-\mathbf{s}_7 z}\mathbf{C}_7 - e^{\mathbf{s}_7 z}\mathbf{B}_7), \quad (34)$$

where

$$\mathbf{s}_7 = \sqrt{\mathbf{q}^2 + j\omega\mu_0\mu_7\sigma_7}. \quad (35)$$

The induced voltage of the pickup coil can still be expressed as (20), but some coefficients need to be changed as follows:

$$\begin{matrix}\mathbf{C}_{79}\\ \mathbf{B}_{79}\end{matrix} = \frac{1}{2}e^{\mp\mathbf{s}_7 d_2}\begin{matrix}[(1\pm\mathbf{s}_7\mathbf{s}_8^{-1})e^{\mathbf{s}_8 d_2}\mathbf{C}_{89}\\ +(1\mp\mathbf{s}_7\mathbf{s}_8^{-1})e^{-\mathbf{s}_8 d_2}\mathbf{B}_{89}]\end{matrix}, \quad (36)$$

$$\begin{matrix}\mathbf{C}_{69}\\ \mathbf{B}_{69}\end{matrix} = \frac{1}{2}e^{\mp\mathbf{s}_6 d_1}\begin{matrix}[(1\pm\mathbf{s}_6\mathbf{s}_7^{-1})e^{\mathbf{s}_7 d_1}\mathbf{C}_{79}\\ +(1\mp\mathbf{s}_6\mathbf{s}_7^{-1})e^{-\mathbf{s}_7 d_1}\mathbf{B}_{79}]\end{matrix}. \quad (37)$$

When the hidden cylindrical conductor of the second layer is absent, the induced voltage in the pickup coil of the probe over multilayer conductor can be calculated using (20) by setting $\sigma_7 = 0$.

When the multilayer conductor is absent, the induced voltage in the pickup coil can also be calculated using (20) by setting $\sigma_6 = \sigma_7 = \sigma_8 = \sigma_9 = 0$.

When the E-core shown in Fig. 2 (a) is absent, only two regions remain above the layered conductor, region 4 above and region 5 below the filamentary coil. The general expression of the magnetic vector potential for region 4 becomes

$$A_4(r,z) = J_1(\mathbf{q}r)\mathbf{q}^{-1}e^{-\mathbf{q}z}\mathbf{C}_4. \quad (38)$$

The expression of the induced voltage in the pickup coil of an air-core probe can be derived as

$$V' = 2V_{co}\cdot\mathbf{E}^{-1}\cdot\mathbf{q}^{-4}\chi(\mathbf{q}r_1,\mathbf{q}r_2)\cdot(\mathbf{W}_5\mathbf{W}_6^{-1}+\mathbf{W}_7)\cdot\mathbf{q}^{-3}\chi(\mathbf{q}r_3,\mathbf{q}r_4), \quad (39)$$

where

$$\chi(x_1,x_2) = \int_{x_1}^{x_2} xJ_1(x)dx, \quad (40)$$

$$\begin{aligned}\mathbf{W}_5 =&[\mathbf{q}(z_4-z_3) - e^{\mathbf{q}(z_4-z_2)} + e^{\mathbf{q}(z_3-z_2)}]\mathbf{B}_{59}\\ &+[e^{-\mathbf{q}(z_4+z_1)} - e^{-\mathbf{q}(z_4+z_2)} - e^{-\mathbf{q}(z_3+z_1)} + e^{-\mathbf{q}(z_3+z_2)}]\mathbf{C}_{59}\end{aligned}, \quad (41)$$

$$\mathbf{W}_6 = (1-\mathbf{q}\mathbf{s}_6^{-1})\mathbf{C}_{69} + (1+\mathbf{q}\mathbf{s}_6^{-1})\mathbf{B}_{69}, \quad (42)$$

$$\mathbf{W}_7 = \frac{1}{2}[\mathbf{q}(z_4-z_3) + e^{\mathbf{q}(z_1-z_4)} - e^{\mathbf{q}(z_1-z_3)}]. \quad (43)$$

When the E-core and the cylindrical conductor in the second-layer are both absent, the induced voltage in the pickup coil of an air-core probe can be calculated using (39) by setting $\sigma_7 = 0$, and the coefficients of C_{79}, B_{79}, C_{69}, and B_{69} are same as (36) and (37). When the E-core and the layered conductor are both absent, the voltage induced in the pickup coil of an air-core probe can also be calculated using (39) by setting $\sigma_6 = \sigma_7 = \sigma_8 = \sigma_9 = 0$.

For the above examined analytical model as shown in Fig. 1, the inner coil is used as driver coil and the outer coil is used as pickup coil. When the excitation is applied to the outer coil and the inner coil is used as pickup coil, the voltage induced in the pickup coil can be expressed as

$$\begin{aligned}V'' = V_{co}\cdot\mathbf{D}^{-1}\cdot\mathbf{p}^{-4}\chi'(\mathbf{p}r_3,\mathbf{p}r_4)\cdot(\mathbf{W}_1'\mathbf{W}_2^{-1}\mathbf{W}_3'+\mathbf{W}_4')\\ \cdot\mathbf{p}^{-3}\chi'(\mathbf{p}r_1,\mathbf{p}r_2)\end{aligned}, \quad (44)$$

where

$$\mathbf{W}_1' = (e^{-\mathbf{p}z_1} - e^{-\mathbf{p}z_2})\mathbf{C}_{49} + (e^{\mathbf{p}z_1} - e^{\mathbf{p}z_2})\mathbf{B}_{49}, \quad (45)$$

$$\mathbf{W}_3' = \lambda_2[e^{\mathbf{p}(h_1-z_3)} - e^{\mathbf{p}(h_1-z_4)}] - \lambda_1[e^{\mathbf{p}(z_4-h_1)} - e^{\mathbf{p}(z_3-h_1)}], \quad (46)$$

$$\mathbf{W}_4' = 2\mathbf{p}(z_2-z_1) + e^{\mathbf{p}(z_3-z_2)} - e^{\mathbf{p}(z_3-z_1)} - e^{\mathbf{p}(z_2-z_3)} + e^{\mathbf{p}(z_1-z_3)}. \quad (47)$$

The other expressions of the coefficients used in calculation are same as (22), (24), and (27)-(33).

IV. FEM AND EXPERIMENT VALIDATION

First, the analytical model is verified using the finite element method (FEM). The software ANSYS Maxwell is used to construct the simulation model according to Fig. 2 (b), and the parameters used are the same as those in Table 1. Maxwell 2D and 3D models as shown in Figs. 3 and 4 can be established respectively. The solution type is chosen to be transient, and a sinusoidal wave current with an effective value of 0.1 A and a frequency range of 0.1 kHz to 10 kHz is applied to the excitation coil. When the stopping time and time step are set, the model can be analyzed, and the results of transient report can be generated after the simulation is finished. The induced voltage waveform in the pickup coil can be plotted as shown in Fig. 5, and the peak value of the induced voltage is extracted and used for comparison.

Since the model examined in this paper is axisymmetric, a 2D model is used for the finite element simulation. Compared with 3D models, 2D models have the advantages of simple modeling and short running time to obtain results.

The correctness of the analytical model is also verified by experimental measurement.

The E-core and homemade driver and pickup coils are shown in Fig. 6. The material characteristic param-

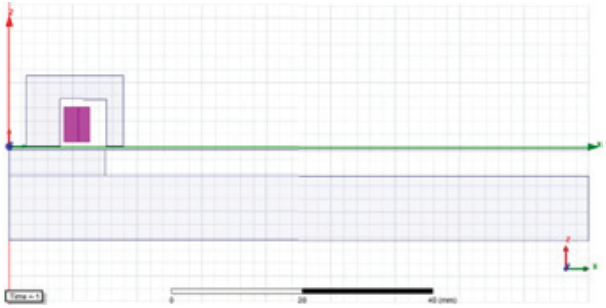

Fig. 3. ANSYS Maxwell 2D model.

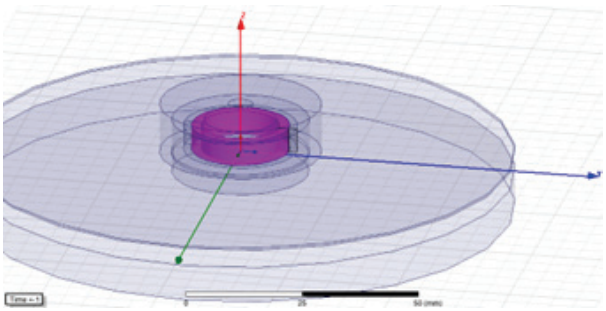

Fig. 4. ANSYS Maxwell 3D model.

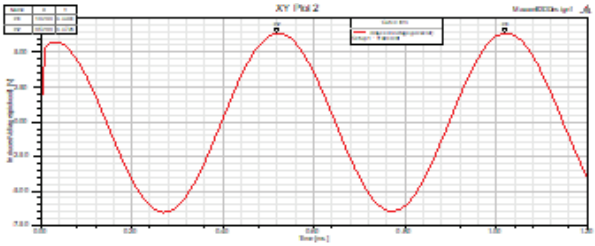

Fig. 5. Induced voltage in the pickup coil and the effective value of excitation current and frequency are 0.1 A and 2 kHz, respectively.

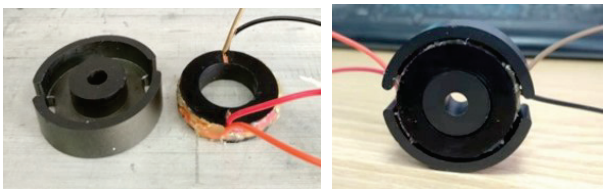

(a) (b)

Fig. 6. (a) E-core, driver-pickup coils and (b) E-core probe used in experiments.

eters of the magnetic core and conductor are collected from the manufacturers. All parameters used in experiments are shown in Table 1.

The effective value of the sinusoidal excitation current applied to the driver coil is maintained at 0.1 A by adjusting the amplitude of the sinusoidal signal in the signal generator and the amplification factor of the power amplifier. The induced voltage in the pickup coil is measured by a millivolt meter.

Firstly, when the driver coil is excited by a sinusoidal signal with a frequency range from 0.1 kHz to 10 kHz, the induced voltage in the pickup coil of the E-core probe located above a layered conductor is measured. The second layer is a cylindrical conductor with a radius of 15 mm and a thickness of 4 mm, and the other layers are square conductive plates with a side length of 15 cm and different thicknesses. Then, the cylindrical conductor of the second layer is replaced with a non-conductive material of equal thickness, and the above measurement is repeated. Finally, when the layered conductor is absent, the above measurements are repeated again.

Table 1: Parameters of E-core, coils, and conductor used in analytical calculation, FEM and experiment

Coil		
Inner radius of driver coil	r_1	8.58 mm
Outer radius of driver coil	r_2	10.7 mm
Inner radius of pickup coil	r_3	10.8 mm
Outer radius of pickup coil	r_4	12.5 mm
Parameter	z_1, z_3	0.74 mm
Parameter	z_2, z_4	6.14 mm
Excitation current	I	0.1 A
Number of turns (driver)	N_d	280
Number of turns (pickup)	N_p	310
Ferrite Core		
Inner column radius	a_1	2.7 mm
Outer column radius	a_2	7.95 mm
Inner core radius	a_3	15.1 mm
Outer core radius	a_4	17.74 mm
Core liftoff	h_0	0.1 mm
Inner core height	h_1	7.4 mm
Outer core height	h_2	11.1 mm
Core permeability	μ_f	3500
Conductor		
Parameter	d_1	0.5 mm
Parameter	d_2	4.5 mm
Parameter	d_3	5 mm
Cylindrical conductor radius	c	15 mm
Relative permeability	μ_6,μ_7,μ_8,μ_9	1
Conductivity	σ_6,σ_7,σ_8,σ_9	36 MS/m
Radius of the domain	b	60 mm

V. RESULTS AND DISCUSSION

First, as shown in Fig. 2 (b), equation (20) is used to calculate the induced voltage in the pickup coil when the E-core probe is located above the multilayer conductor. The excitation current is 0.1 A, and the excitation frequency range is 0.1 kHz to 10 kHz. Then the induced voltages in the pickup coil without layered conductor and without hidden cylindrical conductor are calculated, respectively. The calculations are implemented in Mathematica using the parameters shown in Table 1. In all these calculations, the solution domain truncation value $b = 60$ mm (5 times the outer radius of the outer coil) and the number of summation terms $N_s = 60$.

The analytical calculation results are compared with those of FEM and experiment. When the driver coil is excited by current signals of different frequencies, the relationship between the changes of the effective value

of the induced voltage in the pickup coil and the excitation frequency due to the hidden cylindrical conductor is shown in Fig. 7. When the excitation frequency is increased, the absolute value of the induced voltage change in the pickup coil first increases and then decreases, and the maximum value of the induced voltage change occurs when the excitation frequency is approximately 2.5 kHz. When the excitation frequency is fixed at 2 kHz and only the excitation current is changed, the change of induced voltage in the pickup coil due to the cylindrical conductor is shown in Fig. 8. The results show that as the excitation current increases,

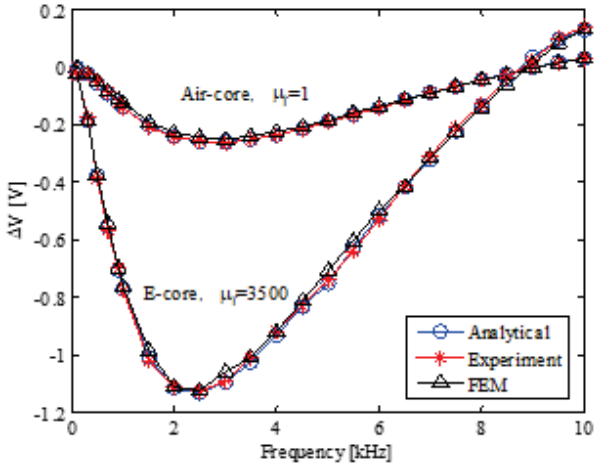

Fig. 7. The relationship between excitation frequency and the change of induced voltage in the pickup coil due to cylindrical conductor for an air-core coil (μ_f = 1) and an E-core coil (μ_f = 3500).

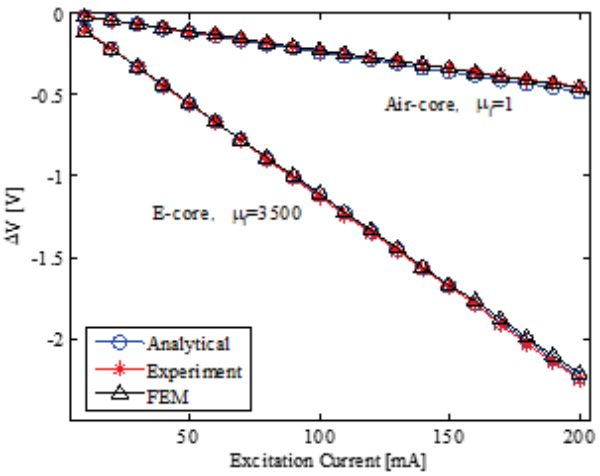

Fig. 8. The relationship between the excitation current and the change of induced voltage in the pickup coil due to the cylindrical conductor for an air-core coil (μ_f = 1) and an E-core coil (μ_f = 3500).

the change of induced voltage in the pickup coil also increases.

In all the above cases, the change of induced voltage in the pickup coil of the E-core probe is larger than that of the air-core probe, which indicates that the E-core probe has a higher sensitivity than that of the air-core probe.

For E-core driver and pickup coils probe, in all cases the relative error of ΔV between analytical calculation and experimental measurement or FEM is less than 2%, which shows a good agreement.

VI. CONCLUSION

The analytical model of an E-core driver and pickup coils probe over a layered conductor containing hidden cylindrical conductor is proposed using the TREE method. The expressions for the induced voltage in the pickup coil are derived for the general case and for several special cases. The analytical results are compared with the results of experiment and FEM, and they are in good agreement. The proposed analytical model can be used for the design of ferrite cored driver-pickup probes, ECT simulation of multilayer conductors, and can also be used directly for the detection and evaluation of hidden metallic components (such as coins and corrosion) in layered conductive materials.

REFERENCES

[1] S. Zhang, "Analytical model of an I-core coil for nondestructive evaluation of a conducting cylinder below an infinite plane conductor," *Measurement Science Review*, vol. 21, no. 4, pp. 99-105, 2021.

[2] T. Theodoulidis and J. R. Bowler, "Impedance of a coil at an arbitrary position and orientation inside a conductive borehole or tube," *IEEE Transactions on Magnetics*, vol. 51, no. 4, pp. 1-6, 2015.

[3] T. Theodoulidis and R. J. Ditchburn, "Mutual impedance of cylindrical coils at an arbitrary position and orientation above a planar conductor," *IEEE Transactions on Magnetics*, vol. 43, no. 8, pp. 3368-3370, 2007.

[4] D. Desjardins, T. W. Krause, and L. Clapham, "Transient response of a driver-pickup coil probe in transient eddy current testing," *NDT & E International*, vol. 75, pp. 8-14, 2015.

[5] H. Huang and T. Takagi, "Inverse analysis for natural and multicracks using signals from a differential transmit-receive ECT probe," *IEEE Transactions on Magnetics*, vol. 38, no. 2, pp. 1009-1012, 2002.

[6] S. Zhang and C. Ye, "Model of ferrite-cored driver-pickup coil probe application of TREE method for eddy current nondestructive evaluation," *Applied Computational Electromagnetics Society (ACES) Journal*, vol. 37, no. 5, pp. 632-638, 2022.

[7] Z. Chen, G. Preda, O. Mihalache, and K. Miya, "Reconstruction of crack shapes from the MFLT signals by using a rapid forward solver and an optimization approach," *IEEE Transactions on Magnetics*, vol. 38, no. 2, pp. 1025-1028, 2002.

[8] W. Cheng, K. Miya, and Z. Chen, "Reconstruction of cracks with multiple eddy current coils using a database approach," *Journal of Nondestructive Evaluation*, vol. 18, no. 4, pp. 149-160, 1999.

[9] C. V. Dodd and W. E. Deeds, "Analytical solutions to eddy current probe coil problems," *Journal of Applied Physics*, vol. 39, no. 6, pp. 2829-2838, 1968.

[10] T. Theodoulidis and E. E. Kriezis, *Eddy Current Canonical Problems (With Applications to Nondestructive Evaluation)*, Tech Sci. Press, Duluth, Georgia, 2006.

[11] S. Zhang, "An analytical model of a new T-cored coil used for eddy current nondestructive evaluation," *Applied Computational Electromagnetics Society (ACES) Journal*, vol. 35, no. 9, pp. 1099-1104, 2020.

[12] G. Tytko and L. Dziczkowski, "E-cored coil with a circular air gap inside the core column used in eddy current testing," *IEEE Transactions on Magnetics*, vol. 51, no. 9, pp. 1-4, 2015.

[13] G. Tytko, "An eddy current model of pot-cored coil for testing multilayer conductors with a hole," *Bulletin of the Polish Academy of Sciences Technical Sciences*, vol. 68, no. 6, pp. 1311-1317, 2020.

[14] G. Tytko, "Measurement of multilayered conductive discs using eddy current method," *Measurement*, vol. 204, pp. 112053, 2022.

[15] S. Zhang, "Analytical model of a T-core coil above a multi-layer conductor with hidden hole using the TREE method for nondestructive evaluation," *COMPEL: The International Journal for Computation and Mathematics in Electrical and Electronic Engineering*, vol. 40, no. 6, pp. 1104-1117, 2021.

[16] D. Vasic, D. Ambrus, and V. Bilas, "Computation of the eigenvalues for bounded domain eddy-current models with coupled regions," *IEEE Transactions on Magnetics*, vol. 52, no. 6, 7004310, 2016.

[17] G. Tytko and L. Dawidowski, "Locating complex eigenvalues for analytical eddy-current models used to detect flaws," *COMPEL: The International Journal for Computation and Mathematics in Electrical and Electronic Engineering*, vol. 38, no. 6, pp. 1800-1809, 2019.

[18] T. Theodoulidis, A. Skarlatos, and G. Tytko, "Computation of eigenvalues and eigenfunctions in the solution of eddy current problems," *Sensors*, vol. 23, no. 6, p. 3055, 2023.

APPENDIX

$$\mathbf{T}=\int_0^{a_1} rJ_0(\mathbf{q}r)J_0(\mathbf{m}r)dr+\int_{a_1}^{a_4} rJ_0(\mathbf{q}r)R_0(\mathbf{m}r)dr + \int_{a_4}^{b} rJ_0(\mathbf{q}r)R_0'(\mathbf{m}r)dr \quad , \tag{A.1}$$

$$\mathbf{U}=\int_0^{a_1} rJ_1(\mathbf{q}r)J_1(\mathbf{m}r)dr+\frac{1}{\mu_f}\int_{a_1}^{a_4} rJ_1(\mathbf{q}r)R_1(\mathbf{m}r)dr + \int_{a_4}^{b} rJ_1(\mathbf{q}r)R_1(\mathbf{m}r)dr \quad , \tag{A.2}$$

$$\mathbf{F}=\int_0^{a_1} rJ_0(\mathbf{m}r)J_0(\mathbf{m}r)+\int_{a_1}^{a_4} rR_0(\mathbf{m}r)R_0(\mathbf{m}r)dr) + \int_{a_4}^{b} rR_0'(\mathbf{m}r)R_0'(\mathbf{m}r)dr \quad , \tag{A.3}$$

$$\mathbf{G}=\int_0^{a_1} rJ_0(\mathbf{m}r)J_0(\mathbf{p}r)dr+\int_{a_1}^{a_2} rR_0(\mathbf{m}r)L_0(\mathbf{p}r)dr + \int_{a_2}^{a_3} rR_0(\mathbf{m}r)L_0'(\mathbf{p}r)dr+\int_{a_3}^{a_4} rR_0(\mathbf{m}r)L_0''(\mathbf{p}r)dr, + \int_{a_4}^{b} rR_0'(\mathbf{m}r)L_0'''(\mathbf{p}r)dr) \tag{A.4}$$

$$\mathbf{H}=\int_0^{a_1} J_1(\mathbf{m}r)J_1(\mathbf{p}r)dr+\frac{1}{\mu_f}\int_{a_1}^{a_2} rR_1(\mathbf{m}r)L_1(\mathbf{p}r)dr + \int_{a_2}^{a_3} rR_1(\mathbf{m}r)L_1'(\mathbf{p}r)dr+\frac{1}{\mu_f}\int_{a_3}^{a_4} rR_1(\mathbf{m}r)L_1''(\mathbf{p}r)dr, + \int_{a_4}^{b} rR_1'(\mathbf{m}r)L_1'''(\mathbf{p}r)dr \tag{A.5}$$

$$\mathbf{D}=\int_0^{a_1} rJ_1(\mathbf{p}r)J_1(\mathbf{p}r)dr+\frac{1}{\mu_f}\int_{a_1}^{a_2} rL_1(\mathbf{p}r)L_1(\mathbf{p}r) + \int_{a_2}^{a_3} rL_1'(\mathbf{p}r)L_1'(\mathbf{p}r)dr+\frac{1}{\mu_f}\int_{a_3}^{a_4} rL_1''(\mathbf{p}r)L_1''(\mathbf{p}r)dr, + \int_{a_4}^{b} rL_1'''(\mathbf{p}r)L_1'''(\mathbf{p}r)dr \tag{A.6}$$

$$\mathbf{G}^*=\int_0^{a_1} rJ_0(\mathbf{p}r)J_0(\mathbf{q}r)+\int_{a_1}^{a_2} rL_0(\mathbf{p}r)J_0(\mathbf{q}r)dr + \int_{a_2}^{a_3} rL_0'(\mathbf{p}r)J_0(\mathbf{q}r)dr+\int_{a_3}^{a_4} rL_0''(\mathbf{p}r)J_0(\mathbf{q}r), + \int_{a_4}^{b} rL_0'''(\mathbf{p}r)J_0(\mathbf{q}r)dr \tag{A.7}$$

$$\mathbf{H}^{*} = \int_{0}^{a_1} rJ_1(\mathbf{p}r)J_1(\mathbf{q}r) + \int_{a_1}^{a_2} rL_1(\mathbf{p}r)J_1(\mathbf{q}r)dr + \int_{a_2}^{a_3} rL_1'(\mathbf{p}r)J_1(\mathbf{q}r)dr + \int_{a_3}^{a_4} rL_1''(\mathbf{p}r)J_1(\mathbf{q}r), + \int_{a_4}^{b} rL_1'''(\mathbf{p}r)J_1(\mathbf{q}r)dr \tag{A.8}$$

$$\mathbf{N} = \mathbf{v}\mathbf{u}^{-1}\mathbf{F}_1(\mathbf{u}c)\int_{0}^{c} rJ_0(\mathbf{q}r)J_0(\mathbf{v}r)dr + J_1(\mathbf{v}c)\int_{c}^{b} rJ_0(\mathbf{q}r)\mathbf{F}_0(\mathbf{u}r)dr, \tag{A.9}$$

$$\mathbf{N}* = F_1(\mathbf{u}c)\int_{0}^{c} rJ_1(\mathbf{q}r)J_1(\mathbf{v}r)dr + J_1(\mathbf{v}c)\int_{c}^{b} rJ_1(\mathbf{q}r)F_1(\mathbf{u}r)dr. \tag{A.10}$$

Siquan Zhang received the Ph.D. degree in material processing engineering from the South China University of Technology, Guangzhou, China. His current research interests include eddy current testing and analytical models in non-destructive testing.